Bubble Size Measurement Via Wave Phase Conjugation: A Numerical Study

Amir Modarreszadeh

Department of Mechanical Engineering McGill University Montréal, Canada

April 2020



A thesis submitted to the McGill University in partial fulfillment of the requirements for the degree of Doctor of Philosophy

© 2020 Amir Modarreszadeh

To my family, for their unconditional love \cdots



Abstract

Measuring characteristics of gas bubbles in a fluid is among essential and challenging tasks in many industrial settings. It has been recently conjectured that such measurements could be more efficiently and accurately carried out by using a Wave Phase Conjugation (WPC) device due to its useful relevant properties, such as signal retro-focusing and compensation for phase distortions. In the present work, this technique in application to bubble size measurements is investigated via numerical modeling.

For this aim, a general physico-mathematical model of magneto-acoustic WPC is proposed, which includes wave propagation both in solid zones (the conjugator itself and other solid regions, if present) and in fluid zones surrounding the conjugator. Acoustic waves in the solid zones are assumed to behave linearly while in the fluid zones the waves may be either linear or non-linear. To accurately resolve these high-frequency transient waves, which have typically short wavelengths, high-order schemes in both time and space domains are required.

The 2D/axisymmetric governing equations of the model are discretized on an unstructured triangular mesh with a modified version of the Nodal Discontinuous Galerkin (NDG) method, which employs non-collocated solution and flux bases. The third-order Strong Stability-Preserving (SSP) Runge-Kutta (RK) scheme is then used for integration in time. To avoid any false reflections from the outer boundaries of the computational domain, the Nearly Perfectly Matched Layer (NPML) technique is adopted. Special attention is paid to the modeling of wave reflection and transmission at material interfaces.

A comprehensive set of test problems addressing all facets of the proposed numerical model is used for verification via comparison with available analytical solutions. After the establishment of the accuracy, performance, and reliability of the proposed model, realistic WPC cases are numerically simulated for the linear and weakly non-linear fluid flow regimes.

The main WPC properties, such as retro-focusing and parametric resonance, are observed in the numerical experiments with good accuracy.

To simulate vibrations of bubbles subjected to acoustic waves, the Keller-Miksis (KM) model is employed. Then, by using the volume-averaging approach, the effects of bubble dynamics are incorporated into the fluid flow governing equations via adding a source term describing variations of local physical properties with the gas volume fraction. Different bubble sets are investigated within the 2D/axisymmetric model: a bubble-plane cloud, a bubble-layer cloud, a single bubble, and a spherical bubble cloud. After verification of the numerical model by evaluating some representative test cases, the interaction of bubble dynamics with the WPC process is examined using a number of descriptive indicators, such as the signal amplification factor (Γ) , the intensity (I), and the relative intensity (I^*) .

The results show that even the signals generated by violent responses of a single bubble have no significant influence on the modulation process. On the other hand, the scattered waves from bubble-plane clouds, in which the bubbles are non-physically synchronized, are strong enough to affect the modulation process if the stimulation frequency is close to the natural frequency of bubbles. For realistic bubble clouds, the modulation process is almost intact; however, conjugate waves, which pass through the cloud, have some signatures of cloud dynamics. For instance, signals with frequencies higher than the natural frequency of bubbles are significantly diminished. Overall, this study demonstrates that the WPC-based technique has a promising potential to be used for measuring bubble dimensions.

Résumé

La mesure des caractéristiques de bulles de gaz dans un fluide fait partie des tâches essentielles et délicates dans de nombreuses applications industrielles. On a récemment émis l'hypothèse que de telles mesures pourraient être conduites de manière plus efficace et précise en utilisant un dispositif de conjugaison de phase (Wave Phase Conjugation ou WPC en anglais) en raison de ses propriétés intéressantes telles que la rétro focalisation du signal et la compensation des distorsions de phase. Dans le travail ici présenté, nous étudions l'application de cette technique pour la mesure de la taille des bulles par modélisation numérique.

Pour cela, nous proposons un modèle physico-mathématique général du WPC magnétoa-coustique, prenant en compte la propagation des ondes à la fois dans les zones solides (le conjugateur lui-même et les autres régions solides, le cas échéant) et dans les zones fluides entourant le conjugateur. Les ondes acoustiques dans les zones solides sont supposées avoir un comportement linéaire, tandis qu'elles peuvent être aussi bien linéaires que non linéaires dans les zones fluides. Dans l'objectif de résoudre avec précision ces ondes transitoires à haute-fréquence, ayant généralement de courtes longueurs d'onde, des schémas d'ordres élevés dans les domaines spatiaux et temporels sont nécessaires.

Les équations gouvernantes 2D/axisymétrique du modèle sont discrétisées sur un maillage triangulaire non structuré à l'aide d'une version modifiée de la méthode discontinue nodale de Galerkin (Nodal Discontinuous Galerkin ou NDG en anglais). Celle-ci utilise des bases différentes non colocalisées pour les solutions et les flux. Le schéma de Runge-Kutta (RK) de troisième ordre à forte conservation de la stabilité (Strong Stability-Preserving ou SSP en anglais) est ensuite utilisé pour l'intégration temporelle. Afin d'éviter toute réflexion non physique aux limites extérieures du domaine de calcul, la méthode de la couche presque parfaitement adaptée (Nearly Perfectly Matched Layer ou NPML en anglais) est employée.

Une attention particulière est portée sur la modélisation de la réflexion et de la transmission des ondes à l'interface des matériaux.

Un ensemble complet de problèmes types, rendant compte de l'ensemble des propriétés du modèle numérique proposé, est utilisé à des fins de vérification par comparaison avec les solutions analytiques disponibles. Après l'établissement de la précision, performance et fiabilité du modèle numérique, des cas réalistes de WPC sont simulés numériquement pour les régimes linéaires et faiblement non linéaires d'écoulement de fluide. Les principales propriétés du WPC, telles que la rétro focalisation et la résonance paramétrique, sont observées avec une bonne précision dans les expériences numériques.

Le modèle de Keller-Miksis (KM) est utilisé pour simuler les vibrations des bulles soumises à des ondes acoustiques. Par la suite, en utilisant la méthode de moyenne des volumes, les effets de la dynamique des bulles sont pris en compte dans les équations régissant les fluides par ajout d'un terme source témoignant des variations des propriétés physiques locales avec la fraction volumique du gaz. Différents ensembles de bulles sont étudiés dans le modèle 2D/axisymétrique: un nuage plan de bulle, un nuage de couche de bulles, une seule bulle et un nuage sphérique de bulles. Après validation du modèle numérique à l'aide des cas de test représentatifs, l'interaction de la dynamique des bulles avec le procédé WPC est examinée au travers de plusieurs indicateurs descriptifs tels que le facteur d'amplification du signal (Γ) , l'intensité (I), et l'intensité relative (I^*) .

Les résultats montrent que même les signaux générés par les réponses brutales d'une seule bulle n'ont pas d'influence significative sur le processus de modulation. D'autre part, les ondes diffusées par les nuages plans de bulles, dans lesquels les bulles sont non synchronisées physiquement, sont suffisamment importantes pour influencer le processus de modulation à condition que la fréquence de stimulation soit proche de la fréquence physique des bulles. Pour les nuages de bulles réalistes, le processus de modélisation est presque préservé; cependant, les ondes conjuguées passant au travers du nuage présentent quelques signatures de la dynamique du nuage. Par exemple, les signaux dont la fréquence est supérieure à la fréquence physique des bulles sont considérablement atténués. Dans l'ensemble, cette étude démontre que la technique basée sur le WPC possède un potentiel prometteur pour la mesure des dimensions des bulles.

Contributions and Claims of Originality

In the current study, the Wave Phase Conjugation (WPC) process is used to measure bubble size dimensions. To the best of the author's knowledge, the original contributions of this study are as follows:

► Contributions to the physical model

- A general physico-mathematical model for the magneto-acoustic WPC was proposed, which is applicable to variety of situations. This comprehensive model handles acoustic wave propagation in solid, fluid, and bubbly zones. The waves are assumed to be linear in solid zones while they might behave either linearly or weakly non-linearly within fluid regions.
- The governing equations of the fluid zones were modified to include the effects of the bubble dynamics.
- In this research, a conceptual model for bubble-plane clouds was proposed. This model had a significant role in better understanding the interactions of the WPC process with bubbles.

▶ Contributions to the numerical method

• As a part of this research, a fully-featured in-house software was developed to numerically assess the WPC phenomenon and bubble cloud dynamics. This software includes the pre-processor, the main solver, and the post-processor.

- A modified version of the Nodal Discontinuous Galerkin (NDG) scheme, which is based on non-collocated solution and flux bases, was proposed by the author to generalize the formulations of the linear and non-linear fluid flow regimes. This new spatial scheme could better mitigate the aliasing error.
- The effects of the linear and non-linear bubble dynamics were incorporated into the modified version of the NDG.
- The numerical model for assessing dynamics of a single bubble in axisymmetric domains was improved.

▶ Contributions to the simulations

- A realistic 2D/axisymmetric model for the WPC process was employed. This model includes the following components:
 - o a flat or a curved transducer, implemented as a special boundary condition;
 - a solid material as the conjugator, which is wrapped in an electrical coil solenoid.
 The physical interaction of the electromagnetic and elastic fields within the conjugator was modeled;
 - the fluid zone, as the base medium, which surrounds the conjugator;
 - and solid or fluid specimens which are located between the transducer and the conjugator for investigations.
- Behaviors of bubble clouds with different specifications were precisely examined, such as bubble clouds with different bubble sizes and cloud dynamics in the weakly non-linear fluid flow regime.
- Interactions of the WPC process with different bubble sets (such as single bubbles, bubble-plane clouds, bubble-layer clouds, and spherical bubble clouds) were investigated for the first time.

- A number of indicators such as the exponential amplification factor (Γ) , the intensity (I), and the relative intensity (I^*) were suggested to be used for the post-processing of the signals interacting with the WPC process and different bubble clouds.
- The numerical studies carried out in this research showed that the WPC-based technique has a promising potential to be used for measuring bubble size dimensions. Hence, some guidelines were suggested to conduct respective experiments in future.

Acknowledgements

Firstly, I would like to acknowledge my supervisor, Professor Evgeny Timofeev, for his continued guidance and support. I always owe Prof. Timofeev a great debt of gratitude for providing me the opportunity to learn and professionally grow under his high-standard supervision. Undoubtedly, this work would not have been possible without his encouragement, kind advice, and valuable expertise.

My thanks and appreciations also go to Prof. Alain Merlen and Prof. Philippe Pernod from the Institut d'électronique de microélectronique et de nanotechnologie, Lille, France, for their support, encouragement, and many consultations regarding various aspects of the wave phase conjugation.

I appreciate the financial supports provided by the Natural Sciences and Engineering Research Council of Canada (NSERC) and the Fonds de recherche du Québec – Nature et technologies (FRQNT). I also acknowledge the MEDA (McGill Engineering Doctoral Award) scholarship provided by the Faculty of Engineering of McGill University. I also appreciate the computational resources provided to us by Compute Canada.

Last but not least, I would like to thank Dr. Farshad Navah, Mr. Aditya Kashi, and the dear departed Mr. Philip Zwanenburg for the helpful discussions we had. I also appreciate Mr. Damien Mancy for helping me with the French abstract. Besides, I acknowledge my family and my friends for their kind supports and helps through all these years.

Abbreviations

BDF Backward Differentiation Formula

DG Discontinuous Galerkin

DOF Degree Of Freedom

FD Finite Difference

FE Finite Element

FV Finite Volume

GL Gauss-Legendre

KM Keller-Miksis

KZK Khokhlov-Zabolotskaya-Kuznetsov

LSODA Livermore Solver for Ordinary Differential equations with Automatic switching

MPML Multi-axial Perfectly Matched Layer

NDG Nodal Discontinuous Galerkin

NPML Nearly Perfectly Matched Layer

ODE Ordinary Differential Equation

PC Phase Conjugation

PD Period-Doubling

PML Perfectly Matched Layer

PSTD Pseudo-Spectral Time Domain

QDG Quadrature-based Discontinuous Galerkin

RK Runge-Kutta

RKDG Runge-Kutta Discontinuous Galerkin

SN Saddle-Node

SSP Strong Stability-Preserving

TVD Total Variation Diminishing

WENO Weighted Essentially Non-Oscillatory

WPC Wave Phase Conjugation

WS Williams-Shunn

WV Witherden-Vincent

Contents

act	v			
mé				
butions and Claims of Originality	ix			
wledgements	xiii			
viations	xv			
Figures	xxi			
Tables	xxxv			
er 1 Introduction	1			
Single Bubbles and Bubble Clouds	1			
Wave Phase Conjugation	10			
Research Objectives	16			
Thesis Outline	17			
er 2 Physical Models	19			
Setup and Assumptions	19			
Solid Model	22			
2.2.1 2D/Axisymmetric Formulation	25			
Fluid Flow Model	27			
2.3.1 Linear Regime	29			
2.3.2 Weakly Non-linear Regime				
2.3.3 2D/Axisymmetric Formulation				
	butions and Claims of Originality wledgements viations Figures Tables er 1 Introduction Single Bubbles and Bubble Clouds Wave Phase Conjugation Research Objectives Thesis Outline er 2 Physical Models Setup and Assumptions Solid Model 2.2.1 2D/Axisymmetric Formulation Fluid Flow Model 2.3.1 Linear Regime 2.3.2 Weakly Non-linear Regime			

2.4	Model for Fluid with Bubbles	30			
	2.4.1 Volume-Averaging Technique				
	2.4.2 2D/Axisymmetric Formulation	32			
	2.4.3 Bubble Cloud Types	33			
	2.4.4 Keller-Miksis Model	36			
	2.4.5 Estimation of the Bubble Stimulating Pressure	37			
2.5	Conclusion	11			
Chapte	er 3 Numerical Method 4	13			
3.1	Introduction	13			
3.2	NPML Boundary Condition	16			
3.3	Modified NDG Method	19			
	3.3.1 Bubble Dynamics in Linear Flow Regime	6			
	3.3.2 Bubble Dynamics in Weakly Non-linear Flow Regime	57			
3.4	Numerical Flux	59			
	3.4.1 Continuity and Slip/No-Slip Conditions	<u>5</u> 2			
	3.4.2 Force Balance Condition	<u>3</u> 2			
3.5	Flux Jacobian	35			
	3.5.1 Weakly Non-linear Fluid Flow	3 6			
	3.5.2 Linear Fluid Flow and Linear Solid	37			
3.6	C^∞ -Diffeomorphism Transformation	i 8			
3.7	Temporal Scheme	70			
	3.7.1 Strong Stability-Preserving Runge-Kutta Scheme	72			
3.8	Conclusion	73			
Chapte	er 4 Results and Discussion 7	' 5			
4.1	Verification of the Proposed Model	76			
	4.1.1 Grid Convergence and Order of Accuracy	76			
	4.1.2 Weakly Non-linear Regime and Modified NDG Scheme	76			
	4.1.3 Wave Propagation in Solid Media	32			
	4.1.4 Wave Propagation in Fluid Media	33			
	4.1.5 Non-reflective Boundaries	36			

	4.1.6	Fluid-Solid Interactions	. 88
	4.1.7	Single Bubbles	. 93
	4.1.8	Bubble-Plane clouds	. 99
	4.1.9	Bubble-Layer Clouds	103
	4.1.10	Spherical Bubble Clouds	115
4.2	WPC	Processes	118
	4.2.1	Paraxial WPC	118
	4.2.2	Axisymmetric WPC	123
4.3	Interac	ction of Bubbles with WPC	131
	4.3.1	Interaction of WPC with Bubble-Plane Clouds	132
	4.3.2	Interaction of WPC with Single Bubbles	138
	4.3.3	Interaction of WPC with Bubble-Layer Clouds	141
	4.3.4	Interaction of WPC with Spherical Bubble Clouds	153
4.4	Conclu	sion	163
Chapte	er 5 I	Final Remarks	165
5.1	Conclu	asions	165
5.2	Future	e Work	168
Appen	dix A	Mapping, Interpolation, and Integration	171
A.1	Geome	etrical Transformation	171
A.2	Numer	rical Interpolation and Integration	173
Bibliog	raphy		191

List of Figures

Figure 1.1. Bubble behaviors in different situations: (a) cavitation damage on	
a pump blade (reproduced from [1]), and (b) emitting light by a bubble	
(reproduced from $[2]$)	2
Figure 1.2. Two types of bubble cloud patterns: (a) a bubble set approximated	
as a spherical bubble cloud (reproduced from [3]), and (b) a bubble web (reproduced from [2])	5
Figure 1.3. Schematic of a WPC device consisting of a conjugator and a focusing transducer.	1 1
Figure 1.4. Experimental images of an incident beam and the respective conjugate	
signal (reproduced from $[4]$)	12
Figure 2.1. Schematic of a WPC device for measuring bubble dimensions. This	
setup consists of a conjugator, a focusing transducer, and a bubble cloud 2	20
Figure 2.2. Schematics of the bubble sets investigated in this study: (a) bubble-	
plane cloud, (b) bubble-layer cloud, (c) single bubble, and (d) spherical bubble	
cloud	33
Figure 3.1. Transformation of an axisymmetric grid element: (a) an annular	
integration volume with triangular cross section in the physical coordinate	
system $(\vec{q} = (z, r))$ along with a volume element with quadrilateral cross section	
shown in blue color (half of the volumes are shown for better illustration); (b)	
transformed cross sections of the integration domain and the volume element	
in the reference coordinate system, $\vec{\theta} = (\xi, \eta)$	51

Figure 3.2. Notations for a flux point, shown by a black circle, on a common	
boundary between two neighboring cells, 'in' and 'out': (a) the normal vectors	
at the flux point on a curved common boundary; (b) different zones created by	
the incoming and outgoing characteristics (with respect to the cell 'in') and	
the contact surface	0
Figure 4.1. Linear advection of a sinusoidal scalar signal, Eq. (4.1a): (a) the	
initial condition and the numerical mesh; (b) L_2 error norm versus the non-	
dimensional mesh size	7
Figure 4.2. Non-linear advection of the Gaussian wave given by Eq. (4.3) $(U_{\text{max}} = 1)$:	
(a) the numerical mesh; (b) the initial condition and comparison of the numer-	
ical result with the analytical solution at $t = 0.14$ s	9
Figure 4.3. Advection of the Gaussian wave given by Eq. (4.3) $(U_{\text{max}} = 8.25)$ in	
the non-linear regime using the original and modified NDG schemes: (a) the	
initial condition and the results at $t = 0.039$ s; (b) the normalized global	
energy versus time for the linear and non-linear regimes	0
Figure 4.4. Linear and non-linear advection of a sinusoidal scalar signal, Eq. (4.5):	
L_2 error norm versus the non-dimensional mesh size at $t=0.05~s$ for the linear,	
original, and modified NDG schemes	2
Figure 4.5. Advection of the sinusoidal wave given by Eq. (4.5) in the non-linear	
regime using the original and modified NDG schemes: (a) the normalized global	
energy; (b) the averaged L_2 error norm versus time. The green dash-dotted	
line indicates the shock formation moment ($t \approx 0.187$ s)	3
Figure 4.6. Spherical wave propagation in a solid medium: (a) the numerical mesh;	
(b) the non-dimensional radial velocity, and the non-dimensional stress tensor	
components (c) $\sigma_{\Re \Re}^*$ and (d) $\sigma_{\theta\theta}^*$ along the radial direction at $t^* = 4$	4
Figure 4.7. Spherical wave propagation in a fluid medium generated by a trans-	
ducer (see Eq. (4.8)): (a) the non-dimensional pressure, p^* , and (b) the	
non-dimensional radial velocity, $v_{\mathcal{R}}^*$, at $t^* = 2$	5

Figure 4.8. Spherical signal (Eqs. (4.9)) propagation in a squared fluid domain:
(a) the numerical mesh including the NPML zones; (b) initial distributions of
non-dimensional density along $r^* = 0$ and $r^* = 0.25$, provided by Eq. (4.9b) 86
Figure 4.9. Spherical signal (Eqs. (4.9)) propagation in a squared fluid domain:
(a) non-dimensional density and (b) non-dimensional velocity magnitude distri-
butions at two time moments for $r^* = 0.25$. The lines represent the analytical
solution; circles show the numerical results with the NPML layer; and triangles— $$
without the NPML zone
Figure 4.10. Cylindrical wave propagation through a fluid-solid interface: the
non-dimensional density stimulation at the source location, shown by the black
circle in Figs. 4.11 and 4.12, which is provided by Eq. (4.10) 89
Figure 4.11. The numerical mesh for propagation of cylindrical waves through a
fluid-solid interface located at $y^* = 0$. The upper and lower zones are filled
with a fluid and a solid, respectively. The black circle indicates the disturbance
source location, and the red squares designate the locations of sensors, where
the signals shown in Figs. 4.13 and 4.14 are recorded
Figure 4.12. Cylindrical wave propagation through a fluid-solid interface (shown as
the thin white line): (a) non-dimensional stress tensor component σ_{xx}^* and (b)
non-dimensional velocity magnitude distributions at $t^* = 0.45$. The black circle
indicates the disturbance source location, and the white squares designate the
locations of sensors, where the signals shown in Figs. 4.13 and 4.14 are recorded. 91
Figure 4.13. Cylindrical wave propagation through a fluid-solid interface. Compar-
ison of the numerical results with the analytical solutions at the upper sensor
in the fluid zone (see Fig. 4.12): histories of (a) non-dimensional pressure, and
non-dimensional velocities (b) v_x^* and (c) v_y^*
Figure 4.14. Cylindrical wave propagation through a fluid-solid interface. Compar-
ison of the numerical results with the analytical solutions at the lower sensor
in the solid zone (see Fig. 4.12): histories of non-dimensional velocities (a) v_x^*
and (b) v_{u}^{*}

Figure 4.20. Two-way stimulation of a bubble-plane cloud ($R_0 = 10 \ \mu m, \ \bar{\beta}_0 = 5 \times 10^{-5}$	$^4)$
by a one-wavelength sinusoidal signal with the amplitude of $80~\mathrm{kPa}$ and the	
frequency of 200 kHz: (a) a schematic of the problem setup (the left boundary	
shown in red is the transducer which becomes an absorbing boundary at	
$t=5~\mu \mathrm{s}$); (b) the analytical solution and numerical results for the pressure	
disturbance history recorded at the sensor S; and (c) the normalized frequency	
spectrum of the bubble radius variations for 6.67 $\mu s < t < 170.5~\mu s.$	100
Figure 4.21. Linear stimulation of a bubble-plane cloud $(R_0 = 10 \ \mu m, \bar{\beta}_0 = 5 \times 10^{-4})$	
by a periodic sinusoidal signal with the amplitude of 1 Pa and the frequency	
of 200 kHz: (a) the simulation sketch including the bubble-plane cloud, the	
sensor S, and the plane source shown in red; (b) the pressure stimulation p'_{stim}	
phase-shifted by $\Delta \phi \approx 3\pi/2$ and the cloud response versus time at the bubble-	
plane location from numerical simulation, both normalized by the respective	
pressure amplitudes at later time moments ($> 0.1 \text{ ms}$); (c) the respective	
normalized frequency spectrum of the pressure disturbance generated by the	
bubble-plane cloud for 6.67 $\mu s < t < 170.5 \ \mu s$	102
Figure 4.22. Comparison of the bubble plane and bubble-layer clouds ($R_0 = 10 \ \mu \text{m}$)	
stimulated by a one-wavelength sinusoidal signal with the amplitude of 80 kPa $$	
and the frequency of 200 kHz: (a) the simulation sketches (not to scale)	
including the bubble clouds, the sensors S, and the transducers (shown in	
red) which become absorbing boundaries at $t = 5 \mu s$; and (b) the pressure	
disturbances generated by the bubble-plane cloud and bubble-layer clouds of	
various thicknesses, which are recorded at the sensor S. All clouds contain the	
same number of bubbles with $R_0 = 10 \mu \text{m}$	104

Figure 4.23. Forced oscillations of two bubble-layer clouds ($L=0.25~\mathrm{mm}$ or	
$L=2.5$ mm with $R_0=10$ µm, $\beta_0=0.01$): (a) the first setup—stimulation	
with the transducer, (b) the second setup—stimulation with the plane source.	
Pressure disturbance amplitudes as a function of the stimulating frequency	
are plotted for the thin bubble-layer cloud ($L=0.25$ mm) in (c) the first and	
(d) the second setups, and for the thick bubble-layer cloud ($L=2.5~\mathrm{mm}$) in	
(e) the first and (f) the second setups. The data are recorded at the upstream,	
S_1 , and the downstream, S_2 , sensors. In plots (d) and (f), direct effects of the	
plane source are excluded from the presented S_1 signals	07
Figure 4.24. Forced oscillation of three bubble-layer clouds ($L = 0.25 \text{ mm}, \beta_0 = 0.01$)	
with different bubble sizes simulated by periodic sinusoidal signals with the	
amplitude of 10 kPa and the frequency f : (a) the simulation sketch includ-	
ing the bubble layer, the stimulating transducer, and the sensors. Pressure	
disturbance amplitudes for various incident-signal frequencies at (b) the up-	
stream, S_1 , and (c) downstream, S_2 , sensors. The first three natural frequencies	
(f_1, f_2, f_3) of the mono-disperse bubble-layer clouds $(L = 0.25 \text{ mm}, \beta_0 = 0.01)$	
with $R_0=8$ $\mu\mathrm{m},~10$ $\mu\mathrm{m},~\mathrm{and}~14$ $\mu\mathrm{m}$ and the natural frequencies (f_b) of	
their constituting bubbles are shown as the blue, black, and red vertical lines,	
respectively	10
Figure 4.25. Free oscillation of a bubble-layer cloud ($L=0.25$ mm, $\beta_0=0.01$,	
$R_0 = 10 \mu \text{m}$) stimulated by a one-wavelength sinusoidal signal with the	
frequency of 100 kHz and the amplitude P : (a) the simulation sketch including	
the cloud, the sensor S, and the plane source shown in red; and (b) frequency	
spectra of the pressure disturbances (0.1 ms $< t < 0.5$ ms) emitted by the	
bubble-layer cloud for different medium viscosities, μ , and different stimulation	
strengths, P . The results are normalized by the pressure value at the minimum	
natural frequency, f_1	12

Figure 4.26. Forced oscillations of a bubble-layer cloud ($L = 0.25$ mm, $\beta_0 = 0.01$,
$R_0 = 10 \mu \text{m}$) under moderate stimulation by periodic sinusoidal signals with
the amplitude of 10 kPa and the frequency f for the linear and weakly non-
linear medium flow regimes: (a) the simulation sketch including the bubble
layer, the stimulating transducer, and the sensors. Pressure disturbance
amplitudes for various stimulating frequencies at (b) the upstream, S_1 , and (c)
the downstream, S_2 , sensors. The strength of the transducer is the same for
both of the flow regimes
Figure 4.27. Strong stimulation of a bubble-layer cloud ($L = 0.25 \text{ mm}$, $\beta_0 = 0.01$,
$R_0 = 10 \mu \text{m}$) under strong stimulation by a periodic sinusoidal signal with the
amplitude of 100 kPa and the frequency of 200 kHz for the linear and weakly
non-linear fluid flow regimes: (a) the simulation sketch including the bubble
layer, the stimulating transducer, and the sensor; (b) pressure disturbances
for $0 \le t \le 250$ µs; and (c) the upper and lower pressure signal envelopes for
$0 \le t \le 2500 \mu s$; both at the upstream sensor, S
Figure 4.28. Forced oscillations of a spherical bubble cloud ($A_0 = 0.5 \text{ mm}$,
$\beta_0 = 0.005, R_0 = 10 \mu \text{m}$) stimulated by periodic signals with the frequency
f: (a) the simulation sketch including the spherical bubble cloud, the sensors,
and the stimulating spherical shell shown as a red sphere; (b) the numerical
mesh, which is a 30° circular sector; frequency responses at (c) the sensor S_1
located at the cloud boundary and (d) the sensor S_2 located at the cloud center. 117
Figure 4.29. Paraxial WPC simulations: (a) the numerical setup and the initial
right-running stimulation within the conjugator and (b) a section of the
numerical mesh around the left interface located at $z=0.01~\mathrm{m}.$
Figure 4.30. Distributions of the axial stress σ_{zz} in the paraxial WPC: (a) water-
solid-water and (b) water-solid-mercury cases at $t=20~\mu s$ along the axis 120
Figure 4.31. Effects of the conjugator length on the modulation process for the
paraxial WPC: (a) schematic of the computational domain (not to scale). The
left boundary (shown in red) is the transducer which becomes an absorbing
boundary at $t = 5 \mu s$. Axial stress distributions for (b) the even case at
$t = 300 \mu s$ and (c) the odd case at $t = 500.5 \mu s$

Figure 4.32. Amplification process in the paraxial WPC: pressure disturbance	
recorded in the middle of the left hand-side fluid zone (at $z=-7.5$ mm) for	
the even and odd cases	123
Figure 4.33. Axisymmetric simulation of WPC: (a) the numerical setup and a	
sketch (to scale); and (b) the coarsest numerical mesh with the minimum grid	
element size of 0.2 mm	125
Figure 4.34. Grid independence studies using three successively refined grids	
(see Fig. 4.33): pressure disturbance profiles along the axis in front of the	
conjugator for (a) the linear regime at $t \approx 30.3~\mu s$ and (b) the non-linear	
regime at $t \approx 17$ µs. ΔL is the minimum characteristic length of grid elements.	126
Figure 4.35. Axisymmetric simulation of the WPC setup shown in Fig. 4.33a:	
(a) the stimulated axial velocity, v_z , by the transducer in time, provided by	
Eq. (4.22); (b) recorded pressure disturbance histories of the incident signal at	
the nominal focal point before the modulation	127
Figure 4.36. Normalized frequency spectra of the density disturbances for the	
incident and conjugate signals (see Fig. 4.33a): (a) linear and (b) non-linear	
fluid flow regimes	128
Figure 4.37. Variation of the Poynting vector in the axisymmetric WPC setup	
shown in Fig. 4.33a: (a) the axial component, P_z , versus time at the nominal	
focal point $(z = -4 \text{ mm})$; (b) the normalized magnitude, $ \vec{P} / \vec{P} _{\text{max}}$, along	
the vertical line passing through the nominal focal point ($z=-4$ mm) at	
$t\approx 17.3~\mu \mathrm{s}$ for the non-linear regime and at $t\approx 30.43~\mu \mathrm{s}$ for the linear one	129
Figure 4.38. Normalized strengths of the pressure disturbance modes in the linear	
(black lines) and non-linear (red lines) regimes (see Fig. 4.33a): (a) along the	
axis $(r=0)$ and (b) along the vertical line passing through the focal point	
(z = -4 mm)	130

Figure 4.39. Distribution of the normalized velocity magnitude, $ \vec{v} ^* = \vec{v} / \vec{v} _{\text{max}}$,	
for (a) the linear regime at $t \approx 30.3~\mu s$ and (b) the non-linear regime at	
$t \approx 17$ µs. Normalized Poynting vector magnitude, $ \vec{P} ^* = \vec{P} / \vec{P} _{\text{max}}$, for (c)	
the linear regime at $t \approx 30.3~\mu s$ and (d) the non-linear regime at $t \approx 17~\mu s$.	
The black triangle points to the nominal focal point located at $z=-4$ mm.	
The thin line in (a) and (b) shows the conjugator boundaries in the setup	
shown in Fig. 4.33a	131
Figure 4.40. Interaction of a paraxial WPC with a bubble-plane cloud ($R_0 = 10 \mu m$,	
$\bar{\beta}_0 = 5 \times 10^{-4}$): (a) the stimulation phase by a one-wavelength sinusoidal signal;	
and (b) the modulation phase, when the bubble-plane cloud is placed and the	
left boundary becomes absorbing. The grey zone is the conjugator, the blue	
ones are filled with water, the red zone is the bubble cloud, and the white	
one is the transducer. The signals are recorded at the upstream, S_1 , and the	
downstream, S_2 , sensors	133
Figure 4.41. Interaction of the paraxial WPC shown in Fig. 4.40 with a bubble-	
plane cloud $(R_0 = 10 \ \mu \text{m}, \ \bar{\beta}_0 = 5 \times 10^{-4})$: (a) exponential amplification	
factor; and normalized frequency spectra of the presence disturbances for the	
stimulation frequencies of (b) 150 kHz, (c) 250 kHz, and (d) 330 kHz	135
Figure 4.42. Interaction of the paraxial WPC shown in Fig. 4.40 with a bubble-	
plane cloud ($R_0 = 10 \mu \text{m}, \bar{\beta}_0 = 5 \times 10^{-4}$) at different locations: (a) variations	
of the exponential amplification factor (Γ) with the stimulation frequency;	
and the normalized intensities $(I/I_{\rm max},~I^0/I_{\rm max}^0)$ and the relative intensity	
(I^*) versus the stimulation frequency when the bubble cloud is located at (b)	
z = -10 mm, (c) $z = -5 mm$, and (d) $z = -15 mm$	137
Figure 4.43. Interaction of an axisymmetric WPC with a single bubble ($R_0 = 10 \mu \text{m}$):	
(a) the numerical setup and the sketch. The gray zone is the conjugator, the	
blue zones are filled with water, the red circle shows the location of the single	
bubble, and S_1 and S_2 are the upstream and downstream sensors. (b) The	
employed numerical grid; the red triangle indicates the location of the single	
bubble	139

Figure 4.44. Interaction of a single bubble ($R_0 = 10 \mu m$) with the axisymmetric	
WPC shown in Fig. 4.43a: variations of the exponential amplification factor	
(Γ) with the stimulation frequency for (a) the conjugate and (b) direct waves;	
and the normalized intensities $(I/I_{\rm max},I^0/I_{\rm max}^0)$ and the relative intensity (I^*)	
	140
Figure 4.45. Interaction of a single bubble $(R_0 = 10 \mu m)$ with the axisymmetric	
WPC shown in Fig. 4.43a for the stimulation frequency of 330 kHz: (a) the	
bubble radius history; (b) the normalized frequency spectrum of the bubble	
radius variations; and the pressure disturbance histories at (c) the upstream	
and (d) downstream sensors	142
Figure 4.46. Interaction of a paraxial WPC with a bubble-layer cloud: (a) the	
stimulation phase by a one-wavelength sinusoidal signal; and (b) the modulation	
phase, when the bubble-layer cloud is placed and the left boundary becomes	
absorbing. The grey zone is the conjugator, the blue ones are filled with water,	
the red zone is the bubble-layer cloud, and the white one is the transducer.	
The signals are recorded at the upstream, S_1 , and the downstream, S_2 , sensors.	143
Figure 4.47. Interaction of a thin bubble-layer cloud ($L=0.25$ mm, $\beta_0=0.01$,	
$R_0 = 10 \ \mu \text{m}$) with the paraxial WPC shown in Fig. 4.46: variations of the	
exponential amplification factor (Γ) with the stimulation frequency for (a)	
the conjugate and (b) direct waves; and the normalized intensities $(I/I_{\rm max},$	
$I^0/I_{ m max}^0$) and the relative intensity (I^*) versus the stimulation frequency for	
(c) the conjugate and (d) direct waves	145
Figure 4.48. Interaction of a thin bubble-layer cloud ($L=0.25$ mm, $\beta_0=0.01$,	
$R_0 = 10 \mu \text{m}$) with the paraxial WPC shown in Fig. 4.46: pressure disturbance	
histories at the stimulation frequency of 180 kHz for (a) the conjugate and (b)	
direct waves	147

Figure 4.49. Interaction of a thick bubble-layer cloud ($L=2.5 \text{ mm}, \beta_0=0.01,$	
$R_0 = 10 \mu \text{m}$) with the paraxial WPC shown in Fig. 4.46: variations of the	
exponential amplification factor (Γ) with the stimulation frequency for (a)	
the conjugate and (b) direct waves; and the normalized intensities $(I/I_{\rm max},$	
$I^0/I_{ m max}^0$) and the relative intensity (I^*) versus the stimulation frequency for	
	148
Figure 4.50. Interaction of a thick bubble-layer cloud ($L = 2.5 \text{ mm}$, $\beta_0 = 0.01$,	
$R_0 = 10 \mu \text{m}$) with the paraxial WPC shown in Fig. 4.46: pressure disturbance	
histories at the stimulation frequency of 250 kHz for (a) the conjugate and (b)	
direct waves in the absence of the cavitation phenomenon	150
Figure 4.51. Interaction of the paraxial WPC shown in Fig. 4.46 with a poly-	
disperse thin bubble-layer cloud ($L=0.25~\mathrm{mm},\beta_0=0.01,R_0=10~\mu\mathrm{m},14~\mu\mathrm{m}$):	
variations of the exponential amplification factor (Γ) with the stimulation	
frequency for (a) the conjugate and (b) direct waves; and the normalized inten-	
sities $(I/I_{\text{max}}, I^0/I_{\text{max}}^0)$ and the relative intensity (I^*) versus the stimulation	
frequency for (c) the conjugate and (d) direct waves	151
Figure 4.52. Interaction of the paraxial WPC shown in Fig. 4.46 with a poly-	
disperse thin bubble-layer cloud ($L=0.25~\mathrm{mm},\beta_0=0.01,R_0=8~\mu\mathrm{m},10~\mu\mathrm{m}$):	
variations of the exponential amplification factor (Γ) with the stimulation	
frequency for (a) the conjugate and (b) direct waves; and the normalized inten-	
sities $(I/I_{\rm max},I^0/I_{\rm max}^0)$ and the relative intensity (I^*) versus the stimulation	
frequency for (c) the conjugate and (d) direct waves	152
Figure 4.53. Interaction of an axisymmetric WPC with a spherical bubble cloud	
$(A_0 = 0.5 \text{ cm}, \beta_0 = 5 \times 10^{-5}, R_0 = 10 \mu\text{m})$: (a) the numerical setup and	
the sketch. The gray zone is the conjugator, the blue zones are filled with	
water, the red sphere is the bubble cloud, and S_1 and S_2 are the upstream and	
downstream sensors. (b) The employed numerical grid	155

Figure 4.54. Interaction of the axisymmetric WPC shown in Fig. 4.53a with a dilute	
spherical bubble cloud ($A_0 = 0.5$ cm, $\beta_0 = 5 \times 10^{-5}$, $R_0 = 10$ µm): variations	
of the exponential amplification factor (Γ) with the stimulation frequency for	
(a) the conjugate and (b) direct waves; and the normalized intensities $(I/I_{\rm max},$	
$I^0/I_{\rm max}^0$) and the relative intensity (I^*) versus the stimulation frequency for	
(c) the conjugate and (d) direct waves	156
Figure 4.55. Interaction of the axisymmetric WPC shown in Fig. 4.53a with a dilute	
spherical bubble cloud ($A_0 = 0.5$ cm, $\beta_0 = 5 \times 10^{-5}$, $R_0 = 10$ µm): pressure	
disturbance histories for the stimulation frequency of 200 kHz recorded at (a)	
S_1 and (b) S_2 , and for the stimulation frequency of 400 kHz recorded at (c) S_1	
and (d) S_2	157
Figure 4.56. Interaction of the axisymmetric WPC shown in Fig. 4.53a with a	
dilute spherical bubble cloud ($A_0 = 0.5$ cm, $\beta_0 = 5 \times 10^{-5}$, $R_0 = 10$ µm):	
pressure disturbance contours for the stimulation frequency of (a) 200 kHz at	
$t = 500 \mu s$ and for the stimulation frequency of (b) 400 kHz at $t = 360 \mu s$.	
The cloud boundary is shown in red, and the location of S_1 is indicated by the	
blue triangle.	159
Figure 4.57. Interaction of the axisymmetric WPC shown in Fig. 4.53a with a	
dense spherical bubble cloud ($A_0 = 0.5$ cm, $\beta_0 = 5 \times 10^{-3}$, $R_0 = 10$ µm): the	
grid independence study using three successively refined grids for evaluation	
of the pressure disturbance profiles along the axis in front of the conjugator at	
$t=500~\mu \text{s}.~\Delta L$ is the minimum characteristic length of the grid elements	160
Figure 4.58. Interaction of the axisymmetric WPC shown in Fig. 4.53a with a dense	
spherical bubble cloud ($A_0 = 0.5$ cm, $\beta_0 = 5 \times 10^{-3}$, $R_0 = 10$ µm): variations	
of the exponential amplification factor (Γ) with the stimulation frequency for	
(a) the conjugate and (b) direct waves; and the normalized intensities $(I/I_{\rm max},$	
$I^0/I_{\rm max}^0$) and the relative intensity (I^*) versus the stimulation frequency for	
(c) the conjugate and (d) direct waves	161

Figure 4.59. Interaction of the axisymmetric WPC shown in Fig. 4.53a with	
a dense spherical bubble cloud ($A_0 = 0.5$ cm, $\beta_0 = 5 \times 10^{-3}$, $R_0 = 10$ µm):	
pressure disturbance contours for the stimulation frequency of (a) 200 kHz at	
$t=500~\mu s$ and for the stimulation frequency of (b) 400 kHz at $t=360~\mu s$.	
The cloud boundary is shown in red, and the location of S_1 is indicated by the	
blue triangle	162
Figure A.1. Reference elements in the ξ - η coordinate system: (a) 1D and (b)	
2D/axisymmetric elements	171
Figure A.2. Mapping of the reference element in the ξ - η coordinate to a physical	
element in the z-r domain with the non-linear transformation $\mathcal{L}(\vec{\theta}) = \vec{q}$. The	
red circles are geometric interpolation nodes for this fourth-order element	172

List of Tables

Table 4.1. Linear advection of a sinusoidal scalar signal, Eq. (4.1a): L_2 error norm	
and the evaluated spatial order of accuracy for different polynomial orders of	
the solution basis, p	78
Table 4.2. Linear and non-linear advection of a sinusoidal scalar signal, Eq. (4.5): L_2	
error norm and the evaluated spatial order of accuracy for different polynomial	
orders of the solution basis, p , at $t = 0.05 s$. In the non-linear regime, the	
results for the original NDG and the modified NDG schemes are provided. $$	81
Table 4.3. Natural frequencies of individual bubbles (f_b) and three mono-disperse	
bubble-layer clouds ($L=0.25~\mathrm{mm}$) with different void fractions, obtained from	
Eq. (4.19)	109
Table 4.4. Parameters of the paraxial WPC setup shown in Fig. 4.29a for investi-	
gating material impedances	120
Table 4.5. Parameters of the paraxial WPC setup shown in Fig. 4.31a for investi-	
gating the conjugator length	121
Table 4.6. Modulation parameters of the axisymmetric WPC setup shown in	
Fig. 4.33a	124
Table A.1. Properties of the WS nodal sets [7]: the polynomial of order p which is represented by N nodes and associated with the quadrature rule of order q ;	
and the nodal distributions within the 2D/axisymmetric reference element	174

Table A.2. Properties of the WV nodal sets [8]: the quadrature rule of order q asso-	
ciated with N nodes; and the nodal distributions within the 2D/axisymmetric	
reference element	175
Table A.3. Properties of the GL nodal sets $[9]$: the polynomial of order p which is	
represented by N nodes and associated with the quadrature rule of order q ;	
and the nodal distributions within the 1D reference element	176
Table A.4. Barycentric coordinates $(\lambda_1, \lambda_2, \lambda_3)$ and the integration weights (w) for	
WS nodal sets [7] for different node numbers, N	177
Table A.5. Barycentric coordinates $(\lambda_1, \lambda_2, \lambda_3)$ and the integration weights (w) for	
WV nodal sets [8] for different node numbers, N	179
Table A.6. Barycentric coordinates (λ_1, λ_2) and the integration weights (w) for	
GL nodal sets [9] for different node numbers, N	187

CHAPTER 1

Introduction

Gas bubbles play a crucial role in many industrial applications. To better understand and interpret their behaviors, it is essential to have reliable means to measure their dimensions. However, there are many obstacles for carrying out reliable and trustworthy measurement, such as focusing issues for small bubble sizes as well as distortion and dissipation of signals used for this purpose. Since some of these difficulties might be overcome by using a Wave Phase Conjugation (WPC) device, the current study investigates potentials of such phenomenon for measuring dimensions of gas bubbles. In the remainder of this chapter, previous investigations on bubble dynamic and the WPC process are provided in Sections 1.1 and 1.2, respectively. The objectives of the current research are presented in Section 1.3, and it is followed by the thesis outline in Section 1.4.

1.1 Single Bubbles and Bubble Clouds

Bubbles have been drawing attentions for decades since they are exceptional objects. These mysterious phenomena need at least two phases to appear. Small soft bubbles in liquids can be so violent to damage any surface (see Fig. 1.1a) and sometimes turn into small light bulbs (see Fig. 1.1b) [2]. Bubble dynamics and cavitation phenomenon have been matters of concern in different applications. In underwater acoustics, bubbles can distort the signals and absorb their energy, which might adversely affect the performance of the acoustic systems.

Considering hydraulic devices, one finds the cavitation damage due to violent bubble collapses causing severe issues for different components such as compressor blades and ship propellers; moreover, presence of bubbles can decrease the thrust and also make acoustic noise, which are all undesirable effects. In the medical applications, bubble formation in the expansion period of stimulating waves can negatively affect the incident acoustic signals, and violent collapses of these bubbles might cause cavitation damages [2, 3, 10].

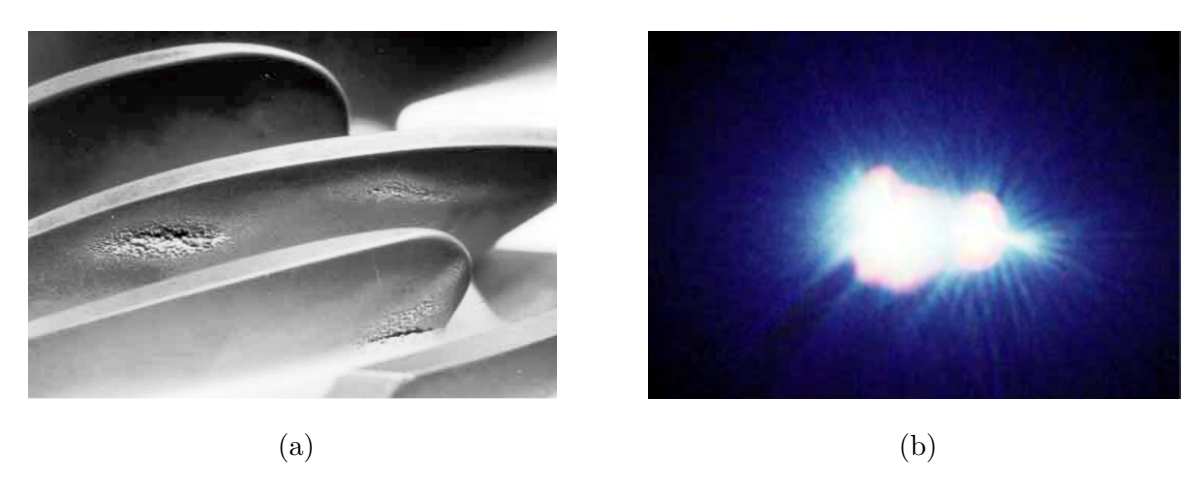


Fig. 1.1. Bubble behaviors in different situations: (a) cavitation damage on a pump blade (reproduced from [1]), and (b) emitting light by a bubble (reproduced from [2]).

When bubbles are subjected to pressure signals, they might show different behaviors depending on many factors such as the amplitude and frequency of the driving pressure, the ambient pressure, and the bubble contents. In this regard, three regimes are defined for bubble responses: 1) the linear regime for weak stimulations; 2) the stable acoustic cavitation, in which non-linear features start to affect the bubble response; and 3) the transient acoustic cavitation that includes explosive growth and violent collapse phases. In this regime, the bubble radius significantly (several orders of magnitude) changes in each cycle [1]. In terms of stability, which means that a small perturbation of the bubble radius is restored, Blake [11] and Neppiras and Noltingk [12] introduced a criterion called 'Blake critical radius' for the static stability. Based on this criterion, bubbles which their radii are above the Blake critical limit are unstable. For the bubbles exposed to oscillatory driving pressure, Apfel [13] showed that if the stimulation frequency is much lower than the natural frequency, the Blake

criterion still holds; otherwise, the necessary (but not sufficient) condition for the transient cavitation to take place is to have some moments in the oscillation cycle in which the ambient pressure would be lower than the vapor pressure. Based on the duration of these moments, an approximate relation for the critical stimulating pressure was also obtained [13].

Bubbles show their full potential when they are periodically stimulated via pressure waves. In such situations, a bubble behaves as a non-linear oscillator with all of its complexities, such as encountering additional resonances, having multiple attractors and basins, and showing chaotic responses [2]. Many of these characteristics can be seen in the frequency response curves, which are quite explanatory while studying bubble dynamics. To obtain these curves, the amplitudes of periodic responses are recorded for different stimulation frequencies. For weak oscillations of a single bubble, the linear behavior is seen, in which only one peak is observed in the response curve occurring at the bubble natural frequency, $f_{\rm b}$. By increasing the driving pressure amplitude, some non-linear features start to appear. For instance, additional resonances are observed around specific frequencies, which are called super- and sub-harmonics. These resonance peaks lean to lower frequencies by increasing the stimulation strength, which eventually make noticeable jumps in the response curve. At each of these resonance frequencies, there might be more than one co-existing stable states, leading to a hysteresis behavior. Depending on the basins of attraction, the dynamic system tends to one of the stable states, which is called the attractor [2].

Another similarity that a bubble shares with other non-linear oscillators is the deterministic chaotic behavior, meaning that responses of a bubble to a deterministic driving pressure might be chaotic. This randomness of the bubble behavior stems from the Period-Doubling (PD) phenomenon in the non-linear regime [2, 14]. In such situations, responses of the dynamic system sensitively depend on initial conditions. In other words, small perturbations of initial conditions exponentially grow in time and eventually are as important as the system variables. As a result, after some time, the truncated precision of the initial conditions which are beyond the experimental or numerical simulations become significant, making the system prediction impossible, despite the fact that both the dynamic system and the inputs are determined [14].

Lauterborn and Suchla [15] were apparently the first group who investigated PD structures of bubble dynamics by using bifurcation diagrams and attractor maps. These patterns were later assessed in detail by Parlitz et al. [14], and Parlitz and Lauterborn [16]. Using bifurcation

and phase diagrams, they observed different types of bifurcations such as Saddle-Node (SN) and PD. They showed that PD cascades with their inherent co-existing attractors eventually lead to bubble chaotic responses. To better distinguish different modes of oscillations, they introduced two numbers, torsion and period, and associated each oscillation mode with these numbers. They also demonstrated that stable bubble oscillations either reach a periodic condition or stay fluctuating in a chaotic manner, which depends on the frequency and the amplitude of the driving pressure. The chaotic behavior of bubble clouds were examined by Smereka and Banerjee [17] and Birnir and Smereka [18], and their results showed bifurcation patterns and chaotic responses as well.

Due to important roles that bubbles might play in different applications, appropriate modeling of bubble dynamics has been a matter of interest over past few decades. There are a number of physical aspects, such as multi-scale interactions and bubble non-linear responses, which add complexities to such investigations. The most accurate model is the 'direct method' which is able to capture and resolve the interfaces between the bubbles and the surrounding fluid. Since this method is highly computationally expensive, its usage is limited to simulation of a few bubbles in a short period of time [10]. Hence, a number of simplified models have been suggested to simulate dynamics of a single bubble as an oscillatory system.

The first model was proposed by Rayleigh [19], in which the pressure difference across the bubble surface is considered as the driving pressure. This model has evolved over time and called 'Rayleigh-Plesset' model, which includes different factors such as the surrounding liquid viscosity and the bubble surface tension. In this model, the surrounding liquid is considered incompressible [1, 2]. Gilmore [20] proposed a more advanced model in order to include effects of disturbances emitted by the bubble surface via considering the surrounding liquid compressibility. Another popular model is Keller-Miksis (KM) which includes the liquid compressibility and signal radiation effects as well [21]. In order to eliminate the terms including retarded time in this model, another formulation based on the KM model was proposed by Parlitz et al. [14] which is shown to be as accurate as the original model. This model, denoted as the modified KM model, is employed to simulate bubble dynamics in the present study.

Examining these models for assessing bubble dynamics shows acceptable accuracy for spherical bubbles [2, 22]; however, Prosperetti and Lezzi [23] showed that these models are

valid for the bubble surface Mach number up to 0.3. In the range of oscillations in which the amplitudes are still small but the non-linear features start to appear, a weakly non-linear model for bubble dynamics was obtained via eliminating the terms with the order higher than two [24]. Although the weakly non-linear model can qualitatively describe the bubble dynamics, it lacks some non-linear features such as skewing of the resonant peaks toward lower frequencies.

Bubbles are not usually isolated in different situations; as illustrated in Fig. 1.2, they come in large numbers with different patterns such as clusters, filaments, clouds, etc [2]. Dynamics of bubble clouds have been a matter of interest due to their importance in different applications, such as medical devices, hydraulic systems, and underwater instruments; moreover, bubble clouds show some interesting features. Acoustic waves generated by bubble clouds are among the first features which were investigated in the past [3]. These signals are strong enough to be easily detected [2], as opposed to those generated by a single bubble (except for violent collapsing phases). The acoustic emissions from spherical bubble clouds were initially studied by Morch [25], Chahine [26], and Omta [27].

Morch [25] analytically showed that pressure rises in the exterior zone might lead to formation of a spherical shock moving toward the center of the cloud, which leads to collapsing

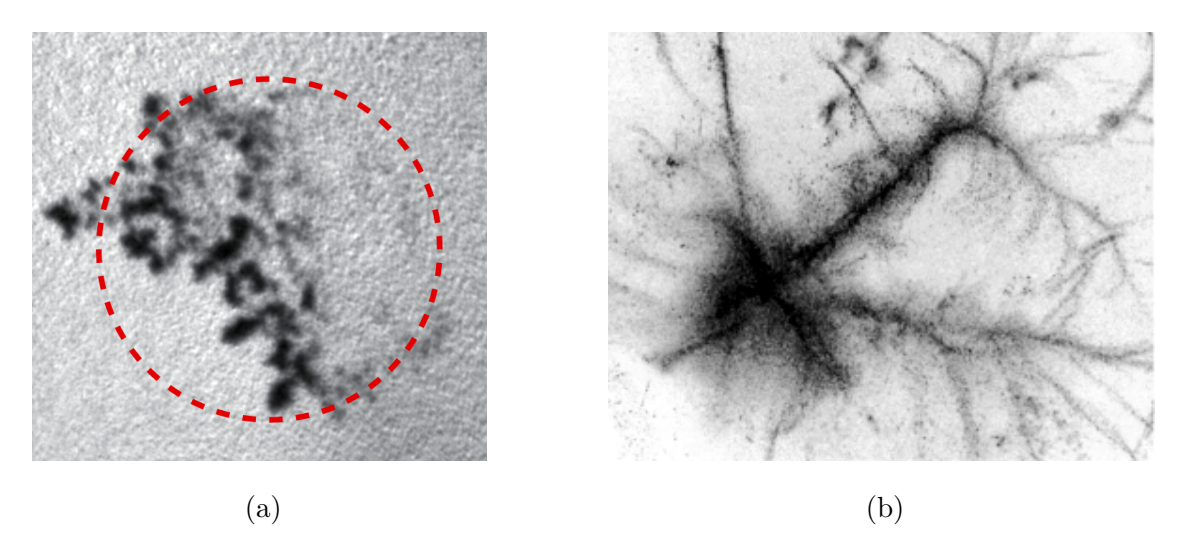


Fig. 1.2. Two types of bubble cloud patterns: (a) a bubble set approximated as a spherical bubble cloud (reproduced from [3]), and (b) a bubble web (reproduced from [2]).

of bubbles. He compared these results with some experimental data as well. Chahine [26] numerically investigated all individual bubbles in a cloud separately for dilute mixtures. He showed that under the same conditions, bubbles within a cloud collapse more violently compared to individual ones. In addition, at the end of the collapse phase, generated signals significantly increase as a result of collective effects within the cloud. Omta [27] investigated sound emissions and dynamics of bubble clouds containing large number of bubbles analytically in the linear, and numerically in the non-linear regimes. He showed that the frequency spectra of the signals emitted by bubble clouds are mainly controlled by the total gas volume within the cloud, and the peak response occurs at frequencies lower than the one for individual bubbles. In addition, the efficiency of the signal emission is determined by the number of bubbles within a cloud. For bubble clouds which are strongly stimulated, he observed very high pressure at the center of the clouds.

Since bubble clouds contain a large number of bubbles, some assumptions are necessary to decrease the cost of cloud analyses [3]. One of the methods, which has been widely used, is the volume-averaging technique. Brennen [1] employed this method to analyze well-mixed bubble clouds which include sufficiently small bubbles. Assuming that responses of bubbles to variations of the driving pressure are almost instantaneous, he treated the liquid-gas mixture as a barotropic medium, in which both phases are always in dynamic equilibrium. This assumption is valid when the stimulation frequencies are much lower than the natural frequencies of bubbles. For the cases in which the assumption of existing dynamic equilibrium between phases no longer holds, the effects of bubble dynamics need to be implicitly incorporated into the fluid flow governing equations. In this approach, individual bubbles are usually considered as spherical cavities (an acceptable approximation due to the surface tension effect [2]), and the changes in their radii are obtained via one of the non-linear models proposed for assessing a single bubble dynamics (such as Rayleigh-Plesset [19], Gilmore [20], or KM [14, 21] models).

Following the aforementioned approach, Wijngaarden [28] linearized the volume-averaged governing equations for dilute mixtures using the Rayleigh-Plesset model. He found a relation for the speed of sound which was in line with the one analytically obtained by Foldy [29], who employed the multiple scattering approach for this purpose. Their results showed that the speed of sound in bubble clouds might be much lower than that of the consisting components

(even as low as 20 m/s), which yet was consistent with a number of experimental data [30–32]. Furthermore, Wijngaarden [28] assessed the thermodynamic behavior of oscillating bubbles and provided a number of criteria according to which the contents of bubbles can be considered to behave either isothermally or adiabatically.

A rigorous derivation of the volume-averaged governing equations for bubble clouds was provided by Caflisch et al. [33]. This formulation is different in some unimportant terms from the one heuristically found by Wijngaarden [34], which tends to the analytical results obtained by Foldy [29] in the linear regime. An important assumption in this derivation is that each bubble feels the macroscopic pressure and velocity fields of the medium; in other words, bubbles are not affected by each other, which is the case for dilute mixtures [33, 35]. In terms of the bubble cloud properties, they also showed that very small volume of bubbles can drastically change the mixture properties, such as the speed of sound. In the present study, the bubble-related additional source term obtained with the volume-averaging approach is included into the governing equations using the modified KM model (see [14]); in addition, it is also assumed that bubbles within a cloud are only affected directly by the medium flow field.

Using the volume-averaging method, Commander and Prosperetti [35] compared the numerical simulation of bubble cloud responses in the linear regime with available experimental data [30–32, 36, 37]. They reported that the numerical results satisfactorily agree with those experiments including wide bubble size distributions [30] and those using two-dimensional bubble screens for the accurate control on the bubble size distributions [31] in a cloud. They claimed that near the bubble resonance frequency, the scattering effect increases, making the gas volume fraction be sensed higher than the actual value. In such situations, the bubble interactions would be noticeable. However, for low volume fractions, this effect would be negligible.

Smereka and Banerjee [17] investigated the nature of the volume-averaged governing equations analytically in the linear and numerically in the non-linear regimes. By assessing the bubble clouds subjected to forced oscillations in 1D domains, they showed that bubble clouds have the same temporal periodicity as that of the stimulating pressure after reaching the periodic situation. They showed that there is a cutoff frequency in both the linear and non-linear regimes, which is the same as the natural frequency of the single bubble for

linear oscillations, f_b . As a result, when the stimulation frequency is lower than the cutoff one, resonances may occur, and clouds show wave-like behaviors. Otherwise, the waves are exponentially damped, and the outer layer of the cloud behaves as a shield, preventing the signals from reaching the cloud center. In the non-linear regime, the resonance peaks in the frequency response curve lean to the lower frequencies, similarly to those for stimulations of single bubbles. In terms of bifurcation structures of bubble clouds, they showed that the chaotic responses start rapidly with no obvious bifurcation cascades, as apposed to single bubble responses.

Using the Fourier analysis, Kumar and Brennen [24] investigated dynamics of bubble-layer clouds (1D clouds) in the weakly non-linear regime via assessing the frequency responses of cloud layers stimulated by an oscillating boundary. They could make a number of analogies between the dynamics of 1D bubble clouds and the results provided by d'Agostino and Brennen [38] for spherical bubble clouds. Analytically, they showed that a bubble-layer cloud has infinite number of natural frequencies that all of them are lower than $f_{\rm b}$. Evaluating the natural modes of different bubble clouds, they showed that both the volume fraction and the closeness of the cloud natural frequencies to $f_b/2$ determine strengths of the natural modes. In addition, the cloud natural frequencies spread over a wider range as the cloud becomes thicker, eventually tending to the natural frequency distribution of semi-infinite bubble-layer clouds. Furthermore, Smereka and Banerjee [17] observed that for $f > f_b$, the signals are decayed fast by getting farther from the oscillating wall. They could also observe the harmonic cascading phenomenon as a non-linear feature of the clouds including bubbles with different dimensions. This process occurs when the non-linear modes of bubbles with a specific size would be able to stimulate natural frequencies of bubbles with another sizes. As a result, a low-frequency stimulation might lead to strong responses with higher frequencies.

d'Agostino and Brennen [38, 39] analytically assessed dynamics of spherical bubble clouds by linearizing the volume-averaged governing equations. They found an infinite number of resonances with frequencies lower than f_b , where the main responses are for $f < f_b$, as also shown by Smereka and Banerjee [17], Kumar and Brennen [24], and Omta [27]. Accordingly, they introduced three regimes for the bubble cloud behavior based on the stimulation frequency: sub-, trans-, and super-resonant regimes, which have different spatial features. In the sub-resonant regime, the stimulation frequency is lower than the lowest natural frequency of the cloud $(f < f_1)$. In this regime, the individual bubbles have enough time to react to the excitation. On the other hand, in the super-resonant regime, where $f > f_b$, the bubbles are not able to react as fast as the stimulation due to their virtual mass. As a result, the cloud responses appear to be stiffer in this regime, and these responses become weaker by getting farther from the source of excitation. In the trans-resonant regime, where $f_1 < f < f_b$, the cloud behavior is more complicated due to presence of different natural modes.

Wang and Brennen [40] numerically investigated the non-linear dynamics of spherical bubble clouds during the cavitation phenomenon. Using the 'cloud interaction parameter' suggested by d'Agostino and Brennen [38], they showed that when this parameter is small, the bubbles within the cloud behave individually, and, consequently, the dominant natural frequency of the cloud would be close to that of the individual bubbles. In such situations, the bubbles located in middle of the cloud collapse earlier and generate outward waves. On the other hand, dominant interactions between bubbles yield higher values of the interaction parameter and a lower dominant natural frequency. In this case, shock waves propagate inward and generate very high pressure values at the center of the cloud due to the focusing effect.

Maeda and Colonius [10] and Fuster and Colonius [41] used an Eulerian-Lagrangian method to assess bubble cloud dynamics. This method tracks the bubbles using a Lagrangian approach; then, the instantaneous volumes of bubbles are considered in the governing equations of the base medium. They proposed analytical relations with some levels of approximation to evaluate the effective pressure field, which is the stimulating pressure of the individual bubbles within the cloud. This pressure field can be modified in such a way to add effects of bubble interactions, when they are noticeable [10]. For analyzing dynamics of single bubbles or bubble-plane clouds, the current study suggests another relations to estimate the stimulating pressure of individual bubbles with fewer approximations. Employing the Eulerian-Lagrangian method mentioned above, Maeda and Colonius [3] investigated dynamics of bubble clouds subjected to focused high-intensity ultrasound signals, where the wavelength of the stimulating wave is of the cloud size order. Introducing a new scaling parameter to better express the energy localization and the anisotropy of the bubble clouds, they observed that the bubble clouds show asymmetrical behavior in the sense that the bubbles which are

near the energy source oscillate with higher amplitudes than the farther ones.

In order to better interpret and predict bubble behaviors in various situations, different experimental techniques have been proposed to estimate bubble size dimensions. The ordinary methods (e.g., echographic imaging [42]) have some disadvantages such as generating image artifacts and having poor spatial focusing [43]. There are some studies employing the resonance properties of bubbles for this purpose [44]. This method also has some drawbacks such as unintended echos from non-resonant surrounding bubbles and poor focusing due to low resonance frequencies. To overcome these downsides, the dual-frequency excitation method was proposed, in which the bubbles are stimulated by high and low frequencies at the same time. Due to non-linear behavior of bubble oscillations, the wave-mixing phenomenon generates waves with the frequencies which are the sum and the difference of the stimulation frequencies. It has been shown that analyzing these new generated signals increases the spatial resolution while estimating the bubble dimensions [45–47]. However, this technique is limited by requiring con-focal high frequency transducers and applicable to dilute bubble clouds.

The techniques employed for assessing randomly scattering media, such as bubble clouds, might not necessarily provide desired outcomes since the back-scattered signals from these media depend on their internal statistic features; hence, it would be of interest to use coherent signals for measurement purposes [43]. This study aims to employ the coherent conjugate waves generated by the WPC process in order to better estimate dimensions of bubbles within a cloud.

1.2 Wave Phase Conjugation

Phase Conjugation (PC) or WPC is a physical transformation of a wave field in such a way that the direction of wave propagation is reversed while the initial spatial distributions of amplitudes and phases are kept unchanged. Contrary to the common specular reflection, in which one of the spatial coordinates is reversed, PC is a time inversion transformation [48]. The PC phenomenon was first reported for stimulated scattering light [49].

For acoustic waves PC may be obtained via modulation of the speed of sound in a solid by an alternating electromagnetic field [50]. Such WPC in acoustics may be viewed as a result

of non-linear coupling between an acoustic wave and an oscillatory magnetic field within an active medium called 'conjugator' [51, 52]. The conjugator is a cylindrical magnetostrictive material sample (e.g., a nickel ferrite), which is wrapped in an electrical coil solenoid (Fig. 1.3). It is typically about 10 centimeters long and a few centimeters in diameter. An oscillatory magnetic field in the conjugator is generated by applying alternating electrical current through the solenoid, leading to the modulation (up to 4% in magnitude) of the bulk modulus and the speed of sound of the conjugator material [51, 52]. As shown in Fig. 1.3, a typical WPC device also includes a standard focusing ultrasonic transducer to generate incident waves and record conjugate ones [53]. The waves may be focused on an object situated between the transducer and the conjugator with the goal of its probing or treatment, depending on a particular application.

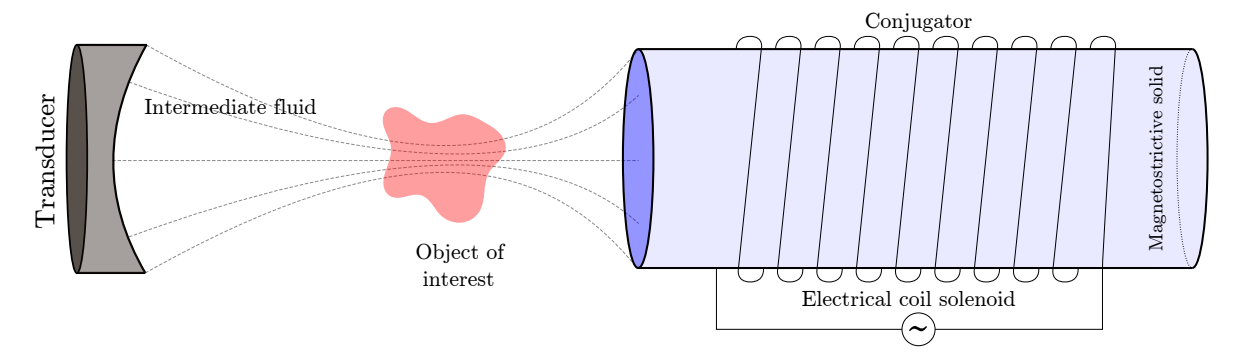


Fig. 1.3. Schematic of a WPC device consisting of a conjugator and a focusing transducer.

As the velocity of electromagnetic waves is five orders of magnitude higher than the velocity of acoustic waves, an almost uniform active region can be generated in the conjugator medium [48]. Conjugate waves are generated due to the conservation of momentum and energy in the active region; physically, it is a result of interactions between elastic field modulation and incident acoustic waves [51, 52, 54]. WPC is a frequency selective phenomenon in the sense that the dominant frequency of the conjugate wave is half of the modulation frequency [51]. If, under this parametric resonance condition, the energy supplied by the magnetic field exceeds the energy loss, the wave amplitude increases exponentially. Since in this case the energy pumping intensity should exceed a threshold reported in [54, 55], the phenomenon is called the supercritical mode of WPC.

Ultrasonic WPC has been drawing attention for years due to its unique characteristics and attractive applications stemming from them. Among the most interesting features of WPC are the amplification of the incident acoustic waves and their retro-focusing towards the initial source based on the time-reversed wave propagation rules [52, 56]. In this regard, the incident and the generated conjugate beams are coherent in the sense of having the same spatial phase [4, 53], as illustrated in Fig. 1.4. Brysev et al. [48] elaborated on such WPC-related effects and phenomena as anomalous wave reflection, auto-focusing, self-targeting, and lens-less formation of acoustic images. In view of these, the WPC devices can be used in many applications, e.g., in ultrasonic imaging (echography of biological tissues, high-resolution self-corrected acoustical microscopy) [57–60], medical diagnostics and treatments (hyperthermical treatment of cancer cells, kidney stones) [61, 62], non-intrusive fluid flow metrology [63, 64], and other areas.

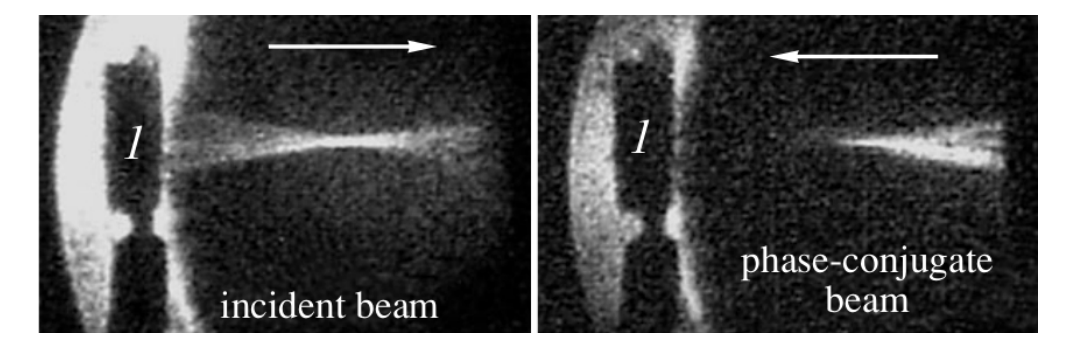


Fig. 1.4. Experimental images of an incident beam and the respective conjugate signal (reproduced from [4]).

It is quite likely to encounter non-linear effects in WPC processes. It may occur when either the incident wave is initially weak (linear) and then significantly amplified, or when the incident beam is strong enough from the beginning to generate non-linear effects. The first case is typical for acoustic microscopy, where the main advantage of WPC is the possibility to compensate wavefront distortions along the propagation path [4, 53, 58–60, 65]. It is also possible to obtain images with better resolution due to the fact that the harmonics added to the conjugate beam, which are phase coherent with the incident wave, have narrower focal region [4]. In the second case, when the incident waves are strong enough to generate harmonic content, there is a potential to improve many applications. For instance, in order

to exploit the non-linear effects of the incident signal, the second (or higher) harmonic can be conjugated, and, in this way, better focal properties can be obtained due to narrower focal zone, the reduction of reverberation in the propagation path, and a lower level of side peaks in the second (or higher) harmonic [4, 66].

The vast array of attractive applications mentioned above stimulates basic and applied research on WPC. Experimental studies of WPC, although being quite important, encounter a number of difficulties typical for experimental research in general, for example, a relatively limited amount of data which could be obtained from experimental measurements. In view of that, in the past two decades there were many analytical and numerical efforts on the modeling of WPC processes. Merlen and Zhang [51, 67, 68] provided an analytical solution for resonant modes in one-dimensional conjugators in contact with passive media. Merlen et al. [52] provided a new kind of solution for supercritical wave phase conjugation. They proved that the previous solutions [54, 67, 68] can be seen as particular types of that result and showed that the transition from one solution to the other strongly depends on the ratio of the active zone length to the quarter of the wavelength. The previous analytical solutions generally showed the lowest threshold of the input energy, which could be detected more easily both in experiments [69] and in numerical simulations [54, 70, 71].

Since the available analytical solutions are obtained under a number of restrictive assumptions (e.g., one-dimensional flow etc.), numerical simulations of WPC phenomena represent a very important research tool, especially for realistic geometrical configurations and setups. The present study is aimed to contribute further to the development of universal, comprehensive, and efficient WPC solvers. In the remainder of this section, previous numerical WPC studies are reviewed.

In one of the first numerical WPC studies, Khelil et al. [70] used a purely one-dimensional (1D) model based on the linearized Euler equations (i.e., the linear acoustics equations) in the fluid zone and similar equations in the solid zone (the conjugator) derived from the Navier equation under the assumptions of linearly elastic isotropic solid and uni-directional stress and displacement. In this case, the system of governing equations is a hyperbolic one with a source term originating from the modulation of the elastic properties and the speed of sound in the conjugator by the external magnetic field.

Voinovich and Merlen [71] extended this linear analysis to a two-dimensional (planar)

geometry. The hyperbolic system of elastodynamic equations was used, in which the first two equations represent Cartesian projections of the equation of motion and the last three equations stem from the generalized Hooke's law for an isotropic elastic material under a small strain. The source terms similar to the ones used in [70] are again present on the right-hand side of the system to represent the magnetic field modulation effect. Following the ideas of Voinovich et al. [72], the Lamé coefficients are evaluated in [71] by using the bulk compression modulus and Poisson's ratio. This makes the governing equations valid universally for linear elastic solids and linear liquids.

More sophisticated models for the PC process as compared to the above linear and isotropic ones were also considered. Bou Matar et al. [73] analyzed the WPC process in an isotropic and anisotropic elastic solid as the conjugator in an axisymmetric domain while not considering the fluid zones around the conjugator. They investigated the effects of lateral and axial conjugator size on the PC properties. Modarreszadeh and Timofeev [74] extended the model suggested by Bou Matar et al. [73] via including the fluid zones surrounding an isotropic conjugator. With this general model, Modarreszadeh and Timofeev [74] could obtain the main WPC properties such as the frequency selectivity, giant amplification, and the retro-focusing. Merlen et al. [54] investigated numerically the saturation mechanism of the non-stationary supercritical mode of parametric wave phase conjugation in an infinite one-dimensional magnetostrictive medium with a finite active zone. The two most probable nonlinear mechanisms of interaction between elastic deformation and electromagnetic excitation were considered. Comparison with experiments showed that only one mechanism, namely the amplitude depletion, corresponds to the experimental behavior.

Some efforts were put forward to include various non-linear effects of the WPC process in the fluid zones surrounding the conjugator by employing the Khokhlov-Zabolotskaya-Kuznetsov (KZK) equation, which is a nonlinear parabolic wave equation [4, 53, 63, 66, 75]. In these studies, some experimental data were used instead of modeling the physical process within the active zone in axisymmetric domains. Although the KZK equation is capable of modeling non-linear acoustic signals, there are some limitations such as difficulties with the inclusion of different materials along the wave propagation path. These disadvantages make this equation inappropriate for some applications, such as biomedical imaging. As a viable and potentially more universal alternative, Leadbetter et al. [76], Leadbetter [77], and

Modarreszadeh and Timofeev [74] employed a weakly nonlinear model for the fluid regions by keeping the first- and second-order terms in the linearized one-dimensional Euler equations and the Tait-Kirkwood equation of state for liquids. The model was shown to accurately account for non-linear signal distortion.

Due to the interesting features of the WPC process, such as coherent retro-focusing of the time-reversed signals with compensated phase distortions, this phenomenon can be used for investigating the bubble clouds. Considering the fact that the conjugate wave amplitude is proportional to the energy of the signals scattered toward the conjugator by the bubbles, the concentration and other features of the bubble clouds can affect the conjugate wave strength [43]. Having this idea, Shirkovskiy et al. [43] used a WPC setup to measure the bubble concentration of the clouds, which are randomly scattering media. In comparison with the conventional measurement technique in which the waves scattered from bubble clouds are analyzed [46], Shirkovskiy et al. [43] showed that the conjugate waves passing through bubble clouds form undisturbed reversed signals which are more sensitive to the bubble concentration of the clouds. Hence, employing the conjugate waves leads to more accurate and reliable measurement results because these signals have no dependency on the cloud statistic features. These advantages were also observed while analyzing an agar gel medium containing glass spheres [78]. The WPC setups were also shown to be capable of measuring the velocity of the flow carrying bubbles and estimating the bubble concentration of the clouds at the same time [79].

Since WPC setups have been successfully employed to estimate some characteristics of the bubble clouds (such as the bubble concentration and the cloud dimensions [43, 79]), it has been of interest to study the potentials of WPC for measuring bubble dimensions within clouds. Preobrazhensky et al. [80] used the non-linear mixing of high- and low-frequency waves within a WPC setup to stimulate bubbles located at the focal zone in a cloud. Employing this method, they could obtain the distribution of bubble size dimensions in the cloud with a better spatial resolution. As opposed to the experiments conducted by Cavaro et al. [47], the setup proposed by Preobrazhensky et al. [80] implies no limitation on the cloud void fraction. Although Preobrazhensky et al. [80] could show the possibility of using the WPC-based setups for measuring bubble size dimensions in a cloud, their study relies on the statistical features of bubble clouds since a portion of the cloud within the focal zone is evaluated at the

time. Therefore, in-depth investigation of the interactions between the whole bubble clouds, as complicated dynamic systems, and the WPC process appears to be essential.

1.3 Research Objectives

The review of previous research on bubble dynamics revealed that bubbles might show complicated behaviors in different situations. To better understand these behaviors, it is essential to have an estimation for the bubble dimensions; however, there are some difficulties for this purpose such as focusing the signals to detect small bubbles as well as distortion and dissipation of those signals. Hence, the WPC-based techniques appears to be an interesting tool for this aim. Previous studies showed that with the WPC process, the bubble concentration and dimensions of a cloud can be estimated. Nevertheless, there is no reliable and in-depth study on employing the WPC-based techniques to measure bubble size dimensions. The current study aims to fill this gap.

For this goal, a comprehensive, flexible, and efficient WPC simulator needs to be developed, which is lacking in the literature. This multi-dimensional simulator is envisioned to be capable of modeling the entire WPC process and, therefore, must include wave propagation both in the conjugator (and other solids, if necessary, the surrounding fluid, and the bubble clouds in the planar and axisymmetric configurations. In addition, to better simulate the WPC phenomenon, the physical modulation process within the conjugator requires to be modeled.

For solid media, the linear isotropic elastodynamic equations [71] with the source term due to the modulation of elastic coefficients in the active region are chosen. The fluid zones, on the other hand, might behave either linearly or weakly non-linearly [74, 77, 81]. Then, the effects of bubble dynamics needs to be incorporated into the linear and non-linear fluid flow regimes. The selected options are deemed to include the most essential elements of the physical phenomenon under study and to be comprehensive enough to cover a range of WPC applications.

As previously mentioned, the WPC process deals with high-frequency waves, which have short wavelengths. Hence, employing high-order numerical schemes are essential to decrease the computational cost, particularly in multi-directional cases. In addition, special attention should be paid to the modeling of the open boundaries, interactions of waves with material 1.4. THESIS OUTLINE 17

interfaces, simulation of the weakly non-linear flow regime, and resolving violent behaviors of bubbles during their excitations. The final step of this research is to investigate the feasibility of the bubble size measurement with the aid of the WPC setup for various bubble clouds. This step provides more comprehensive understanding of the interactions between the bubble clouds and the WPC phenomenon.

1.4 Thesis Outline

The remainder of this thesis is organized as follows. In Chapter 2, the 2D/axisymmetric governing equations and the employed physical models are presented for solid, fluid, and bubbly zones. In Chapter 3, a modified version of the Nodal Discontinuous Galerkin (NDG) method in the weak formulation is proposed. Special attention is given to the treatment of the fluid/solid interfaces. It is supplemented with the devised temporal scheme for marching in time and the Nearly Perfectly Matched Layer (NPML) method to prevent any false reflections from the external boundaries. Besides, numerical considerations for modeling the bubble dynamics within the fluid zones are also elaborated. In Chapter 4, first, the verification of the numerical model is carried out using various test problems with either analytical solutions or experimental data, which cover all facets of the numerical technique for the WPC process and the bubble dynamics. Then, interactions of different bubble clouds with the WPC phenomenon are investigated. The main conclusions and the recommendations for future research are then provided in Chapter 5. The details of the geometrical mapping and the numerical interpolation and integration are discussed in Appendix A, where the employed nodal sets within the reference elements are also tabulated.

CHAPTER 2

Physical Models

In this chapter, first the simplified physical setup along with the assumptions made in this study are discussed in Section 2.1. The physical models for the solid and fluid zones are provided in Sections 2.2 and 2.3, respectively. The respective model for the bubbly zones is elaborated in Section 2.4, followed by the conclusions of this chapter in Section 2.5.

2.1 Setup and Assumptions

To measure bubble dimensions, bubble clouds are placed between the conjugator and the transducer, as illustrated in Fig. 2.1. In this setup, the transducer first emits signals with the desired range of frequencies and for a short period of time. These incident signals then pass through the bubble cloud and reach the conjugator. The presence of the bubble cloud can significantly slow down the incident signals, and, as a result, the simulation time noticeably increases. Hence, it is assumed in the current study that the bubble cloud is initially absent, and then it will be included when the signals reach the conjugator. The incident waves then interact with the electromagnetic field within the conjugator, and the resonating process takes place for the signals which their frequencies are half of the modulation frequency ($\omega = \frac{\Omega}{2}$). The amplified signals, which are called conjugate waves, then propagate back into the fluid medium along the incident signal paths, due to the retro-focusing feature of the Wave Phase Conjugation (WPC) process. After interacting with the bubble cloud, these conjugate signals

are recorded by the transducer. It is also assumed that the transducer does not reflect the conjugate waves back into the domain.

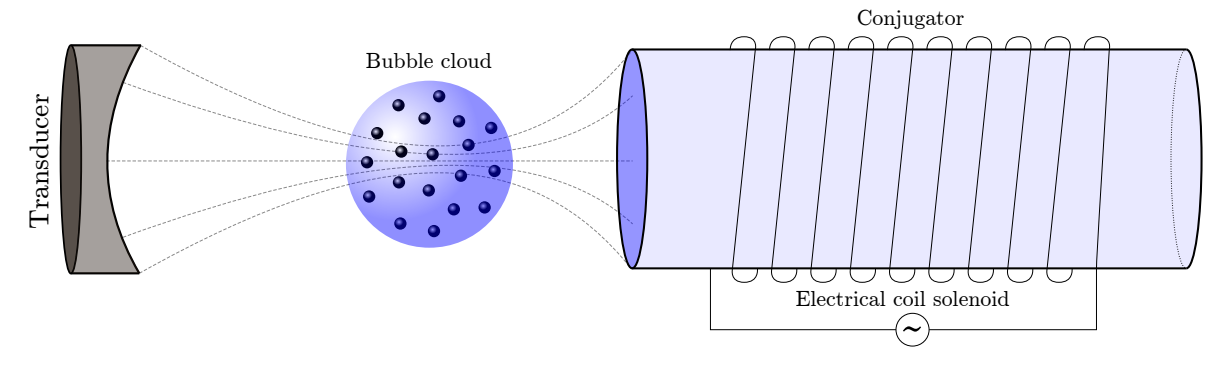


Fig. 2.1. Schematic of a WPC device for measuring bubble dimensions. This setup consists of a conjugator, a focusing transducer, and a bubble cloud.

As discussed in Section 1.2, the conjugate waves generated within the setup shown in Fig. 2.1 have some noticeable features, such as retro-focusing, compensation for phase distortions, and exponential amplification. These properties make the conjugate signal a viable option for investigating randomly scattering media, such as bubble clouds. One of the methods for generating conjugate waves is to use a conjugator which its elastic properties are modulated by an electromagnetic field, as illustrated in Fig. 2.1. This method is easy to implement in experiments, and it is relatively inexpensive. In addition, the time-reversing phenomenon takes place within the conjugator automatically as a result of a physical process. Another way to generate conjugate waves is to replace the conjugator in Fig. 2.1 with another transducer which records the incident waves and then emits the time-reversed signals via real-time signal processing. The implementation of this setup is not straightforward, particularly for multi-dimensional cases. Hence, the former technique, which includes the conjugator, has been chosen in the current study.

To simulate the propagation of acoustic waves in the setup shown in Fig. 2.1, it is necessary to introduce physico-mathematical models for the solid zone (the conjugator itself and other solid regions, if present), for the surrounding fluid, and for the fluid region including bubbles. In addition, a number of assumptions are made, which are deemed to be suitable for WPC-related problems. In some prospective WPC applications, such as lithotripsy, peak pressure

values as high as 100 MPa are reported in the focal region within the fluid medium [82]. However, the conjugator is usually located away from the focal zone, and in any case even such high pressure values are lower than the yield thresholds of ferromagnetic ceramics, which constitute typical materials of the conjugator [83]. Thus, the linear elastic solid model for the conjugator appears to be appropriate, which is also employed for other solid regions, if present.

The acoustical waves within the fluid zones are assumed to behave either linearly or non-linearly. The non-linear features, such as wave distortions, may appear at high signal strength. To capture these non-linear characteristics, a weakly non-linear model is employed in this study. The model is valid when the flow Mach number is much lower than one. This condition is valid for most applications of non-linear acoustics [82]. Furthermore, the physical attenuation processes within the fluid zones are neglected because the non-linear signal steepening dominates the dissipation processes in the typical WPC applications, as also elaborated in [77, 82]. The non-dimensional variable comparing these two factors is the Gol'dberg number with the following definition [82]:

$$G = \frac{\omega p_0 \beta}{\rho_0 c_0^3 \alpha_\omega}, \qquad (2.1)$$

where p_0 and ρ_0 are the initial pressure amplitude and the initial density, respectively; β is the coefficient of non-linearity; c_0 is the undisturbed speed of sound; and α_{ω} is the signal attenuation coefficient for the angular frequency of ω . For the desired applications in this study, $\mathcal{G} \gg 1$ [77]. Hence, in comparison with the non-linear steepening, the attenuation process can be neglected. In this study, the volume-averaging approach is used to account for the presence of bubbles. It is supplemented with a model describing the variation of bubble radii in time. This model includes the effects of the medium fluid viscosity on variations of the bubble radii.

All these models are presented in detail in the following sections. The governing equations are written for 2D/axisymmetric domains, where z (with unit vector \vec{e}_z) is the coordinate along the axis of symmetry and r (with unit vector \vec{e}_r) is the radial one.

2.2 Solid Model

In this section, the governing equations for linear solid media are provided, similarly to the approach followed by Voinovich and Merlen [71] and Modarreszadeh and Timofeev [74]. As opposed to fluid particles, solid ones can withstand shearing forces without continuous deformation. Hence, two different modes of disturbance can propagate within a solid: first, longitudinal waves, in which the particles vibrate in the direction of the wave propagation; and, second, shear waves that particles oscillate at the right angle to the wave propagation path. The speeds of wave propagation for both longitudinal and shear modes depend on the elastic properties of the solid medium.

The main solid part, which is modeled in this study, is the conjugator. In the active parts of the conjugator, where the electromagnetic field is effective (see Section 1.2), the speeds of sounds and the elastic coefficients vary with time as follows:

$$c_1^2 = (c_1^2)_0 \cdot [1 + M \cdot \cos(2\pi\Omega t + \phi)],$$
 (2.2a)

$$c_2^2 = (c_2^2)_0 \cdot [1 + M \cdot \cos(2\pi\Omega t + \phi)],$$
 (2.2b)

$$(c_1)_0 = \sqrt{\frac{\lambda_0 + 2\mu_0}{\rho_0}}, \ (c_2)_0 = \sqrt{\frac{\mu_0}{\rho_0}},$$
 (2.2c)

$$\lambda_0 = \frac{3\nu_0 K_0}{1+\nu_0}, \ \mu_0 = \frac{3(1-2\nu_0) K_0}{2(1+\nu_0)},$$
 (2.2d)

where c_1 and c_2 are the longitudinal and transverse speeds of sounds; Ω is the frequency of the electromagnetic field; M is the modulation depth; ϕ is an arbitrary phase shift; λ and μ are the Lamé coefficients; ρ_0 is the density of the solid material; ν is the Poisson's ratio; and K is the bulk modulus [71]. The subscript 0 indicates the values of c_1 , c_2 , μ , λ , ν , and K in the absence of the electromagnetic field (M = 0). It is worth noting that for an anisotropic conjugator, the modulation depths of the longitudinal and transverse speeds of sound are generally not the same [71, 73].

Let $\vec{u}(u_z, u_r)$ be the displacement vector of a solid particle in the 2D/axisymmetric domain, where the coordinate z is along the axis of symmetry and r is the radial coordinate;

2.2. SOLID MODEL 23

then the strain tensor $\boldsymbol{\mathcal{E}}$ would be:

$$\mathcal{E} = \frac{1}{2} \left[\vec{\nabla} \vec{u} + (\vec{\nabla} \vec{u})^{\mathrm{T}} \right] = \begin{bmatrix} \frac{\partial u_z}{\partial z} & 0 & \frac{1}{2} \left(\frac{\partial u_z}{\partial r} + \frac{\partial u_r}{\partial z} \right) \\ 0 & \frac{u_r}{r} & 0 \\ \frac{1}{2} \left(\frac{\partial u_z}{\partial r} + \frac{\partial u_r}{\partial z} \right) & 0 & \frac{\partial u_r}{\partial r} \end{bmatrix} . \tag{2.3}$$

Dilatation of the solid particle (e), which is the trace of the strain tensor, is computed as:

$$e = \frac{\partial u_z}{\partial z} + \frac{\partial u_r}{\partial r} + \frac{u_r}{r} \,. \tag{2.4}$$

In order to find the stress tensor σ , the following constitutive relation, which is valid for linear elastic isotropic solids, is employed:

$$\boldsymbol{\sigma} = \lambda \, e \, \boldsymbol{I} + 2 \, \mu \, \boldsymbol{\mathcal{E}} \,, \tag{2.5}$$

where I is the identity tensor. Accordingly, the stress tensor components are [84]:

$$\boldsymbol{\sigma} = \begin{bmatrix} \sigma_{zz} & \sigma_{zr} & 0\\ \sigma_{zr} & \sigma_{rr} & 0\\ 0 & 0 & \sigma_{\theta\theta} \end{bmatrix}, \tag{2.6a}$$

$$\sigma_{zz} = \lambda \frac{\partial u_r}{\partial r} + (\lambda + 2\mu) \frac{\partial u_z}{\partial z} + \lambda \frac{u_r}{r}, \qquad (2.6b)$$

$$\sigma_{rr} = (\lambda + 2\mu) \frac{\partial u_r}{\partial r} + \lambda \frac{\partial u_z}{\partial z} + \lambda \frac{u_r}{r}, \qquad (2.6c)$$

$$\sigma_{zr} = \mu \frac{\partial u_r}{\partial z} + \mu \frac{\partial u_z}{\partial r}, \qquad (2.6d)$$

$$\sigma_{\theta\theta} = \lambda \frac{\partial u_r}{\partial r} + \lambda \frac{\partial u_z}{\partial z} + (\lambda + 2\mu) \frac{u_r}{r}. \tag{2.6e}$$

Trace of the stress tensor, σ_{kk} , is then obtained as follows:

$$\sigma_{kk} = 3 \lambda e + 2 \mu e$$

$$= (3\lambda + 2\mu)e. \tag{2.7}$$

The first two governing equations for solid particles are the Newton's second law (Navier equations) in the 2D/axisymmetric domain [71, 74], which are:

$$\rho_0 \frac{\partial \vec{v}}{\partial t} = \vec{\nabla} \cdot \boldsymbol{\sigma} \,, \tag{2.8}$$

where $\vec{v}(v_z, v_r)$ is the velocity vector of the solid particle $(\vec{v} = \frac{d\vec{u}}{dt})$. For the z and r directions, Eq. (2.8) reads:

$$\frac{\partial v_z}{\partial t} = \frac{\partial}{\partial z} \left(\frac{\sigma_{zz}}{\rho_0} \right) + \frac{\partial}{\partial r} \left(\frac{\sigma_{zr}}{\rho_0} \right) + \frac{\sigma_{zr}}{r\rho_0} , \qquad (2.9a)$$

$$\frac{\partial v_r}{\partial t} = \frac{\partial}{\partial z} \left(\frac{\sigma_{zr}}{\rho_0} \right) + \frac{\partial}{\partial r} \left(\frac{\sigma_{rr}}{\rho_0} \right) + \frac{\sigma_{rr} - \sigma_{\theta\theta}}{r \rho_0} \,. \tag{2.9b}$$

The rest of the governing equations are obtained by taking temporal derivative from the constitutive relation, Eq. (2.5). In the Einstein's indicial notation, they would be:

$$\frac{\partial \sigma_{ij}}{\partial t} = \underbrace{\lambda \frac{\partial}{\partial t} \left(e \, \delta_{ij} \right) + \mu \frac{\partial}{\partial t} \left(2 \, \mathcal{E}_{ij} \right)}_{L_{ij}} + \underbrace{\frac{\partial \lambda}{\partial t} \left(e \, \delta_{ij} \right) + \frac{\partial \mu}{\partial t} \left(2 \, \mathcal{E}_{ij} \right)}_{H_{ij}}, \tag{2.10}$$

where δ_{ij} is the Kronecker delta. By employing Eqs. (2.3) and (2.4), L_{ij} in Eq. (2.10) becomes:

$$L_{zz} = \lambda \frac{\partial e}{\partial t} + \mu \frac{\partial}{\partial t} \left(2 \frac{\partial u_z}{\partial z} \right) = c_1^2 \rho_0 \frac{\partial v_z}{\partial z} + c_3^2 \rho_0 \frac{\partial v_r}{\partial r} + c_3^2 \rho_0 \frac{v_r}{r}, \qquad (2.11a)$$

$$L_{zr} = \mu \frac{\partial}{\partial t} \left(\frac{\partial u_r}{\partial z} + \frac{\partial u_z}{\partial r} \right) = c_2^2 \rho_0 \frac{\partial v_r}{\partial z} + c_2^2 \rho_0 \frac{\partial v_z}{\partial r}, \qquad (2.11b)$$

$$L_{rr} = \lambda \frac{\partial e}{\partial t} + \mu \frac{\partial}{\partial t} \left(2 \frac{\partial u_r}{\partial r} \right) = c_1^2 \rho_0 \frac{\partial v_r}{\partial r} + c_3^2 \rho_0 \frac{\partial v_z}{\partial z} + c_3^2 \rho_0 \frac{v_r}{r}$$
 (2.11c)

$$L_{\theta\theta} = \lambda \frac{\partial e}{\partial t} + \mu \frac{\partial}{\partial t} \left(2 \frac{u_r}{r} \right) = c_3^2 \rho_0 \frac{\partial v_r}{\partial r} + c_3^2 \rho_0 \frac{\partial v_z}{\partial z} + c_1^2 \rho_0 \frac{v_r}{r}, \qquad (2.11d)$$

2.2. SOLID MODEL 25

where $c_3^2=c_1^2-2\,c_2^2$. The term H_{ij} in Eq. (2.10) reads:

$$H_{ij} = \frac{1}{\lambda} \frac{\partial \lambda}{\partial t} \left(e \, \delta_{ij} \lambda \right) + \frac{1}{\mu} \frac{\partial \mu}{\partial t} \left(2 \, \mathcal{E}_{ij} \, \mu \right)$$

$$= \frac{1}{\lambda} \frac{\partial \lambda}{\partial t} \left(e \, \delta_{ij} \lambda \right) + \frac{1}{\mu} \frac{\partial \mu}{\partial t} \left(\sigma_{ij} - \lambda \, e \, \delta_{ij} \right)$$

$$= \lambda \, e \, \delta_{ij} \left(\frac{1}{\lambda} \frac{\partial \lambda}{\partial t} - \frac{1}{\mu} \frac{\partial \mu}{\partial t} \right) + \frac{1}{\mu} \frac{\partial \mu}{\partial t} \, \sigma_{ij} \,. \tag{2.12}$$

Using Eq. (2.7), one obtains:

$$H_{ij} = \frac{\lambda \sigma_{kk}}{3 \lambda + 2 \mu} \delta_{ij} \left(\frac{1}{\lambda} \frac{\partial \lambda}{\partial t} - \frac{1}{\mu} \frac{\partial \mu}{\partial t} \right) + \frac{1}{\mu} \frac{\partial \mu}{\partial t} \sigma_{ij}$$

$$= \frac{c_1^2 - 2 c_2^2}{3 c_1^2 - 4 c_2^2} \sigma_{kk} \left[\frac{1}{c_1^2 - 2 c_2^2} \frac{\partial}{\partial t} \left(c_1^2 - 2 c_2^2 \right) - \frac{1}{c_2^2} \frac{\partial c_2^2}{\partial t} \right] \delta_{ij} + \frac{1}{c_2^2} \frac{\partial c_2^2}{\partial t} \sigma_{ij}$$

$$= \frac{2 c_1}{3 c_1^2 - 4 c_2^2} \sigma_{kk} \left[\frac{\partial c_1}{\partial t} - \frac{c_1}{c_2} \frac{\partial c_2}{\partial t} \right] \delta_{ij} + \frac{2}{c_2} \frac{\partial c_2}{\partial t} \sigma_{ij}. \tag{2.13}$$

2.2.1 2D/Axisymmetric Formulation

In order to have an analogy between the governing equations in 2D and axisymmetric domains, it is more convenient to define a new gradient operator $\vec{\nabla}^{zr}$ as follows:

$$\vec{\nabla}^{zr} = \frac{\partial}{\partial z} \vec{e}_z + \frac{\partial}{\partial r} \vec{e}_r \,, \tag{2.14}$$

where the coordinate z (unit vector \vec{e}_z) is along the axis of symmetry and r (unit vector \vec{e}_r) is the radial coordinate. With this definition, for an arbitrary vector \vec{A} (A_z, A_r) , one obtains the following relation in the axisymmetric domain:

$$\vec{\nabla} \cdot \vec{A} = \frac{\partial A_z}{\partial z} + \frac{1}{r} \frac{\partial (r A_r)}{\partial r}$$

$$= \frac{\partial A_z}{\partial z} + \frac{\partial A_r}{\partial r} + \frac{A_r}{r}$$

$$= \vec{\nabla}^{zr} \cdot \vec{A} + \frac{A_r}{r}, \qquad (2.15)$$

and for an arbitrary scalar f:

$$\vec{\nabla}f = \frac{\partial f}{\partial z} + \frac{\partial f}{\partial r} = \vec{\nabla}^{zr}f.$$
 (2.16)

Hence, the linear elastodynamic equations within the active region (Eqs. (2.9) and Eq. (2.10)) can be recast as:

$$\frac{\partial \mathbf{U}}{\partial t} + \vec{\nabla}^{zr} \cdot \vec{\mathbf{F}} = \mathbf{E} + \mathbf{H} , \quad \vec{\nabla}^{zr} = \frac{\partial}{\partial z} \vec{e}_z + \frac{\partial}{\partial r} \vec{e}_r , \qquad (2.17a)$$

$$\mathbf{U} = \begin{bmatrix} v_z \\ v_r \\ \sigma_{zz} \\ \sigma_{zr} \\ \sigma_{rr} \\ \sigma_{\theta\theta} \end{bmatrix}, \quad \vec{F} = \begin{bmatrix} -\frac{\sigma_{zz}}{\rho_0} \vec{e}_z - \frac{\sigma_{zr}}{\rho_0} \vec{e}_r \\ -\frac{\sigma_{zr}}{\rho_0} \vec{e}_z - \frac{\sigma_{rr}}{\rho_0} \vec{e}_r \\ -\rho_0 c_1^2 v_z \vec{e}_z - \rho_0 c_3^2 v_r \vec{e}_r \\ -\rho_0 c_2^2 v_r \vec{e}_z - \rho_0 c_2^2 v_z \vec{e}_r \\ -\rho_0 c_3^2 v_z \vec{e}_z - \rho_0 c_1^2 v_r \vec{e}_r \\ -\rho_0 c_3^2 v_z \vec{e}_z - \rho_0 c_3^2 v_r \vec{e}_r \end{bmatrix}, \quad \mathbf{E} = \begin{bmatrix} \frac{\sigma_{zr}}{r \rho_0} \\ \frac{\sigma_{rr} - \sigma_{\theta\theta}}{r \rho_0} \\ \rho_0 c_3^2 \frac{v_r}{r} \\ 0 \\ \rho_0 c_3^2 \frac{v_r}{r} \\ \rho_0 c_1^2 \frac{v_r}{r} \end{bmatrix},$$

$$(2.17b)$$

$$\begin{bmatrix} -\rho_0 c_3^2 v_z \vec{e}_z - \rho_0 c_3^2 v_r \vec{e}_r \end{bmatrix} \qquad \begin{bmatrix} \rho_0 c_1^2 \frac{v_r}{r} \end{bmatrix}$$

$$H = \begin{bmatrix} 0 \\ H_{zz} \\ H_{zr} \\ H_{rr} \\ H_{\theta\theta} \end{bmatrix}, \quad H_{ij} = \frac{2c_1}{3c_1^2 - 4c_2^2} \sigma_{kk} \left[\frac{\partial c_1}{\partial t} - \frac{c_1}{c_2} \frac{\partial c_2}{\partial t} \right] \delta_{ij} + \frac{2}{c_2} \frac{\partial c_2}{\partial t} \sigma_{ij}, \qquad (2.17c)$$

where U and \vec{F} are the acoustic state variables and the respective flux vectors; the source term E is due to the axisymmetric formulation; and the source term H originates from the modulation of the longitudinal and transverse speeds of sounds, c_1 and c_2 , according to Eqs. (2.2a) and (2.2b). Furthermore, $\vec{v}(v_z, v_r)$ is the velocity vector; σ_{ij} are the components of the stress tensor with the trace of σ_{kk} ; and δ_{ij} is the Kronecker delta. The quantity c_3 is

2.3. FLUID FLOW MODEL 27

the following combination of c_1 and c_2 : $c_3^2 = c_1^2 - 2c_2^2$.

2.3 Fluid Flow Model

To properly describe the thermodynamic behavior of fluid particles, an appropriate equation of state needs to be employed. In this study, the Tait-Kirkwood equation of state for homentropic flows is used, which is as follows [82]:

$$\frac{p+D}{p_0+D} = \left(\frac{\rho}{\rho_0}\right)^{\gamma},\tag{2.18}$$

where p is the pressure; ρ is the density; p_0 and ρ_0 are reference pressure and density, respectively; D is a material coefficient; and γ is the power coefficient. In order to model wave propagation in the linear and non-linear fluid flow regimes, the perturbed state variables are employed [85]:

$$p = p_0 + p', (2.19a)$$

$$\rho = \rho_0 + \rho' \,, \tag{2.19b}$$

where ρ' and p' are the density and pressure disturbances. Accordingly, the equation of state provided by Eq. (2.18) is expanded about the reference state as follows:

$$p' = \rho_0 c_0^2 \left(\frac{\rho'}{\rho_0}\right) + \rho_0 c_0^2 \cdot \frac{\gamma - 1}{2} \left(\frac{\rho'}{\rho_0}\right)^2 + \cdots$$
 (2.20)

where c_0 is the speed of sound at the reference state and constant entropy, s, which is evaluated as:

$$c_0^2 = \left[\left(\frac{\partial p}{\partial \rho} \right)_s \right]_0 . \tag{2.21}$$

By keeping either only the first-order or up to the second-order terms in Eq. (2.20), the equations of state, respectively, for the linear and weakly non-linear regimes would be:

linear:
$$p' = c_0^2 \rho'$$
, (2.22a)

weakly non-linear:
$$p' = \rho_0 c_0^2 \left[\frac{\rho'}{\rho_0} + \frac{\gamma - 1}{2} \left(\frac{\rho'}{\rho_0} \right)^2 \right]$$
. (2.22b)

The speed of sound c in these two regimes can then be computed from the following relations:

linear:
$$c^2 = \left(\frac{\partial p'}{\partial \rho'}\right)_s = c_0^2$$
, (2.23a)

weakly non-linear:
$$c^2 = \left(\frac{\partial p'}{\partial \rho'}\right)_s = c_0^2 \left[1 + (\gamma - 1)\left(\frac{\rho'}{\rho_0}\right)\right].$$
 (2.23b)

In both the linear and non-linear regimes, it is assumed that the flow is homentropic; hence, the Euler set of equations, constituting the continuity and the momentum relations, are considered as the governing equations for fluid particles, which are:

$$\frac{\partial \rho}{\partial t} + \vec{\nabla} \cdot (\rho \, \vec{v}) = 0, \qquad (2.24a)$$

$$\rho \frac{\mathbf{D}\vec{v}}{\mathbf{D}t} + \vec{\nabla}p = 0, \qquad (2.24b)$$

where $\frac{D}{Dt}$ is the material derivative. By employing the perturbed variables $(p', \rho', \text{ and } \vec{v})$, Eqs. (2.24) become:

$$\frac{\partial \rho'}{\partial t} + \vec{\nabla} \cdot [(\rho_0 + \rho') \vec{v}] = 0, \qquad (2.25a)$$

$$(\rho_0 + \rho') \frac{\mathbf{D}\vec{v}}{\mathbf{D}t} + \vec{\nabla}p' = 0. \tag{2.25b}$$

2.3. FLUID FLOW MODEL 29

2.3.1 Linear Regime

Keeping the first-order terms in Eqs. (2.25) and using Eq. (2.22a) result in the governing equations for the linear regime, which are [85]:

$$\frac{\partial \rho'}{\partial t} + \vec{\nabla} \cdot (\rho_0 \, \vec{v}) = 0 \,, \tag{2.26a}$$

$$\frac{\partial \vec{v}}{\partial t} + \vec{\nabla} \left[c_0^2 \left(\frac{\rho'}{\rho_0} \right) \right] = 0.$$
 (2.26b)

2.3.2 Weakly Non-linear Regime

The governing equations in the weakly non-linear regime are obtained by keeping the first-and second-order terms of Eqs. (2.25) and using Eq. (2.22b) [74, 77, 81], which leads to:

$$\frac{\partial \rho'}{\partial t} + \vec{\nabla} \cdot [(\rho_0 + \rho') \, \vec{v}\,] = 0\,, \tag{2.27a}$$

$$(\rho_0 + \rho') \frac{\partial \vec{v}}{\partial t} + \rho_0 \vec{v} \cdot \vec{\nabla} \vec{v} + \vec{\nabla} \left[\rho_0 c_0^2 \left(\frac{\rho'}{\rho_0} + \frac{\gamma - 1}{2} \left(\frac{\rho'}{\rho_0} \right)^2 \right) \right] = 0.$$
 (2.27b)

To obtain the conservative form of Eq. (2.27b) for an irrotational flow, both sides of this equation are multiplied by:

$$\frac{1}{\rho_0 + \rho'} = \frac{1}{\rho_0} - \frac{\rho'}{\rho_0^2} + \cdots$$
 (2.28)

Hence, the conservative set of equations for the weakly non-linear regime becomes [77]:

$$\frac{\partial \rho'}{\partial t} + \vec{\nabla} \cdot [(\rho_0 + \rho') \vec{v}] = 0, \qquad (2.29a)$$

$$\frac{\partial \vec{v}}{\partial t} + \vec{\nabla} \left[\frac{\vec{v} \cdot \vec{v}}{2} + c_0^2 \left(\frac{\rho'}{\rho_0} \right) + c_0^2 \frac{\gamma - 2}{2} \left(\frac{\rho'}{\rho_0} \right)^2 \right] = 0.$$
 (2.29b)

2.3.3 2D/Axisymmetric Formulation

The governing equations in the linear (Eqs. (2.26)) and non-linear (Eqs. (2.29)) regimes are provided in invariant forms, which can be used in any coordinate system. To have these equations in the axisymmetric domain, Eqs. (2.14)–(2.16) are used. Consequently, by introducing the set of acoustic state variables U and the corresponding linear (subscript L) or non-linear (subscript NL) flux vectors \vec{F} , the governing equations can be written as follows:

$$\frac{\partial \mathbf{U}}{\partial t} + \vec{\nabla}^{zr} \cdot \vec{\mathbf{F}} = \mathbf{E}, \quad \vec{\nabla}^{zr} = \frac{\partial}{\partial z} \vec{e}_z + \frac{\partial}{\partial r} \vec{e}_r, \qquad (2.30a)$$

$$\boldsymbol{U} = \begin{bmatrix} \rho' \\ v_z \\ v_r \end{bmatrix}, \tag{2.30b}$$

$$\vec{F}_{L} = \begin{bmatrix} \rho_{0} \vec{v} \\ c_{0}^{2} \left(\frac{\rho'}{\rho_{0}} \right) \vec{e}_{z} \\ c_{0}^{2} \left(\frac{\rho'}{\rho_{0}} \right) \vec{e}_{z} \end{bmatrix}, \quad \vec{F}_{NL} = \begin{bmatrix} (\rho_{0} + \rho') \vec{v} \\ \left(\frac{1}{2} \left(v_{z}^{2} + v_{r}^{2} \right) + c_{0}^{2} \left(\frac{\rho'}{\rho_{0}} \right) + c_{0}^{2} \frac{\gamma - 2}{2} \left(\frac{\rho'}{\rho_{0}} \right)^{2} \right) \vec{e}_{z} \\ \left(\frac{1}{2} \left(v_{z}^{2} + v_{r}^{2} \right) + c_{0}^{2} \left(\frac{\rho'}{\rho_{0}} \right) + c_{0}^{2} \frac{\gamma - 2}{2} \left(\frac{\rho'}{\rho_{0}} \right)^{2} \right) \vec{e}_{r} \end{bmatrix}, \quad (2.30c)$$

$$\boldsymbol{E}_{L} = \begin{bmatrix} -\rho_{0} \frac{v_{r}}{r} \\ 0 \\ 0 \end{bmatrix}, \ \boldsymbol{E}_{NL} = \begin{bmatrix} -(\rho_{0} + \rho') \frac{v_{r}}{r} \\ 0 \\ 0 \end{bmatrix},$$

$$(2.30d)$$

where $\vec{v}(v_z, v_r)$ is the fluid flow velocity vector, and the source term \mathbf{E} is present due to the axisymmetric formulation. As previously mentioned, z coordinate is along the axis of symmetry, and r is the radial one. Their unit vectors are \vec{e}_z and \vec{e}_r , respectively.

2.4 Model for Fluid with Bubbles

If a fluid region contains gas (vapor) bubbles, the presence of bubbles must be accounted for. In this study, the volume-averaging technique based on the gas volume fraction is used. To find the gas volume fraction in bubbly zones, the modified version of the Keller-Miksis (KM) method [14] is employed to compute instantaneous changes of bubble radii. The details of this model are elaborated in the following subsections.

2.4.1 Volume-Averaging Technique

The volume-averaging technique employed in this study is based on the gas volume fraction β , with $0 \le \beta < 1$ and $\beta = 0$ in the absence of bubbles. Accordingly, the volume-averaging operator \Box is defined as follows [10, 28]:

$$\bar{\Box} = (1 - \beta) \,\Box_{\ell} + \beta \,\Box_{g} \,, \tag{2.31}$$

where the subscripts ℓ and g indicate the liquid and gas properties, respectively. Considering the fact that $\rho_{\ell} \gg \rho_{\rm g}$ and ignoring the velocity slip at the liquid-gas interfaces (i.e., assuming $\vec{v}_{\ell} \approx \vec{v}_{\rm g}$), Wijngaarden [28] and Caflisch et al. [33] suggested the following approximations for the averaged density and velocity:

$$\bar{\rho} \approx (1 - \beta) \, \rho_{\ell} \,, \tag{2.32a}$$

$$\bar{\vec{v}} \approx \vec{v}_{\ell} \approx \vec{v}_{\rm g} \,,$$
(2.32b)

which are valid for bubbly zones with void fractions up to the order of 10^{-2} [35].

Starting with the conservation of mass and the conservation of momentum for an infinitesimally small volume containing both liquid and gas at pressure p, the volume-averaged continuity and momentum equations for liquid-gas mixtures can be written as:

$$\frac{\partial \bar{\rho}}{\partial t} + \vec{\nabla} \cdot \left(\bar{\rho} \, \bar{\vec{v}} \right) = 0 \,, \tag{2.33a}$$

$$\bar{\rho} \frac{\mathbf{D}\bar{\vec{v}}}{\mathbf{D}t} + \vec{\nabla}p = 0, \qquad (2.33b)$$

where the assumption stated in Eq. (2.32b) is already taken into account. In Eq. (2.33b), $\frac{DD}{Dt}$ is the material derivative operator. Applying the approximation for the averaged density provided by Eq. (2.32a) and omitting the averaging operator above the velocity vector, one

obtains:

$$\frac{\partial \rho_{\ell}}{\partial t} + \vec{\nabla} \cdot (\rho_{\ell} \, \vec{v}) = \frac{\rho_{\ell}}{1 - \beta} \, \frac{\mathrm{D}\beta}{\mathrm{D}t} \,, \tag{2.34a}$$

$$\rho_{\ell} \frac{\mathbf{D}\vec{v}}{\mathbf{D}t} + \vec{\nabla}p = \rho_{\ell} \beta \frac{\mathbf{D}\vec{v}}{\mathbf{D}t}. \tag{2.34b}$$

After substituting $\rho_{\ell} = \rho_0 + \rho'$ and $p = p_0 + p'$ in Eqs. (2.34) (p_0 is the reference pressure) and using Eqs. (2.22), the linear and weakly non-linear governing equations for bubbly zones can be derived by keeping either only the first-order or up to the second-order terms, respectively.

2.4.2 2D/Axisymmetric Formulation

With applying Eqs. (2.14)–(2.16), then Eqs. (2.34) in axisymmetric domains read:

$$\frac{\partial \boldsymbol{U}}{\partial t} + \vec{\nabla}^{zr} \cdot \vec{\boldsymbol{F}} = \boldsymbol{E} + \boldsymbol{B},\tag{2.35a}$$

$$\boldsymbol{B}_{L} = \begin{bmatrix} \rho_{0} \frac{\partial \beta}{\partial t} \\ 0 \\ 0 \end{bmatrix}, \ \boldsymbol{B}_{NL} = \begin{bmatrix} \rho_{0} \frac{\partial \beta}{\partial t} \left(1 + \beta + \frac{\rho'}{\rho_{0}} \right) + \rho_{0} \, \vec{v} \cdot \vec{\nabla}^{zr} \beta \\ \beta \frac{\partial v_{z}}{\partial t} \\ \beta \frac{\partial v_{r}}{\partial t} \end{bmatrix}. \tag{2.35b}$$

In Eqs. (2.35), U, \vec{F} , and E are the same as those in Eqs. (2.30) for a bubble-less fluid. The additional term B represents the effects of bubble dynamics in a fluid medium, with the subscripts L and NL indicating the linear and weakly non-linear fluid flow regimes, respectively.

The instantaneous volume fraction of the gas inside the bubble cloud (void fraction), β , can be found from the distribution of the bubble radius at a given time moment, $R(\vec{r},t)$, as follows:

$$\beta = \sum_{b} \left[\beta_0^b \left(\vec{r} \right) \left(\frac{R^b \left(\vec{r}, t \right)}{R_0^b} \right)^3 \right], \tag{2.36}$$

where b is the index for a specific bubble size in the bubble cloud; $\beta_0(\vec{r})$ and R_0 are the initial void fraction distribution and the initial bubble radius, respectively; and $\vec{r}(z,r)$ is the position vector. The time derivative of β can be then found as:

$$\frac{\partial \beta}{\partial t} = 3 \sum_{b} \left[\beta_0^b(\vec{r}) \left(\frac{R^b(\vec{r}, t)}{R_0^b} \right)^2 \frac{\dot{R}^b(\vec{r}, t)}{R_0^b} \right], \tag{2.37}$$

where \dot{R} denotes the time derivative of R.

2.4.3 Bubble Cloud Types

The present physical models are formulated for 2D or axisymmetric flows. This imposes certain restrictions on the bubble set types, which could be considered. For example, arbitrary three-dimensional bubble clouds cannot be treated. In the current study, acoustic interactions of four types of bubble sets are investigated. These bubble sets are illustrated in Fig. 2.2, and they are described in detail in the following subsections.

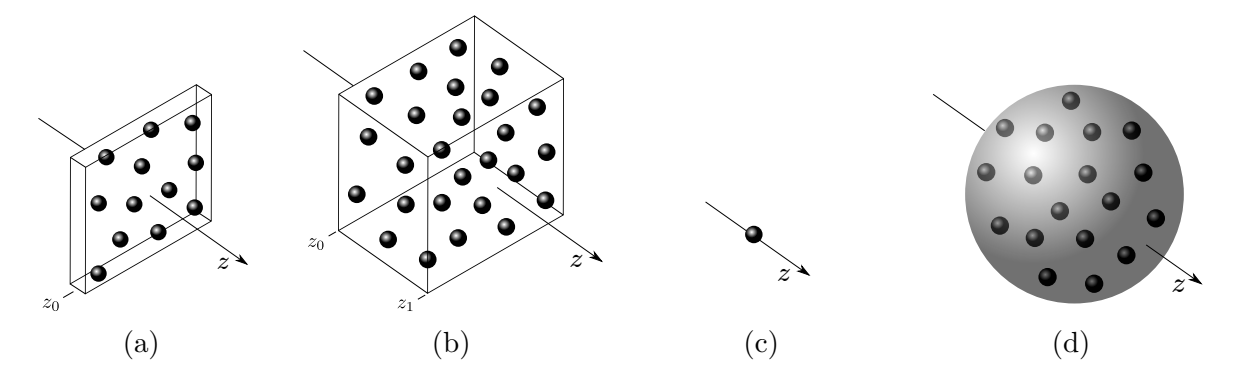


Fig. 2.2. Schematics of the bubble sets investigated in this study: (a) bubble-plane cloud, (b) bubble-layer cloud, (c) single bubble, and (d) spherical bubble cloud.

2.4.3.1 Bubble-plane cloud

A bubble-plane cloud, as shown in Fig. 2.2a, is evaluated under the paraxial approximation, i.e., all variables are considered to be functions of the coordinate z only. In a bubble-plane cloud, an infinite number of bubbles are located on an infinite plane $z = z_0$. In view

of the paraxial approximation, there is no variation, neither in the geometry nor in the acoustic variables, along the directions normal to the axis. Hence, the constituting bubbles of this cloud are under the same dynamic condition at any time moment. As a result, the oscillations of these bubbles are inevitably synchronized. This restriction stems from the paraxial formulation.

This type of the bubble cloud involves a singularity from the point of view of the volume-averaging approach since the bubbles are assumed to be located on a single plane. Hence, the initial void fraction β_0 of a bubble-plane cloud located at $z = z_0$ is defined as:

$$\beta_0 = \alpha \, \delta \left(z_0 \right), \tag{2.38}$$

where δ is the Kronecker-delta function. To find the coefficient α , let us consider a finite part of a very thin bubble cloud (see Fig. 2.2a) with the area A, the thickness $L = D_0 = 2 R_0$, and the volume $V = A D_0$, where R_0 and D_0 are the bubble radius and diameter, respectively.

The definition of the void fraction leads to the following relations:

$$\sum V_{\rm b} = \int_{V} \beta_0 \, \mathrm{d}V = \int_{L} \alpha \, \delta(z_0) \, A \, \mathrm{d}z = \alpha \, A \,, \tag{2.39}$$

where $V_{\rm b}$ is the volume of each individual bubble. Using the definition of the void fraction and Eq. (2.39), the physical void fraction of this bubble set, $\bar{\beta}_0$, can be written as:

$$\bar{\beta}_0 = \frac{\sum V_{\rm b}}{A D_0} = \frac{\alpha}{D_0} \,,$$
 (2.40)

which represents the volume of bubbles per unit volume of a very thin planar bubble cloud. From Eq. (2.40) one can find that

$$\alpha = \bar{\beta}_0 \, D_0 = 2 \, R_0 \, \bar{\beta}_0 \,. \tag{2.41}$$

Therefore, the initial void fraction of a bubble-plane cloud, β_0 , is obtained as:

$$\beta_0 = \alpha \,\delta\left(z_0\right) = 2\,R_0\,\bar{\beta}_0\,\delta\left(z_0\right). \tag{2.42}$$

Hence, the bubble-plane cloud model with the initial void fraction of β_0 can be defined on the basis of the physical void fraction $(\bar{\beta}_0)$.

2.4.3.2 Bubble-Layer Cloud

If the aforementioned bubble-plane cloud has a thickness along the z-axis (from z_0 to z_1), it becomes a bubble-layer cloud, as illustrated in Fig. 2.2b. Similarly, due to the paraxial formulation, there is no variation within the planes that are normal to the axis. In other words, the bubbles located on the same z-plane are dynamically synchronized. However, the bubbles located at different z-locations are dynamically independent.

For these bubble clouds, the initial volume fraction β_0 may be given as a smooth function, for example, a constant (representing a uniform distribution) or a Gaussian distribution.

2.4.3.3 Single Bubble

Realistic behaviors of an oscillating single bubble can be simulated in an axisymmetric model, as illustrated in Fig. 2.2c.

Similarly to bubble-plane clouds, this type also involves a singularity from the point of view of the volume-averaging approach since the bubble is assumed to be located at a single point. In such a model, the initial void fraction can be defined as:

$$\beta_0 = \alpha \,\delta(x_0) \,\delta(y_0) \,\delta(z_0) \,, \tag{2.43}$$

where $\vec{r}_0 = \vec{r}(x_0, y_0, z_0)$ is the location of the bubble, and δ is the Kronecker-delta function. The coefficient α is found as follows:

$$V_0 = \int_V \beta_0 \, dV = \int_V \alpha \, \delta(x_0) \, \delta(y_0) \, \delta(z_0) \, dV = \alpha \,. \tag{2.44}$$

Therefore,

$$\alpha = V_0, \tag{2.45}$$

where V_0 is the initial volume of the single bubble, which equals $\frac{4}{3}\pi R_0^3$. Hence,

$$\beta_0 = V_b \,\delta(x_0) \,\delta(y_0) \,\delta(z_0) \,. \tag{2.46}$$

2.4.3.4 Spherical Bubble Cloud

Spherical bubble clouds are investigated in axisymmetric domains, as demonstrated in Fig. 2.2d. In contrast with the bubble-plane and bubble-layer clouds, which are assumed to extend to infinity along the directions normal to the axis, spherical bubble clouds have a limited number of bubbles confined within a sphere. Due to the axisymmetric formulation, the bubbles which are on the same z-plane and located at the same distance r from the axis are dynamically synchronized.

Similarly to bubble-layer clouds, β_0 of spherical bubble clouds is assumed to be a smooth function, such as a uniform or a Gaussian distribution.

2.4.4 Keller-Miksis Model

For all bubble sets shown in Fig. 2.2, the modified version of the Keller-Miksis (KM) model proposed by Parlitz et al. [14] is employed to find the variation of the bubble radius, R(t), in time at a given location:

$$\left(1 - \frac{\dot{R}}{c}\right)R\ddot{R} + \frac{3}{2}\dot{R}^2\left(1 - \frac{\dot{R}}{3c}\right) = \left(1 + \frac{\dot{R}}{c}\right)\frac{P}{\rho} + \frac{R}{\rho c}\frac{\mathrm{d}P}{\mathrm{d}t},$$
(2.47a)

$$P = \left(p_0 - p_v + \frac{2\sigma}{R_0}\right) \left(\frac{R_0}{R}\right)^{3k} + p_v - p_0 - \frac{2\sigma}{R} - \frac{4\mu}{R}\dot{R} - p'_{\text{ext}}(t), \qquad (2.47b)$$

where R_0 is the initial undisturbed bubble radius; c is the speed of sound in the fluid region provided by Eqs. (2.23); ρ is the local fluid density, which equals $\rho_0 + \rho'$; p_0 is the undisturbed ambient static pressure; p_v is the vapor pressure within the bubble; p'_{ext} is the external pressure disturbance, which is the bubble-stimulating factor; k is the polytropic exponent of the gas content; σ is the bubble surface tension; μ is the local fluid viscosity; and \dot{R} and \ddot{R} are the first and second time derivatives of R.

Although the flow surrounding the bubble is considered to be inviscid, the fluid viscosity at

the bubble location has a noticeable effect on the bubble dynamics and cannot be ignored, as also discussed by Smereka and Banerjee [17]. The linear resonance frequency, $f_b = \omega_b/(2\pi)$, of a bubble oscillating according to Eqs. (2.47) is given by [2]:

$$f_{\rm b} = \frac{1}{2\pi R_0 \sqrt{\rho}} \sqrt{3k \left(p_0 + \frac{2\sigma}{R_0} - p_{\rm v}\right) - \frac{2\sigma}{R_0} - \frac{4\mu^2}{\rho R_0^2}}.$$
 (2.48)

It should be noted that in this study, the fully non-linear model provided by Eqs. (2.47) is employed to simulate bubble dynamics regardless whether the surrounding fluid behaves linearly or non-linearly.

2.4.5 Estimation of the Bubble Stimulating Pressure

In order to accurately compute radii of bubbles by Eqs. (2.47), a proper estimation of the external stimulating pressure, which is denoted by p'_{ext} in Eq. (2.47b), is required. When each bubble in a cloud is stimulated by p'_{ext} , it is excited and generates some pressure disturbances propagating back into the domain, which are denoted as p'_{out} . Therefore, the total pressure disturbance in the fluid medium at the bubble location, p', includes the effects of both the p'_{ext} and the p'_{out} pressure fields. In this study, in the cases of dilute bubble-layer and spherical bubble clouds (Figs. 2.2b and 2.2d), the pressure disturbance at the bubble location, p', is considered to be the stimulating pressure of that bubble, which appears to be an acceptable estimate (see [28, 29, 33, 35]). In other words, for bubble-layer and spherical bubble clouds, p'_{ext} is assumed to be equal to p'.

For bubble-plane clouds and single bubbles (Figs. 2.2a and 2.2c), the void fraction is represented by a discontinuous function (Kronecker-delta); therefore, the pressure p' at the bubble location does not properly represent the stimulating pressure. In such cases, the effects of p'_{out} need to be excluded from p' in order to obtain a more accurate stimulating pressure field. Considering a domain surrounding a single bubble (or a bubble-plane cloud) with the volume V, one can assume [10, 41] that

$$p'_{\text{ext}} \approx \frac{1}{V} \left[\int_{V} p' \, dV - \int_{V} p'_{\text{out}} \, dV \right].$$
 (2.49)

In the above relation, it is assumed that the $p'_{\rm ext}$ field is uniform over V. Hence, V, as an arbitrary surrounding volume, needs to be as small as possible to make this assumption valid. In addition, Eq. (2.49) represents superposition of the first modes of the pressure fields. As a result, Eq. (2.49) should be expected to produce erroneous results where signal amplification and non-linear effects dominate. Thus, to have a better estimation for the $p'_{\rm out}$ term, the regions where such effects are dominant should be excluded from the integration volume V. The choices of the volume V in the numerical integration of the proposed model are discussed in Section 3.7.

After choosing a proper integration domain in Eq. (2.49), the pressure disturbance scattered by the cloud (p'_{out}) needs to be estimated in the whole surrounding domain, V. The suggested relations for p'_{out} in this study, which include fewer approximations than those available in the literature [10, 41], are derived in the following subsections. These relations are obtained for the linear fluid flow model, and, accordingly, the problems involving bubble-plane clouds and single bubbles are considered only in the linear fluid regime.

2.4.5.1 Scattered Signals from bubble-plane clouds

Under the paraxial approximation, wave fronts are planar; hence, to simulate the scattered signals from the bubble surfaces, which are spherical waves, it is assumed that many bubbles of the same size are placed on a plane, as shown in Fig. 2.2a. If the number of bubbles on this plane is sufficiently high, it is feasible to assume that the resultant wave front generated by this set of bubbles would be planar as well.

According to Eqs. (2.30) and (2.35), if the fluid flow regime is linear, the presence of bubbly zones changes the governing equations by adding a source term to the continuity relation. Based on this observation, an analytical relation for the signals scattered from a bubble-plane cloud can be obtained for the linear flow regime. By using the mass source term provided by Eq. (2.35b) for the linear regime, the derivative of the void fraction given by Eq. (2.36), and Eq. (2.42) for the initial void fraction, the mass flow rate generated by an oscillating bubble-plane cloud is found as:

$$\dot{m} = \int_{V} \rho_0 \frac{\partial \beta}{\partial t} \, dV = \int_{L} \rho_0 \left[3 \left(\frac{R}{R_0} \right)^2 \frac{\dot{R}}{R_0} \, \beta_0 \right] A \, dz$$

$$= \rho_0 \left[3 \left(\frac{R}{R_0} \right)^2 \frac{\dot{R}}{R_0} \alpha \right] A, \qquad (2.50)$$

where α is provided by Eq. (2.41). In paraxial domains, each of the right- and left-running waves (indicated by the RR and LR subscripts, respectively) carries half of the mass flow rate generated by a bubble-plane cloud. Therefore, the velocity \mathcal{V} of the fluid particles carried by these signals at the bubble-plane cloud location are:

$$\dot{m}_{\rm RR} = \dot{m}_{\rm LR} = \frac{\dot{m}}{2} = \rho_0 \, A \, \mathcal{V}_{\rm RR} \,,$$
 (2.51a)

$$\mathcal{V}_{RR}(t) = -\mathcal{V}_{LR}(t) = \frac{\dot{m}}{2\rho_0 A} = \frac{3}{2} \left(\frac{R}{R_0}\right)^2 \frac{\dot{R}}{R_0} \alpha.$$
 (2.51b)

The respective pressures in paraxial domains read:

$$\mathcal{P}_{RR}(t) \approx \rho_0 c_0 \mathcal{V}_{RR},$$
 (2.52a)

$$\mathcal{P}_{LR}(t) \approx -\rho_0 c_0 \mathcal{V}_{LR}$$
 (2.52b)

The approximation made in the above equations is that the speed of sound within the undisturbed medium, c_0 , is used. Hence, the pressure disturbance generated by a bubble-plane cloud is:

$$\mathscr{P}(t) = \mathscr{P}_{RR}(t) = \mathscr{P}_{LR}(t) \approx \frac{3}{2} \rho_0 c_0 \left(\frac{R(t)}{R_0}\right)^2 \frac{\dot{R}(t)}{R_0} \alpha, \qquad (2.53)$$

where the coefficient α is provided by Eq. (2.41). If a bubble-plane cloud is located at z_0 , the scattered pressure disturbance from this cloud recorded at the location z and the time moment t is obtained as follows:

$$p'_{\text{out}}(z,t) = \mathcal{P}(t^*); \quad t^* = t - \frac{|z - z_0|}{c_0}.$$
 (2.54)

The relation provided by Eq. (2.54) for p'_{out} can then be used in Eq. (2.49) to estimate the stimulating pressure p'_{ext} for bubble-plane clouds.

2.4.5.2 Scattered Signals from Single Bubbles

A single bubble can be considered as a spherical transducer whose surface vibrates with the velocity $\mathcal{V}(t) = \dot{R}$. This boundary condition can also be obtained by following the approach described in Section 2.4.5.1. Indeed, as it was already mentioned, the effects of an oscillating single bubble on the governing equations of the linear flow regime is an extra mass source term provided by Eq. (2.35b). Hence, by using Eqs. (2.37), (2.43) and (2.45), the mass flow rate generated by the vibrating surface of a single bubble in the linear flow regime would be:

$$\dot{m} = \int_{V} \rho_0 \frac{\partial \beta}{\partial t} \, dV = \int_{V} \rho_0 \left[3 \left(\frac{R}{R_0} \right)^2 \frac{\dot{R}}{R_0} \beta_0 \right] dx \, dy \, dz$$

$$= \rho_0 \left[3 \left(\frac{R}{R_0} \right)^2 \frac{\dot{R}}{R_0} \alpha \right] = \rho_0 \left[\left(4 \pi R^2 \right) \dot{R} \right], \qquad (2.55)$$

where α is provided by Eq. (2.45). Finally, since in the current model single bubbles are considered to be points with no volume, the velocity of the fluid particles carried by the out-going signals (\mathcal{V}) generated by the bubble surface can be approximated as follows at the bubble surface:

$$\mathcal{V}(t) \approx \frac{\dot{m}}{\rho_0 A_{\rm b}} = \dot{R} \,, \tag{2.56}$$

where $A_{\rm b} = 4 \pi R^2$ is the area of the bubble surface.

For a single bubble considered as a spherical transducer, the generated pressure disturbances may be found by solving the wave equation,

$$\nabla^2 p = \frac{1}{c_0^2} \frac{\partial^2 p}{\partial t^2} \,, \tag{2.57}$$

the solution of which for the out-going signals is as follows:

$$\rho = \frac{f(\mathcal{R} - c_0 t)}{\mathcal{R}} = \frac{f(u)}{\mathcal{R}}; \quad u = \mathcal{R} - c_0 t, \qquad (2.58)$$

where \mathcal{R} is the spherical radial coordinate with the origin at the bubble location. In the above equations, the speed of sound is approximated by its value in undisturbed media, c_0 .

2.5. CONCLUSION 41

In addition, the momentum equation reads:

$$\rho_0 \frac{\partial v_{\mathcal{R}}}{\partial t} = -\frac{\partial p}{\partial \mathcal{R}} = \frac{f}{\mathcal{R}^2} - \frac{f'}{\mathcal{R}}; \quad f' = \frac{\mathrm{d}f}{\mathrm{d}u}, \tag{2.59}$$

where $v_{\mathscr{R}}$ is the radial velocity along \mathscr{R} . Now, let $g(t) = f(R_0 - c_0 t)$ at the bubble surface, where $\mathscr{R} = R_0$ and $v_{\mathscr{R}} = \dot{R}$; then Eq. (2.59) is simplified to:

$$\rho_0 \left. \frac{\partial v_{\mathscr{R}}}{\partial t} \right|_{\mathscr{R}=R_0} = \rho_0 \, \ddot{R} = \frac{g}{R_0^2} + \frac{\dot{g}}{R_0 \, c_0} \,. \tag{2.60}$$

Therefore,

$$\dot{g}(t) = c_0 \left(\rho_0 R_0 \ddot{R}(t) - \frac{g(t)}{R_0} \right). \tag{2.61}$$

Hence, the out-going pressure disturbance at the bubble surface would be:

$$\mathscr{P}(t) = \frac{g(t)}{R_0} \,. \tag{2.62}$$

The scattered pressure disturbance at the distance \mathcal{R} from the bubble center and at the time moment t is then obtained as follows:

$$p'_{\text{out}}(\mathcal{R}, t) = \frac{\mathcal{P}(t^*) \cdot R_0}{\mathcal{R}}; \quad t^* = t - \frac{\mathcal{R} - R_0}{c_0}.$$
(2.63)

Then, p'_{out} obtained from Eq. (2.63) can be used in Eq. (2.49) to estimate the stimulating pressure p'_{ext} for single bubbles.

2.5 Conclusion

In this chapter, a general physico-mathematical model for the magneto-acoustic WPC in the 2D/axisymmetric domain was proposed. In the solid zones (such as the conjugator), the Navier equation and temporal derivate of the constitutive relation make a hyperbolic set of equations in the conservative form for propagation of linear waves. To have a more realistic

model for the WPC process, the physical interaction of electromagnetic and elastic fields within the conjugator was also considered, which adds an extra source term to the governing equation of the conjugator. For the fluid zones surrounding the conjugator, the continuity and the momentum equations in both linear and weakly non-nonlinear flow regimes make a conservative set of hyperbolic equations. In the non-linear regime, the Tait-Kirkwood equation of state for homentropic flows was employed.

This physical model was then tailored to be used for measuring bubble dimensions. By using the volume-averaging technique, the governing equations in both the linear and weakly non-linear regimes were modified to include effects of bubble dynamics in the fluid zones. These effects add extra source terms to the governing equation, which are evaluated by the KM model. Among different possible types of bubble clouds, four patterns are adopted in this study: bubble-plane clouds, bubble-layer clouds, single bubbles, and spherical bubble clouds. The physical models pertaining to these bubble clouds were provided in this chapter.

CHAPTER 3

Numerical Method

In this chapter, first, some relevant numerical approaches and the previous numerical Wave Phase Conjugation (WPC) studies are reviewed in Section 3.1 with the goal to elucidate the choices made in the present study. Then, the numerical methods and techniques employed in this study will be thoroughly elaborated in Sections 3.2–3.7. Conclusions of this chapter follow in Section 3.8.

3.1 Introduction

Wave propagation analysis in an unbounded medium requires special boundary conditions at the external computational domain boundaries, which would prevent spurious signal reflections from the boundaries and the subsequent contamination of the computational domain with the reflected non-physical waves. Berenger [86] introduced an effective boundary condition, called Perfectly Matched Layer (PML), and showed that it is properly matched to the physical domain in the sense that for an arbitrary wave, no reflection occurs at the boundary. As the PML method caused some difficulties with its numerical implementation, another method based on the PML was introduced and extended for modeling wave propagations [87–89]. This method, which was called Nearly Perfectly Matched Layer (NPML), can be appropriately incorporated into the numerical schemes based on the Godunov-type flux. It also prevents instabilities in anisotropic media.

The NPML method has two important advantages: under this method, the system of equations still remains hyperbolic; and the respective NPML variables are updated via ordinary differential equations, while the classical PML method employs partial differential equations. The Multi-axial Perfectly Matched Layer (MPML) approach is another method introduced to stabilize the PML technique for anisotropic media; however, it was shown that this method is not perfectly matched to the physical domain [87]. In the present study, the NPML method is followed.

Reviewing the literature revealed that various numerical approaches were applied to solve the sets of governing equations outlined in Chapter 2. Second-order Godunov-type Total Variation Diminishing (TVD) Finite Volume (FV) schemes were used for hyperbolic equations [51, 54, 70, 71]. Some Finite Difference (FD) schemes were employed for the Khokhlov-Zabolotskaya-Kuznetsov (KZK) equation [53, 63, 75]. Such low-order techniques are generally more robust than high-order ones. However, in WPC applications one considers propagation of high-frequency (~1–10 MHz), and hence short wavelength, waves over relatively long distances (of the order of tens of centimeters). In such a situation, low-order methods may not provide sufficient accuracy [90–92] unless very fine meshes are used, leading to high computational costs.

High-order methods would allow to obtain a similar accuracy at markedly lower computational cost or higher accuracy at the same computational cost [93, 94]. In WPC studies, Bou Matar et al. [73] applied the Pseudo-Spectral Time Domain (PSTD) method, which uses Fourier transforms for high-order estimation of spatial derivatives, to simulate the conjugation process within solid domains. Leadbetter [77] implemented a high-order FV Weighted Essentially Non-Oscillatory (WENO) scheme for one-dimensional WPC simulations including both the conjugator and the surrounding fluid domains. This approach was shown to be a reliable and accurate method for modeling of the propagation of high-frequency waves. However, the well-known deficiency of the WENO technique is relative difficulty with its extension to 2D/3D domains due to its wide selective numerical stencils. In the present work, in an attempt to avoid such issues, we turn our attention to compact high-order schemes, which use data just from the immediate neighbors of a given cell.

The assessment of recent efforts on the development and application of compact high-order schemes shows that the Discontinuous Galerkin (DG) method on unstructured grids is widely 3.1. INTRODUCTION 45

used for compressible flows [90, 93, 95, 96]. In order to obtain a high order of accuracy, the DG method incorporates two important features of the FV and Finite Element (FE) methods, namely, the wave propagation concept via Riemann solvers at the cell interfaces and high-order polynomials as solution basis. It is derived via the weighted residual form of the governing equations and can be categorized into the modal and nodal types based on how Degrees Of Freedom (DOFs) are defined and updated [92]. For the first time, the DG method was employed by Reed and Hill [97] for the neutron transport equation. Van Leer [98] used this method for unsteady advection laws. Cockburn et al. [99] and Cockburn and Shu [100] applied the Runge-Kutta Discontinuous Galerkin (RKDG) method to hyperbolic conservation laws. Bassi and Rebay [101, 102] implemented the DG method for the compressible Euler and Navier-Stokes equations and also included the curved boundary elements.

One of the widely-used formulations of the DG method is the Quadrature-based Discontinuous Galerkin (QDG) technique in which the quadrature method is used to evaluate surface and volume integrations. Hesthaven and Warburton [103] presented an efficient DG method storing data at nodal points, denoted as Nodal Discontinuous Galerkin (NDG). They proposed to use the solution basis for expanding the flux, and, as a result, some numerical interpolations are avoided. In addition, they suggested to pre-compute the numerical integrations on reference elements in order to enhance the numerical efficiency. Comparing these two methods, one can realize that the QDG technique is more computationally expensive than the NDG method [95, 104]. However, in non-linear regimes the NDG scheme exhibits some errors, such as aliasing errors which may lead to highly oscillatory solutions due to using the same basis for representation of solution and flux terms.

An efficient and general high-order numerical scheme (a non-collocated NDG method) is proposed in this study [74] to simulate WPC processes in 2D/axisymmetric domains. This general numerical framework can properly handle both linear and weakly non-linear flow regimes. Employing this scheme, Modarreszadeh and Timofeev [74] numerically assessed and verified different properties of the WPC process including giant amplification, frequency selectivity, and the wave retro-focusing. In the present work, this scheme is used as the basis for development of the model including gas bubbles in the fluid zone.

In this study, interactions of bubble dynamics with WPC processes are investigated. During these interactions, depending on the stimulation conditions, bubbles might undergo violent collapses and rebounds. Dimensions of bubbles in such phases experience rapid changes which cause some issues in numerical simulations. In order to avoid very small time steps to capture these rapid changes, Parlitz et al. [14] employed a non-linear C^{∞} -diffeomorphism map that preserves features of the dynamic system. Such maps are invertible, and both the map and its inverse are infinite-time differentiable. Using this transformation, they could obtain smoother variations in new coordinates, leading to less problematic numerical simulations. To avoid such numerical issues, this transformation is applied in this study.

A proper high-order scheme for marching in time is another crucial point in modeling WPC processes. Although a number of previous studies implemented the conventional Runge-Kutta (RK) scheme for discretization in time [77], there were also some efforts to modify the RK scheme in order to address its stability issues. The Strong Stability-Preserving (SSP)-RK method was designed to maintain the TVD property of the scheme, which is essential for solving hyperbolic systems of equations near regions with high spatial gradients [105–107]. This approach is followed in the present study.

In the remainder of this chapter, first the NPML boundary condition is elaborated in Section 3.2. Then, the proposed modified NDG scheme is provided in Section 3.3, which is followed by the formulations for the numerical fluxes and the flux Jacobian in Sections 3.4 and 3.5, respectively. In Section 3.6, the C^{∞} -diffeomorphism transformation of bubble dynamics is explained. The temporal scheme is elaborated in Section 3.7, and the conclusions are outlined in Section 3.8.

3.2 NPML Boundary Condition

In order to avoid any false reflections from the outer boundaries of the computational domain, an appropriate boundary condition must be set. For this purpose, the physical domain is wrapped in a special layer (NPML—Nearly Perfectly Matched Layer) in which the outgoing disturbances are damped with no reflection back into the physical computational domain. To implement the NPML zone, a complex coordinate system \tilde{z} - \tilde{r} is considered as follows [87]:

$$\tilde{z}(z) = z + j f(z), \qquad (3.1a)$$

$$\tilde{r}(r) = r + j g(r), \qquad (3.1b)$$

where f and g are the functions implying deformations along the imaginary axis (with the unit of j) in the z and r directions, respectively. Hence,

$$\frac{\partial}{\partial \tilde{z}} = \frac{1}{1 + j \frac{\mathrm{d}f}{\mathrm{d}z}} \frac{\partial}{\partial z} = \frac{1}{s^z(z)} \frac{\partial}{\partial z}, \qquad (3.2a)$$

$$\frac{\partial}{\partial \tilde{r}} = \frac{1}{1 + j \frac{\mathrm{d}g}{\mathrm{d}r}} \frac{\partial}{\partial r} = \frac{1}{s^r(r)} \frac{\partial}{\partial r}.$$
 (3.2b)

The coordinate stretching metrics s^z and s^r in Eqs. (3.2) are defined as:

$$s^{z}(z) = 1 + \frac{\sigma^{z}(z)}{j\omega}, \qquad (3.3a)$$

$$s^{r}(r) = 1 + \frac{\sigma^{r}(r)}{j\omega}, \qquad (3.3b)$$

where ω is the frequency of a signal which propagates within the NPML zone. In the above equations, σ^z and σ^r are the stretching functions in the z and r directions, respectively, given by the following relations:

$$\sigma^z = \sigma_{\text{max}} \left(\frac{z - z_0}{d^z} \right)^2 \,, \tag{3.4a}$$

$$\sigma^r = \sigma_{\text{max}} \left(\frac{r - r_0}{d^r} \right)^2, \tag{3.4b}$$

where σ_{max} is a parameter of the coordinate transformation; d^z and d^r are the NPML layer thicknesses in the respective directions; and z_0 and r_0 are coordinates of the location where the NPML layer starts within the domain [87].

To show the performance of the complex coordinate stretching provided by Eqs. (3.1), a plane signal \tilde{P} with the amplitude \hat{P} and the wavenumbers k_z and k_r along the respective directions is considered in the complex coordinate system \tilde{z} - \tilde{r} as follows:

$$\tilde{P} = \hat{P} \cdot \exp\left[j\left(\omega t - k_z \,\tilde{z} - k_r \,\tilde{r}\right)\right]. \tag{3.5}$$

By using Eqs. (3.1)–(3.3), this signal becomes:

$$\tilde{P} = \hat{P} \cdot \exp\left[j\left(\omega t - k_z z - j k_z f(z) - k_r r - j k_r g(r)\right)\right]
= \left[\hat{P} \cdot \exp\left[j\left(\omega t - k_z z - k_r r\right)\right]\right] \cdot \exp\left[k_z f(z) + k_r g(r)\right]
= \left[\hat{P} \cdot \exp\left[j\left(\omega t - k_z z - k_r r\right)\right]\right] \cdot \exp\left[-k_z \int \frac{\sigma^z}{\omega} dz - k_r \int \frac{\sigma^r}{\omega} dr\right]
= \left[\hat{P} \cdot \exp\left[j\left(\omega t - k_z z - k_r r\right)\right]\right] \cdot \exp\left[-\frac{1}{c} \int \sigma^z dz - \frac{1}{c} \int \sigma^r dr\right],$$
(3.6)

where c is the wave propagation speed. Equation (3.6) clearly characterizes a damped plane wave in the physical z-r coordinate system.

Taking the Fourier transform of Eq. (2.17a), Eq. (2.30a), or Eq. (2.35a) (as general conservation relations) and employing the above complex coordinate result in the following governing equations:

$$j\,\omega\,\widehat{\boldsymbol{U}} + \frac{1}{s^z}\frac{\partial\widehat{\boldsymbol{F}}^z}{\partial z} + \frac{1}{s^r}\frac{\partial\widehat{\boldsymbol{F}}^r}{\partial r} = \widehat{\boldsymbol{E}} + \widehat{\boldsymbol{H}} + \widehat{\boldsymbol{B}},\,\,(3.7)$$

where $\widehat{\Box}$ are the variables in the frequency domain. By neglecting the spatial dependency of the stretching metrics, Eq. (3.7) becomes:

$$j\,\omega\,\widehat{\boldsymbol{U}} + \frac{\partial\widehat{\boldsymbol{F}'}^z}{\partial z} + \frac{\partial\widehat{\boldsymbol{F}'}^r}{\partial r} = \widehat{\boldsymbol{E}} + \widehat{\boldsymbol{H}} + \widehat{\boldsymbol{B}}$$

$$\widehat{\boldsymbol{F}'}^z = \frac{\widehat{\boldsymbol{F}}^z}{s^z},$$
(3.8a)

$$\widehat{\boldsymbol{F}'}^z = \frac{\widehat{\boldsymbol{F}}^z}{s^z},\tag{3.8b}$$

$$\widehat{\boldsymbol{F}'}^r = \frac{\widehat{\boldsymbol{F}}^r}{s^r} \,. \tag{3.8c}$$

Berenger [108] showed that the approximations used to obtain Eqs. (3.8) have no effects on the performance of the NPML layer, and this zone still remains a perfectly matched one. Taking the inverse Fourier transform of Eqs. (3.8) yields:

$$\frac{\partial \boldsymbol{U}}{\partial t} + \vec{\nabla}^{zr} \cdot \vec{\boldsymbol{F}}' = \boldsymbol{E} + \boldsymbol{H} + \boldsymbol{B}, \qquad (3.9a)$$

$$\frac{\partial \mathbf{F}^{\prime z}}{\partial t} + \sigma^z \mathbf{F}^{\prime z} = \frac{\partial \mathbf{F}^z}{\partial t}, \qquad (3.9b)$$

$$\frac{\partial \mathbf{F'}^r}{\partial t} + \sigma^r \mathbf{F'}^r = \frac{\partial \mathbf{F}^r}{\partial t}.$$
 (3.9c)

To simplify Eqs. (3.9), a new variable $\vec{\boldsymbol{G}}$ is defined as follows:

$$\vec{G} = \vec{F}' - \vec{F}. \tag{3.10}$$

Hence, the modified governing equations within the NPML zones would be:

$$\frac{\partial \mathbf{U}}{\partial t} + \vec{\nabla}^{zr} \cdot (\vec{\mathbf{F}} + \vec{\mathbf{G}}) = \mathbf{E} + \mathbf{H} + \mathbf{B}, \qquad (3.11a)$$

$$\frac{\partial \mathbf{G}^z}{\partial t} = -\sigma^z \left(\mathbf{F}^z + \mathbf{G}^z \right), \tag{3.11b}$$

$$\frac{\partial \mathbf{G}^r}{\partial t} = -\sigma^r \left(\mathbf{F}^r + \mathbf{G}^r \right). \tag{3.11c}$$

As seen in Eq. (3.11a), an additional flux correction term \vec{G} is added to the governing equations in the NPML regions. This term is found via solution of the supplemental ordinary differential equations (3.11b) and (3.11c).

3.3 Modified NDG Method

The NDG scheme achieves higher spatial orders of accuracy by increasing the number of solution points within each grid element. In order to represent variables in a reference triangular element, appropriate sets of points for interpolation are required. However, these sets are not usually associated with efficient quadrature rules [7]. Therefore, two sets of points are usually needed in a reference triangular element: one for representation/interpolation and another for efficient numerical integration. From the point of view of numerical efficiency, decreasing the number of interpolations (from solution points to either integration or flux points) would improve the overall numerical performance.

Following this idea, the NDG method proposed by Hesthaven and Warburton [103] eliminates the interpolations by representing the flux terms using the solution basis, and

also by pre-computing the integrations. Although using the same basis for representing the solution and the flux is acceptable for the linear equations, it causes aliasing errors in the case of non-linear equations due to poor representation of the flux terms, which might lead to some stability issues [103]. This type of errors is more pronounced in under-resolved cases where the energy of modes which are outside of the representation span is aliased on to the lower modes [109]. To overcome them, Hesthaven and Warburton [103] proposed a number of approaches, including projection of the flux terms on the solution basis instead of interpolation and addition of numerical dissipation by employing limiters or filters.

In this study, a modified version of the NDG method in weak formulation for triangular elements is proposed, which can be referred to as a non-collocated NDG technique with pre-computed integrations. This scheme retrieves the collocation property in linear regimes and better represents and integrates the flux terms in weakly non-linear regimes within the same numerical framework, which would make it suitable, in particular, for simulating multi-physics cases, such as WPC processes and others in which the numerical accuracy is the main concern. To achieve that, independent bases are used to represent the solution and the flux terms as follows:

$$\boldsymbol{U} = \boldsymbol{U}_j \,\phi_j^{\mathrm{S}} \,, \tag{3.12a}$$

$$\vec{F} = \vec{F}_j \, \phi_j^{\mathrm{F}}, \quad \vec{G} = \vec{G}_j \, \phi_j^{\mathrm{F}},$$
 (3.12b)

$$(\boldsymbol{F}^{\mathrm{n}})^* = (\boldsymbol{F}_{j}^{\mathrm{n}})^* \phi_{j}^{\mathrm{Fb}}, \quad (\boldsymbol{G}^{\mathrm{n}})^* = (\boldsymbol{G}_{j}^{\mathrm{n}})^* \phi_{j}^{\mathrm{Fb}},$$
 (3.12c)

where $\phi_j^{\rm S}$, $\phi_j^{\rm F}$, and $\phi_j^{\rm Fb}$ are the Lagrange shape functions associated with the node j for representing the solution, the flux, and the normal flux across the grid element boundaries, respectively. In the above and subsequent equations, the Einstein's indicial notation is used. In weakly non-linear regimes, the order of the flux basis is set twice that of the solution, while in linear regimes they share the same basis ($\phi^{\rm S} = \phi^{\rm F}$), leading to the original NDG method. In the present study, the Williams-Shunn (WS) [7] and Witherden-Vincent (WV) [8] sets of nodes are employed for representation and numerical integration, respectively, within triangular elements, while the Gauss-Legendre (GL) [9] nodes are used for both representation and integration along the element boundaries. These sets of nodes for different orders are provided in Appendix A.2.

Starting with Eq. (3.11a) as the general conservation relation, which is valid for different zones (such as fluid, solid, bubbly, and NPML zones), and tending the numerical residual to zero in the Galerkin sense, one obtains the following integral equation for a grid element:

$$\int_{V} \frac{\partial \boldsymbol{U}}{\partial t} \, \phi_{i}^{S} \, dV + \int_{V} \vec{\nabla}^{zr} \cdot (\vec{\boldsymbol{F}} + \vec{\boldsymbol{G}}) \, \phi_{i}^{S} \, dV = \int_{V} \boldsymbol{E} \, \phi_{i}^{S} \, dV + \int_{V} \boldsymbol{H} \, \phi_{i}^{S} \, dV + \int_{V} \boldsymbol{B} \, \phi_{i}^{S} \, dV ,$$
(3.13)

where $\phi_i^{\rm S}$ is the weighting function, which is the same as the *i*-th shape function in the present scheme. The volume integration domain, V, in Eq. (3.13) is an annular volume created by revolving a triangular grid element around the axis in an axisymmetric domain, as shown in Fig. 3.1a. Also, Fig. 3.1a illustrates the axisymmetric volume element, dV, which is shown in blue color.

Equation (3.13) then needs to be transformed from the physical axisymmetric coordinate

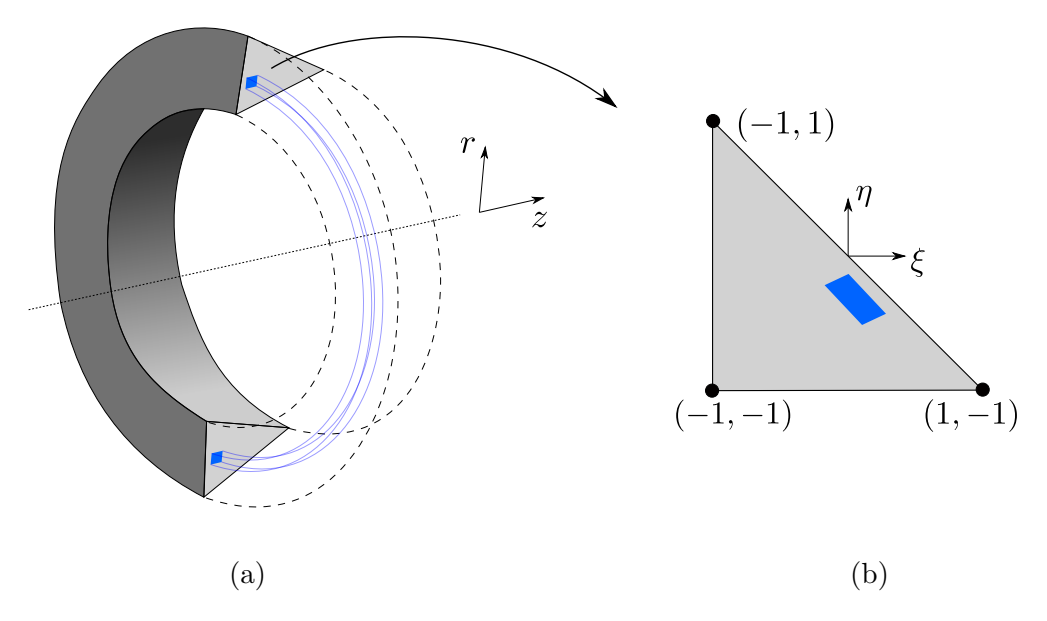


Fig. 3.1. Transformation of an axisymmetric grid element: (a) an annular integration volume with triangular cross section in the physical coordinate system $(\vec{q} = (z, r))$ along with a volume element with quadrilateral cross section shown in blue color (half of the volumes are shown for better illustration); (b) transformed cross sections of the integration domain and the volume element in the reference coordinate system, $\vec{\theta} = (\xi, \eta)$.

system, $\vec{q} = (z, r)$, to the reference one, $\vec{\theta} = (\xi, \eta)$ [103]. The transformed cross sections of the integration domain and the volume element are depicted in Fig. 3.1b. The transformation relations between these two coordinates are:

$$dV = (2\pi r) dA = (2\pi r) |J| dA^{\theta}, \qquad (3.14)$$

$$dS = (2\pi r) d\ell = (2\pi r) J_s d\ell^{\theta}, \qquad (3.15)$$

where dV and dS are the physical volume and surface elements; and dA and $d\ell$ are the physical area and length elements of the volume element cross section, as depicted in Fig. 3.1. In addition, the superscript θ refers to the reference coordinate; |J| and J_s are the volumetric and surface transformation Jacobians, respectively. The details of this geometrical transformation are provided in Appendix A.1.

Let LHS denote the left-hand side of Eq. (3.13):

LHS =
$$\int_{V} \frac{\partial \boldsymbol{U}}{\partial t} \,\phi_{i}^{S} \,dV + \int_{V} \vec{\nabla}^{zr} \cdot (\vec{\boldsymbol{F}} + \vec{\boldsymbol{G}}) \,\phi_{i}^{S} \,dV.$$
 (3.16)

By representing the variables with the appropriate shape functions provided by Eqs. (3.12), the first term of Eq. (3.16) is further simplified as follows:

$$\int_{V} \frac{\partial \boldsymbol{U}}{\partial t} \, \phi_{i}^{S} \, dV = \int_{A} \frac{\partial \boldsymbol{U}}{\partial t} \, \phi_{i}^{S} (2 \pi r) \, dA = \int_{A^{\theta}} \frac{\partial \boldsymbol{U}}{\partial t} \, \phi_{i}^{S} (2 \pi r) \, |\boldsymbol{J}| \, dA^{\theta}
= \frac{d\boldsymbol{U}_{j}}{dt} \cdot \int_{A^{\theta}} \phi_{j}^{S} \, \phi_{i}^{S} (2 \pi r) \, |\boldsymbol{J}| \, dA^{\theta} = M_{ij} \, \frac{d\boldsymbol{U}_{j}}{dt} ,$$
(3.17)

where M_{ij} are the components of the mass matrix, which are defined as:

$$M_{ij} = \int_{A^{\theta}} \phi_j^{S} \phi_i^{S} |\boldsymbol{J}| (2\pi r) dA^{\theta}.$$
 (3.18)

The physical flux divergence term in Eq. (3.16) is simplified as follows:

$$\int_{V} \left(\vec{\nabla}^{zr} \cdot \vec{\boldsymbol{F}} \right) \phi_{i}^{S} dV = \int_{A} \left(\vec{\nabla}^{zr} \cdot \vec{\boldsymbol{F}} \right) \phi_{i}^{S} (2 \pi r) dA
= \int_{A} \vec{\nabla}^{zr} \cdot \left(\vec{\boldsymbol{F}} \phi_{i}^{S} (2 \pi r) \right) dA - \int_{A} \vec{\boldsymbol{F}} \cdot \vec{\nabla}^{zr} \left(\phi_{i}^{S} (2 \pi r) \right) dA$$

$$= \int_{\ell} \left(\vec{\boldsymbol{F}} \, \phi_i^{\mathrm{S}} \left(2 \, \pi \, r \right) \right) \cdot \vec{n} \, \mathrm{d}\ell - \int_{A} \vec{\boldsymbol{F}} \cdot \vec{\nabla}^{zr} \left(\phi_i^{\mathrm{S}} \left(2 \, \pi \, r \right) \right) \mathrm{d}A \,, \tag{3.19}$$

where the Gauss theorem was employed to change the area integral into the one over the element boundaries. By applying Eqs. (3.14) and (3.15) and representing the flux terms with the respective bases given by Eqs. (3.12), the physical divergence term in Eq. (3.19) is transformed as follows:

$$\int_{V} \left(\vec{\nabla}^{zr} \cdot \vec{F} \right) \phi_{i}^{S} dV = \int_{\ell^{\theta}} \left(\vec{F} \phi_{i}^{S} (2 \pi r) \right) \cdot \vec{n} J_{s} d\ell^{\theta} - \int_{A^{\theta}} F^{r} (2 \pi) \phi_{i}^{S} |J| dA^{\theta} - \int_{A^{\theta}} \vec{F} \cdot \left(J^{T} \right)^{-1} \left(\vec{\nabla}^{\theta} \phi_{i}^{S} \right) (2 \pi r) |J| dA^{\theta}$$

$$= \left(F_{j}^{n} \right)^{*} \cdot \int_{\ell^{\theta}} \phi_{j}^{Fb} \phi_{i}^{S} (2 \pi r) J_{s} d\ell^{\theta} - F_{j}^{r} \cdot \int_{A^{\theta}} \phi_{j}^{F} (2 \pi) \phi_{i}^{S} |J| dA^{\theta} - F_{j}^{r} \cdot \int_{A^{\theta}} \phi_{j}^{F} (2 \pi) \phi_{i}^{S} |J| dA^{\theta}$$

$$= M_{ij}^{e} \left(F_{j}^{n} \right)^{*} - M_{ij}^{ax} F_{j}^{r} - \left(S_{ij}^{z} F_{j}^{z} + S_{ij}^{r} F_{j}^{r} \right). \tag{3.20}$$

The NPML fluxes can also be represented with the flux bases as:

$$\vec{\boldsymbol{G}} = \sum_{j} \vec{\boldsymbol{G}}_{j} \,\phi_{j}^{\mathrm{F}} \,, \tag{3.21a}$$

$$(\mathbf{G}^{\mathrm{n}})^* = \sum_{j} (\mathbf{G}_{j}^{\mathrm{n}})^* \phi_{j}^{\mathrm{Fb}}. \tag{3.21b}$$

Hence, by following the same approach as the one used to obtain Eqs. (3.19) and (3.20), the NPML flux divergence term in Eq. (3.16) would be:

$$\int_{V} \left(\vec{\nabla}^{zr} \cdot \vec{\boldsymbol{G}} \right) \phi_{i}^{S} dV = M_{ij}^{e} \left(\boldsymbol{G}_{j}^{n} \right)^{*} - M_{ij}^{ax} \boldsymbol{G}_{j}^{r} - \left(S_{ij}^{z} \boldsymbol{G}_{j}^{z} + S_{ij}^{r} \boldsymbol{G}_{j}^{r} \right),$$
(3.22)

where $M_{ij}^{\rm e}$ and $M_{ij}^{\rm ax}$ in Eqs. (3.20) and (3.22) are the components of the edge and axis mass matrices, respectively, which are defined as:

$$M_{ij}^{\mathrm{e}} = \int_{\ell^{\theta}} \phi_j^{\mathrm{Fb}} \,\phi_i^{\mathrm{S}} \, J_s \left(2 \,\pi \,r\right) \,\mathrm{d}\ell^{\theta} \,, \tag{3.23}$$

$$M_{ij}^{\text{ax}} = \int_{A\theta} \phi_j^{\text{F}}(2\pi) \,\phi_i^{\text{S}} |\boldsymbol{J}| \,\mathrm{d}A^{\theta} \,. \tag{3.24}$$

Besides, S_{ij}^z and S_{ij}^r in Eqs. (3.20) and (3.22) are the components of the stiffness matrices for the z and r directions given by:

$$\begin{bmatrix} S_{ij}^{z} \\ S_{ij}^{r} \end{bmatrix} = \int_{A^{\theta}} \phi_{j}^{F} \left(\boldsymbol{J}^{T} \right)^{-1} \vec{\nabla}^{\theta} \phi_{i}^{S} (2 \pi r) |\boldsymbol{J}| dA^{\theta}$$

$$= \int_{A^{\theta}} \phi_{j}^{F} \frac{1}{|\boldsymbol{J}|} \begin{bmatrix} \frac{\partial y}{\partial \eta} & -\frac{\partial y}{\partial \xi} \\ -\frac{\partial x}{\partial \eta} & \frac{\partial x}{\partial \xi} \end{bmatrix} \begin{bmatrix} \frac{\partial \phi_{i}^{S}}{\partial \xi} \\ \frac{\partial \phi_{i}^{S}}{\partial \eta} \end{bmatrix} |\boldsymbol{J}| (2 \pi r) dA^{\theta}$$

$$= \int_{A^{\theta}} \phi_{j}^{F} \begin{bmatrix} \frac{\partial y}{\partial \eta} \cdot \frac{\partial \phi_{i}^{S}}{\partial \xi} - \frac{\partial y}{\partial \xi} \cdot \frac{\partial \phi_{i}^{S}}{\partial \eta} \\ -\frac{\partial x}{\partial \eta} \cdot \frac{\partial \phi_{i}^{S}}{\partial \xi} + \frac{\partial x}{\partial \xi} \cdot \frac{\partial \phi_{i}^{S}}{\partial \eta} \end{bmatrix} (2 \pi r) dA^{\theta}. \tag{3.25}$$

Thus, the matrix formulation of Eq. (3.16) would be:

LHS =
$$M_{ij} \frac{d\mathbf{U}_j}{dt} - \left[S_{ij}^z \left(\mathbf{F}_j^z + \mathbf{G}_j^z \right) + S_{ij}^r \left(\mathbf{F}_j^r + \mathbf{G}_j^r \right) \right] - M_{ij}^{ax} \left(\mathbf{F}_j^r + \mathbf{G}_j^r \right) + M_{ij}^{e} \left(\left(\mathbf{F}_j^n \right)^* + \left(\mathbf{G}_j^n \right)^* \right).$$
 (3.26)

Based on the polynomial order of the elemental matrices provided by Eqs. (3.18) and (3.23)–(3.25), proper sets of WV nodes are used to exactly evaluate numerical integrations.

The right-hand side of Eq. (3.13) is as follows:

RHS =
$$\int_{V} \boldsymbol{H} \, \phi_{i}^{S} \, dV + \int_{V} \boldsymbol{E} \, \phi_{i}^{S} \, dV + \underbrace{\int_{V} \boldsymbol{B} \, \phi_{i}^{S} \, dV}_{\boldsymbol{Q}_{i}},$$
 (3.27)

where the last term accounting for the bubble dynamics is denoted by Q_i and will be elaborated more thoroughly in Sections 3.3.1 and 3.3.2. To simplify Eq. (3.27), the following representations are employed:

$$\boldsymbol{H} = \sum_{j} \boldsymbol{H}_{j} \, \phi_{j}^{\mathrm{S}} \,, \tag{3.28a}$$

$$\mathbf{E}' = \sum_{j} \mathbf{E}'_{j} \,\phi_{j}^{\mathrm{F}} \,, \tag{3.28b}$$

where $\mathbf{E}' = \mathbf{E} \cdot r$, and it is represented with ϕ^{F} as it is originated from the flux terms. Hence, by applying Eqs. (3.14) and (3.15), one obtains:

RHS =
$$\int_{A} \boldsymbol{H} \, \phi_{i}^{S} (2 \pi r) \, dA + \int_{A} \boldsymbol{E} \, \phi_{i}^{S} (2 \pi r) \, dA + \boldsymbol{Q}_{i}$$

= $\int_{A^{\theta}} \boldsymbol{H} \, \phi_{i}^{S} (2 \pi r) |\boldsymbol{J}| \, dA^{\theta} + \int_{A^{\theta}} \boldsymbol{E}' \, \phi_{i}^{S} (2 \pi) |\boldsymbol{J}| \, dA^{\theta} + \boldsymbol{Q}_{i}$. (3.29)

After applying Eqs. (3.28), the RHS becomes:

RHS =
$$\boldsymbol{H}_{j} \cdot \int_{A^{\theta}} \phi_{j}^{S} \phi_{i}^{S} (2 \pi r) |\boldsymbol{J}| dA^{\theta} + \boldsymbol{E}'_{j} \cdot \int_{A^{\theta}} \phi_{j}^{F} \phi_{i}^{S} (2 \pi) |\boldsymbol{J}| dA^{\theta} + \boldsymbol{Q}_{i}$$

= $M_{ij} \boldsymbol{H}_{j} + M_{ij}^{ax} \boldsymbol{E}'_{j} + \boldsymbol{Q}_{i}$, (3.30)

where M_{ij} and M_{ij}^{ax} are the mass and axis mass matrices provided by Eqs. (3.18) and (3.24), respectively. Consequently, Eq. (3.13) is transformed into the following matrix equation:

$$M_{ij} \frac{\mathrm{d}\boldsymbol{U}_{j}}{\mathrm{d}t} - \left[S_{ij}^{z} \left(\boldsymbol{F}_{j}^{z} + \boldsymbol{G}_{j}^{z} \right) + S_{ij}^{r} \left(\boldsymbol{F}_{j}^{r} + \boldsymbol{G}_{j}^{r} \right) \right] - M_{ij}^{\mathrm{ax}} \left(\boldsymbol{F}_{j}^{r} + \boldsymbol{G}_{j}^{r} \right) +$$

$$+ M_{ij}^{\mathrm{e}} \left(\left(\boldsymbol{F}_{j}^{\mathrm{n}} \right)^{*} + \left(\boldsymbol{G}_{j}^{\mathrm{n}} \right)^{*} \right) = M_{ij} \boldsymbol{H}_{j} + M_{ij}^{\mathrm{ax}} \boldsymbol{E}_{j}^{\prime} + \boldsymbol{Q}_{i}; \quad i = 1, \dots, N$$

$$(3.31)$$

In this equation, i is a free index representing the solution points of each grid element $(1 \le i \le N)$; j is the dummy index over which the summation is implied in the Einstein's summation convention; and z and r superscripts indicate the axial and radial components in a 2D/axisymmetric domain, respectively. Equation (3.31) is valid for both geometrically linear and non-linear elements provided that the appropriate transformation Jacobians are used. It should be noted that for non-linear elements, the Jacobian terms in the elemental matrices have spatial variations, so stronger quadrature rules are necessary to adequately evaluate the integration. After evaluating all respective terms, Eq. (3.31) is to be multiplied by the inverse of the mass matrix, M^{-1} , to yield a semi-discrete formulation for each solution node of a grid element. Then, a high-order temporal scheme is needed to accurately compute the acoustic variables at each solution node, (U_i) , at the next time moment, which is elaborated

in detail in Section 3.7.

In the following subsections, the source term Q_i in Eq. (3.31), representing the effects of the bubble dynamics, is obtained for the linear and weakly non-linear flow regimes.

3.3.1 Bubble Dynamics in Linear Flow Regime

In the linear regime, only the continuity relation contains a source term due to the bubble dynamics, as seen from the term $B_{\rm L}$ in Eq. (2.35b). Since representations of bubble distributions are smooth for bubble-layer and spherical bubble clouds (Figs. 2.2b and 2.2d), in these cases the term $B_{\rm L}$ can be represented as follows:

$$\boldsymbol{B} = \boldsymbol{B}_j \, \phi_j^{\mathrm{S}} \,. \tag{3.32}$$

Therefore, the source term Q_i for such bubble clouds equals:

$$\mathbf{Q}_{i} = \int_{V} \mathbf{B}_{j} \, \phi_{j}^{S} \, \phi_{i}^{S} \, dV$$

$$= M_{ij} \, \mathbf{B}_{j}, \qquad (3.33)$$

where, as previously mentioned, M_{ij} are the components of the mass matrix (see Eq. (3.18)). To find \mathbf{B}_j in Eq. (3.33), the modified Keller-Miksis (KM) model (Eqs. (2.47)) needs to be applied to every solution point of each grid element within the bubble cloud.

For single bubbles in axisymmetric flows (Fig. 2.2c) or bubble-plane clouds in paraxial domains (Fig. 2.2a), Eq. (3.32) is not valid anymore since the initial void fraction is represented by the Kronecker-delta function ($\beta_0 = \alpha \, \delta \, (\vec{r}_b)$, where \vec{r}_b is the bubble location), which is a discontinuous function (see Section 2.4). In such situations, let

$$\boldsymbol{Q}_i = \begin{bmatrix} q_i^{(1)} \\ 0 \\ 0 \end{bmatrix}; \tag{3.34}$$

then the continuity source term, $q_i^{(1)}$, would be:

$$q_i^{(1)} = \int_V \rho_0 \frac{\partial \beta}{\partial t} \, \phi_i^{\mathrm{S}} \, \mathrm{d}V = \rho_0 \left[3 \, \alpha \left(\frac{R(t)}{R_0} \right)^2 \frac{\dot{R}(t)}{R_0} \right] \phi_i^{\mathrm{S}}(\vec{r}_{\mathrm{b}}), \tag{3.35}$$

where $\phi_i^{\rm S}(\vec{r}_{\rm b})$ is the shape function associated with the solution node i, which is evaluated at the bubble location $\vec{r}_{\rm b}$ (see Figs. 2.2a and 2.2c). In this equation, α is the coefficient given by Eq. (2.41) or Eq. (2.45). For these bubble clouds, the modified KM model (Eqs. (2.47)) is only applied to where the single bubble or the bubble-plane cloud is located.

3.3.2 Bubble Dynamics in Weakly Non-linear Flow Regime

In this subsection, the source term Q_i in Eq. (3.31) is found for bubble-layer and spherical bubble clouds when the medium fluid flow behaves non-linearly. For this goal, the non-linear source term $B_{\rm NL}$, provided by Eq. (2.35b), is decomposed into two terms as follows:

$$\boldsymbol{B}_{NL} = \begin{bmatrix} \rho_0 \frac{\partial \beta}{\partial t} \left(1 + \beta + \frac{\rho'}{\rho_0} \right) + \rho_0 \, \vec{v} \cdot \vec{\nabla}^{zr} \beta \\ \beta \frac{\partial v_z}{\partial t} \\ \beta \frac{\partial v_r}{\partial t} \end{bmatrix} = \boldsymbol{B}^{(1)} + \boldsymbol{B}^{(2)}, \qquad (3.36)$$

where

$$\boldsymbol{B}^{(1)} = \begin{bmatrix} \rho_0 \frac{\partial \beta}{\partial t} \left(1 + \beta + \frac{\rho'}{\rho_0} \right) \\ \beta \frac{\partial v_z}{\partial t} \\ \beta \frac{\partial v_r}{\partial t} \end{bmatrix}, \ \boldsymbol{B}^{(2)} = \begin{bmatrix} \rho_0 \vec{v} \cdot \vec{\nabla}^{zr} \beta \\ 0 \\ 0 \end{bmatrix}. \tag{3.37}$$

The source terms associated with $B^{(1)}$ and $B^{(2)}$ are denoted by $Q^{(1)}$ and $Q^{(2)}$, respectively. For bubble-layer and spherical bubble clouds (Figs. 2.2b and 2.2d), these terms can be represented with smooth polynomials due to the smoothness of bubble distribution profiles.

If the flow variables are represented with polynomials of order p (order of the solution shape functions, ϕ^{S}), the components of $\boldsymbol{B}^{(1)}$ need polynomials of at least order 2p to be accurately represented. Hence, ϕ^{F} , which are the shape functions associated with the flux points in the grid elements, can be used for such a purpose. As a result, $\boldsymbol{Q}_{i}^{(1)}$, which is associated with $\boldsymbol{B}^{(1)}$, reads:

$$\mathbf{Q}_{i}^{(1)} = \int_{V} \mathbf{B}^{(1)} \,\phi_{i}^{S} \,dV = \int_{V} \mathbf{B}_{j}^{(1)} \,\phi_{j}^{F} \,\phi_{i}^{S} \,dV = M_{ij}^{b} \,\mathbf{B}_{j}^{(1)}, \qquad (3.38)$$

where

$$M_{ij}^{\rm b} = \int_{A^{\theta}} \phi_j^{\rm F} \,\phi_i^{\rm S} \,|\mathbf{J}| \,(2\,\pi\,r) \,\mathrm{d}A^{\theta} \,.$$
 (3.39)

In Eq. (3.39), $M_{ij}^{\rm b}$ are the components of the modified mass matrix; |J| is the Jacobian of the transformation matrix; and $\mathrm{d}A^{\theta}$ is the reference area element (see Fig. 3.1).

Since the representation bases are discontinuous at the element boundaries in the NDG scheme, the source term $\mathbf{Q}_i^{(2)} = \left[q_i^{(21)},0,0\right]^{\mathrm{T}}$, which is associated with $\mathbf{B}^{(2)}$ in Eq. (3.37), requires additional considerations. The term $q_i^{(21)}$, which is the first component of $\mathbf{Q}^{(2)}$ at the solution node i, can be written as:

$$q_i^{(21)} = \int_V \left(\rho_0 \, \vec{v} \cdot \vec{\nabla}^{zr} \beta \right) \phi_i^{\mathrm{S}} \, \mathrm{d}V \,. \tag{3.40}$$

The application of the Gauss theorem to Eq. (3.40) twice results in:

$$q_i^{(21)} = \int_S \left[\left(\rho_0 \, \phi_i^{\mathrm{S}} \, \vec{v} \, \beta \right)^* - \left(\rho_0 \, \phi_i^{\mathrm{S}} \, \vec{v} \, \beta \right) \right] \cdot \vec{n} \, \mathrm{d}S + \int_V \left(\rho_0 \, \vec{v} \cdot \vec{\nabla}^{zr} \beta \right) \phi_i^{\mathrm{S}} \, \mathrm{d}V \,, \tag{3.41}$$

where the superscript '*' refers to the common variables at the boundary between two neighboring grid elements, which are computed with an upwind scheme for the variable in Eq. (3.41). Then, two new variables are defined and represented as follows:

$$\vec{\zeta} = \rho_0 \,\beta \,\vec{v} = \vec{\zeta}_j \,\phi_j^{\mathrm{F}} \,, \tag{3.42a}$$

$$\tau = \rho_0 \, \vec{v} \cdot \vec{\nabla}^{zr} \beta = \tau_j \, \phi_j^{\mathrm{F}} \,. \tag{3.42b}$$

3.4. NUMERICAL FLUX 59

Consequently,

$$\zeta^{\mathbf{n}} = \vec{\zeta} \cdot \vec{n} = \zeta_{j}^{\mathbf{n}} \phi_{j}^{\mathbf{Fb}}, \tag{3.43}$$

where ϕ^{Fb} are the shape functions associated with the flux points along the common boundary between neighboring elements. Therefore, Eq. (3.41) reads:

$$q_i^{(21)} = M_{ij}^{e} \left(\left(\zeta_j^{n} \right)^* - \zeta_j^{n} \right) + M_{ij}^{b} \tau_j.$$
 (3.44)

In the above equation, M_{ij}^{e} are the components of the edge mass matrix, provided by Eq. (3.23). The total source term representing the bubble dynamics in the weakly non-linear flow regime is then obtained by adding Eqs. (3.38) and (3.44), which yields:

$$\mathbf{Q}_{i} = \mathbf{Q}_{i}^{(1)} + \mathbf{Q}_{i}^{(2)} \\
= \begin{bmatrix}
M_{ij}^{b} \left[\rho_{0} \frac{\partial \beta}{\partial t} \left(1 + \beta + \frac{\rho'}{\rho_{0}} \right) \right]_{j} \\
M_{ij}^{b} \left[\beta \frac{\partial v_{z}}{\partial t} \right]_{j} \\
M_{ij}^{b} \left[\beta \frac{\partial v_{r}}{\partial t} \right]_{j}
\end{bmatrix} + \begin{bmatrix}
M_{ij}^{e} \left(\left(\zeta_{j}^{n} \right)^{*} - \zeta_{j}^{n} \right) + M_{ij}^{b} \tau_{j} \\
0 \\
0
\end{bmatrix} .$$
(3.45)

3.4 Numerical Flux

To solve Eq. (3.31), evaluation of the normal common flux at the boundary between two neighboring cells, $(\mathbf{F}^n)^*$, is required. In the present model, each of the two cells may belong to a linear solid, linear fluid, or non-linear fluid region; furthermore, different fluid and solid materials may be present. Thus, the number of possible material and model combinations at an element boundary is quite substantial. In the present section, a general framework to handle all possible cases is developed. For this goal, the flux differencing method is employed. This method was shown to properly handle wave transmissions and reflections at material interfaces [110].

Figure 3.2a illustrates two neighboring cells with curved edges, denoted as 'in' and 'out',

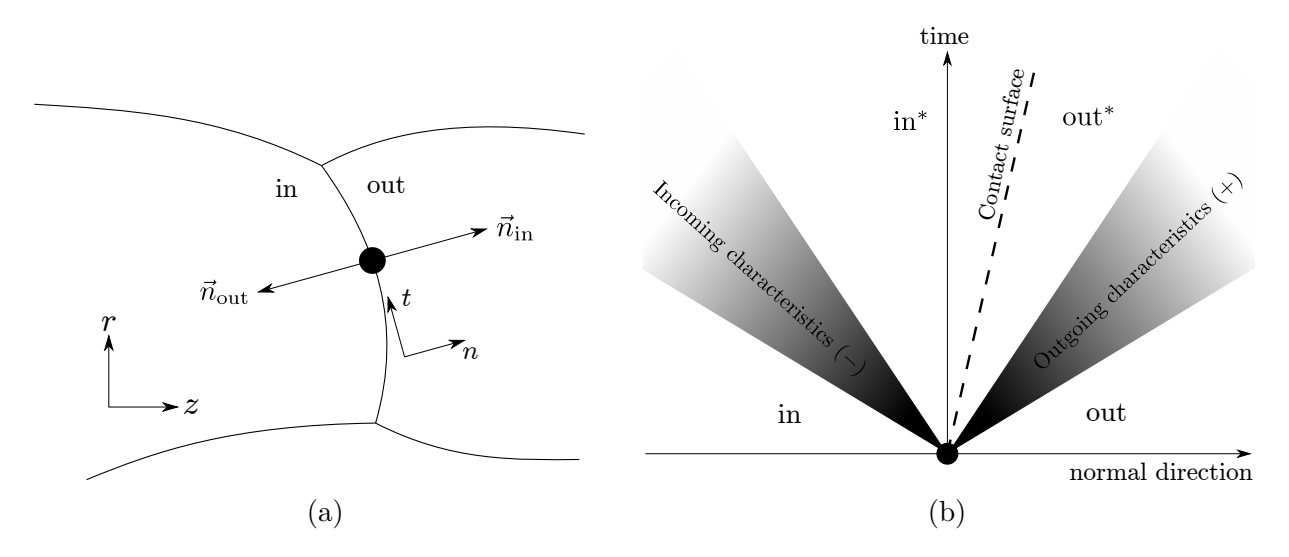


Fig. 3.2. Notations for a flux point, shown by a black circle, on a common boundary between two neighboring cells, 'in' and 'out': (a) the normal vectors at the flux point on a curved common boundary; (b) different zones created by the incoming and outgoing characteristics (with respect to the cell 'in') and the contact surface.

in a 2D/axisymmetric domain. The numerical flux needs to be evaluated at different flux points located at the common boundary. One of these points together with the respective normal vectors is shown in Fig. 3.2a. For the same flux point, Fig. 3.2b depicts how the space-time domain is split into different zones by the incoming and outgoing characteristics and the contact surface, which appears if the two cells have different materials. The variables in zones 'in' and 'out', $U_{\rm in}$ and $U_{\rm out}$, are considered to be given; the goal is to calculate the normal flux in the zone 'in*', $(F_{\rm in}^{\rm n})^*$, which is the numerical normal flux to be used in Eq. (3.31) for the cell 'in'.

By using the flux differencing method for the cell 'in', the numerical flux is evaluated as [111]:

$$(\boldsymbol{F}_{\text{in}}^{\text{n}})^* = \boldsymbol{F}_{\text{in}}^{\text{n}} + \boldsymbol{A}_{\text{in}}^{-} \cdot (\boldsymbol{U}_{\text{in}}^* - \boldsymbol{U}_{\text{in}}), \qquad (3.46)$$

where \mathbf{F}^{n} is the normal flux, \mathbf{U} is the set of variables, and \mathbf{A}^{-} is the normal flux Jacobian based on the incoming characteristics with respect to the cell 'in'. Since \mathbf{U}_{in}^{*} is generally unknown, it must be found using the variables in the zone 'out', \mathbf{U}_{out} . For a general case in

3.4. NUMERICAL FLUX

which the two cells might contain either fluid or solid materials, let f be a function relating U_{in}^* and U_{out}^* by imposing physical boundary conditions, i.e., $U_{\text{in}}^* = f(U_{\text{out}}^*)$. Due to the fact that A_{in}^- does not see the effects of the outgoing characteristics, Eq. (3.46) may be simplified to:

$$(\boldsymbol{F}_{\text{in}}^{\text{n}})^{*} = \boldsymbol{F}_{\text{in}}^{\text{n}} + \boldsymbol{A}_{\text{in}}^{-} \cdot (f(\boldsymbol{U}_{\text{out}}^{*}) - \boldsymbol{U}_{\text{in}})$$

$$= \boldsymbol{F}_{\text{in}}^{\text{n}} + \boldsymbol{A}_{\text{in}}^{-} \cdot (f(\boldsymbol{U}_{\text{out}}) - \boldsymbol{U}_{\text{in}}).$$
(3.47)

Equation (3.47) is the general formulation employed in this study to evaluate the numerical flux of both boundary and non-boundary cells.

As elaborated in Section 3.2, the computational domain is wrapped in an NPML zone, in which the signals are effectively damped. To safely evacuate the residual of damped waves from the boundary cells of NPML zones, the absorbing boundary condition is considered at the outer boundary of the NPML zones. At these absorbing boundaries, $f(\boldsymbol{U}_{\text{out}})$ in Eq. (3.47) is eliminated. Thus, the numerical flux at outer boundaries is computed as:

$$(\boldsymbol{F}_{\text{in}}^{\text{n}})^{*} = \boldsymbol{F}_{\text{in}}^{\text{n}} - \boldsymbol{A}_{\text{in}}^{-} \cdot \boldsymbol{U}_{\text{in}}$$

$$= (\boldsymbol{A}_{\text{in}}^{+} + \boldsymbol{A}_{\text{in}}^{-}) \cdot \boldsymbol{U}_{\text{in}} - \boldsymbol{A}_{\text{in}}^{-} \cdot \boldsymbol{U}_{\text{in}}$$

$$= \boldsymbol{A}_{\text{in}}^{+} \cdot \boldsymbol{U}_{\text{in}}, \qquad (3.48)$$

where $A_{\rm in}^+$ is the normal flux Jacobian based on the outgoing characteristics.

As to non-boundary cells, if both neighboring cells have the same material, the contact surface in Fig. 3.2b disappears ($U_{\text{in}}^* = U_{\text{out}}^*$), which simplifies Eq. (3.47) to:

$$(\boldsymbol{F}_{\text{in}}^{\text{n}})^* = \boldsymbol{F}_{\text{in}}^{\text{n}} + \boldsymbol{A}_{\text{in}}^{-} \cdot (\boldsymbol{U}_{\text{out}} - \boldsymbol{U}_{\text{in}}). \tag{3.49}$$

In order to find the function f in Eq. (3.47) for neighboring cells containing different materials, a number of physical conditions must be met at the contact surface shown in Fig. 3.2b, which are elaborated below.

3.4.1 Continuity and Slip/No-Slip Conditions

Firstly, to impose the continuity condition, both cells must have the same normal velocity at the contact surface. Besides, if either of the cell 'in' or 'out' contains a fluid material, there is a slip condition at the contact surface. In such situation, the continuity relation with the slip condition leads to:

$$\vec{v}_{\text{in}}^* = \vec{v}_{\text{out}}^{\text{n}} + \vec{v}_{\text{in}}^{\text{t}}$$

$$= [(\vec{v}_{\text{out}} \cdot \vec{n}_{\text{in}}) \, \vec{n}_{\text{in}}] + [\vec{v}_{\text{in}} - (\vec{v}_{\text{in}} \cdot \vec{n}_{\text{in}}) \, \vec{n}_{\text{in}}]$$

$$= (v_z)_{\text{in}}^* \, \vec{e}_z + (v_r)_{\text{in}}^* \, \vec{e}_r \,, \tag{3.50}$$

where the superscripts n and t refer to the normal and tangential components with respect to $\vec{n}_{\rm in}$.

If both cells contain solid materials, the tangential velocities must be also the same to ensure the no-slip condition at the contact surface. For this case, Eq. (3.50) is changed to:

$$\vec{v}_{\text{in}}^* = \vec{v}_{\text{out}}^{\text{n}} + \vec{v}_{\text{out}}^{\text{t}} = \vec{v}_{\text{out}}$$

$$= (v_z)_{\text{in}}^* \vec{e}_z + (v_r)_{\text{in}}^* \vec{e}_r . \tag{3.51}$$

Depending on the cell materials, the velocity components of U_{in}^* (i.e., $(v_z)_{\text{in}}^*$ and $(v_r)_{\text{in}}^*$) can be then obtained from Eq. (3.50) or Eq. (3.51).

3.4.2 Force Balance Condition

Secondly, there should be a force balance at the contact surface, from which one obtains:

$$\sigma_{\text{in}}^* \cdot (-\vec{n}_{\text{in}}) + \sigma_{\text{out}} \cdot (-\vec{n}_{\text{out}}) = 0 \quad \text{or}$$

$$\sigma_{\text{in}}^* \cdot (-\vec{n}_{\text{in}}) + \sigma_{\text{out}} \cdot \vec{n}_{\text{in}} = 0.$$
 (3.52)

3.4. NUMERICAL FLUX 63

It is simpler to evaluate the stress tensor, σ , in the *n*-*t* coordinate system, with its unit vector \vec{e}_n being along \vec{n}_{in} (see Fig. 3.2a), as follows:

$$\boldsymbol{\tau} = \begin{bmatrix} \sigma_{nn} & \sigma_{nt} & 0\\ \sigma_{nt} & \sigma_{tt} & 0\\ 0 & 0 & \sigma_{\theta\theta} \end{bmatrix} = \boldsymbol{Q}^{\mathrm{T}} \cdot \boldsymbol{\sigma} \cdot \boldsymbol{Q}, \qquad (3.53)$$

where τ is the transformed stress tensor, and Q is the transformation matrix from the z-r to the n-t coordinate system, which is:

$$\mathbf{Q} = \begin{bmatrix} \vec{e}_n \cdot \vec{e}_z & -\vec{e}_n \cdot \vec{e}_r & 0\\ \vec{e}_n \cdot \vec{e}_r & \vec{e}_n \cdot \vec{e}_z & 0\\ 0 & 0 & 1 \end{bmatrix} . \tag{3.54}$$

In the new coordinate system, Eq. (3.52) is simplified for the following possible cases:

3.4.2.1 Fluid-Solid Interface

When the cell 'in' contains a fluid and the cell 'out' has a solid material, Eq. (3.52) would be:

$$\begin{bmatrix} -p' & 0 & 0 \\ 0 & -p' & 0 \\ 0 & 0 & -p' \end{bmatrix}_{\text{in}}^* \cdot \begin{bmatrix} -1 \\ 0 \\ 0 \end{bmatrix} + \begin{bmatrix} \sigma_{nn} & \sigma_{nt} & 0 \\ \sigma_{nt} & \sigma_{tt} & 0 \\ 0 & 0 & \sigma_{\theta\theta} \end{bmatrix}_{\text{out}} \cdot \begin{bmatrix} 1 \\ 0 \\ 0 \end{bmatrix} = 0,$$
 (3.55)

leading to:

$$(p')_{\text{in}}^* = -(\sigma_{nn})_{\text{out}}$$

= $-(\sigma_{zz} n_z^2 + 2 \sigma_{zr} n_z n_r + \sigma_{rr} n_r^2)_{\text{out}}.$ (3.56)

Therefore, the first component of the fluid flow variable set, ρ' , in the 'in*' region can be obtained using Eq. (3.56) and the respective equation of state. The other two components of U_{in}^* (velocity components) are already obtained via Eq. (3.50).

3.4.2.2 Solid-Fluid Interface

For the reversed situation in which the 'in' and 'out' cells contain solid and fluid materials, respectively, similar relation to Eq. (3.50) is used to find the velocity components in the 'in*' region. Employing Eqs. (3.52) and (3.53), one obtains:

$$\begin{bmatrix} \sigma_{nn} & \sigma_{nt} & 0 \\ \sigma_{nt} & \sigma_{tt} & 0 \\ 0 & 0 & \sigma_{\theta\theta} \end{bmatrix}_{in}^{*} \cdot \begin{bmatrix} -1 \\ 0 \\ 0 \end{bmatrix} + \begin{bmatrix} -p' & 0 & 0 \\ 0 & -p' & 0 \\ 0 & 0 & -p' \end{bmatrix}_{out} \cdot \begin{bmatrix} 1 \\ 0 \\ 0 \end{bmatrix} = 0.$$
 (3.57)

Hence,

$$(\sigma_{nn})_{in}^* = -(p')_{out},$$
 (3.58a)

$$(\sigma_{nt})_{in}^* = 0.$$
 (3.58b)

As a result, the stress tensors $\boldsymbol{\tau}$ and $\boldsymbol{\sigma}$ in the 'in*' region are calculated as:

$$\boldsymbol{\tau}_{\text{in}}^* = \begin{bmatrix} -(p')_{\text{out}} & 0 & 0\\ 0 & (\sigma_{tt})_{\text{in}} & 0\\ 0 & 0 & (\sigma_{\theta\theta})_{\text{in}} \end{bmatrix},$$
(3.59a)

$$\boldsymbol{\sigma}_{\text{in}}^* = \boldsymbol{Q} \cdot \boldsymbol{\tau}_{\text{in}}^* \cdot \boldsymbol{Q}^{\text{T}}. \tag{3.59b}$$

In Eq. (3.59a), two stress tensor components from the zone 'in' are used since the neighboring fluid cell does not explicitly impose any physical condition on them.

3.4.2.3 Fluid-Fluid Interface

For the cases in which the cells contain different fluids, the force balance provided by Eq. (3.52) is simplified to:

$$\begin{bmatrix} -p' & 0 & 0 \\ 0 & -p' & 0 \\ 0 & 0 & -p' \end{bmatrix}_{\text{in}}^* \cdot \begin{bmatrix} -1 \\ 0 \\ 0 \end{bmatrix} + \begin{bmatrix} -p' & 0 & 0 \\ 0 & -p' & 0 \\ 0 & 0 & -p' \end{bmatrix}_{\text{out}} \cdot \begin{bmatrix} 1 \\ 0 \\ 0 \end{bmatrix} = 0,$$
 (3.60)

3.5. FLUX JACOBIAN 65

which results in:

$$(p')_{\rm in}^* = (p')_{\rm out}^*$$
 (3.61)

The velocity components of the 'in*' region are also obtained from Eq. (3.50).

3.4.2.4 Solid-Solid Interface

As previously mentioned, when two neighboring cells contain two different solid materials, the continuity relation along with the no-slip condition provided by Eq. (3.51) is employed to find the velocity components in the 'in*' zone. Regarding the force balance, Eq. (3.52) leads to:

$$\begin{bmatrix} \sigma_{nn} & \sigma_{nt} & 0 \\ \sigma_{nt} & \sigma_{tt} & 0 \\ 0 & 0 & \sigma_{\theta\theta} \end{bmatrix}_{\text{in}}^* \cdot \begin{bmatrix} -1 \\ 0 \\ 0 \end{bmatrix} + \begin{bmatrix} \sigma_{nn} & \sigma_{nt} & 0 \\ \sigma_{nt} & \sigma_{tt} & 0 \\ 0 & 0 & \sigma_{\theta\theta} \end{bmatrix}_{\text{out}} \cdot \begin{bmatrix} 1 \\ 0 \\ 0 \end{bmatrix} = 0.$$
 (3.62)

Consequently,

$$(\sigma_{nn})_{in}^* = (\sigma_{nn})_{out} , \qquad (3.63a)$$

$$(\sigma_{nt})_{\text{in}}^* = (\sigma_{nt})_{\text{out}} . \tag{3.63b}$$

Thus, in the 'in*' zone, the stress tensors τ and σ are as follows:

$$\boldsymbol{\tau}_{\text{in}}^* = \begin{bmatrix} (\sigma_{nn})_{\text{out}} & (\sigma_{nt})_{\text{out}} & 0\\ (\sigma_{nt})_{\text{out}} & (\sigma_{tt})_{\text{in}} & 0\\ 0 & 0 & (\sigma_{\theta\theta})_{\text{in}} \end{bmatrix}, \tag{3.64a}$$

$$\boldsymbol{\sigma}_{\text{in}}^* = \boldsymbol{Q} \cdot \boldsymbol{\tau}_{\text{in}}^* \cdot \boldsymbol{Q}^{\text{T}}. \tag{3.64b}$$

3.5 Flux Jacobian

In this section, the relations for the normal flux Jacobian based on the incoming $(A_{\rm in}^-)$ or outgoing $(A_{\rm in}^+)$ characteristics are provided for different zones including linear and weakly

non-linear fluid and linear solid media.

3.5.1 Weakly Non-linear Fluid Flow

In order to find the normal flux Jacobian in the weakly non-linear regime, the Roe method is adapted. By considering the non-linear flux in Eq. (2.30c), the normal flux for a unit normal vector \vec{n} (n_z , n_r) can be written as:

$$\boldsymbol{F}_{NL}^{n} = \begin{bmatrix} (\rho_{0} + \rho') (v_{z}n_{z} + v_{r}n_{r}) \\ \frac{1}{2} (v_{z}^{2} + v_{r}^{2}) + c_{0}^{2} \left(\frac{\rho'}{\rho_{0}}\right) + c_{0}^{2} \frac{\gamma - 2}{2} \left(\frac{\rho'}{\rho_{0}}\right)^{2} \right) n_{z} \\ \left(\frac{1}{2} (v_{z}^{2} + v_{r}^{2}) + c_{0}^{2} \left(\frac{\rho'}{\rho_{0}}\right) + c_{0}^{2} \frac{\gamma - 2}{2} \left(\frac{\rho'}{\rho_{0}}\right)^{2} \right) n_{r} \end{bmatrix}$$
(3.65)

The Jacobian of the non-linear normal flux is linearized to satisfy the relation $\Delta \mathbf{F}^{n} = \tilde{\mathbf{A}} \cdot \Delta \mathbf{U}$, resulting in the following linear flux Jacobian $\tilde{\mathbf{A}}$:

$$\tilde{\mathbf{A}} = \begin{bmatrix} n_z \, \bar{v}_z + n_r \, \bar{v}_r & \left(\rho_0 + \bar{\rho'}\right) n_z & \left(\rho_0 + \bar{\rho'}\right) n_r \\ \frac{c_0^2}{\rho_0} \, n_z \left(1 + (\gamma - 2) \, \frac{\bar{\rho'}}{\rho_0}\right) & n_z \, \bar{v}_z & n_z \, \bar{v}_r \\ \frac{c_0^2}{\rho_0} \, n_r \left(1 + (\gamma - 2) \, \frac{\bar{\rho'}}{\rho_0}\right) & n_r \, \bar{v}_z & n_r \, \bar{v}_r \end{bmatrix}, \tag{3.66}$$

where $\bar{\Box} = \frac{\Box_{\text{in}} + \Box_{\text{out}}}{2}$. Then, the matrix \tilde{A} is diagonalized using the left and right eigenvectors as follows:

$$\tilde{A} = R \cdot \Lambda \cdot L, \quad L = R^{-1},$$
 (3.67a)

3.5. FLUX JACOBIAN 67

$$\mathbf{R} = \begin{bmatrix} \frac{-\left(\rho_{0} + \bar{\rho}'\right)}{c^{*}} & \frac{\left(\rho_{0} + \bar{\rho}'\right)\left(n_{r}\,\bar{v}_{z} - n_{z}\,\bar{v}_{r}\right)}{c^{*2}} & \frac{\rho_{0} + \bar{\rho}'}{c^{*}} \\ n_{z} & \frac{\bar{v}_{r}\left(\bar{v}_{z}\,n_{z} + \bar{v}_{r}\,n_{r}\right)}{c^{*2}} - n_{r} & n_{z} \\ n_{r} & n_{z} - \frac{\bar{v}_{z}\left(\bar{v}_{z}\,n_{z} + \bar{v}_{r}\,n_{r}\right)}{c^{*2}} & n_{r} \end{bmatrix},$$
(3.67b)

$$\mathbf{\Lambda} = \begin{bmatrix} (\overline{v}_z \, n_z + \overline{v}_r \, n_r) - c^* & 0 & 0 \\ 0 & 0 & 0 \\ 0 & 0 & (\overline{v}_z \, n_z + \overline{v}_r \, n_r) + c^* \end{bmatrix}, \tag{3.67c}$$

$$c^* = c_0 \sqrt{1 + (\gamma - 1) \left(\frac{\bar{\rho}'}{\rho_0}\right) + (\gamma - 2) \left(\frac{\bar{\rho}'}{\rho_0}\right)^2}.$$
 (3.67d)

The above relations are then used to evaluate A_{in}^- and A_{in}^+ in Eqs. (3.47) and (3.48), respectively.

3.5.2 Linear Fluid Flow and Linear Solid

For linear fluid and solid zones, the normal flux Jacobian is already linear $(\mathbf{A} = \tilde{\mathbf{A}})$, and the same diagonalization approach given by Eqs. (3.67) is applied. The respective eigenvalue and eigenvector matrices for a linear fluid flow are:

$$\mathbf{R} = \begin{bmatrix} -\frac{\rho_0}{c_0} & 0 & \frac{\rho_0}{c_0} \\ n_z & -n_r & n_z \\ n_r & n_z & n_r \end{bmatrix}, \tag{3.68a}$$

$$\mathbf{\Lambda} = \begin{bmatrix} -c_0 & 0 & 0 \\ 0 & 0 & 0 \\ 0 & 0 & c_0 \end{bmatrix}, \tag{3.68b}$$

and for a linear solid are:

$$\mathbf{R} = \begin{bmatrix} n_z c_1 & -n_r c_2 & 0 & 0 & n_r c_2 & -n_z c_1 \\ n_r c_1 & n_z c_2 & 0 & 0 & -n_z c_2 & -n_r c_1 \\ \lambda + 2 \mu n_z^2 & -2 \mu n_z n_r & n_r^2 & 0 & -2 \mu n_z n_r & \lambda + 2 \mu n_z^2 \\ 2 \mu n_z n_r & \mu (n_z^2 - n_r^2) & -n_z n_r & 0 & \mu (n_z^2 - n_r^2) & 2 \mu n_z n_r \\ \lambda + 2 \mu n_r^2 & 2 \mu n_z n_r & n_z^2 & 0 & 2 \mu n_z n_r & \lambda + 2 \mu n_r^2 \\ \lambda & 0 & 0 & 1 & 0 & \lambda \end{bmatrix},$$
(3.69a)

$$\boldsymbol{\Lambda} = \begin{bmatrix}
-c_1 & 0 & 0 & 0 & 0 & 0 \\
0 & -c_2 & 0 & 0 & 0 & 0 \\
0 & 0 & 0 & 0 & 0 & 0 \\
0 & 0 & 0 & 0 & 0 & 0 \\
0 & 0 & 0 & 0 & c_2 & 0 \\
0 & 0 & 0 & 0 & 0 & c_1
\end{bmatrix},$$
(3.69b)

where $\lambda = \rho_0 (c_1^2 - 2 c_2^2)$ and $\mu = \rho_0 c_2^2$ are the time-varying Lamé coefficients.

3.6 C^{∞} -Diffeomorphism Transformation

During strong stimulations bubbles may show violent behaviors, such as steep collapse phases, which cause the stability issue during the numerical assessments. To overcome this issue, very small time steps are usually required, making the numerical scheme highly inefficient. A better solution to this problem is to use a non-linear transformation to obtain smoother variations of the bubble radius in time. In this study, the C^{∞} -diffeomorphism transformation \mathcal{F} suggested by Parlitz et al. [14] is used to decrease the stiffness of the non-linear Ordinary Differential Equation (ODE) of the KM model provided by Eqs. (2.47). In this transformation, both \mathcal{F} and its inverse \mathcal{F}^{-1} are infinite-time differentiable.

Starting with Eqs. (2.47), one obtains the following system of first-order ODEs:

$$\dot{R} = S \,, \tag{3.70a}$$

$$\dot{S} = \frac{\left(1 + \frac{S}{c}\right)\frac{P}{\rho} + \frac{R}{\rho c}\frac{\mathrm{d}P}{\mathrm{d}t} - \frac{3}{2}S^2\left(1 - \frac{S}{3c}\right)}{R\left(1 - \frac{S}{c}\right)}.$$
(3.70b)

As suggested by Parlitz et al. [14], \mathcal{F} transforms (R, S) into (x_1, x_2) as follows:

$$\mathcal{F}: (R,S) \to (x_1, x_2), \tag{3.71a}$$

$$x_1 = a_1 \cdot \exp\left(a_2 \frac{R}{R_0}\right),\tag{3.71b}$$

$$x_2 = a_3 S \cdot \exp\left(a_2 \frac{R}{R_0}\right),\tag{3.71c}$$

where a_1 , a_2 , and a_3 are the parameters of the transformation determining smoothness of the transformed variables. In this study, $a_1 = 1$, $a_2 = 2$, and $a_3 = 0.001$ are considered, as suggested by Parlitz et al. [14]. In addition, a scaled time variable t' is employed for the transformed variables as follows:

$$t' = \frac{a_1 \, a_2}{a_3 \, R_0} \cdot t \tag{3.72}$$

The transformed system of ODE then becomes:

$$\frac{\mathrm{d}x_1}{\mathrm{d}t'} = x_2 \,, \tag{3.73a}$$

$$\frac{\mathrm{d}x_2}{\mathrm{d}t'} = y \cdot x_2 + \frac{N_1}{N_2} \,, \tag{3.73b}$$

where

$$N_1 = x_1 \cdot \left[(g_3 + g_4 \cdot y) \cdot y^2 + (g_5 - g_6 \cdot y) \cdot z^{-3k} - (g_7 + g_8 \cdot y) / z - \right]$$
(3.74a)

$$-(1+g_9\cdot y)\cdot (g_{10}+g_2)-z\cdot g_{11}], \qquad (3.74b)$$

$$N_2 = (1 - g_9 \cdot y) \cdot z + g_{12}, \qquad (3.74c)$$

$$y = \frac{x_2}{x_1}, \quad z = \frac{1}{a_2} \ln\left(\frac{x_1}{a_1}\right), \quad \delta = \frac{a_1}{a_3},$$
 (3.74d)

$$g_2 = \frac{p'_{\text{ext}}(t')}{\rho \, a_2 \, \delta^2}, \quad g_3 = \frac{-3}{2 \, a_2}, \quad g_4 = \frac{\delta}{2 \, a_2 \, c}, \quad g_5 = \frac{1}{\rho \, a_2 \, \delta^2} \left[p_{\text{st}} - p_{\text{v}} + \frac{2 \, \sigma}{R_0} \right],$$
 (3.74e)

$$g_6 = g_5 \frac{\delta}{c} (3 k - 1), \quad g_7 = \frac{2 \sigma}{a_2 \rho R_0 \delta^2}, \quad g_8 = \frac{4 \mu}{\delta a_2 \rho R_0}, \quad g_9 = \frac{\delta}{c},$$
 (3.74f)

$$g_{10} = \frac{p_{\text{stat}} - p_{\text{v}}}{\rho \, a_2 \, \delta^2}, \quad g_{11} = \frac{\mathrm{d}p'_{\text{ext}}}{\mathrm{d}t'} \cdot \frac{R_0}{a_2 \, \rho \, c \, \delta^2}, \quad g_{12} = \frac{4 \, \mu}{\rho \, c \, R_0}.$$
 (3.74g)

The transformed Eqs. (3.73) are then solved with the LSODA scheme [112] in each flow time step when all the flow variables are updated. The LSODA scheme automatically switches between the Adams scheme (explicit) for non-stiff and the BDF scheme (implicit) for stiff phases of the bubble responses.

3.7 Temporal Scheme

Beside the main temporal derivative $(\frac{\mathrm{d}U_j}{\mathrm{d}t})$ in Eq. (3.31), the source term Q_i implicitly has other temporal derivatives as it originates from Eqs. (2.47). However, since the modified KM model is a stiff non-linear ODE, it requires significantly smaller time steps compared to the ones required for the flow evolution in bubble-less domains to ensure numerical stability. To handle this disparity, computation of the flow variables is de-coupled from the bubble-related terms at each time step. The physical splitting procedure includes two steps. First, the third order SSP-RK scheme [105] is used to advance the acoustical variables U_j from the time step n, at which all the variables are known, to the next time step n + 1 while considering the values of the bubble-related source term Q_i frozen at the time step n. The details of the SSP-RK scheme are provided in Section 3.7.1. Second, upon finding the acoustic variables at the time step n + 1, the source term Q_i is to be updated using the newly found variables.

As the first step of the Q_i update, the external stimulating pressure p'_{ext} should be obtained at the bubble locations since it is needed to integrate Eqs. (2.47), which provide the bubble radius R and hence the void fraction β for the evaluation of Q_i . As explained in Section 2.4.5, for bubble-layer and spherical bubble clouds p'_{ext} is simply equal to p', while for the case of a single bubble or a bubble-plane cloud Eq. (2.49) should be used, which involves the integration over a surrounding volume V. Following the considerations regarding the selection of V provided in Section 2.4.5, for bubble-plane clouds the smallest possible volume

3.7. TEMPORAL SCHEME 71

V is chosen as the set of numerical grid elements containing the cloud. For single bubbles, on the other hand, the region in the immediate vicinity of the bubble is to be excluded since the accumulation of signals in axisymmetric domains yields very high pressure values near the bubble location. Therefore, for single bubbles, the volume between two concentric spheres centered at the single bubble location is considered as the integration volume V in Eq. (2.49). As previously discussed, there is a trade-off for choosing appropriate sizes for these two concentric spheres: Eq. (2.49) is not accurate enough for very small V near the bubble location, where the signal amplification and/or non-linear effects are dominant; on the other hand, some modes of the $p'_{\rm ext}$ field are filtered out in a large integration domain. The specific values of the sphere radii are provided in Chapter 4.

Once the external stimulating pressure $p'_{\rm ext}$ is obtained, the term Q_i needs to be computed at the time step n+1 by solving Eqs. (2.47), which are highly stiff. To deal with the numerical difficulties originating from the stiffness of Eqs. (2.47), as suggested by Parlitz et al. [14], a C^{∞} -diffeomorphism transformation is implemented to map this ODE onto a new domain where the equation becomes less stiff. The details of this transformation are provided in Section 3.6. This transformed equation is then solved using the Livermore Solver for Ordinary Differential equations with Automatic switching (LSODA) scheme [112] to obtain Q_i at the time step n+1. The LSODA scheme automatically switches between the Adams scheme (explicit) for non-stiff and the Backward Differentiation Formula (BDF) scheme (implicit) for stiff phases of bubble responses. For bubble-plane clouds and single bubbles, after updating Q_i and thus having all the flow and bubble variables updated, the scattered pressure signals from the bubbles (\mathcal{P}) are computed from Eq. (2.53) or Eq. (2.62), respectively, to be used at the next time step. In particular, Eq. (2.61) is discretized via the following scheme:

$$g^{n+1} = \frac{g^n R_0 + \rho_0 c_0 R_0^2 \left(\ddot{R}\right)^{n+1} \Delta t}{R_0 + c_0 \Delta t},$$
(3.75)

where the superscripts n+1 and n refer to the values at the time moments $t+\Delta t$ and t, respectively, and Δt is the time step. The scheme is implicit but the values of \ddot{R} for the time level n+1 are already known. The entire acoustic-flowfield/bubble-dynamics splitting procedure described above is repeated at each numerical time step.

3.7.1 Strong Stability-Preserving Runge-Kutta Scheme

After multiplying Eq. (3.31) by the inverse of the mass matrix, M^{-1} , the following semi-discrete relation for the acoustic variables set U is obtained at each solution node (i) of a grid element:

$$\frac{\mathrm{d}\boldsymbol{U}_{i}}{\mathrm{d}t} = L\left(\boldsymbol{U}_{i}, t\right),\tag{3.76}$$

where the operator L includes spatially-discretized terms of the governing equations. As previously mentioned, explicit schemes represent a reasonable option for simulating the WPC processes. In this study, the SSP-RK scheme is used, which maintains the TVD property [105, 106].

The optimal three-stage third-order SSP-RK scheme to update the variable U_i in time can be written as:

$$\boldsymbol{V}_{i}^{(1)} = \boldsymbol{U}_{i}^{n} + \Delta t \cdot L\left(\boldsymbol{U}_{i}^{n}, t^{n}\right), \tag{3.77a}$$

$$\boldsymbol{V}_{i}^{(2)} = \frac{1}{4} \left[3 \boldsymbol{U}_{i}^{n} + \boldsymbol{V}_{i}^{(1)} + \Delta t \cdot L \left(\boldsymbol{V}_{i}^{(1)}, t^{n} + \Delta t \right) \right], \tag{3.77b}$$

$$U_i^{n+1} = \frac{1}{3} \left[U_i^n + 2 V_i^{(2)} + 2 \Delta t \cdot L \left(V_i^{(2)}, t^n + \frac{1}{2} \Delta t \right) \right],$$
 (3.77c)

where \boldsymbol{U}_i^n and \boldsymbol{U}_i^{n+1} are the variable set values at t^n and $t^n + \Delta t$, respectively; and $\boldsymbol{V}_i^{(1)}$ and $\boldsymbol{V}_i^{(2)}$ are auxiliary variable sets. It should be noted that at each RK stage, the initial value, \boldsymbol{U}_i^n , and at most one auxiliary variable are required. This property makes the scheme efficient in terms of memory usage.

Regarding the stability restriction on the time step, the following relation proposed by Hesthaven and Warburton [103] is used:

$$\Delta t \le A \cdot \left(\frac{2}{3} \min\left(\Delta \ell\right)\right) \cdot \min\left(\frac{r_D}{\max\left(|\lambda_F|\right)}\right),$$
 (3.78)

where A is a constant of order 1; $\Delta \ell$ is the distance between nodes in the reference element; r_D is the radius of the inscribed circle for triangular elements; and λ_F is the flux Jacobian

3.8. CONCLUSION 73

eigenvalue. Equation (3.78) is evaluated for all grid elements; then the minimum computed Δt among elements is used for the numerical simulation.

3.8 Conclusion

In this chapter, a general high-order numerical model was proposed to accurately model the WPC process and its interaction with different bubble clouds. This numerical model is briefly outlined in this section.

First, multi-block computational domains consisting, in general, of a conjugator (solid zone) as well as surrounding media and bubbly zones, which are fluid media, are discretized with unstructured triangular elements by the *Gmsh* software [113]. Unstructured grids with triangular elements make grid generation easier for complex geometries which may be encountered in WPC applications. In the current numerical formulation, it is possible to use geometrically non-linear elements (i.e., with curved edges) in order to obtain higher accuracy by better representing complex geometries. Since bubbles might behave violently, particularly upon strong excitation, the fluid zones containing bubbles usually need finer numerical mesh to provide better spatial resolution.

In order to minimize false reflections of signals from outer boundaries, the computational domain is wrapped in an NPML zone, where the signals are effectively damped. For this goal, a complex coordinate transformation is used, which results in an extra flux term in the governing equations, as explained in Section 3.2.

Since the WPC applications deal with high-frequency waves (with short wavelengths), a high-order numerical scheme is then required to discretize the governing equations in order to appropriately handle propagation and interaction of waves. As for the spatial scheme, a modified version of the NDG method was proposed in this study [74], which was elaborated in Section 3.3. This spatial scheme better handles non-linear regimes via de-coupling of the solution and flux points [74].

This scheme is compact in the sense that only the information from the immediate neighboring grid cells is used to evaluate the common flux crossing the cell boundaries. This feature allows for easy parallelization, which is very important for efficient simulations of 2D/axisymmetric WPC problems. The necessary numerical flux at different material

interfaces and the flux Jacobian for different regimes were obtained in Sections 3.4 and 3.5, respectively.

Then, the effects of bubble dynamics in bubbly zones were incorporated into the NDG scheme (see Sections 3.3.1 and 3.3.2). For this goal, the modified KM model was applied to find variations of bubble radii in time. This model includes a stiff non-linear ODE, causing some numerical difficulties, particularly during violent collapse phases of the bubbles. To handle this issue, as suggested by Parlitz et al. [14], a C^{∞} -diffeomorphism transformation was implemented to solve this ODE in a domain where the mapped variables are less stiff, as elaborated in Section 3.6.

Since for the essentially unsteady problems under study the time step is limited by accuracy considerations, an explicit temporal scheme is a reasonable option. In this study, the third order SSP-RK method [105, 106] was used. As the bubble-related terms requires smaller time steps compared to the bubble-less zones, marching in time is de-coupled for the flow evolution and the bubble excitation. The details of this temporal scheme were provided in Section 3.7.

The numerical model elaborated in this chapter was implemented via an MPI/OpenMP modern FORTRAN code to investigate the WPC process and to assess its interactions with different bubble clouds.

CHAPTER 4

Results and Discussion

In this chapter, first, different verification problems are investigated in Section 4.1 to evaluate various aspects of the proposed model. In Section 4.2, the developed model is applied to the numerical simulation of Wave Phase Conjugation (WPC) processes with realistic settings including both the conjugator and the surrounding fluid media. Then, interactions of bubbles and bubble clouds with the WPC phenomenon are numerically investigated in Section 4.3 with the emphasis on the possibility to extract bubble-size-related information from the recorded signals. Eventually, conclusion follow in Section 4.4. All cases, even those based on one-dimensional problems, are performed with the 2D/axisymmetric code and the computational domains are discretized with triangular elements. Besides, if not specified otherwise, schemes of the fourth order of accuracy in space are employed in the simulations.

The linear regime for fluid zones is implied unless the non-linear regime is mentioned explicitly. In the cases including bubbles, the relevant properties are as follows (unless it is indicated otherwise): the undisturbed ambient pressure $p_0 = 100$ kPa, the undisturbed fluid density $\rho_0 = 998$ kg/m³, the local fluid viscosity $\mu = 0.001$ Pa·s, the speed of sound in the undisturbed fluid $c_0 = 1500$ m/s, the surface tension $\sigma = 0.0725$ N/m, the vapor pressure $p_v = 2.33$ kPa, and the polytropic exponent of the bubble content k = 4/3, as suggested by Parlitz et al. [14]. For bubble-layer and spherical bubble clouds, the initial distribution of the void fraction, β_0 , is assumed to be uniform. For visualization purposes, the *ParaView* software [114] is used in this study.

4.1 Verification of the Proposed Model

A comprehensive set of verification problems is used in this section to test thoroughly various aspects of the proposed numerical model by comparison with available analytical solutions or experimental data.

4.1.1 Grid Convergence and Order of Accuracy

In order to evaluate the grid convergence and the order of accuracy of the implemented numerical scheme, the paraxial advection of sinusoidal scalar disturbances, $U = U\left(z^*, r^*, t^*\right)$, in the linear regime, obeying $\frac{\partial U}{\partial t^*} + \frac{\partial U}{\partial z^*} = 0$ with the periodic boundary conditions, is modeled for different orders of accuracy on a sequence of successively refined meshes. The initial condition (see Fig. 4.1a) and the employed non-dimensional variables in a domain where $0 \le z^* \le 1$ and $0 \le r^* \le 1$ are as follows:

$$U_0 = U(z^*, r^*, 0) = \sin(2\pi z^*) \cdot \sin(2\pi r^*), \tag{4.1a}$$

$$t^* = t \cdot \frac{c_0}{L}, \ z^* = \frac{z}{L}, \ r^* = \frac{r}{L},$$
 (4.1b)

where L is the wavelength. The variations of L_2 error norm with the non-dimensional mesh size are shown in Fig. 4.1b, and the respective values are provided in Table 4.1. As seen in Table 4.1 and Fig. 4.1b, the grid convergence takes place, and the slopes of L_2 error norm are in correspondence with the formal order of accuracy of the scheme, which is p + 1, where p is the polynomial order of the solution basis.

4.1.2 Weakly Non-linear Regime and Modified NDG Scheme

To assess the accuracy of the numerical method for the non-linear regime, the paraxial advection of a Gaussian wave obeying the following equation is investigated:

$$\frac{\partial U}{\partial t} + (c_0 + \beta U) \frac{\partial U}{\partial z} = 0, \qquad (4.2)$$

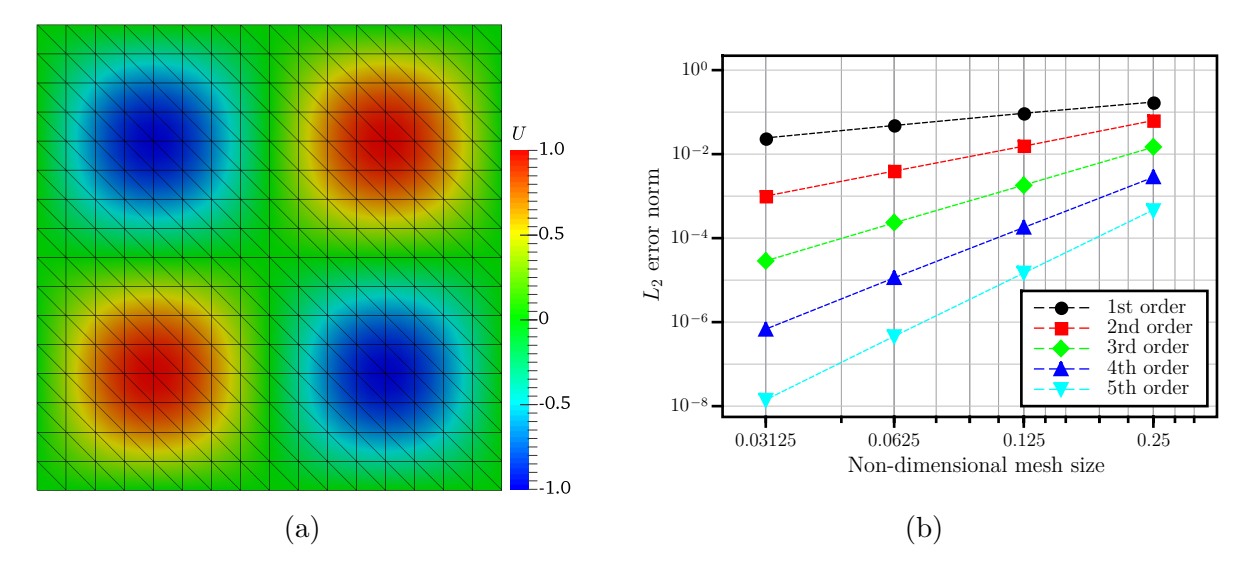


Fig. 4.1. Linear advection of a sinusoidal scalar signal, Eq. (4.1a): (a) the initial condition and the numerical mesh; (b) L_2 error norm versus the non-dimensional mesh size.

where U is a scalar function of z and t; β is the coefficient of non-linearity which is set to 0.5; and $c_0 = 1$ m/s. The initial condition (see Fig. 4.2b) is given by:

$$U(z,0) = U_{\text{max}} \cdot \exp\left(-\frac{(z-a)^2}{b}\right),\tag{4.3}$$

where a=0.5 m, b=0.005 m², and $U_{\rm max}=1$. In this simulation, the grid size and the time step are 0.02 m and 1 ms, respectively. The computational domain, as shown in Fig. 4.2a, is considered to be long enough in the z direction in order to exclude the effects of boundaries. Figure 4.2b shows how this right-running signal is distorted due to converging characteristics in the non-linear regime at t=0.14 s when the shock wave is not formed yet. As demonstrated, there is satisfactory correspondence between the numerical and analytical results (obtained via the method of characteristics) even in the high-gradient region.

To demonstrate that the proposed Nodal Discontinuous Galerkin (NDG) scheme is more capable of controlling the aliasing error as compared to the original NDG method, the initial Gaussian wave distribution provided by Eq. (4.3) is scaled by a factor of 8.25 ($U_{\text{max}} = 8.25$) to enhance non-linear effects leading to the shock formation. The other physical and numerical

Table 4.1. Linear advection of a sinusoidal scalar signal, Eq. (4.1a): L_2 error norm and the evaluated spatial order of accuracy for different polynomial orders of the solution basis, p.

\overline{p}	Mesh size	L_2 error	Order of accuracy	
0	$2.500e{-1}$	$1.6929e{-1}$	0.8836	
	$1.250e{-1}$	$9.1753e{-2}$	0.9223	
	$6.250e{-2}$	$4.7132e{-2}$	0.9746	
	$3.125\mathrm{e}{-2}$	$2.3761e{-2}$	0.9881	
1	$2.500e{-1}$	$6.1526e{-2}$	2.0194	
	$1.250e{-1}$	$1.5176e{-2}$	1.9884	
	$6.250e{-2}$	$3.9076e{-3}$	1.9717	
	$3.125e{-2}$	$9.8642e{-4}$	1.9860	
2	$2.500e{-1}$	$1.4281e{-2}$	2.9827	
	$1.250e{-1}$	$1.8066e{-3}$	2.9768	
	$6.250e{-2}$	$2.3042e{-4}$	2.9945	
	$3.125e{-2}$	$2.8444e{-5}$	3.0181	
3	$2.500e{-1}$	2.7554e - 3	3.9553	
	$1.250e{-1}$	1.7763e - 4	3.9580	
	$6.250e{-2}$	$1.1408e{-5}$	4.0162	
	$3.125e{-2}$	$6.7847e{-7}$	4.0717	
4	$2.500e{-1}$	4.6083e - 4	4.9682	
	$1.250e{-1}$	$1.4722e{-5}$	4.9703	
	$6.250 e{-2}$	$4.6892e{-7}$	5.0087	
	$3.125e{-2}$	1.4204e - 8	5.0450	

settings are the same as those in the previous test case, shown in Fig. 4.2. Figure 4.3a shows that representation of the non-linear flux with the solution basis (the original NDG scheme) leads to a highly-oscillatory solution which eventually blows up during the simulation at a later time moment. This behavior is due to the aliasing error as was previously explained (see also [103]). As also seen in Fig. 4.3a, the modified NDG scheme, which employs an independent basis for the non-linear flux representation (the order of the flux basis is twice that of the solution basis), mitigates the non-physical oscillations noticeably, and keeps the solution stable for the entire duration of the simulation. In other words, better flux representation and stronger associated quadrature rule of the modified NDG scheme controls the aliasing error. It should be noted that, if it is desirable, filters or limiters can be used to eliminate non-physical oscillations entirely near high-gradient zones.

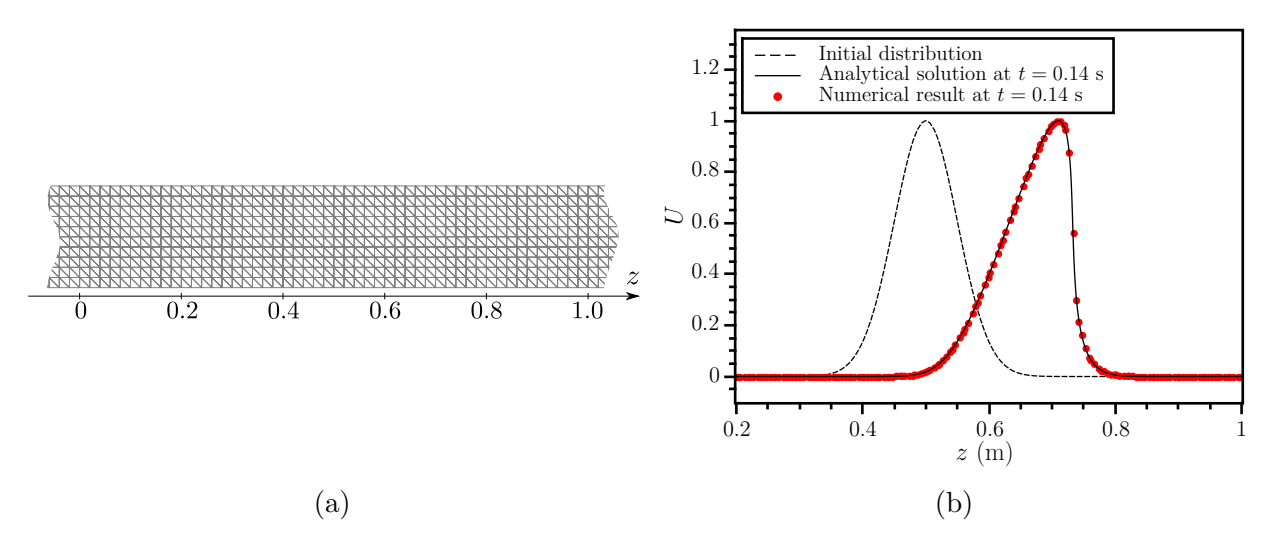


Fig. 4.2. Non-linear advection of the Gaussian wave given by Eq. (4.3) $(U_{\text{max}} = 1)$: (a) the numerical mesh; (b) the initial condition and comparison of the numerical result with the analytical solution at t = 0.14 s.

For the same test problem with $U_{\text{max}} = 8.25$, Fig. 4.3b illustrates how the global energy changes in time for different flow regimes and numerical methods. The global energy is defined as follows [103]:

$$E = \sum_{i} E_{i} = \sum_{i} \int_{V_{i}} U^{2} \, dV_{i} \,, \tag{4.4}$$

where E_i is the energy in each grid element with volume V_i . As seen in Fig. 4.3b, at the beginning of the signal propagation the energy remains fairly constant and is the same for the linear and non-linear regimes, meaning that the distorted signal is adequately resolved. As time goes on, the signal becomes more distorted, and the global energy is more affected by a number of competing factors. On one hand, discontinuities are numerically represented in grid elements with inherently not sufficiently rich solution basis; hence, the energy of higher non-resolved modes would be transferred to the lower ones, leading to an increase in the global energy, which might result in instability. On the other hand, based on the weak shock theory, there is some energy dissipation concentrated at the shock location [82]. Furthermore, high-frequency modes are associated with higher numerical dissipation decreasing the energy.

In this test case, when the modified NDG method is used, the first factor, which increases the energy by adding some aliasing errors, is confined via better representation and integration of the flux terms. Consequently, the two other factors outweigh, which decreases the energy and stabilize the numerical scheme.

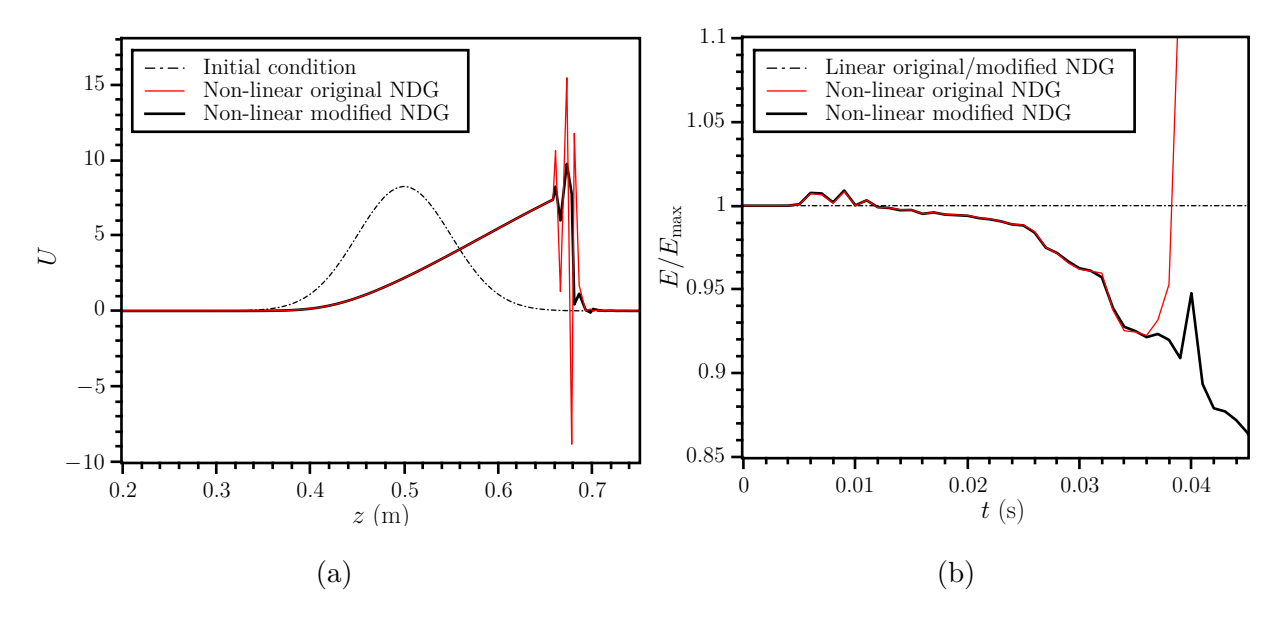


Fig. 4.3. Advection of the Gaussian wave given by Eq. (4.3) ($U_{\text{max}} = 8.25$) in the non-linear regime using the original and modified NDG schemes: (a) the initial condition and the results at t = 0.039 s; (b) the normalized global energy versus time for the linear and non-linear regimes.

To further elaborate the difference between the original and modified NDG methods, non-linear propagation of the following sinusoidal signal with the same physical and numerical settings as those in the previous test case is investigated:

$$U(z,0) = U_{\text{max}} \cdot \sin(2\pi f z + \phi), \qquad (4.5)$$

where U_{max} , f, and ϕ are set to 1.7, 1.0 m⁻¹, and π , respectively. Equation (4.5) is a distorting signal, which forms a shock at $t \approx 0.187$ s. Compared with the Fay-Fubini analytical solution provided by Hamilton et al. [82] and Enflo and Hedberg [115], the L_2 error norm and the order of accuracy of the numerical scheme are provided in Table 4.2 at the time moment

 $t = 0.05 \, s$, when the signal profile is still smooth. The results are also illustrated in Fig. 4.4. As shown in Table 4.2 and Fig. 4.4, the non-linear scheme can satisfactorily retrieve the formal order of accuracy. However, as Hesthaven and Warburton [103] also pointed out, higher error levels and lower orders of accuracy can be generally expected due to presence of non-linear terms, as compared to the linear regime.

Table 4.2. Linear and non-linear advection of a sinusoidal scalar signal, Eq. (4.5): L_2 error norm and the evaluated spatial order of accuracy for different polynomial orders of the solution basis, p, at $t = 0.05 \ s$. In the non-linear regime, the results for the original NDG and the modified NDG schemes are provided.

\overline{p}	Mesh size	Linear		Non-linear (original NDG)		Non-linear (modified NDG)	
		L_2 error	Order of acc.	L_2 error	Order of acc.	L_2 error	Order of acc.
0	$2.500e{-1}$	$1.7009e{-1}$	0.8097	$2.1948e{-1}$	0.9698	$2.1948e{-1}$	0.9698
	$1.250e{-1}$	9.7037e - 2	0.8457	$1.1206e{-1}$	0.9208	$1.1206e{-1}$	0.9208
	$6.250e{-2}$	$5.2660e{-2}$	0.9253	$6.1240e{-2}$	0.9066	$6.1240e{-2}$	0.9066
	$3.125e{-2}$	$2.6905e{-2}$	0.9688	$3.1888e{-2}$	0.9415	$3.1888e{-2}$	0.9415
1	$2.500e{-1}$	$6.5342e{-2}$	1.6097	$6.2776e{-2}$	1.7920	$6.2776e{-2}$	1.7920
	$1.250e{-1}$	$2.1410e{-2}$	1.8085	$1.8128e{-2}$	1.7934	$1.8128e{-2}$	1.7934
	$6.250e{-2}$	$5.3256e{-3}$	2.0024	$5.2243e{-3}$	1.8181	$5.2243e{-3}$	1.8181
	$3.125e{-2}$	$1.3338e{-3}$	1.9974	$1.4579e{-3}$	1.8414	$1.4579e{-3}$	1.8414
2	$2.500e{-1}$	$1.1238e{-2}$	2.6092	$8.2371e{-3}$	2.0556	$8.3133e{-3}$	2.0776
	$1.250e{-1}$	$1.8418e{-3}$	2.9322	$1.9814e{-3}$	2.4417	$1.9694e{-3}$	2.4526
	$6.250e{-2}$	$1.9291e{-4}$	3.1136	2.7907e - 4	2.8823	$2.7743e{-4}$	2.8789
	$3.125e{-2}$	$2.4584e{-5}$	2.9721	$3.6448e{-5}$	2.9367	$3.6399e{-5}$	2.9302
3	$2.500e{-1}$	$1.3060e{-3}$	3.7839	$3.2592e{-3}$	3.8394	$2.8393e{-3}$	3.6322
	$1.250e{-1}$	$9.4818e{-5}$	3.8563	$2.2768e{-4}$	3.8337	$2.2898e{-4}$	3.7460
	$6.250e{-2}$	$6.2260e{-6}$	3.9903	$1.6031e{-5}$	3.8309	$1.5773e{-5}$	3.8456
	$3.125e{-2}$	$3.7540e{-7}$	4.0518	$1.1243e{-6}$	3.8338	$1.1079e{-6}$	3.8315

The results provided in Table 4.2 and Fig. 4.4 are for the time moment t = 0.05 s, when the signal is still smooth, and the aliasing errors are not significant. Hence, there is no noticeable difference between the results obtained by the original and the modified NDG schemes. However, after more advancing in time, the signal (Eq. (4.5)) becomes more distorted, and the aliasing errors increase. Therefore, to show the advantage of the proposed modified NDG scheme, the signal is allowed to advance more in time and form a shock.

Figure 4.5a shows that the energy starts to decline after the shock formation moment $(t \approx 0.187 \text{ s})$. However, after some time, the energy computed by the original NDG method increases, and the simulation eventually blows up. As previously discussed, this behavior is due to the fact that the shock is not resolved well enough with the original NDG method. As demonstrated in Fig. 4.5b, the L_2 error norm significantly increases after the shock formation

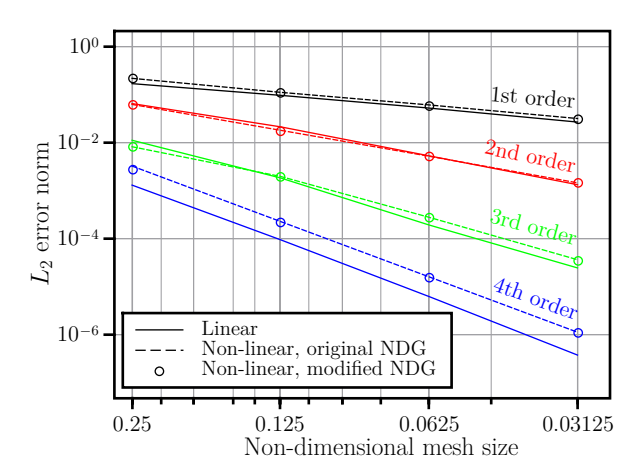


Fig. 4.4. Linear and non-linear advection of a sinusoidal scalar signal, Eq. (4.5): L_2 error norm versus the non-dimensional mesh size at $t = 0.05 \ s$ for the linear, original, and modified NDG schemes.

due to the presence of Gibbs oscillations near the shock. As depicted, not only does the modified NDG method stabilize the numerical scheme, but it also outperforms the original one in terms of leading to a lower error level.

4.1.3 Wave Propagation in Solid Media

In order to assess the performance of the numerical method in solid media, numerical results for longitudinal spherical waves generated by a transducer are compared with the analytical solution provided by Beltzer [116]. The computational domain is a circular sector with $0.2 \mathcal{R}_0 \leq \mathcal{R} \leq \mathcal{R}_0$, where \mathcal{R} is the spherical radial coordinate, and \mathcal{R}_0 is a given external radius, as shown in Fig. 4.6a. The boundary $\mathcal{R} = 0.2 \mathcal{R}_0$ is considered to be a transducer generating the waves. The following non-dimensional variables are used:

$$\vec{v}^* = \frac{\vec{v}}{c_1}, \ \sigma^* = \frac{\sigma}{\rho_0 c_1^2}, \ c_2^* = \frac{c_2}{c_1}, \ c_3^* = \frac{c_3}{c_1}, \ t^* = t \cdot \frac{c_1}{L},$$
 (4.6a)

$$z^* = \frac{z}{L}, \ r^* = \frac{r}{L}, \ \mathcal{R}^* = \frac{\mathcal{R}}{L} = \sqrt{z^{*2} + r^{*2}},$$
 (4.6b)

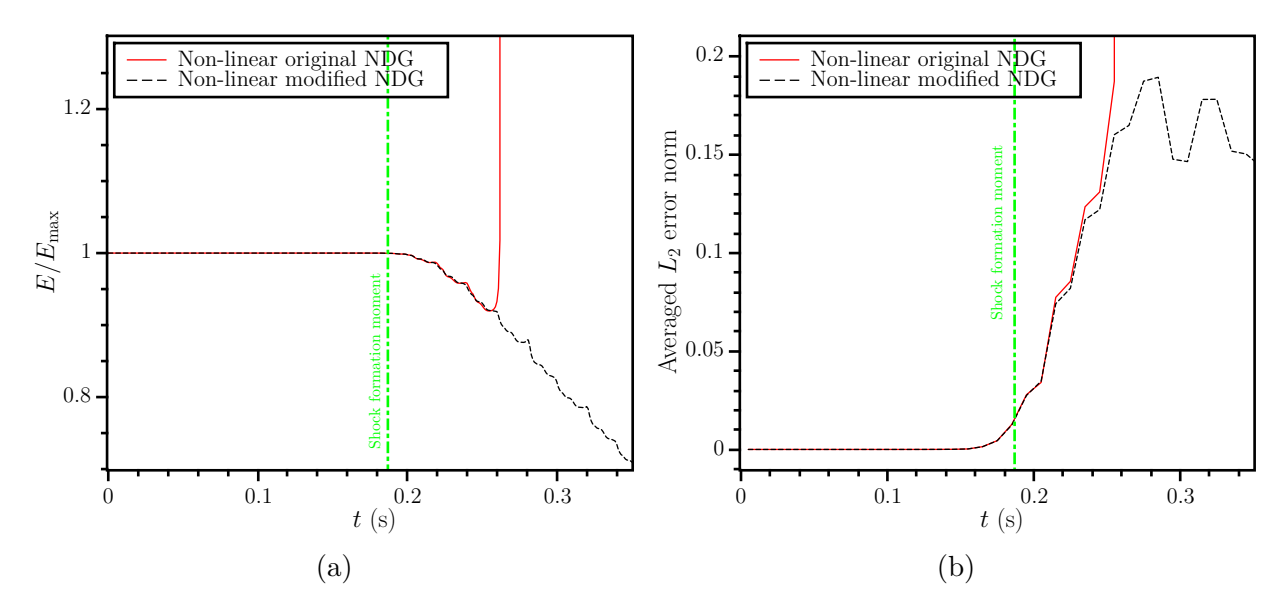


Fig. 4.5. Advection of the sinusoidal wave given by Eq. (4.5) in the non-linear regime using the original and modified NDG schemes: (a) the normalized global energy; (b) the averaged L_2 error norm versus time. The green dash-dotted line indicates the shock formation moment $(t \approx 0.187 \text{ s})$.

where the length scale L is set to \mathcal{R}_0 . Therefore, in the non-dimensional coordinates the computational domain extends from $\mathcal{R}^* = 0.2$ to $\mathcal{R}^* = 1$. In this simulation, c_2^{*2} , c_3^{*2} , the non-dimensional grid size, and the time step are 0.375, 0.25, 0.025, and 10^{-3} , respectively. The transducer generates temporal displacement $d^* = d/\mathcal{R}_0 = 0.001 \cdot \sin{(20\,t^*)}$ at $\mathcal{R}^* = 0.2$, and $\mathcal{R}^* = 1.0$ is set to be an absorbing boundary. The numerical results for the non-dimensional radial velocity $(v_{\mathcal{R}}^*)$, $\sigma_{\mathcal{R}\mathcal{R}}^*$, and $\sigma_{\theta\theta}^*$ are presented in Figs. 4.6b–4.6d, which are barely distinguishable from the analytical solutions. It is also to be noted that in this case of normal interaction of outgoing waves with the external boundary ($\mathcal{R}^* = 1.0$), the simple absorbing boundary condition works very well, without any false reflections.

4.1.4 Wave Propagation in Fluid Media

Propagation of spherical waves within a fluid medium is simulated in this subsection. Such disturbances are generated, for instance, when a single bubble is stimulated and generates signals. For this goal, the same circular sector shown in Fig. 4.6a is used. The employed

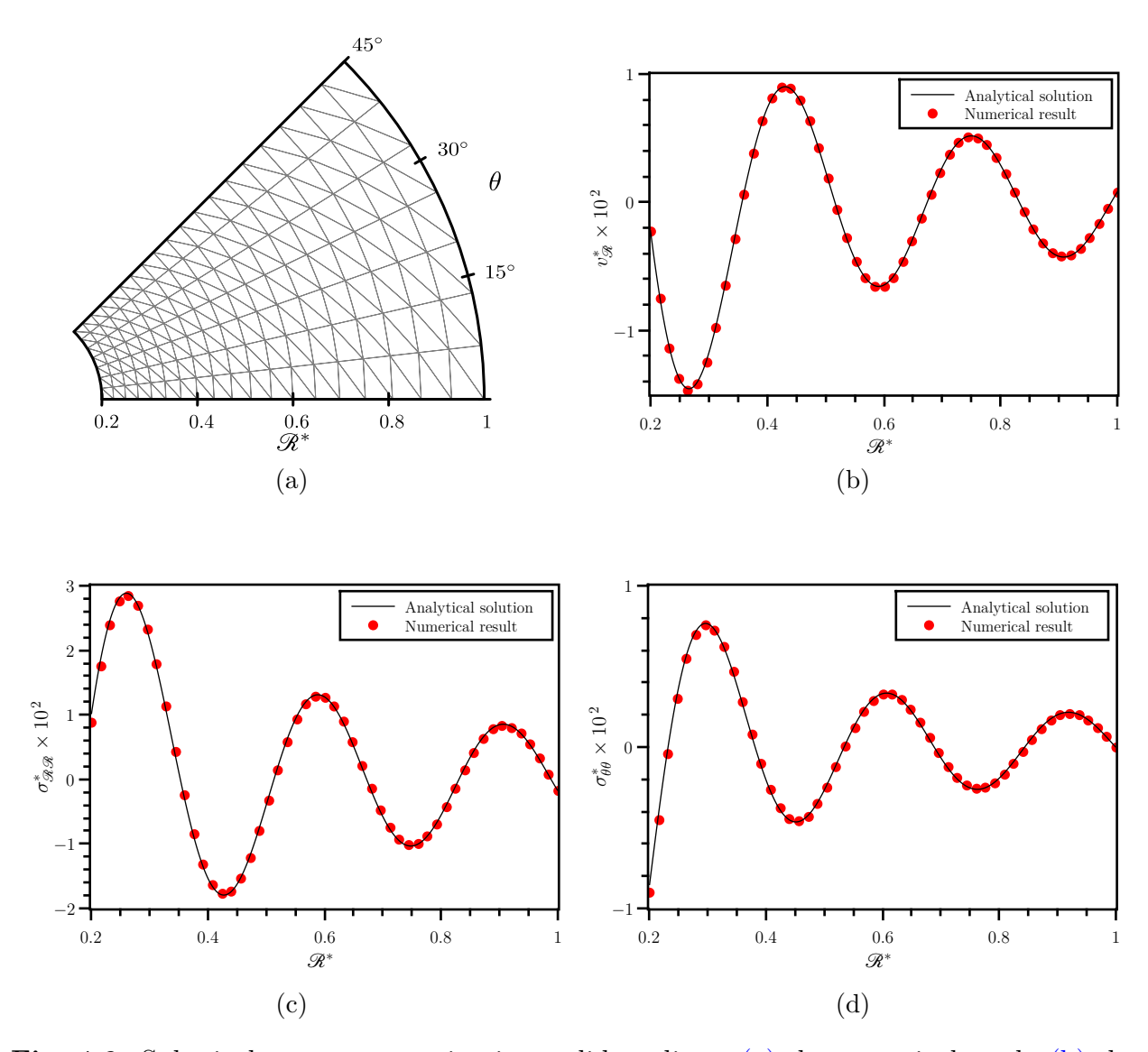


Fig. 4.6. Spherical wave propagation in a solid medium: (a) the numerical mesh; (b) the non-dimensional radial velocity, and the non-dimensional stress tensor components (c) $\sigma_{\Re \Re}^*$ and (d) $\sigma_{\theta\theta}^*$ along the radial direction at $t^*=4$.

non-dimensional variables are as follows:

$$\vec{v}^* = \frac{\vec{v}}{c_0}, \ \rho^* = \frac{\rho'}{\rho_0}, \ p^* = \frac{p'}{\rho_0 c_0^2}, \ t^* = t \cdot \frac{c_0}{L},$$
 (4.7a)

$$z^* = \frac{z}{L}, \ r^* = \frac{r}{L}, \ \mathcal{R}^* = \frac{\mathcal{R}}{L} = \sqrt{z^{*2} + r^{*2}},$$
 (4.7b)

where the length scale L equals \mathcal{R}_0 . The boundary condition at the transducer location, $\mathcal{R}^* = 0.2$, is set to:

$$v_{\mathcal{R}}^* = 0.001 \cdot \sin(20 t^*)$$
 at $\mathcal{R}^* = 0.2$. (4.8)

In this simulation, the non-dimensional time step and the grid size are 5.0×10^{-4} and 0.013, respectively. As demonstrated in Fig. 4.7, the numerical results and the analytical solutions, provided in Section 2.4.5.2, for the non-dimensional pressure and radial velocity are hardly distinguishable.

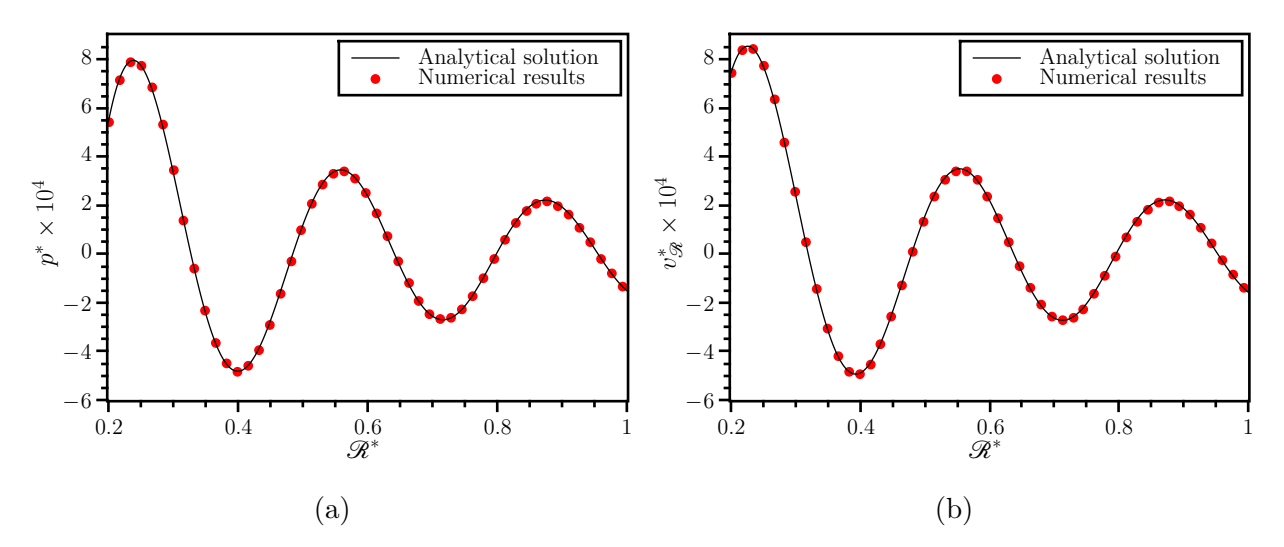


Fig. 4.7. Spherical wave propagation in a fluid medium generated by a transducer (see Eq. (4.8)): (a) the non-dimensional pressure, p^* , and (b) the non-dimensional radial velocity, $v_{\mathcal{R}}^*$, at $t^* = 2$.

4.1.5 Non-reflective Boundaries

As previously mentioned, non-reflective outer boundaries are crucial for numerical simulation of acoustic wave propagation. To assess the implementation of this feature in the proposed numerical model, propagation of waves within a fluid medium in the linear regime and an axisymmetric domain is investigated. A square $(0.0 \le z^* \le 0.5 \text{ and } 0.0 \le r^* \le 0.5$, where $r^* = 0$ is the axis and $z^* = 0$ is a symmetry plane) computational domain is considered to induce oblique wave interactions with boundaries. With the non-dimensional variables provided by Eqs. (4.7), the initial non-dimensional density and velocity (see Fig. 4.8b) have the following distributions:

$$\rho^* = 0.01 \cdot \exp\left(-\frac{z^{*2} + r^{*2}}{0.02}\right), \tag{4.9a}$$

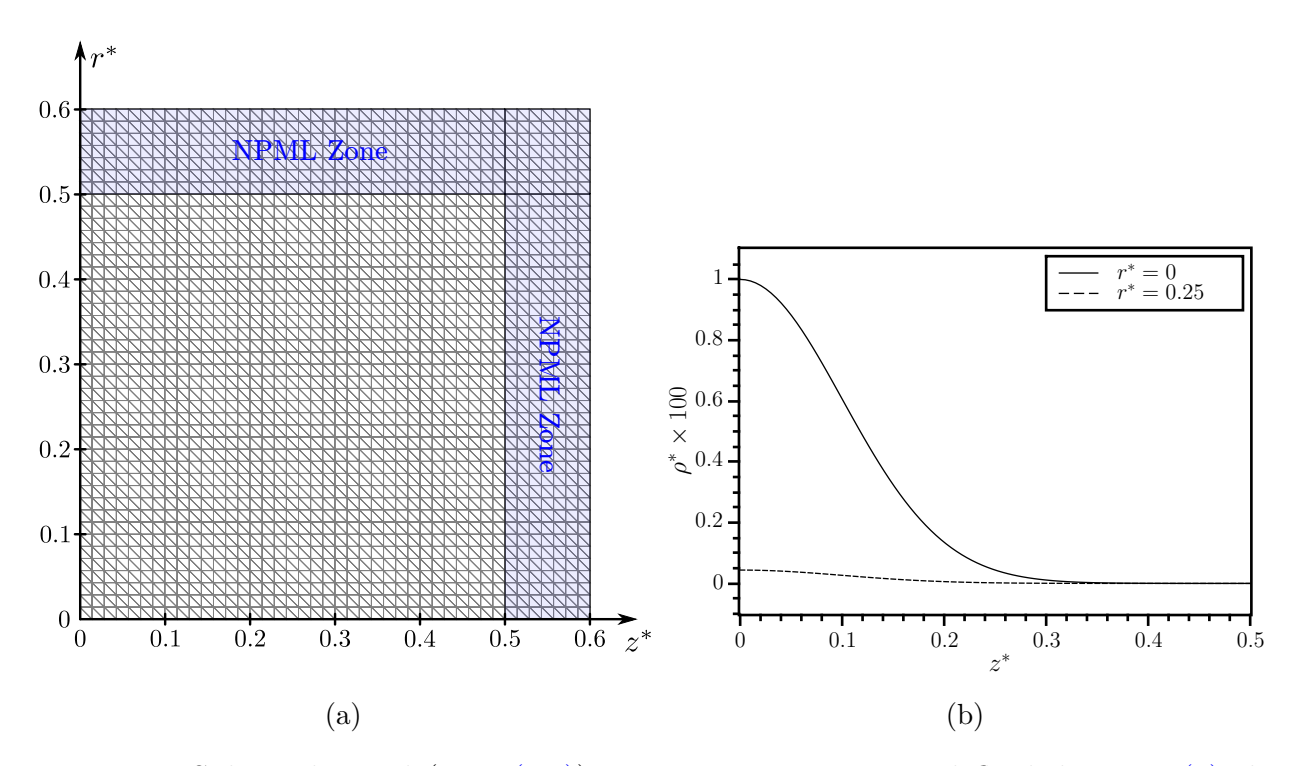


Fig. 4.8. Spherical signal (Eqs. (4.9)) propagation in a squared fluid domain: (a) the numerical mesh including the NPML zones; (b) initial distributions of non-dimensional density along $r^* = 0$ and $r^* = 0.25$, provided by Eq. (4.9b).

$$\vec{v}^* = (0.0, 0.0)$$
. (4.9b)

The non-dimensional grid size and time step are 0.014 and 10^{-3} , respectively.

To assess the effects of external boundaries on the solution inside the computational domain, $z^* = 0.5$ and $r^* = 0.5$ are first set to be absorbing boundaries. In this case, Fig. 4.9 demonstrates noticeable differences between the analytical solution [85] (lines) and the numerical results (triangles) at two time moments, $t^* = 0.6$ and $t^* = 0.8$, along $r^* = 0.25$. Such discrepancies are due to false reflections of outgoing waves. To remedy this deficiency, the domain is wrapped in an Nearly Perfectly Matched Layer (NPML) layer as illustrated in Fig. 4.8a, where the non-dimensional thicknesses, $d^{r*} = d^r/L$ and $d^{z*} = d^z/L$, and the parameter σ_{max} in Eqs. (3.4) are set to 0.1, 0.1, and 100, respectively. As seen in Fig. 4.9, the NPML layer does help to eliminate effectively these false reflections and obtain consistent results with the analytical solution.

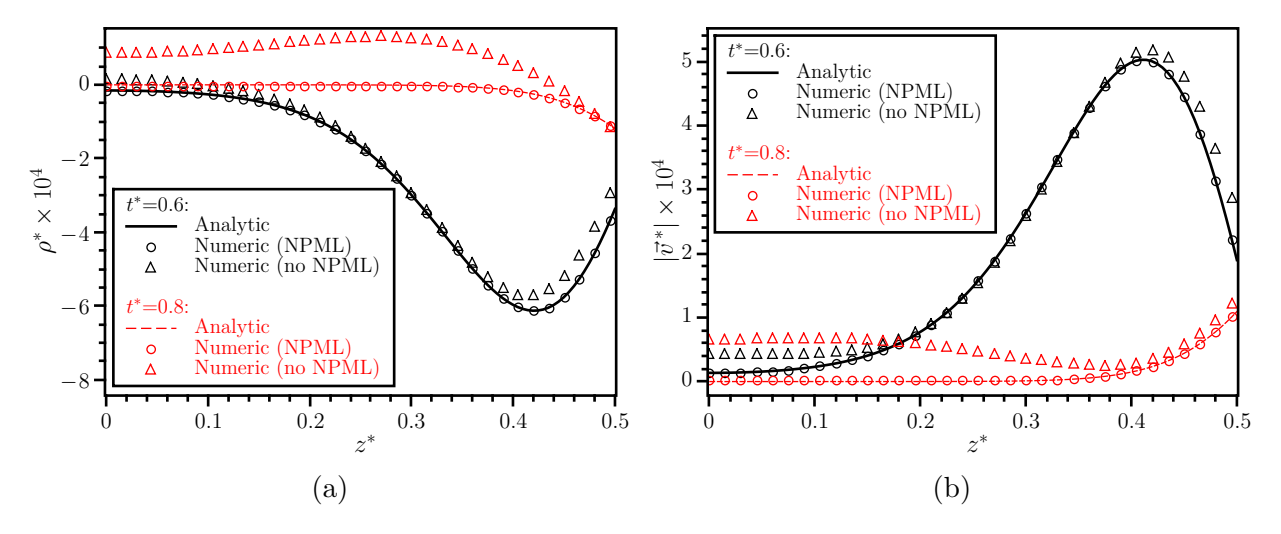


Fig. 4.9. Spherical signal (Eqs. (4.9)) propagation in a squared fluid domain: (a) non-dimensional density and (b) non-dimensional velocity magnitude distributions at two time moments for $r^* = 0.25$. The lines represent the analytical solution; circles show the numerical results with the NPML layer; and triangles—without the NPML zone.

4.1.6 Fluid-Solid Interactions

The propagation and interaction of waves at fluid-solid interfaces are other important features to be verified before modeling realistic WPC processes. For this test case, a 2D (non-axisymmetric) computational domain of rectangular shape $(0.0 \le x^* \le 0.5, -0.5 \le y^* \le 0.5,$ where $x^* = x/L$, $y^* = y/L$, and L is a characteristic length) is considered, as seen in Fig. 4.11. The upper zone, where $0.0 \le y^* \le 0.5$, is filled with a fluid, and the lower one, $-0.5 \le y^* \le 0.0$, is a solid, i.e., the fluid-solid interface corresponds to $y^* = 0$ (the thin white line in Fig. 4.12). The waves are generated by a density stimulation at $(x^*, y^*) = (0.0, 0.125)$ within the fluid zone (the site is shown by the black circle in Figs. 4.11 and 4.12). With the non-dimensional variables mentioned in Eqs. (4.6) and (4.7), the stimulation strength, which is also illustrated in Fig. 4.10, and other specifications are as follows:

$$\rho_{\text{stimulation}}^* = 0.01 \cdot (t^* - 0.1) \cdot \exp\left(-\left(20\pi (t^* - 0.1)\right)^2\right),\tag{4.10}$$

$$(\rho_0)_{\text{solid}} = 1.2 (\rho_0)_{\text{fluid}}, (c_1)_{\text{solid}} = (c_0)_{\text{fluid}}, c_2^{*2} = 0.375, c_3^{*2} = 0.25.$$
 (4.11)

In this simulation, the non-dimensional grid size and time step are 8×10^{-3} and 10^{-4} , respectively. The computational domain shown in Fig. 4.11 is partitioned into 48 sections, which are assigned to 2.66 GHz CPUs (Dual Intel Westmere EP Xeon X5650) on Compute Canada supercomputers. In this simulation, t^* requires almost 36 minutes to increase 0.1 in value.

As seen in Fig. 4.12, a portion of the initial longitudinal signal emitted from the source is reflected at the fluid-solid interface and propagates back into the fluid zone. Another portion is decomposed into the longitudinal and transverse waves which penetrate into the solid zone (below the white line in Fig. 4.12). As the speeds of sounds associated with longitudinal and transverse signals are different in solid media, two distinct wave fronts are formed and propagate in the solid medium. The numerical results are compared with the analytical data obtained via the Cagniard-De Hoop method [117, 118]. As seen in Figs. 4.13 and 4.14, the numerical results at two sensors located in the fluid and solid zones at $(x^*, y^*) = (0.125, 0.125)$ and $(x^*, y^*) = (0.125, -0.125)$ (shown by the white squares in Fig. 4.12) closely follow the analytical solution.

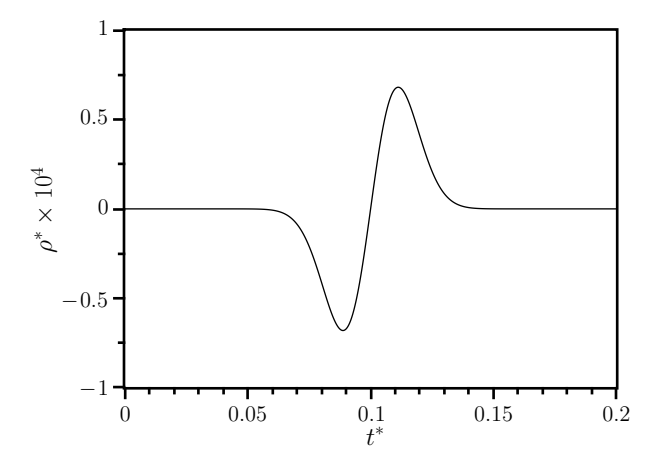


Fig. 4.10. Cylindrical wave propagation through a fluid-solid interface: the non-dimensional density stimulation at the source location, shown by the black circle in Figs. 4.11 and 4.12, which is provided by Eq. (4.10).

To test the proposed model in heterogeneous media while the fluid medium behaves non-linearly, the interaction of paraxial waves with a fluid-solid interface is investigated in an axisymmetric domain. For this purpose, a cylinder consisting of a solid ($0 \le z^* \le 0.5$) and a fluid ($0.5 \le z^* \le 1$) zones is considered as illustrated in Fig. 4.15a. The initial condition (see Fig. 4.15b) and other specifications, based on the non-dimensional variables in Eqs. (4.6) and (4.7), are as follows:

$$\sigma_{zz}^* = -0.5 \cdot \exp\left(-\frac{(z^* - 0.2)^2}{0.0032}\right),\tag{4.12}$$

$$(\rho_0)_{\text{solid}} = 2.0 (\rho_0)_{\text{fluid}}, (c_0)_{\text{fluid}} = 0.8 (c_1)_{\text{solid}}, c_2^{*2} = 0.375, c_3^{*2} = 0.25.$$
 (4.13)

In this simulation, the non-dimensional grid size and time step are 10^{-2} and 10^{-4} , respectively. The instant signal distributions around the interface in the linear and weakly non-linear regimes are shown in Fig. 4.16. It is seen that the numerical results and the analytical solutions, which are based on the method of characteristics, are hardly distinguishable. It is to be especially noted that the normal velocity and the traction are continuous at the fluid-solid interface.

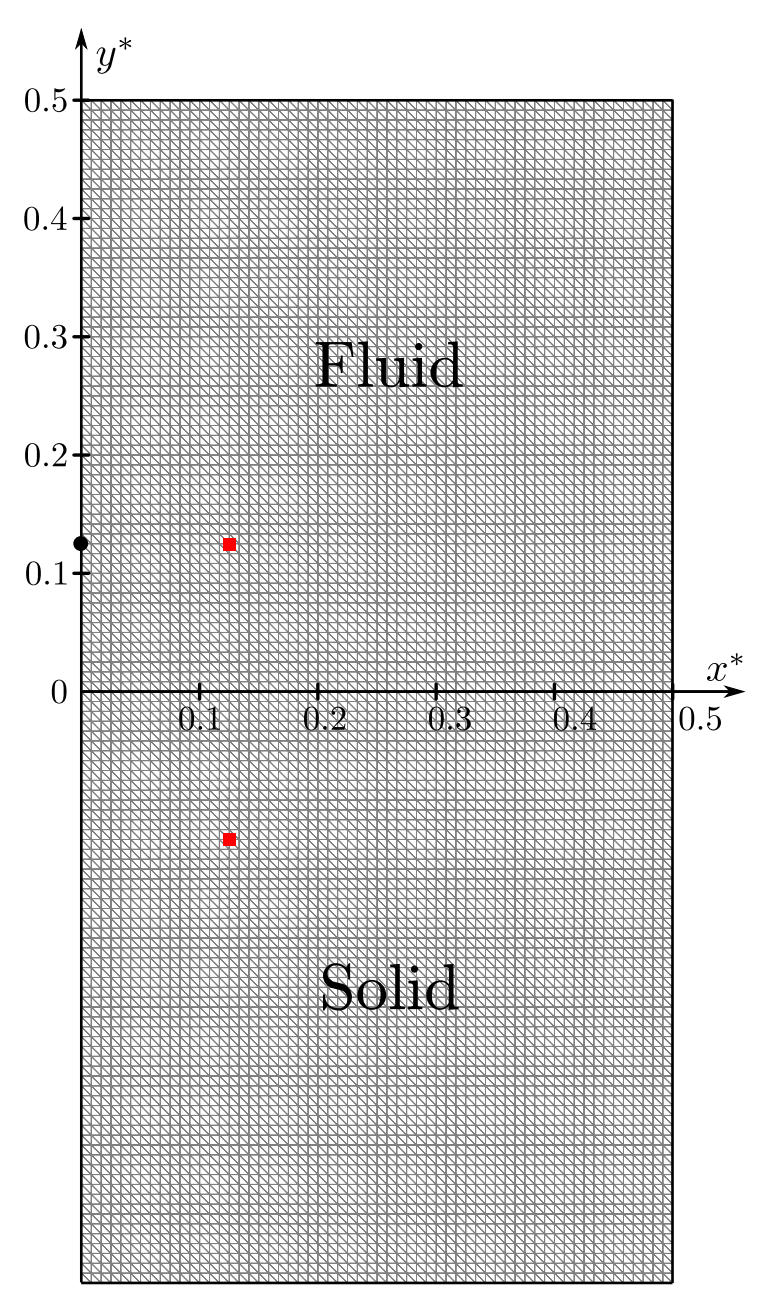


Fig. 4.11. The numerical mesh for propagation of cylindrical waves through a fluid-solid interface located at $y^* = 0$. The upper and lower zones are filled with a fluid and a solid, respectively. The black circle indicates the disturbance source location, and the red squares designate the locations of sensors, where the signals shown in Figs. 4.13 and 4.14 are recorded.

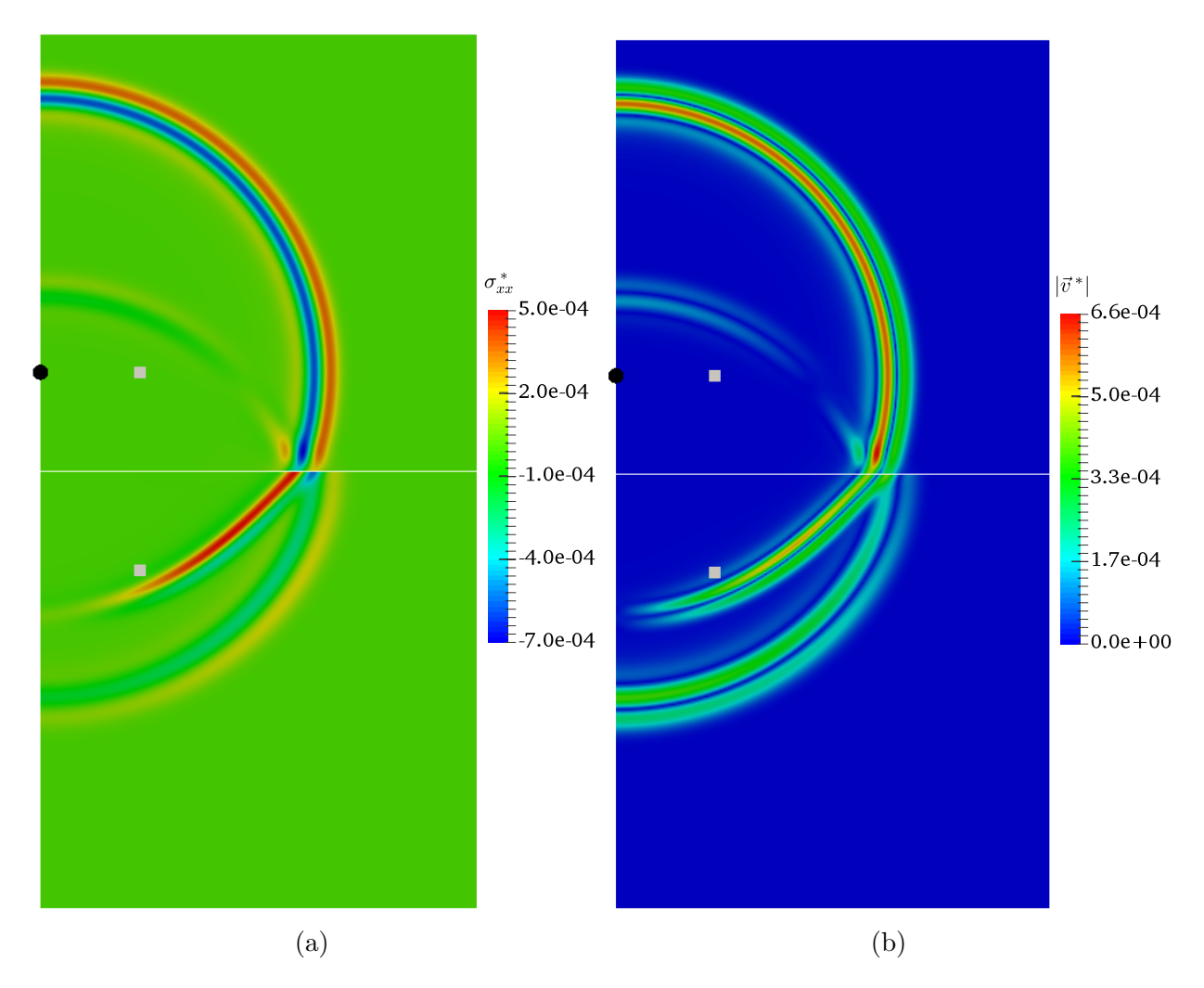


Fig. 4.12. Cylindrical wave propagation through a fluid-solid interface (shown as the thin white line): (a) non-dimensional stress tensor component σ_{xx}^* and (b) non-dimensional velocity magnitude distributions at $t^* = 0.45$. The black circle indicates the disturbance source location, and the white squares designate the locations of sensors, where the signals shown in Figs. 4.13 and 4.14 are recorded.

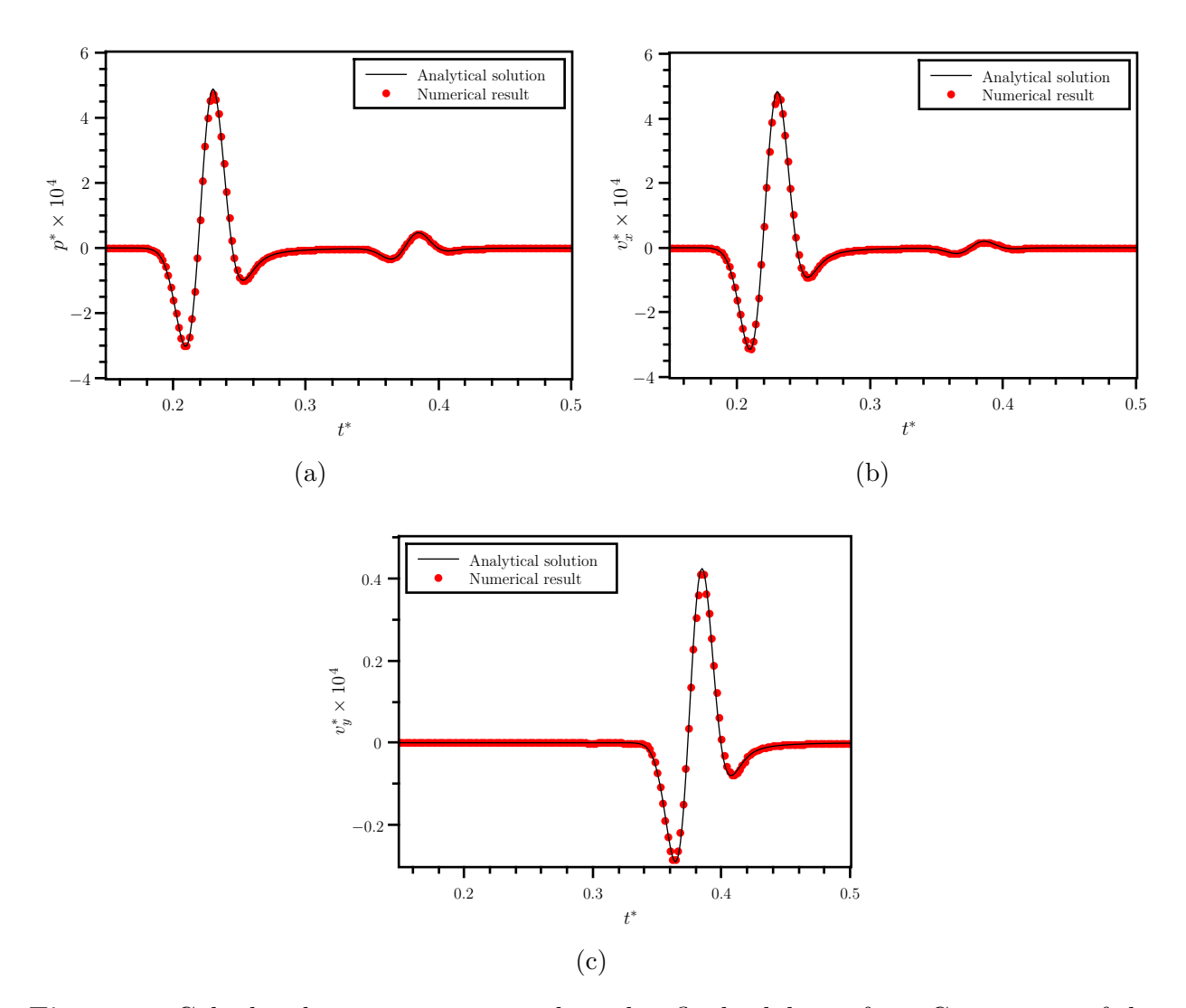


Fig. 4.13. Cylindrical wave propagation through a fluid-solid interface. Comparison of the numerical results with the analytical solutions at the upper sensor in the fluid zone (see Fig. 4.12): histories of (a) non-dimensional pressure, and non-dimensional velocities (b) v_x^* and (c) v_y^* .

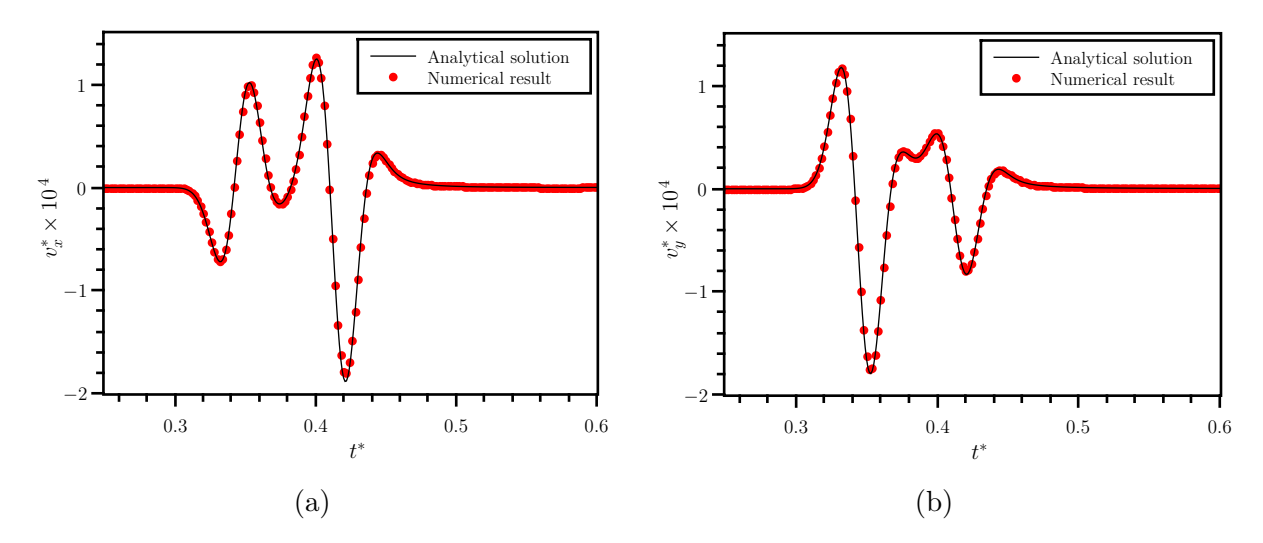


Fig. 4.14. Cylindrical wave propagation through a fluid-solid interface. Comparison of the numerical results with the analytical solutions at the lower sensor in the solid zone (see Fig. 4.12): histories of non-dimensional velocities (a) v_x^* and (b) v_y^* .

4.1.7 Single Bubbles

In the model for fluids with bubbles proposed in Section 2.4.3.3, void fractions of single bubbles in the axisymmetric formulation are represented by the discontinuous Kroneckerdelta function. The present section is devoted to the verification of this model. At first, one-way simulations are undertaken, which means that bubble dynamics has no effect on the surrounding flow field and, hence, on the external stimulating pressure disturbance p'_{ext} . These tests are essentially aimed at the verification of the modified Keller-Miksis (KM) model of Eqs. (2.47) in a stand-alone mode. At the second stage, two-way simulations are conducted, in which bubbles are affected by the surrounding fluid and at the same time bubble dynamics leads to changes in flow variables. In this case, an appropriate estimation for the stimulating pressure is required as discussed in Section 2.4.5, see Eq. (2.49).

Bubble dynamics is a complicated phenomenon having many peculiarities, particularly for strong stimulation of a bubble. In this case, bubble behavior exhibits very fast, successive compression and rebound phases making the governing Ordinary Differential Equation (ODE) (Eqs. (2.47)) stiff. As mentioned in Section 3.6, the C $^{\infty}$ -diffeomorphism transformation, suggested by Parlitz et al. [14], is employed to handle such a situation. To verify the

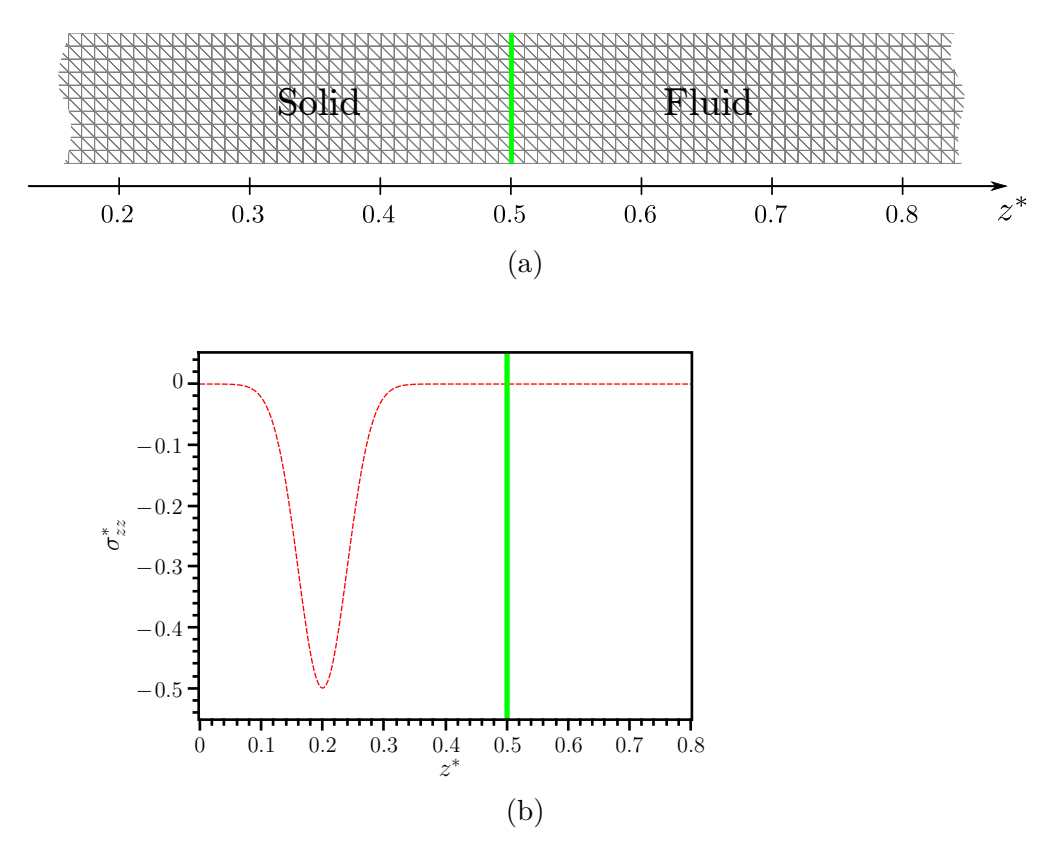


Fig. 4.15. Paraxial wave propagation through a fluid-solid interface, shown by the green line: (a) the numerical mesh and (b) the initial distribution of the non-dimensional axial stress, σ_{zz}^* , provided by Eq. (4.12).

performance of this non-linear transformation, a bubble with the radius of 10 μ m is subjected to a signal with the amplitude of 150 kPa and the frequency of 200 kHz, which, in this one-way simulation, also represents the bubble-stimulating pressure $p'_{\rm ext}$. This simulation sketch is shown in Fig. 4.17a.

By solving Eqs. (3.73), the transformed bubble radius (exp $[2R/R_0]$) is obtained at each transformed time moment $(2t/R_0)$, as shown in Fig. 4.17b. Then, the bubble radius (R) at the respective time moment (t) is obtained by inverting the transformation, which is illustrated in Fig. 4.17c. As depicted in these figures, the present numerical results coincide with those obtained by Parlitz et al. [14], for the time step of 10 ns. The comparison of Figs. 4.17b and 4.17c shows that the bubble radius transformed by the C^{∞} -diffeomorphism mapping

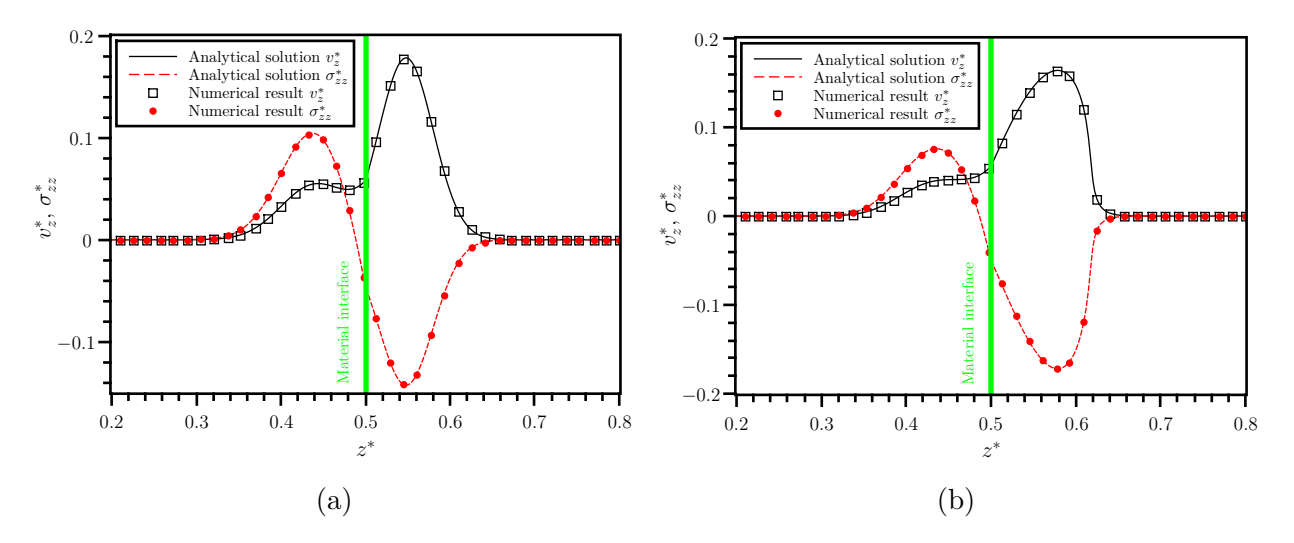


Fig. 4.16. Paraxial wave propagation through a fluid-solid interface, shown by the green line, for (a) linear and (b) non-linear fluid flow regimes. Axial distributions of the non-dimensional velocity v_z^* and the non-dimensional stress tensor component σ_{zz}^* at $t^* = 0.36$ are shown.

(exp $[2R/R_0]$) undergoes smoother variations, particularly during the bubble collapse phases. Such smoother variations of bubble radius are much easier to resolve numerically and allow larger time steps.

To validate the present numerical model for single bubble dynamics, the experimental data provided by Geisler [5] and Lauterborn et al. [6] are used. In a one-way simulation, a bubble with the initial radius of 8.1 μ m is subjected to a periodic sinusoidal signal with the amplitude of 132 kPa and the frequency of 21.4 kHz, as shown in Fig. 4.18a. For this case, the vapor pressure $p_{\rm v}=0$, the polytropic exponent of the bubble content k=1.2, and the density and viscosity of the surrounding fluid are 1000 kg/m³ and 0.0018 Pa·s, respectively [6]. In this simulation, the time step is set to 5 ns. The bubble radius history is shown in Fig. 4.18b for one cycle of bubble vibrations, starting from $t_0=494.1~\mu$ s, where the retarded time $t^*=t-t_0$. As illustrated, the results of the modified KM model are consistent with the experimental data. These results are provided for the giant response phase, in which a large bubble radius expansion is followed by a steep collapse and successive lower-amplitude after-bounces.

The two previous test cases were one-way simulations, meaning that the surrounding flow affects bubbles, but bubble dynamics do not change the flow variables. For realistic situations

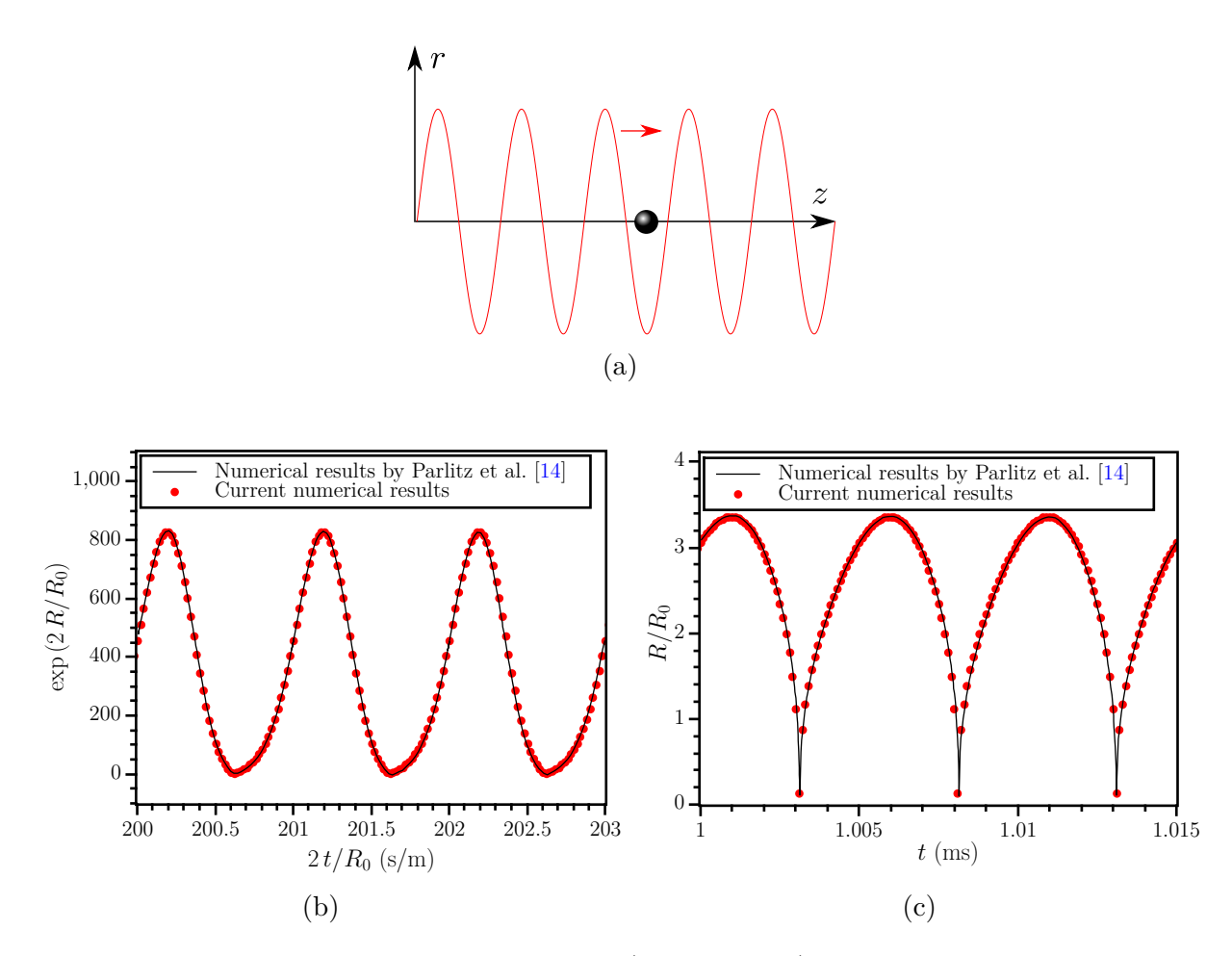


Fig. 4.17. One-way stimulation of a bubble ($R_0 = 10 \mu m$) by a periodic sinusoidal signal with the frequency of 200 kHz and the amplitude of 150 kPa: (a) the simulation sketch including the bubble and the stimulating sinusoidal signal; and bubble radius histories in (b) the transformed and (c) physical domains.

it is essential to conduct two-way simulations, which require an appropriate estimation for the stimulating pressure. The rest of the simulations in this chapter are two-way, in which both flow fields and bubbles affect each other.

A one-wavelength sinusoidal signal with the amplitude of 80 kPa and the frequency of 200 kHz stimulates a bubble with the radius of 10 μ m, as shown in Fig. 4.19a. This signal is emitted from the transducer which is located on the left boundary (Fig. 4.19a) 6 mm away from the bubble. This transducer becomes an absorbing boundary at $t = 5 \mu$ s. In this case,

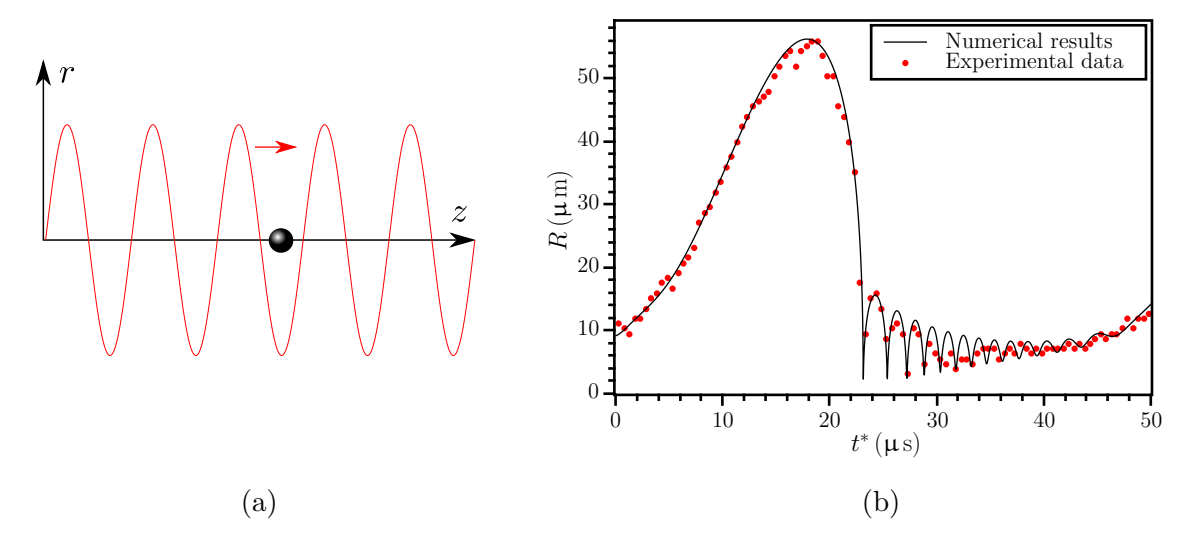


Fig. 4.18. One-way stimulation of a bubble ($R_0 = 8.1 \,\mu\text{m}$) by a periodic sinusoidal signal with the amplitude of 132 kPa and the frequency of 21.4 kHz: (a) the simulation sketch including the bubble and the stimulating sinusoidal signal; and (b) the numerical results for variations of the bubble radius versus the retarded time, $t^* = t - 494.1 \,\mu\text{s}$, compared with the experimental data provided by Geisler [5] and Lauterborn et al. [6].

the minimum grid size of 0.25 mm and the time step of 10 ns are used. A method based on the analytical solution is proposed in Section 2.4.5 to properly estimate the stimulating pressure at the bubble location. The concentric spheres used to estimate the stimulating pressure with Eq. (2.49) have radii of 0.2 and 0.3 mm. A section of the numerical mesh close to the bubble is illustrated in Fig. 4.19b, where the bubble location is indicated by the red arrow.

Figure 4.19c shows that the numerical results for the pressure disturbances recorded at the distance of 4 mm from the bubble location are in good agreement with the analytical solution provided by Eq. (2.63), in which the exact stimulating pressure is used. Thus, the proposed model for estimation of the stimulating pressure performs satisfactorily while it includes fewer approximations in comparison with the other methods available in the literature [10, 41]. The frequency spectrum for variations of the bubble radius is provided in Fig. 4.19d. As depicted, the main peak occurs at $f \approx 329.5$ kHz, which is slightly lower than the natural frequency of the bubble (≈ 332 kHz). This behavior is expected for non-linear stimulation of a bubble, as

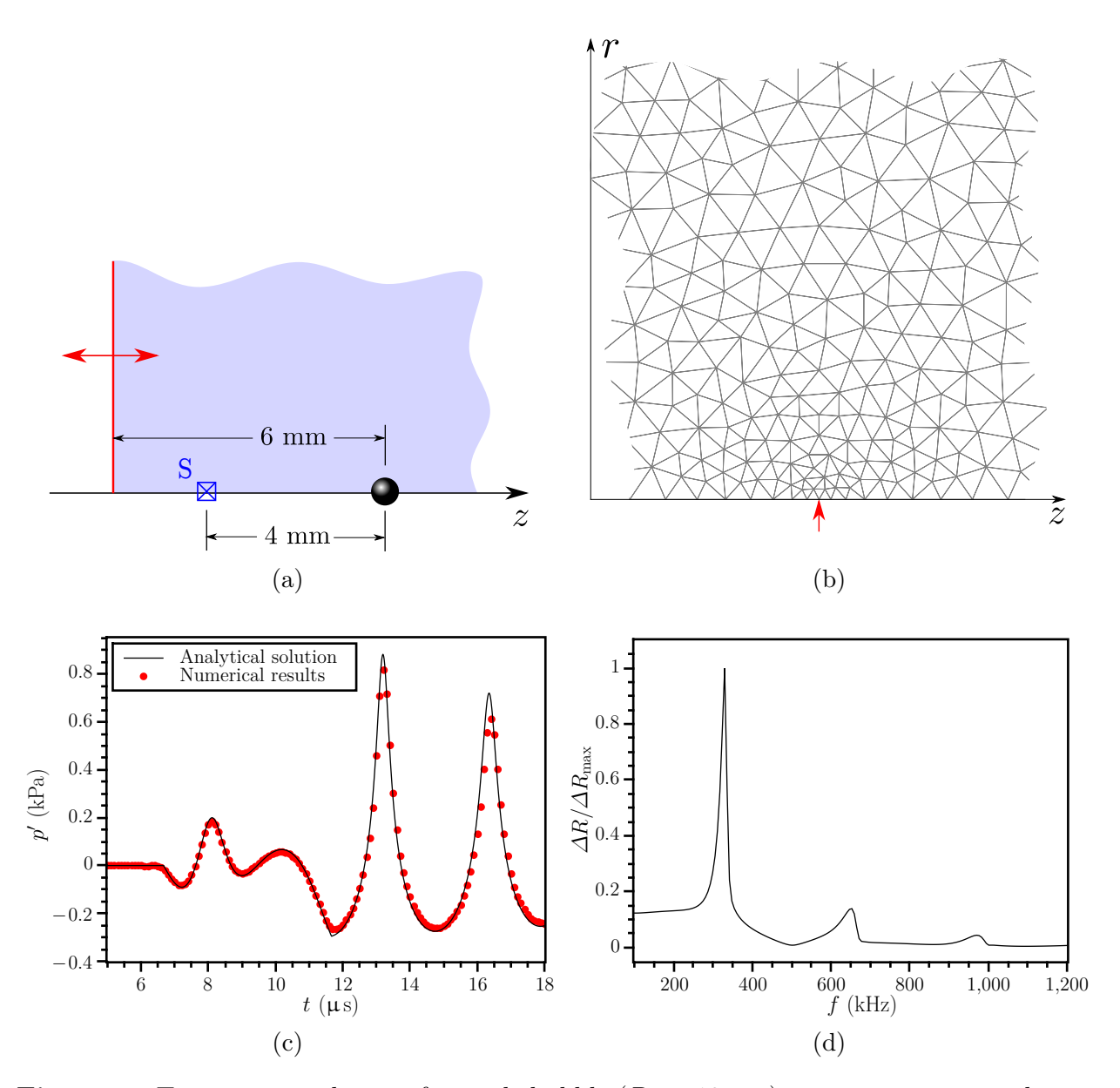


Fig. 4.19. Two-way stimulation of a single bubble ($R_0 = 10 \, \mu \text{m}$) in an axisymmetric domain by a one-wavelength sinusoidal signal with the amplitude of 80 kPa and the frequency of 200 kHz: (a) a schematic of the problem setup (the left boundary is the transducer which becomes an absorbing boundary at $t = 5 \, \mu \text{s}$); (b) a section of the numerical mesh close to the bubble location indicated by the red arrow; (c) the analytical and numerical pressure disturbance histories at the distance of 4 mm from the bubble; and (d) the normalized frequency spectrum of the bubble radius variations for 4 μs < $t < 168 \, \mu \text{s}$.

reported by Lauterborn and Kurz [2] and Brennen [1]. The next two super-harmonics of the natural frequency are also stimulated due to the non-linear excitation of the bubble.

4.1.8 Bubble-Plane clouds

The void fraction of bubble-plane clouds in paraxial domains is modeled by a discontinuous function, the Kronecker-delta. The proposed model for such bubble clouds, which is provided in Section 2.4.3.1, is verified in more details in the current subsection. In paraxial domains, it is assumed that a sufficiently large number of bubbles per unit area are located at the bubble plane, which is normal to the axis, in such a way that dynamic responses of the cloud would remain paraxial. In this model, the bubbles within bubble-plane clouds are dynamically synchronized.

Under the paraxial approximation, a bubble-plane cloud (see Fig. 2.2a) consisting of bubbles with the radius of 10 μ m and the physical void fraction ($\bar{\beta}_0$) of 5×10^{-4} (see Eq. (2.40)) is stimulated by a one-wavelength sinusoidal signal with the frequency of 200 kHz and the amplitude of 80 kPa. As illustrated in Fig. 4.20a, this stimulating sinusoidal signal is emitted from a transducer on the left boundary, which becomes an absorbing boundary at $t = 5 \mu s$. The grid size and the time step are 0.25 mm and 10 ns, respectively. In addition, the volume V in Eq. (2.49) is chosen as the set of numerical grid elements containing the cloud.

Figure 4.20b shows satisfactory agreement between the pressure disturbance generated by this bubble plane at the sensor S located 1 cm away from the plane and the respective analytical solution derived in Eq. (2.54), in which the exact stimulation pressure is used. The frequency spectrum of the bubble radius variations, depicted in Fig. 4.20c, is the same as the one for the single bubble case shown in Fig. 4.19d because in both cases the bubbles are subjected to the same stimulation yielding the same changes in bubble radii; however, the response signals are not the same due to distinct bubble arrangements.

A bubble-plane cloud within a fluid medium is a non-linear oscillator, as seen in Fig. 4.20. However, it is also of interest to assess responses of bubble-plane clouds to weak stimulations and to compare the results with the analytical solutions available for linear oscillators. If we assume $R(t) = R_0 + R'(t)$ and $p'_{\text{ext}} = p'(t)$, where R'(t) and p'(t) are small perturbations of

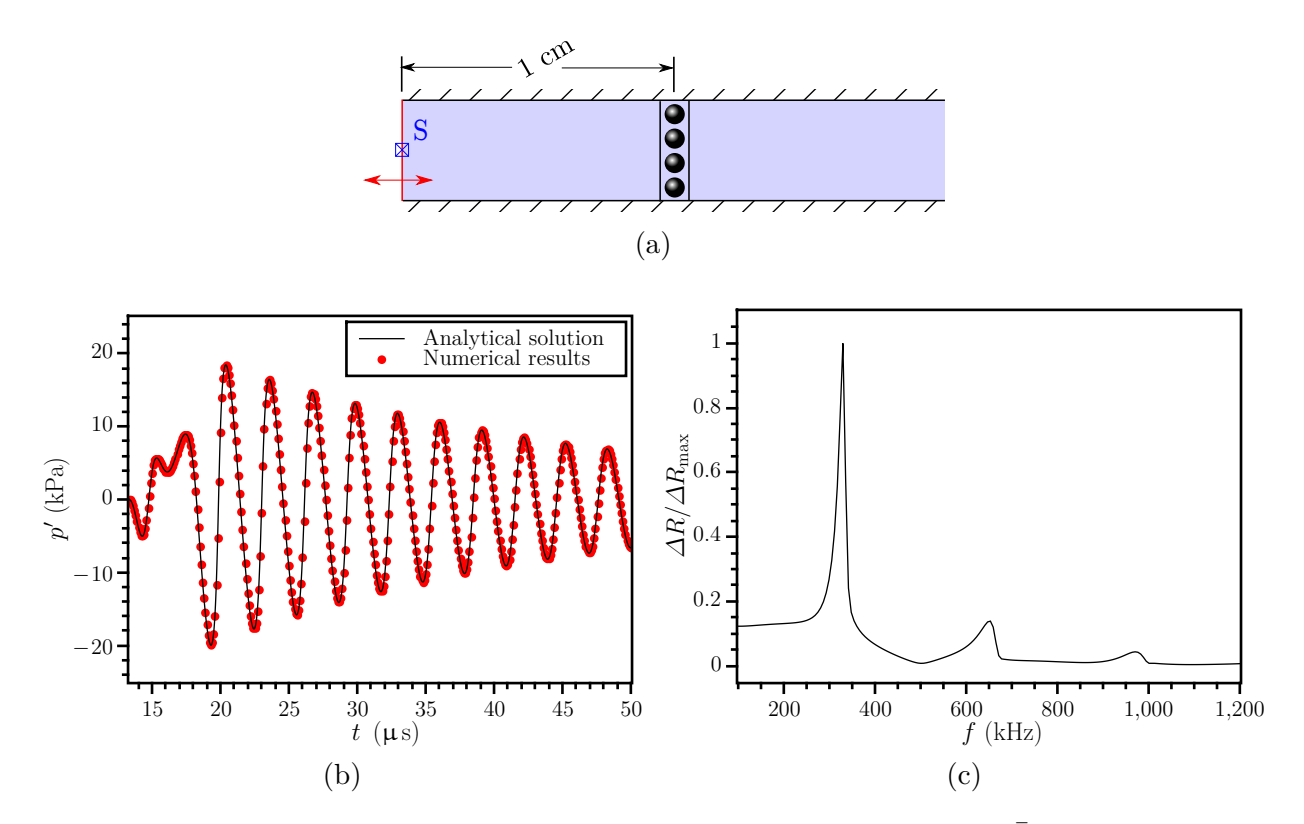


Fig. 4.20. Two-way stimulation of a bubble-plane cloud ($R_0 = 10 \, \mu \text{m}$, $\bar{\beta}_0 = 5 \times 10^{-4}$) by a one-wavelength sinusoidal signal with the amplitude of 80 kPa and the frequency of 200 kHz: (a) a schematic of the problem setup (the left boundary shown in red is the transducer which becomes an absorbing boundary at $t = 5 \, \mu \text{s}$); (b) the analytical solution and numerical results for the pressure disturbance history recorded at the sensor S; and (c) the normalized frequency spectrum of the bubble radius variations for 6.67 μs < $t < 170.5 \, \mu \text{s}$.

the bubble radius and the stimulation pressure, respectively, Eqs. (2.47) would read:

$$C_1 \cdot \frac{\mathrm{d}^2 R'}{\mathrm{d}t^2} + C_2 \cdot \frac{\mathrm{d}R'}{\mathrm{d}t} + C_3 \cdot R' = \left[-\frac{p'}{\rho} - \frac{R_0}{\rho c} \frac{\mathrm{d}p'}{\mathrm{d}t} \right],\tag{4.14}$$

where

$$C_1 = \left[R_0 + \frac{4\,\mu}{\rho\,c} \right],\tag{4.15a}$$

$$C_2 = \left[\frac{4\,\mu}{R_0\,\rho} + \frac{3\,k\,B}{\rho\,c} - \frac{2\,\sigma}{R_0\,\rho\,c} \right],\tag{4.15b}$$

$$C_3 = \left[\frac{3 k B}{\rho R_0} - \frac{2 \sigma}{R_0^2 \rho} \right], \tag{4.15c}$$

$$B = p_0 - p_v + \frac{2\sigma}{R_0}. (4.15d)$$

When stimulated by $p'_{\text{stim}} = p' = A_1 \exp(j \omega t)$, the bubble radius changes as follows:

$$R'(t) = A_2 \exp\left[j\left(\omega t + \chi + \psi\right)\right],\tag{4.16}$$

where

$$\chi = \tan^{-1} \left(\frac{R_0 \,\omega}{c} \right) + \pi \,, \tag{4.17a}$$

$$\psi = \tan^{-1} \left(\frac{C_1 \left(\omega_0^2 - \omega^2 \right)}{\omega C_2} \right) - \frac{\pi}{2},$$
(4.17b)

$$\omega_0 = \sqrt{\frac{C_3}{C_1}}. (4.17c)$$

In the above relations, ω is the stimulation frequency, and j is the imaginary unit. Equation (2.53) is then used to relate variations of the bubble radius to the pressure signal generated by the bubble-plane cloud as follows:

$$p'_{\text{resp}} = A_3 \exp\left[j\left(\omega t + \chi + \psi + \frac{\pi}{2}\right)\right],\tag{4.18a}$$

$$\Delta \phi = \phi_{\text{resp}} - \phi_{\text{stim}} = \chi + \psi + \frac{\pi}{2}, \qquad (4.18b)$$

where p'_{resp} is the response of the bubble-plane cloud to the weak stimulation at the cloud location, and $\Delta \phi$ is the total phase difference between the stimulation and response signals.

To verify Eqs. (4.18), the same bubble-plane cloud used in the previous test case $(\bar{\beta}_0 = 5 \times 10^{-4}, R_0 = 10 \text{ }\mu\text{m})$ is stimulated by a continuous sinusoidal signal with the amplitude of 1 Pa and the frequency of 200 kHz in the numerical setup shown in Fig. 4.21a. This stimulation signal is emitted by a plane source, which is located at the distance of 1 cm from the cloud. In this case, the phase shift $\Delta \phi$ from Eqs. (4.18) is equal to $\approx 3\pi/2$. The grid

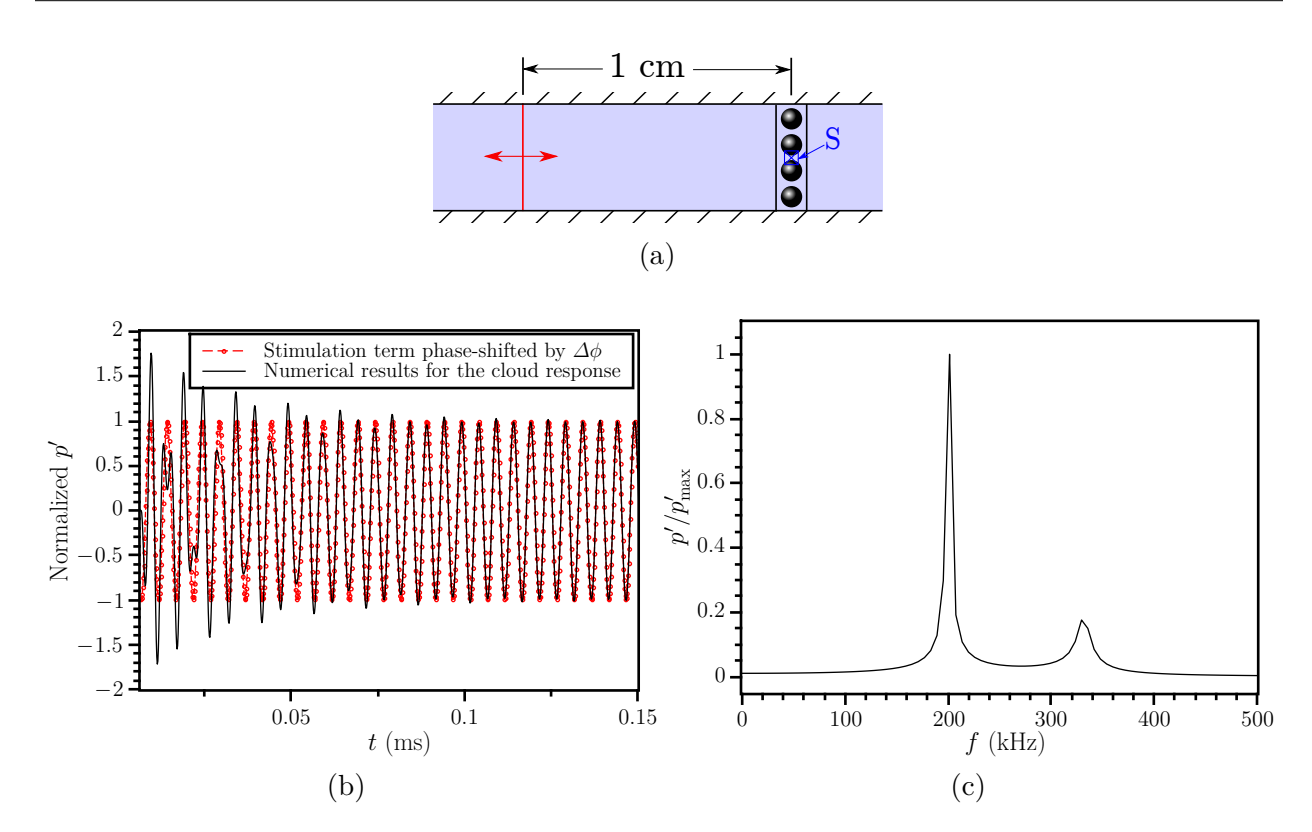


Fig. 4.21. Linear stimulation of a bubble-plane cloud ($R_0 = 10 \, \mu \text{m}$, $\bar{\beta}_0 = 5 \times 10^{-4}$) by a periodic sinusoidal signal with the amplitude of 1 Pa and the frequency of 200 kHz: (a) the simulation sketch including the bubble-plane cloud, the sensor S, and the plane source shown in red; (b) the pressure stimulation p'_{stim} phase-shifted by $\Delta \phi \approx 3\pi/2$ and the cloud response versus time at the bubble-plane location from numerical simulation, both normalized by the respective pressure amplitudes at later time moments (> 0.1 ms); (c) the respective normalized frequency spectrum of the pressure disturbance generated by the bubble-plane cloud for 6.67 μs < $t < 170.5 \, \mu \text{s}$.

size and the time step are 0.2 mm and 10 ns, respectively. As anticipated for linear oscillators, the vibrations consist of the forced mode (with the frequency of the driving pressure) and the free ones (with the natural frequencies of the system). After some time, free vibration modes are diminished, and the system is fully controlled by the driving term. As seen in Fig. 4.21b, the phase-shifted (by $3\pi/2$) stimulation signal $p'_{\rm stim}$ (or the response signal $p'_{\rm resp}$, Eq. (4.18a)) and the cloud response at the bubble location from the numerical simulation (recorded at the sensor S) are hardly distinguishable after 0.1 ms. These pressure disturbance histories

are normalized to have the same amplitudes for t > 0.1 ms. Figure 4.21c depicts two peaks in the frequency spectrum of the pressure disturbances generated by the cloud, which are associated with the forced- and free-oscillation frequencies. The longer oscillations last, the more the forced-oscillation mode dominates.

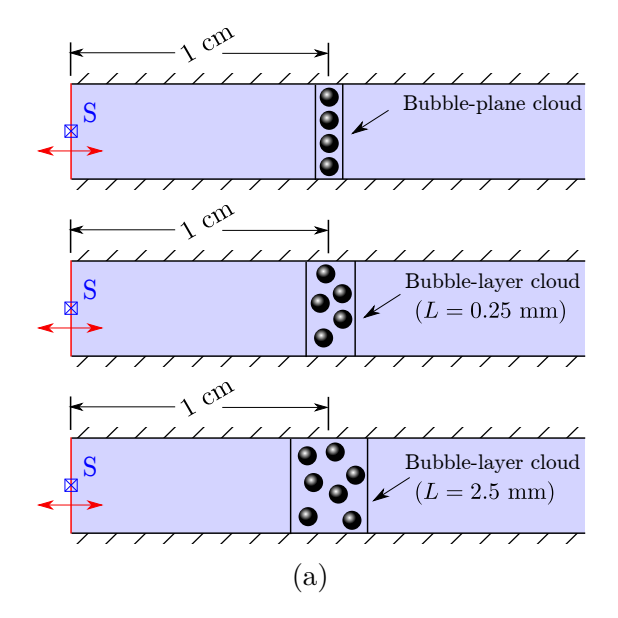
4.1.9 Bubble-Layer Clouds

In this subsection, bubble-layer clouds (Fig. 2.2b) in paraxial domains are investigated, and the proposed numerical model is verified via comparison with the data available in the literature.

Bubble clouds are dynamic systems with associated natural modes. In bubble-layer and spherical bubble clouds, oscillations of bubbles are not fully synchronized, as opposed to bubble-plane clouds (see more details in Section 2.4.3). To reveal the consequences of that, the previously investigated bubble-plane cloud in Fig. 4.20a ($\bar{\beta}_0 = 5 \times 10^{-4}$, $R_0 = 10 \,\mu\text{m}$) is first replaced by a bubble-layer cloud with the thickness of 0.25 mm, as shown in Fig. 4.22a. The bubble radius remains to be 10 μ m so that the bubble layer is rather thin: it is just 12.5 bubble diameters wide. To have the same number of bubbles in both clouds, the void fraction of the bubble-layer cloud is set to 4×10^{-5} . The problem setup and simulation parameters for the bubble-layer and bubble-plane cases are the same; in particular, similarly to the setup shown in Fig. 4.20a, bubble responses are recorded at the distance of 1 cm from the bubble-layer-cloud center. In this case, the grid size and the time step are 83.3 μ m and 3 ns, respectively.

Figure 4.22b shows that the pressure signals generated by this bubble-layer cloud (solid blue line) are weaker than those produced by the bubble-plane cloud (solid black line), even though the total number of bubbles is the same for both clouds. To verify that this noticeable difference can be attributed to the fact that oscillations of bubbles in different planes of the bubble-layer cloud are not synced, all the bubbles of this thin bubble-layer cloud are non-physically forced to oscillate synchronously; as a result, the same generated signal as from the bubble-plane cloud is recorded, see the red full circles in Fig. 4.22b.

In the next numerical experiment the bubble layer is made one order of magnitude thicker (2.5 mm), as illustrated in Fig. 4.22a. To keep the same number of bubbles as in the thinner



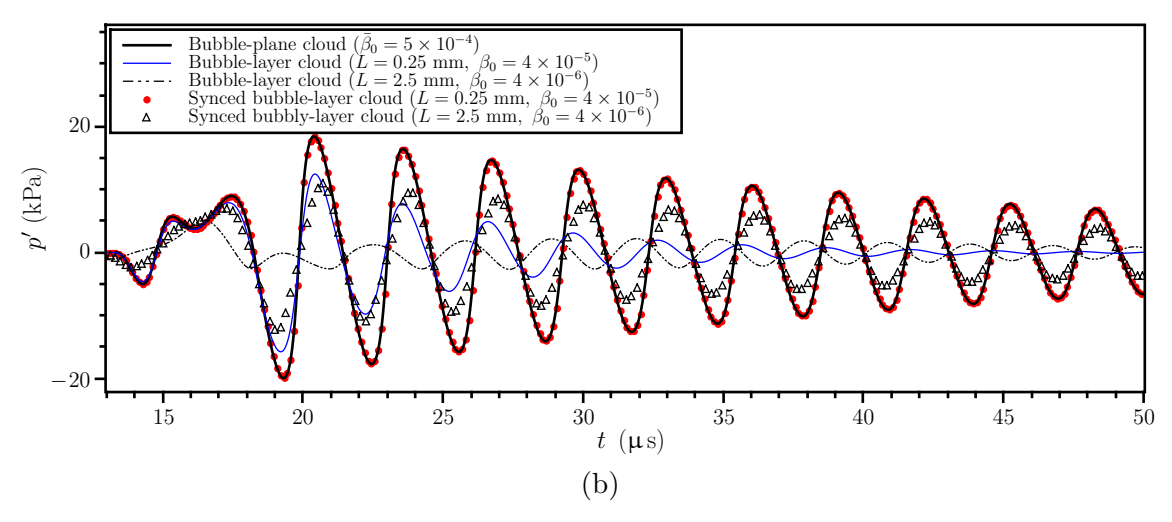


Fig. 4.22. Comparison of the bubble plane and bubble-layer clouds ($R_0 = 10 \ \mu \text{m}$) stimulated by a one-wavelength sinusoidal signal with the amplitude of 80 kPa and the frequency of 200 kHz: (a) the simulation sketches (not to scale) including the bubble clouds, the sensors S, and the transducers (shown in red) which become absorbing boundaries at $t = 5 \ \mu \text{s}$; and (b) the pressure disturbances generated by the bubble-plane cloud and bubble-layer clouds of various thicknesses, which are recorded at the sensor S. All clouds contain the same number of bubbles with $R_0 = 10 \ \mu \text{m}$.

(0.25 mm) bubble-layer cloud and in the bubble-plane cloud, the volume fraction is reduced to 4×10^{-6} . The results are also shown in Fig. 4.22b. The increased thickness leads to further decrease of strength of the recorded signal (see the dash-dotted line in Fig. 4.22b). Furthermore, even if all the bubbles of the 2.5-mm-thick bubble-layer cloud are non-physically synced, the resulting pressure signal (open triangles in Fig. 4.22b) is markedly weaker than that for the bubble-plane cloud. This effect results from the phase interference of the signals emitted from each bubble within the cloud—the factor which is negligible in thin bubble-layer clouds.

As mentioned earlier, Kumar and Brennen [24] investigated dynamics of various bubblelayer clouds of finite thickness, which are confined between an oscillatory wall and a fluid medium. They analytically derived the following relation for the natural frequencies of such dynamic systems with a uniform initial void fraction β_0 in the absence of damping mechanisms:

$$\frac{f_n}{f_b} = \left[1 + \frac{3\beta_0 (1 - \beta_0)}{\pi^2 n^2} \left(\frac{L}{R_0}\right)^2\right]^{-\frac{1}{2}}; \quad n = 1, 2, \dots$$
(4.19)

where f_n is the natural frequency of the bubble-layer cloud for the mode n; f_b is the natural frequency of the bubbles within the cloud; and L is the bubble-layer thickness. This means that the bubble-layer cloud, as a dynamic system, has an infinite number of natural frequencies, with the highest one, f_{∞} , tending to the natural frequency of cloud bubbles, f_b . The results provided by Kumar and Brennen [24] show that the first few natural frequencies are dominant while the strength of those which are close to f_b is strongly diminished.

To verify the numerical model developed for bubble-layer clouds with the aid of the conclusions drawn by Kumar and Brennen [24], two numerical setups are considered. In the first one, shown in Fig. 4.23a and analytically evaluated by Kumar and Brennen [24], the bubble-layer cloud is confined by a transducer on the left and a fluid medium on the right. In this setup, the waves generated by the cloud leave the domain from the right open boundary. Since bubble-layer clouds are not always in contact with stimulating sources, it is also of interest to investigate the second setup depicted in Fig. 4.23b, in which the bubble-layer cloud is adjacent to two fluid layers and stimulated by a plane source located in the left fluid medium. The waves generated by this cloud may leave the domain from both the left and

the right open boundaries.

The numerical experiments to find the response of the clouds to signals of various frequencies are organized as follows. The strengths of the transducer and the plane source in both of the setups are set to generate continuous right-running sinusoidal signals with a chosen frequency and the amplitude of 10 kPa in the absence of bubble clouds. In each numerical experiment, the generated single-frequency stimulating signal interacts with the bubble layer, and the simulation continues until a periodic steady state is reached. Then the amplitude of pressure signals is registered at the upstream (S_1) and downstream (S_2) sensors (the recordings are independent from the actual location of the sensors and the plane source in the fluid zones). Then, the stimulation frequency is changed and the same procedure is repeated until a desired range of frequencies is covered. Two bubble-layer thicknesses were considered: L=0.25 mm and L=2.5 mm. For the 0.25-mm-thick cloud the frequency interval is 1 kHz while for the 2.5-mm-thick one it is 2 kHz. In these numerical setups, the bubble-layer clouds contain bubbles with a radius of 10 μ m; the void fraction is 0.01; the grid element size is 83.3 μ m; and the time step is set to 3 ns.

Figure 4.23c illustrates how the thin bubble-layer cloud with the thickness of 0.25 mm reacts to a sinusoidal signal generated by the transducer. According to Eq. (4.19), the first three natural frequencies of this bubble-layer cloud with the same boundary conditions are $f_1 = 195.6$ kHz, $f_2 = 273.8$ kHz, and $f_3 = 301.9$ kHz, matching well with the extremums of the pressure amplitudes recorded at both S_1 and S_2 . The same trends of the frequency responses at both sensors in Fig. 4.23c suggest that signals with the frequencies close to the natural frequencies of the bubble layer can more easily pass through the layer and reach S_2 . In addition, the frequency response at S_1 shows a gradual increase starting from $f_b = 331.9$ kHz, which is the natural frequency of the individual bubbles within the layer. The regime for the stimulation frequencies higher than 331.9 kHz is called super-resonant, in which the bubbles within the cloud are not able to respond fast to the stimulation. As a result, the bubble-layer cloud behaves more stiffly when the stimulation frequency is increased above the natural frequency of the constituting bubbles [24, 38].

In the second setup (Fig. 4.23b), the left boundary is relaxed by replacing the transducer by a fluid layer and stimulating the cloud by a plane source. As shown in Fig. 4.23d, the responses at the sensor S_2 are almost similar to the ones in the first setup, with the peaks

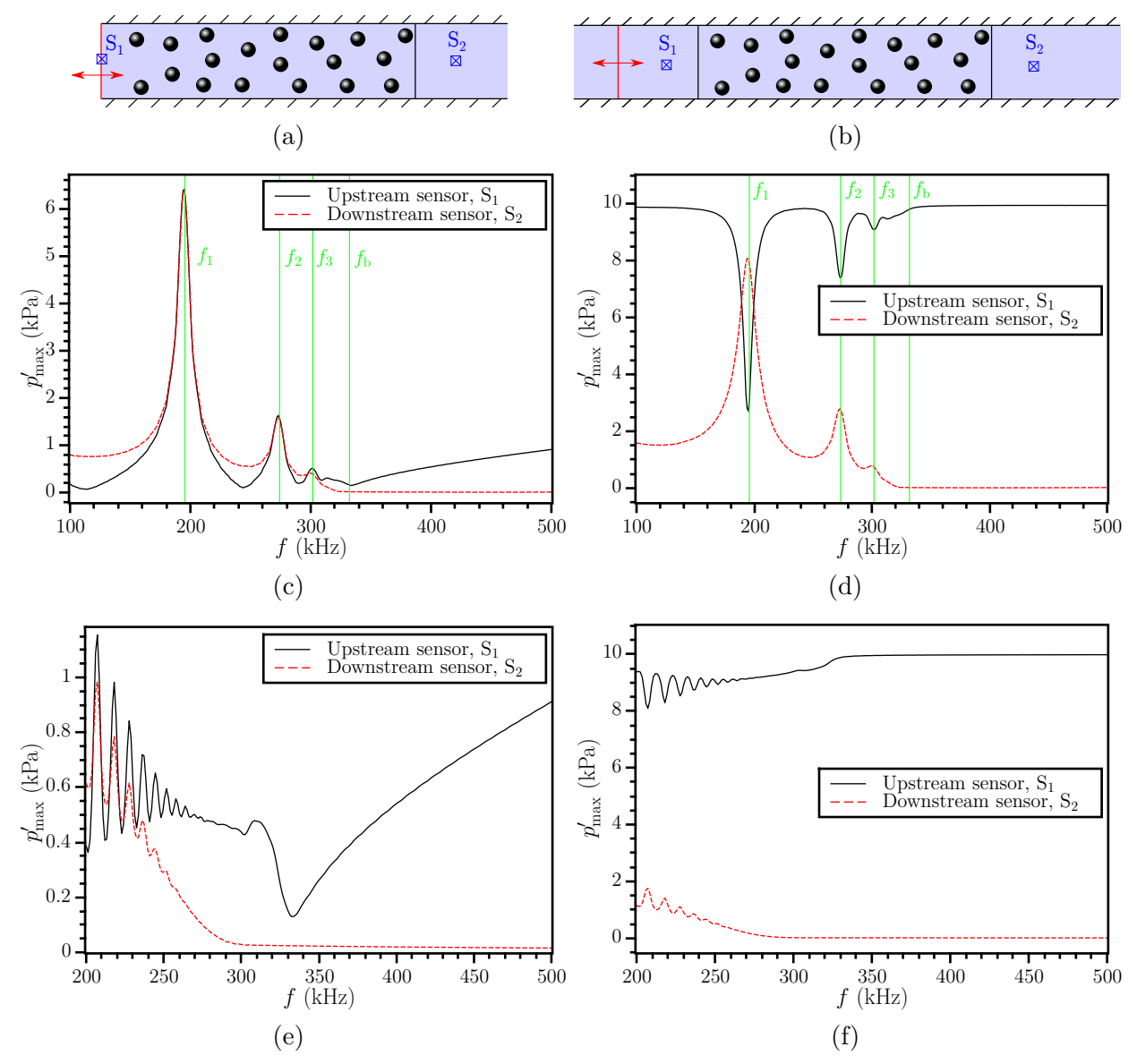


Fig. 4.23. Forced oscillations of two bubble-layer clouds (L=0.25 mm or L=2.5 mm with $R_0=10$ µm, $\beta_0=0.01$): (a) the first setup—stimulation with the transducer, (b) the second setup—stimulation with the plane source. Pressure disturbance amplitudes as a function of the stimulating frequency are plotted for the thin bubble-layer cloud (L=0.25 mm) in (c) the first and (d) the second setups, and for the thick bubble-layer cloud (L=2.5 mm) in (e) the first and (f) the second setups. The data are recorded at the upstream, S_1 , and the downstream, S_2 , sensors. In plots (d) and (f), direct effects of the plane source are excluded from the presented S_1 signals.

occurring at the natural frequencies of the bubble layer. This behavior shows that relaxing the left boundary has no significant impact on the values of the bubble-layer natural frequencies. After excluding direct effects of the plane source to attain pure reflected signals, the pressure amplitudes at S_1 are quite different from the first setup due to changing of the left boundary condition. The frequency responses at S_1 show that the cloud is generally a good acoustic reflector, except for frequencies close to the natural frequencies of the bubble layer. Similarly to the first setup, signals which frequencies are close to the natural frequencies of the bubble layer can more easily pass through the layer and reach S_2 . Hence, the local maximums of the frequency responses at S_2 and the local minimums at S_1 both occur at the natural frequencies of the layer.

To assess the effects of bubble-layer thickness, a bubble-layer cloud with the thickness of 2.5 mm is also evaluated in the two aforementioned setups (Figs. 4.23a and 4.23b). High variations of the frequency responses seen in Figs. 4.23e and 4.23f for the stimulation frequencies in the range of 200–332 kHz are due to the presence of numerous natural frequencies of the bubble layer in this range (the minimum natural frequency of this layer $f_1 = 24.14$ kHz, given by Eq. (4.19), is out of the explored stimulation frequency range). Figures 4.23e and 4.23f depict generally the same behavior for the thick bubble layer as the one seen in Figs. 4.23c and 4.23d for the thin bubble layer: signals with frequencies close to the natural frequencies of the layer can pass through the cloud more easily. Similarly to the thin layer, the thick one also behaves more stiffly when the stimulation frequency increases above the natural frequency of the constituting bubbles (331.9 kHz), as shown in Fig. 4.23e.

Comparing the pressure signals recorded at S_2 in Fig. 4.23, one may notice important behavior of the bubble-layer clouds. Regardless of the values of bubble-layer thickness, the clouds filter out signals with the frequencies above the natural frequency of the constituting bubbles. Hence, this property may be potentially employed to estimate dimensions of bubbles within different clouds.

In real-life applications involving bubbles, their clouds usually consist of bubbles of different sizes. Hence, it is essential to investigate dynamics of such mixed bubble clouds. For this goal, three different clouds with the thickness of 0.25 mm are considered: (1) a cloud consisting of bubbles with the radius of 10 μ m; (2) a cloud containing bubbles with the radii of 10 μ m and 14 μ m; and (3) a cloud which has bubbles with the radii of 10 μ m and 8 μ m.

To make these clouds comparable, it is assumed that all the clouds have the same amount of gas content. In addition, the gas content is equally divided between bubbles with different radii in such a way that the total volume fractions of these clouds would be 0.01. Therefore, the second and the third clouds have two bubble sets with the volume fraction of 0.005 for each set. Other simulation properties and the procedure of numerical experiments are the same as those for the mono-disperse clouds discussed above in relation to the results shown in Fig. 4.23. Similarly, the grid element size and the time step are set to 83.3 µm and 3 ns, respectively. This simulation sketch is shown again in Fig. 4.24a.

Having two bubble sets in a bubble-layer cloud, i.e., two dynamic systems which non-linearly interact, one can expect a mixed and complicated frequency response, particularly in the trans-resonant regime. Nevertheless, some useful information can be extracted from the frequency response curves. Figure 4.24b compares frequency responses of the three described clouds at the upstream sensor, S_1 . To better discuss and compare the results, the natural frequencies of some relevant mono-disperse clouds with different bubble sizes and void fractions are provided in Table 4.3.

Table 4.3. Natural frequencies of individual bubbles (f_b) and three mono-disperse bubble-layer clouds (L = 0.25 mm) with different void fractions, obtained from Eq. (4.19).

	$R_0 = 8 \ \mu \text{m}$	$R_0 = 10 \ \mu \mathrm{m}$	$R_0 = 14 \ \mu \mathrm{m}$
$f_{ m b}~({ m kHz})$	420.1	331.9	233.7
$f_1 - f_3$ (kHz) for $\beta_0 = 0.005$	266.9	238.0	192.0
	359.0	298.5	220.8
	389.4	315.8	227.7
$f_1 - f_3$ (kHz) for $\beta_0 = 0.01$	211.7	195.6	166.9
	319.0	273.8	209.9
	364.7	301.9	222.1

In the trans-resonant regime, as demonstrated in Fig. 4.24b, a number of peaks in the pressure amplitude curves are observed. It is to be noted that for the second and third clouds, i.e., the clouds with mixed composition, the first, the second, and even the third pressure amplitude peak correspond to frequencies which are between the first, second, and third natural frequencies, respectively, of mono-disperse clouds consisting of bubbles with the same radii and having the same void fraction $\beta_0 = 0.01$ and thickness L = 0.25 mm. For example,

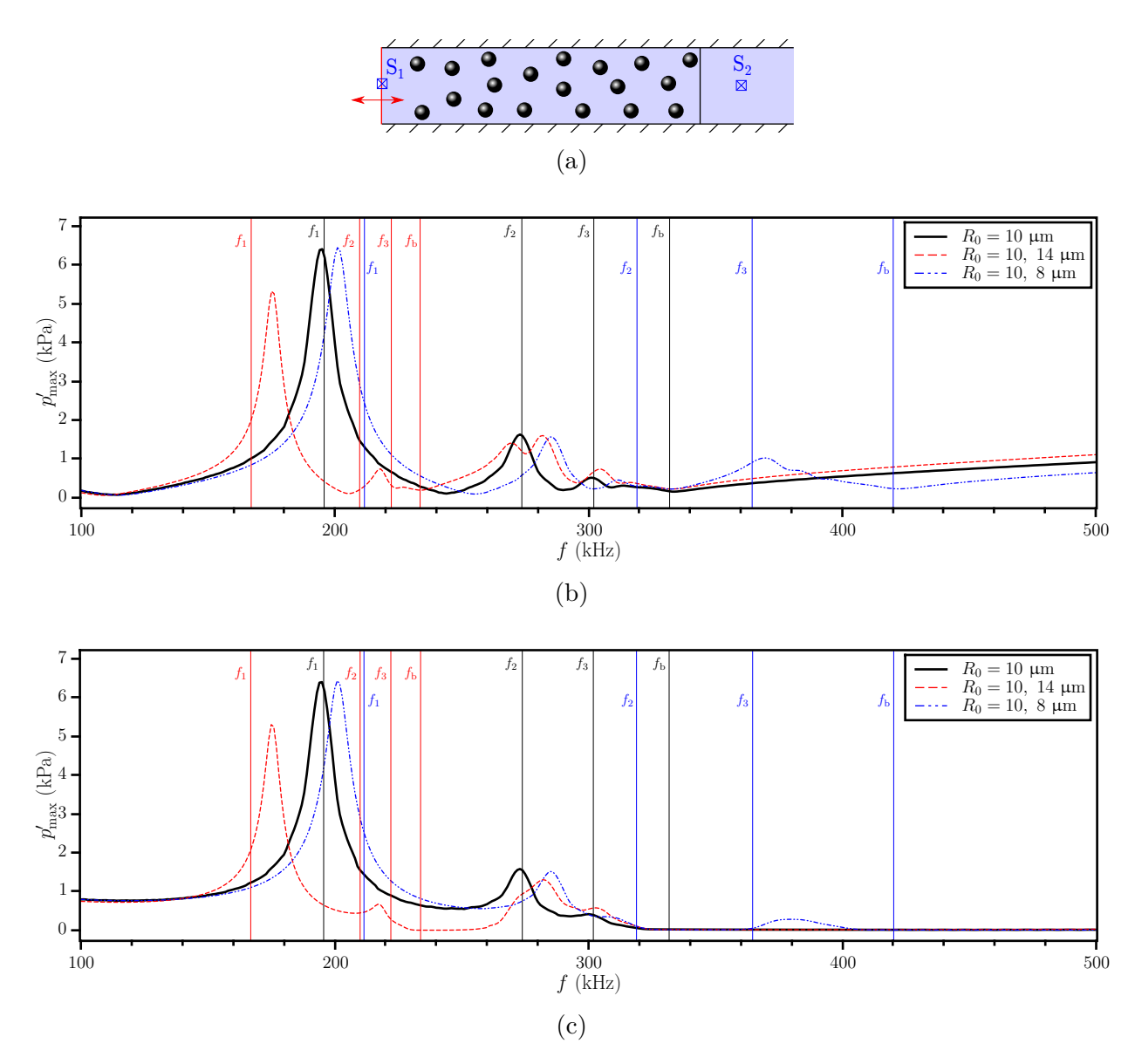


Fig. 4.24. Forced oscillation of three bubble-layer clouds (L=0.25 mm, $β_0=0.01$) with different bubble sizes simulated by periodic sinusoidal signals with the amplitude of 10 kPa and the frequency f: (a) the simulation sketch including the bubble layer, the stimulating transducer, and the sensors. Pressure disturbance amplitudes for various incident-signal frequencies at (b) the upstream, S_1 , and (c) downstream, S_2 , sensors. The first three natural frequencies (f_1 , f_2 , f_3) of the mono-disperse bubble-layer clouds (L=0.25 mm, $β_0=0.01$) with $R_0=8$ μm, 10 μm, and 14 μm and the natural frequencies (f_b) of their constituting bubbles are shown as the blue, black, and red vertical lines, respectively.

for the second cloud consisting of bubbles with the radii of 10 μ m and 14 μ m, although each of its bubble sets has the void fraction of 0.005, the first pressure amplitude peak at 175 kHz, which may be interpreted as the minimum natural frequency of the whole cloud f_1 , occurs between 166.9 kHz and 195.6 kHz. These two frequencies are the first natural frequencies f_1 of the mono-disperse clouds with the bubble radius of 14 μ m and 10 μ m, respectively, and the void fraction of 0.01 (see Table 4.3).

The analysis of the trans-resonant regime of this complex nonlinear dynamic system is complicated but a very rough estimate of f_1 for a mixed-composition cloud could be obtained by introducing an average bubble radius in the cloud, $R_{\rm av}$, based on the numbers of bubbles of each radius in the cloud and using this value in Eqs. (2.48) and (4.19). For the second cloud (10 µm and 14 µm bubbles) this results in $R_{\rm av} = 11.07$ µm and $f_1 = 187$ kHz, which is in reasonable agreement with the numerically determined first peak location at 175 kHz. The same observation can also be made for the third cloud, consisting of bubbles with the radii of 10 µm and 8 µm: the first pressure amplitude peak is observed at 201 kHz, between 195.6 kHz and 211.7 kHz—the first natural frequencies of 10 µm and 8 µm mono-disperse clouds, respectively. The above-mentioned average-radius approach yields $f_1 = 206.1$ kHz—the agreement with the numerical 201 kHz value is better due to lower difference in bubble radii.

Another noticeable feature which can be observed in Fig. 4.24b is the stiffening behavior which manifests itself in the gradual pressure increase above a certain frequency. It begins from the highest natural frequency of the individual bubbles, which is 331.9 kHz for the first two and 420.1 kHz for the third cloud. The filtering property is clearly seen in Fig. 4.24c, where the frequency responses at the downstream sensor (S_2) are depicted. For the second cloud, consisting of 14 μ m and 10 μ m bubbles, there is a significant decrease in the amplitudes of the pressure signals after reaching the frequency of 233.7 kHz, which is the natural frequency f_b of the bubbles with the radius of 14 μ m. After some rise due to oscillating modes of bubbles with the radius of 10 μ m, another noticeable decrease is observed at 331.9 kHz—the natural frequency f_b of 10 μ m bubbles. The third cloud also shows the same behavior with two filtered frequency ranges, starting almost at the natural frequency f_b of bubbles with the radii of 10 μ m and 8 μ m. The results provided in Fig. 4.24 show that analyzing data recorded at both the upstream and the downstream sensors would be of help to estimate bubble size dimensions in different bubble clouds.

To assess effects of such factors as dissipation and non-linear mechanisms of the bubble dynamics, free oscillations of a thin bubble-layer cloud with the thickness of 0.25 mm, the initial void fraction of 0.01, and 10 μ m-radius bubbles are evaluated. Under the numerical setup shown in Fig. 4.25a, which is the same as Fig. 4.23b, this bubble layer is subjected to a one-wavelength sinusoidal signal with the frequency of 100 kHz and the amplitude P. The signals generated by this cloud are recorded at the sensor S₁. Both the plane source and the sensor are located 1 cm away from the center of the bubble-layer cloud. In this simulation, the grid element size and the time step are set to 83.3 μ m and 3 ns, respectively. Figure 4.25b compares frequency spectra of the recorded data for different stimulation strengths and fluid viscosities. As depicted, the natural frequencies are accentuated as peaks in the frequency spectra, and their values agree well with those provided by the analytical relation (4.19) (see the vertical lines in Fig. 4.25b). Some difference may be due to the lack of time for the cloud to fully respond to the stimulation (in the present simulation a final periodic steady

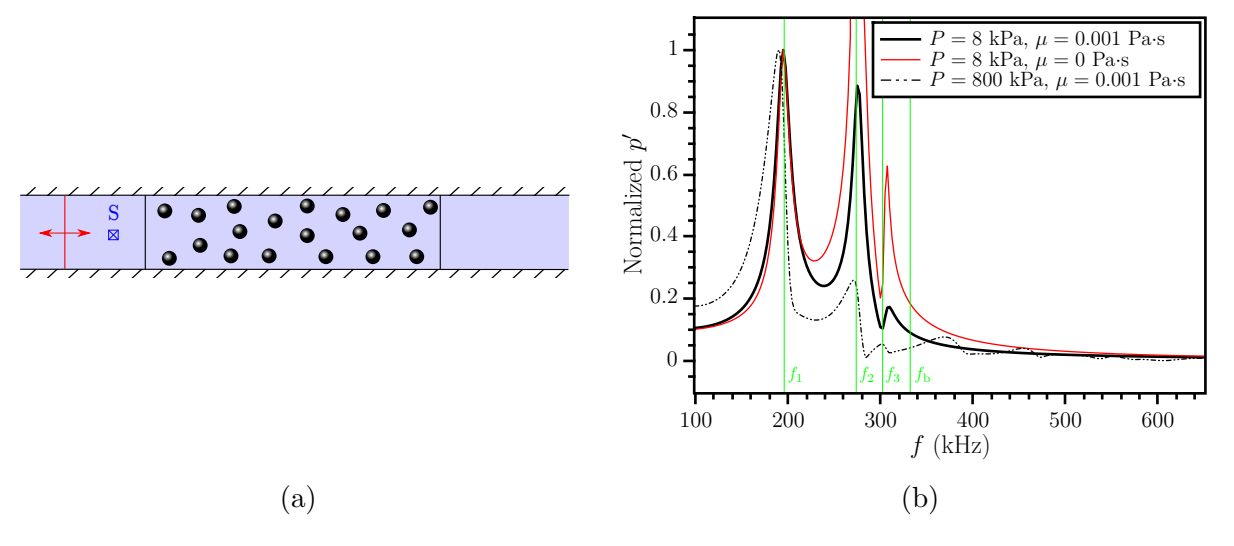


Fig. 4.25. Free oscillation of a bubble-layer cloud (L=0.25 mm, $\beta_0=0.01$, $R_0=10$ µm) stimulated by a one-wavelength sinusoidal signal with the frequency of 100 kHz and the amplitude P: (a) the simulation sketch including the cloud, the sensor S, and the plane source shown in red; and (b) frequency spectra of the pressure disturbances (0.1 ms < t < 0.5 ms) emitted by the bubble-layer cloud for different medium viscosities, μ , and different stimulation strengths, P. The results are normalized by the pressure value at the minimum natural frequency, f_1 .

state is not reached, as opposed to the previously discussed forced stimulation cases). These frequency spectra show that viscosity of the fluid, which is the main damping mechanism, has no significant impact on the value of the natural frequencies. However, their strengths in the spectra are decreased due to dissipation processes, which is more evident for higher frequencies.

In order to see the influence of non-linear aspects of the bubble dynamics, the amplitude of the incident one-wavelength sinusoidal signal is increased to become 800 kPa. It is assumed that no cavitation occurs, and the medium flow regime is still linear. Although the pressure changes in this case are quite high, the bubbles within the cloud do not have sufficient time to become unstable. As illustrated in Fig. 4.25b, the natural frequencies are almost the same as those in the case of low intensity stimulation. However, a number of additional modes with higher frequencies are detected, which are due to non-linear responses of the individual bubbles within the cloud.

To investigate how non-linearities of the medium flow affect the bubble dynamics, the numerical setup illustrated in Fig. 4.23a is employed with the same physical properties and the same numerical experiment procedure as for the results shown in Fig. 4.23, except that the fluid is allowed to behave non-linearly with the non-linear power exponent $\gamma=6$ (see Section 2.3 and [74, 119]). The simulation sketch is illustrated again in Fig. 4.26a, where the transducer's strength is set to generate right-running sinusoidal signals with the amplitude of 10 kPa in the absence of the bubble cloud. The grid element size and the time step are also set to 83.3 μ m and 3 ns, respectively. These signals interact with a thin bubble-layer cloud (L=0.25 mm) with the initial void fraction of 0.01 and individual bubbles with the radius of 10 μ m. Figure 4.26 shows that the frequency response at the upstream and downstream sensors are not significantly affected by the non-linearity of the fluid flow.

To accentuate the non-linear character of the fluid flow, the strength of the transducer in the previous test case is increased tenfold, to be 100 kPa. The pressure disturbances are recorded at the upstream sensor S for the stimulation frequency of 200 kHz in the linear and weakly non-linear fluid flow regimes. The simulation sketch is demonstrated in Fig. 4.27a, where the grid element size and the time step are set to 83.3 μ m and 3 ns, respectively. Although the excitation in this case is rather strong, the results for the weakly non-linear regime do not substantially deviate from those for the linear regime, as shown in Fig. 4.27b.

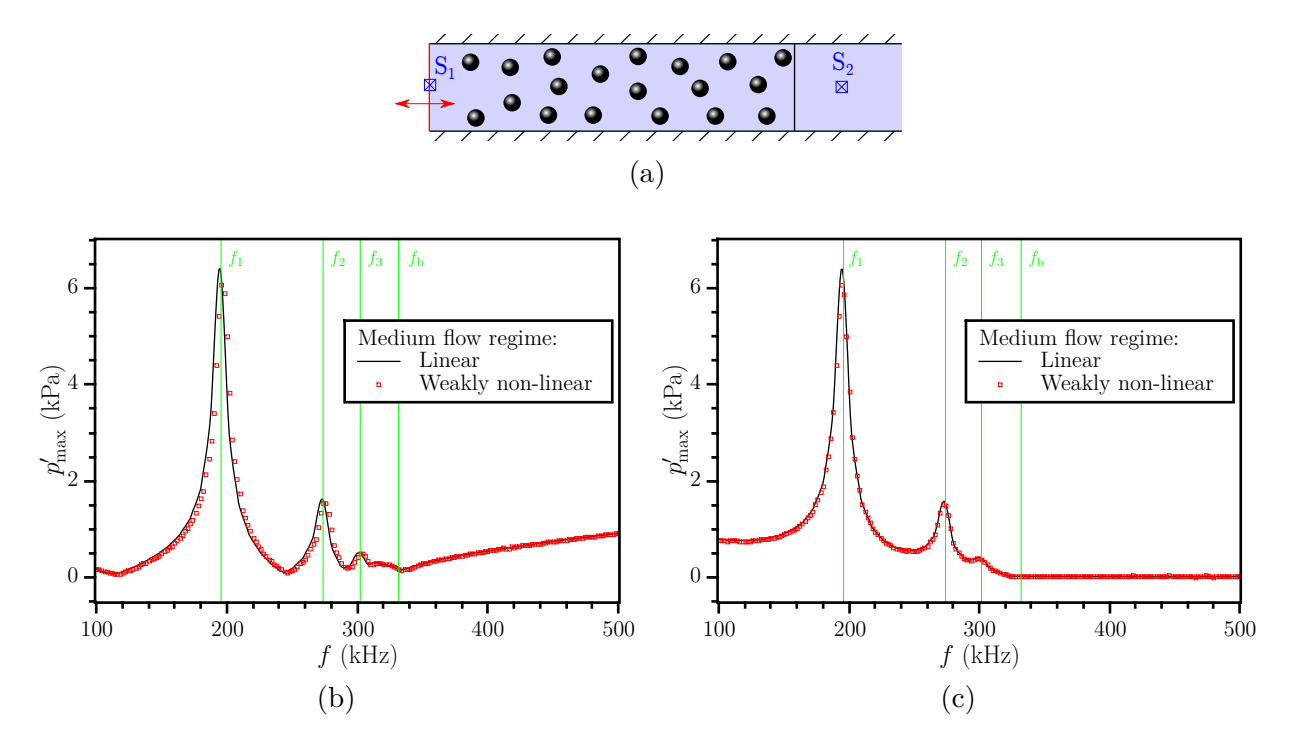


Fig. 4.26. Forced oscillations of a bubble-layer cloud (L = 0.25 mm, $β_0 = 0.01$, $R_0 = 10$ μm) under moderate stimulation by periodic sinusoidal signals with the amplitude of 10 kPa and the frequency f for the linear and weakly non-linear medium flow regimes: (a) the simulation sketch including the bubble layer, the stimulating transducer, and the sensors. Pressure disturbance amplitudes for various stimulating frequencies at (b) the upstream, S_1 , and (c) the downstream, S_2 , sensors. The strength of the transducer is the same for both of the flow regimes.

Hence, it appears that non-linear features of the medium flow do not play a significant role in this case. However, regardless of the medium flow regime, this strong excitation noticeably populates a number of non-linear modes of the bubble layer with quite low frequencies.

These long-lasting natural modes under the strong forced stimulation are better observed in Fig. 4.27c, where the upper and lower envelopes of the pressure signals recorded at S are provided. These modes need more time to diminish; as a result, obtaining the frequency response curves, which requires to achieve a final periodic steady state, is quite time-consuming. Comparison of the pressure signals recorded at S for the linear and weakly non-linear flow regimes in Fig. 4.27c shows that, even after a very long time, contributions of non-linearity

of the medium flow are not substantial. The results provided in Figs. 4.25b, 4.26 and 4.27 suggest that the bubble cloud dynamics is more affected by non-linear features of the bubble oscillations than the medium flow non-linearities. Hence, in the current numerical model, the non-linear KM equations (2.47) are considered regardless of the medium flow regime, which might be either linear or weakly non-linear.

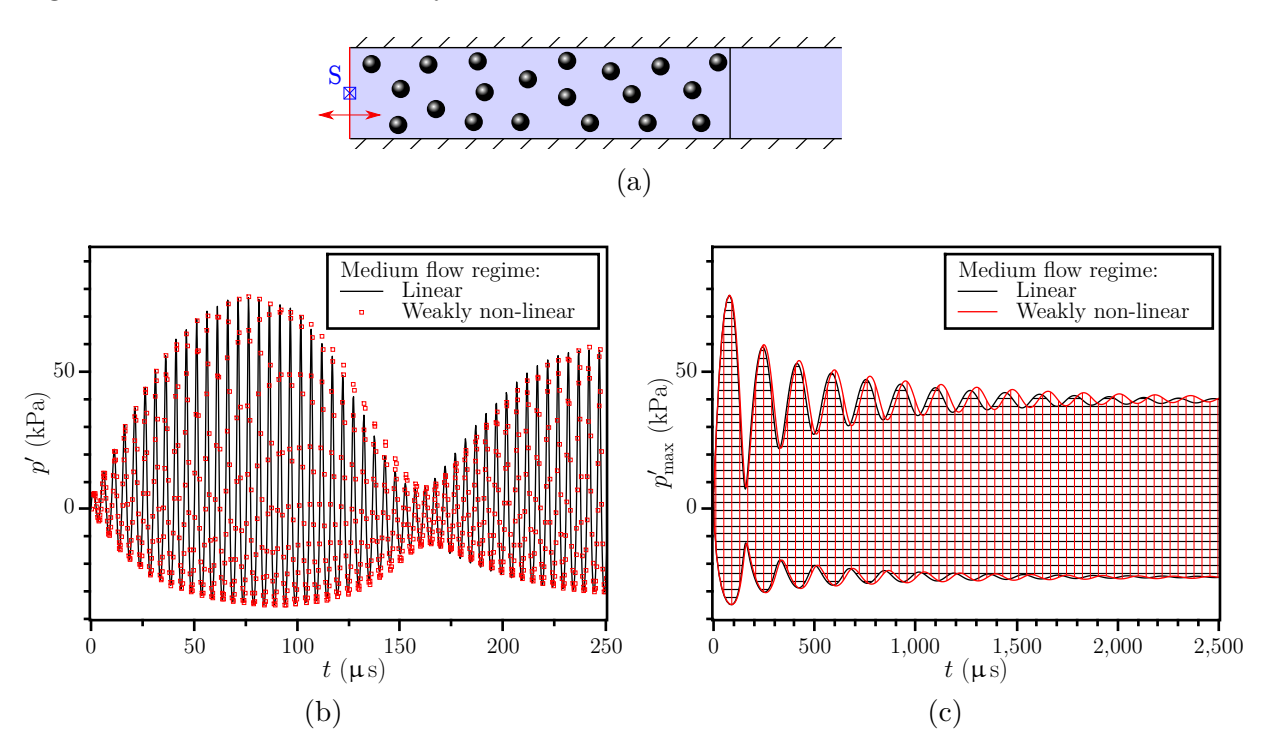


Fig. 4.27. Strong stimulation of a bubble-layer cloud (L=0.25 mm, $\beta_0=0.01$, $R_0=10$ µm) under strong stimulation by a periodic sinusoidal signal with the amplitude of 100 kPa and the frequency of 200 kHz for the linear and weakly non-linear fluid flow regimes: (a) the simulation sketch including the bubble layer, the stimulating transducer, and the sensor; (b) pressure disturbances for $0 \le t \le 250$ µs; and (c) the upper and lower pressure signal envelopes for $0 \le t \le 2500$ µs; both at the upstream sensor, S.

4.1.10 Spherical Bubble Clouds

In this subsection, spherical bubble clouds in axisymmetric domains (Fig. 2.2d) are assessed. The proposed numerical model is investigated by comparing the numerical results with the

available data in the literature.

d'Agostino and Brennen [38] analyzed the dynamics of spherical bubble clouds confined by a fluid medium and reported their natural frequencies in the absence of damping mechanisms as follows:

$$\frac{f_n}{f_b} = \left[1 + \frac{3\beta_0 (1 - \beta_0)}{\pi^2 (n - 0.5)^2} \left(\frac{A_0}{R_0}\right)^2\right]^{-\frac{1}{2}}; \quad n = 1, 2, \dots$$
(4.20)

where f_n is the natural frequency of the spherical bubble cloud for the mode n; f_b and R_0 are the natural frequency and the initial radius of the constituting bubbles, respectively; A_0 is the spherical bubble cloud radius; and β_0 is the initial void fraction.

The problem setup is shown in Fig. 4.28a. A small spherical bubble cloud with the radius of 0.5 mm, the initial void fraction of 0.005, and 10 μ m bubbles is surrounded by a fluid medium. To stimulate this cloud, a spherical shell with the radius of 0.75 mm (the red sphere in Fig. 4.28a) generates mono-frequency sinusoidal disturbances in the frequency range of 150–500 kHz. The stimulation frequency is changed with the interval of 1 kHz, and at each particular stimulation frequency the computation proceeds until a periodic steady state is reached. The stimulator induces a mass flow rate with the amplitude of $9 \pi \times 10^{-6}$ kg/s across the spherical shell. The minimum grid size element and the time step in this simulation are set to 0.125 mm and 5 ns, respectively. Since this model is axisymmetric, a 30° circular sector is modeled with symmetric boundaries. The employed geometry along with the numerical mesh and the shell source are shown in Fig. 4.28b.

Figures 4.28c and 4.28d show the frequency responses at the sensors S₁ and S₂. The natural frequencies of the spherical bubble cloud from Eq. (4.20) are shown as vertical lines (the respective values are 202.8 kHz, 262.0 kHz, 290.2 kHz, and 304.7 kHz). The agreement with the pressure amplitude peaks observed in Figs. 4.28c and 4.28d is quite satisfactory for lower frequencies. The deviations at higher frequencies may be attributed to at least two factors. First of all, damping mechanisms may slightly change the natural frequencies as reported by d'Agostino and Brennen [38]. More importantly, the analytical study by d'Agostino and Brennen [38] relies on a condition for the flow field in the fluid surrounding the cloud, which is very difficult to reproduce in numerical simulations, and hence the analytically and numerically studied dynamic bubble systems are not fully identical. As seen in Fig. 4.28d,

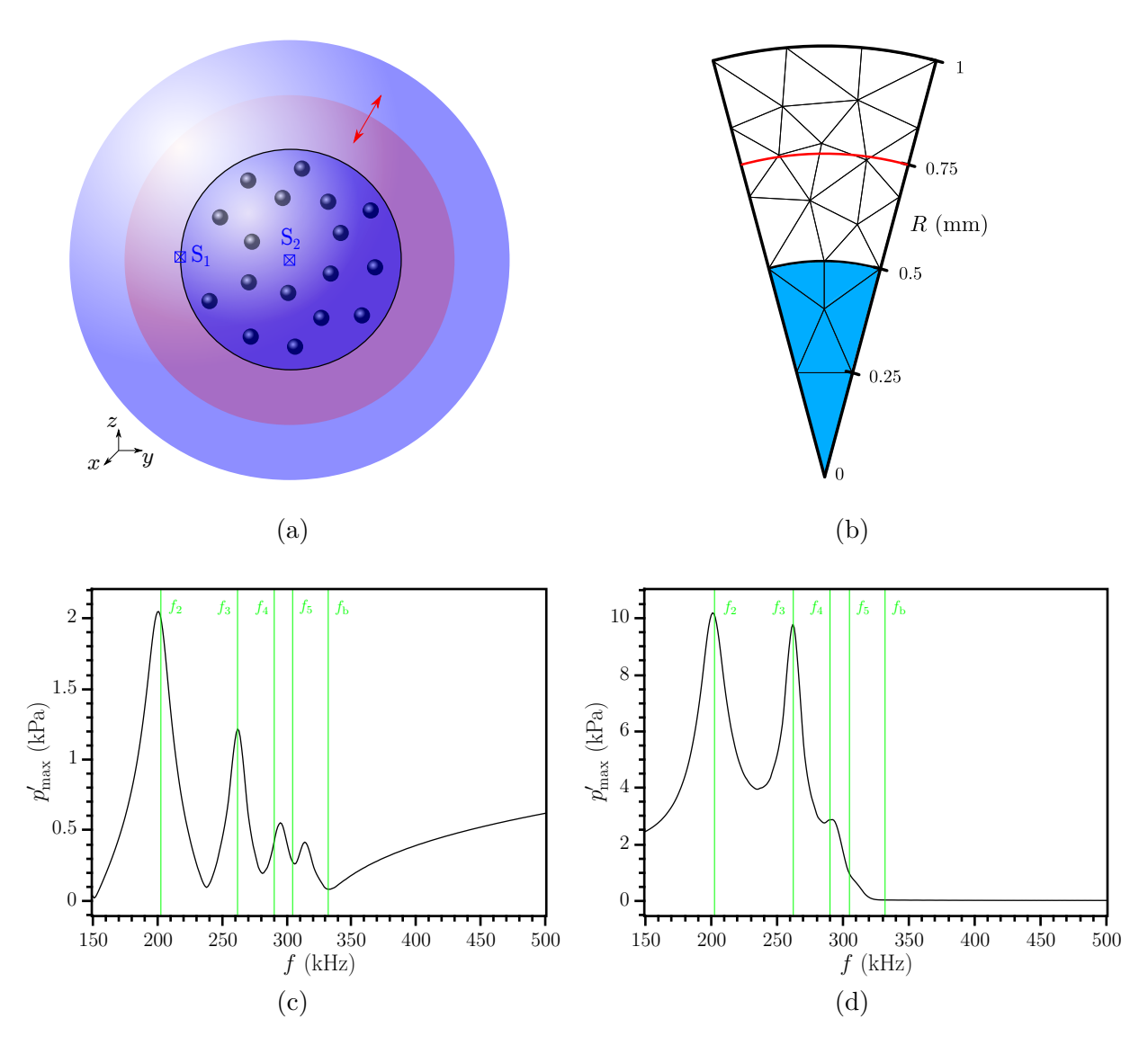


Fig. 4.28. Forced oscillations of a spherical bubble cloud ($A_0 = 0.5$ mm, $\beta_0 = 0.005$, $R_0 = 10$ µm) stimulated by periodic signals with the frequency f: (a) the simulation sketch including the spherical bubble cloud, the sensors, and the stimulating spherical shell shown as a red sphere; (b) the numerical mesh, which is a 30° circular sector; frequency responses at (c) the sensor S_1 located at the cloud boundary and (d) the sensor S_2 located at the cloud center.

a filtering effect is observed for the stimulation frequencies above 331.9 kHz, which is the natural frequency f_b of the individual bubbles within this cloud. In other words, signals with frequencies higher than 331.9 kHz can hardly penetrate into this bubble cloud, which results in low signal strengths at S_2 . In addition, for frequencies higher than f_b , the stiffening behavior leads to a gradual increase in the signal strengths at S_1 , as illustrated in Fig. 4.28c.

4.2 WPC Processes

The previous section demonstrates that the proposed numerical model is capable of accurately and reliably simulating acoustic wave propagation within different fluid flow regimes, solid media, and bubbly zones. In the present section the proposed numerical model is applied to the simulation of the WPC phenomenon, when the speeds of sounds in the conjugator are modulated by the applied magnetic field based on Eqs. (2.2), and, as a result, the term \boldsymbol{H} in Eqs. (2.17) is no longer zero. In this section, first, simple paraxial setups are considered to verify the numerical modeling of the modulation process in Section 4.2.1. In these cases, effects of the material acoustic impedances and the conjugator length are assessed. Then, full simulations of the WPC process in axisymmetric domains are carried out in Section 4.2.2.

4.2.1 Paraxial WPC

Merlen et al. [52] provided the analytical relations for the paraxial WPC, which are convenient to use for verification of the solver with the presence of the modulation phenomenon. The problem setup and initial conditions are shown in Fig. 4.29a. To investigate effects of acoustic impedance, two different paraxial cases are simulated under the linear fluid flow regime: a) the conjugator is surrounded by water; b) the left-hand-side fluid is water and the right-hand-side one is mercury. These two fluids are chosen due to the considerable difference in their acoustic impedances. The physical properties of the materials and the simulation parameters are provided in Table 4.4, as suggested by Bou Matar et al. [73] for the solid zone (conjugator). The total length of the computational domain is 4 cm, and the conjugator is 2 cm long. In both cases, the fluid-solid interfaces are located at z = 1 cm and z = 3 cm. The boundaries at z = 0 and z = 4 cm are set to be absorbing ones (due to the normal interaction of acoustic

waves with the boundaries it is not necessary to use an NPML layer there). As illustrated in Fig. 4.29a, a right-running initial stimulation with the frequency of 3 MHz starting from z = 1 cm and extending for three wavelengths to z = 1.6 cm is applied as follows:

$$\sigma_{zz} = \sin(1000 \,\pi \,(z - 0.01)) \text{ kPa}; \quad 0.01 \text{ m} \le z \le 0.016 \text{ m},$$
(4.21a)

$$v_z = -\frac{10^{-4}}{3}\sin(1000 \,\pi \,(z - 0.01)) \,\frac{\mathrm{m}}{\mathrm{s}}; \quad 0.01 \,\mathrm{m} \le z \le 0.016 \,\mathrm{m}.$$
 (4.21b)

A section of the numerical mesh around the left interface (z = 0.01 m) is shown in Fig. 4.29b, where the grid size and the time step are 66 μ m and 1 ns, respectively.

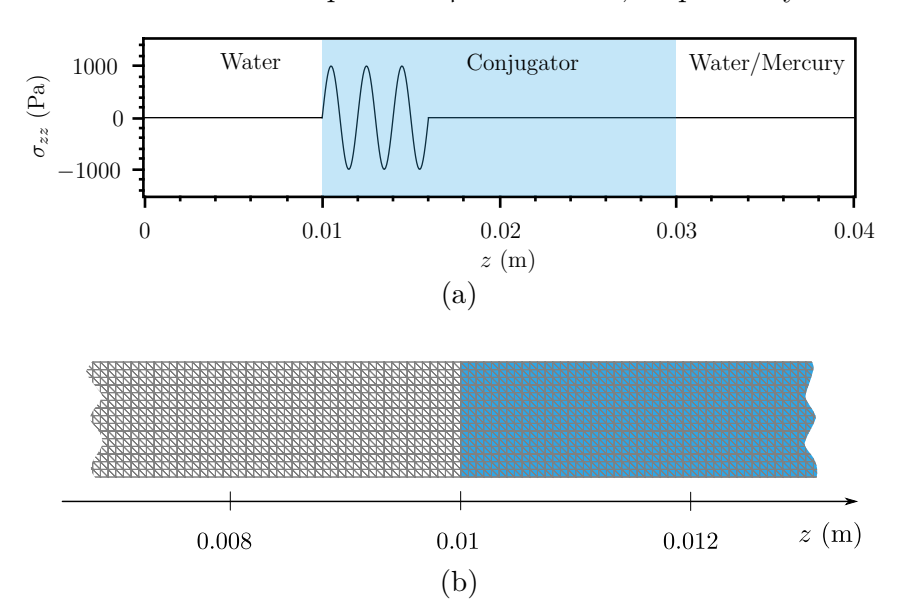


Fig. 4.29. Paraxial WPC simulations: (a) the numerical setup and the initial right-running stimulation within the conjugator and (b) a section of the numerical mesh around the left interface located at z = 0.01 m.

As shown in Fig. 4.30, the initial signal with the amplitude of 1 kPa is significantly amplified due to modulation of the elastic properties. In both cases, satisfactory correspondence with the analytical results is found. The comparison of Figs. 4.30a and 4.30b clearly shows that closer material impedances on the right-hand interface for the water-solid-mercury case facilitate evacuation of the acoustic energy, which results in a different pressure disturbance envelope with lower extremums within the conjugator.

Table 4.4. Parameters of the paraxial WPC setup shown in Fig. 4.29a for investigating material impedances.

Parameter	Value
Modulation depth M	0.1
Modulation frequency Ω (MHz)	6
Modulation duration (µs)	20
Length of active region (cm)	2.0
Density ρ_0 , solid $\left(\frac{\text{kg}}{\text{m}^3}\right)$	5000
Bulk modulus K_0 , solid (Pa)	7.33×10^{10}
Poisson's ratio, solid	0.1
Density ρ_0 , water $\left(\frac{\text{kg}}{\text{m}^3}\right)$	1000
Bulk modulus K_0 , water (Pa)	2.25×10^9
Density ρ_0 , mercury $\left(\frac{kg}{m^3}\right)$	13870
Bulk modulus K_0 , mercury (Pa)	27.97×10^9

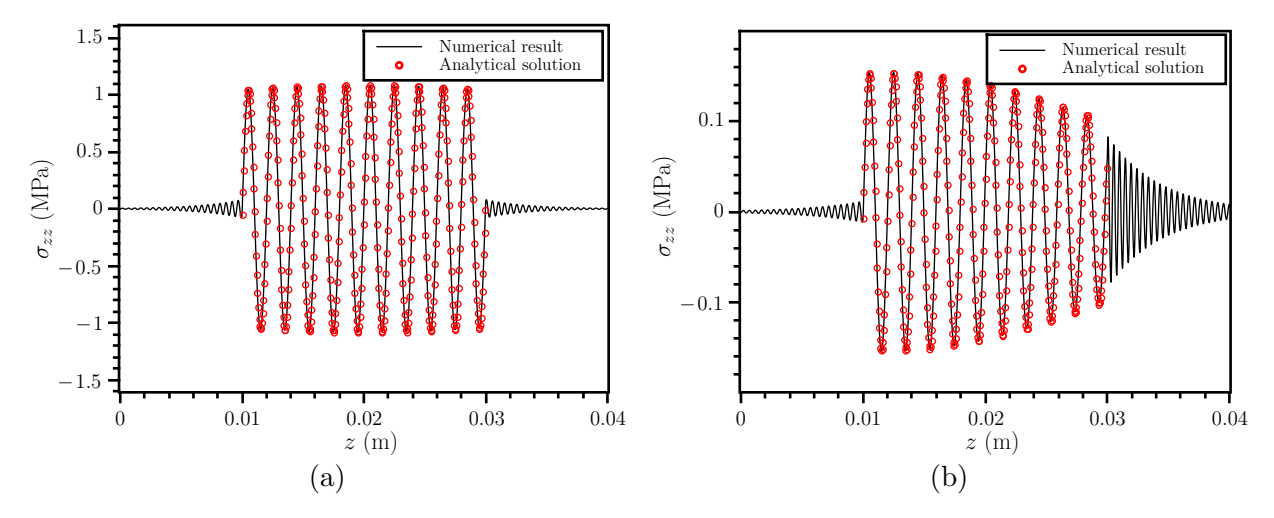


Fig. 4.30. Distributions of the axial stress σ_{zz} in the paraxial WPC: (a) water-solid-water and (b) water-solid-mercury cases at $t = 20 \mu s$ along the axis.

Merlen et al. [52] also showed analytically that the amplification process in the conjugator strongly depends on the ratio of the conjugator length to the signal wavelength. Since this finding is relevant to the present study, two paraxial WPC cases with different conjugator lengths are considered as the next test problem. In the first case, the conjugator length

 $(L=36~{\rm cm})$ is an even multiple of $\lambda_{\rm s}/4$, where $\lambda_{\rm s}$ is the signal wavelength within the conjugator. In the second case, the conjugator length $(L=36.75~{\rm cm})$ is an odd multiple of $\lambda_{\rm s}/4$. In both cases, the conjugator is surrounded by fluid zones with the length of 1.5 cm filled with water, as illustrated in Fig. 4.31a. The left boundary of the computational domain (see Fig. 4.31a) serves initially as a transducer sending a one-wavelength sinusoidal signal with the frequency of 200 kHz (corresponding to the signal wavelength $\lambda_{\rm s}=3~{\rm cm}$ in the conjugator, where the longitudinal speed of sound is 6000 m/s) and the amplitude of 10 kPa to stimulate the conjugator. It becomes an absorbing boundary at $t=5~{\rm \mu s}$. The simulation parameters and the physical properties for these two cases are provided in Table 4.5. In these setups, the signals propagating within the left-hand side fluid zone are called conjugate waves, and those propagating in the right-hand side fluid zone are denoted as direct waves. The grid size and the time step for both cases are 1 mm and 0.01 ${\rm \mu s}$, respectively.

Table 4.5. Parameters of the paraxial WPC setup shown in Fig. 4.31a for investigating the conjugator length.

Parameter	Value
Conjugator length [Even case] (cm)	36
Conjugator length [Odd case] (cm)	36.75
Modulation depth	0.1
Modulation frequency (kHz)	400
Density, solid $\left(\frac{\text{kg}}{\text{m}^3}\right)$	5000
Bulk modulus, solid (Pa)	7.33×10^{10}
Poisson's ratio, solid	0.1
Density, water $\left(\frac{\text{kg}}{\text{m}^3}\right)$	998
Bulk modulus, water (Pa)	2.2455×10^{9}

Figures 4.31b and 4.31c compare the analytical solution for the axial stress (σ_{zz}) distribution with the numerical results in the even and odd cases at two different time moments, when the wave propagation is fully controlled by the modulation process. The agreement between the analytical and numerical data is quite satisfactory. One may notice different signal profiles in the odd and even cases. To compare the amplification processes in the even and odd cases, a sensor is placed in the middle of the left-hand-side fluid zone (at z = -7.5 mm), and its readings are plotted in Fig. 4.32. Figure 4.32 shows that the odd case

has much lower pressure gain compared to the even one, which is in accordance with the analytical study by Merlen et al. [52].

The reason for such different behaviors is that there are two factors in these cases which affect the amplification feature. First, the energy supplied by the electromagnetic field stimulates the direct and conjugate signals, which propagate within the conjugator. Second, the generated direct and conjugate waves reflect at the boundaries and propagate back into the conjugator. These reflected signals might contribute to the amplification process either positively or negatively, depending on how their phases match with that of the waves generated by the electromagnetic field. Hence, changing the conjugator length by very small

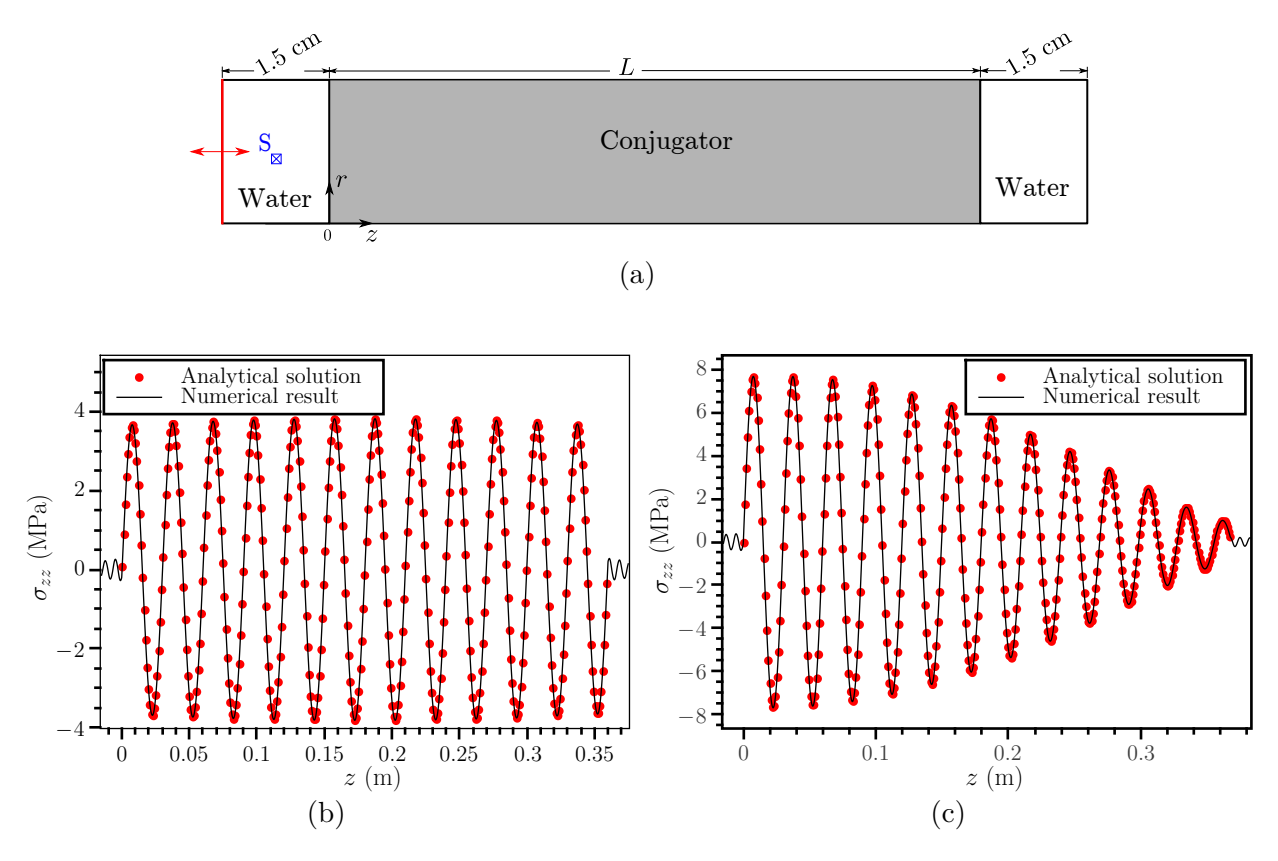


Fig. 4.31. Effects of the conjugator length on the modulation process for the paraxial WPC: (a) schematic of the computational domain (not to scale). The left boundary (shown in red) is the transducer which becomes an absorbing boundary at $t = 5 \mu s$. Axial stress distributions for (b) the even case at $t = 300 \mu s$ and (c) the odd case at $t = 500.5 \mu s$.

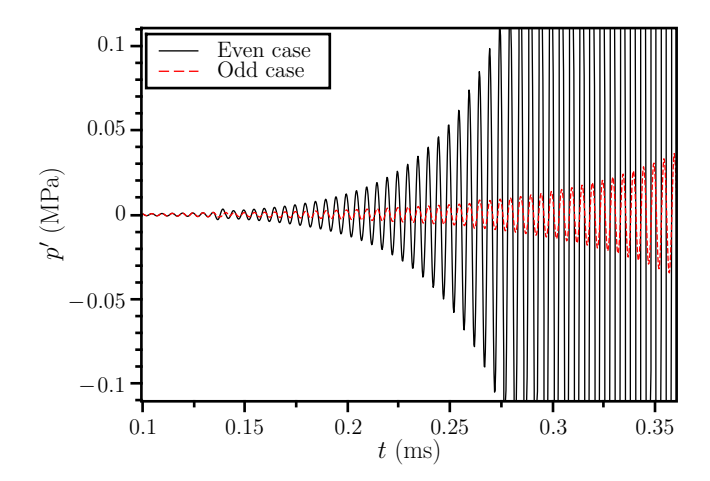


Fig. 4.32. Amplification process in the paraxial WPC: pressure disturbance recorded in the middle of the left hand-side fluid zone (at z = -7.5 mm) for the even and odd cases.

value can have significant effect on the amplification process due to the variations of the signal phases. Compared with the even one, this feature adversely affects the pressure gain in the odd case. Thus, it can be concluded that the present WPC simulator faithfully reproduces the influence of the conjugator-length/signal-wavelength ratio.

4.2.2 Axisymmetric WPC

Full simulations of the WPC process in an axisymmetric domain for both linear and non-linear regimes are then carried out using the setup shown in Fig. 4.33a. The length of the conjugator and its radius are 2 cm and 1 cm, respectively, and the conjugator is surrounded by water. The densities, Poisson's ratios, and bulk moduli of the conjugator and the surrounding medium are the same as those in the paraxial case provided in Table 4.4. In the non-linear fluid flow regime, the parameter γ in Eq. (2.22b) is set to 6 [82]. The modulation properties of the conjugator for both linear and non-linear regimes are given in Table 4.6.

As shown in Fig. 4.33a, the coordinate origin is located on the axis at the left end of the conjugator. The physical domain is wrapped in an NPML zone with the thickness of 1 mm and the parameter σ_{max} of 3×10^6 . The NPML zone prevents contamination of the computational domain with spurious reflected signals and allows to place the outer boundaries

just 3 mm away from the conjugator.

A 4-mm-radius flat focusing transducer with the nominal focal length of 6 mm is located at the boundary which is 1 cm away from the conjugator. This transducer stimulates the normal velocity at the boundary according to the following relation:

$$v_z = A \cdot \exp\left(-1.5 \times 10^{12} \cdot \left(t - 2 \times 10^{-6}\right)^2\right) \cdot \sin\left(2\pi f\left(t - 2 \times 10^{-6}\right)\right),\tag{4.22}$$

where f is the carrier frequency equal to 3.5 MHz, and time t is in seconds. This stimulated axial velocity is also illustrated in Fig. 4.35a. In the linear regime, the parameter A is set to 4 mm/s, and in the non-linear regime, it is increased 100 fold. The transducer emits the signal during 10 μ s from the start of the simulation. During this time period, the NPML zone is not activated so that it would not interfere with the incident signal. After 10 μ s, the transducer is switched off; its boundary is treated as an absorbing boundary for the rest of the simulation; and the NPML zone is activated.

Table 4.6. Modulation parameters of the axisymmetric WPC setup shown in Fig. 4.33a.

Parameter	Linear	Non-linear
Modulation depth M	0.1	0.1
Modulation frequency Ω (MHz)	7	14
Modulation starting moment (µs)	8.0	8.0
Modulation duration (µs)	22.3	9.0

In order to set an appropriate element size for the numerical mesh, grid independence studies are conducted. The pressure disturbance profiles along the axis in front of the conjugator ($-3.5 \le z \le 0.0$ mm) are shown in Fig. 4.34 for three successively refined grids in the linear (at $t \approx 30.3$ µs) and non-linear (at $t \approx 17$ µs) regimes. At these time moments, the wave propagation has been fully controlled by the modulation process, and the exponential amplification has taken place. Since the results show no appreciable changes after the last refinement step, the minimum grid element size is set to 0.1 mm and 0.05 mm for the linear and non-linear regimes, respectively. The coarsest numerical mesh with the grid element size of 0.2 mm is depicted in Fig. 4.33b for the illustration purposes. The time step is also set to 0.8 ns and 0.4 ns for the linear and non-linear regimes, respectively, to satisfy the stability criterion, which is more restrictive than the accuracy requirement. The numerical

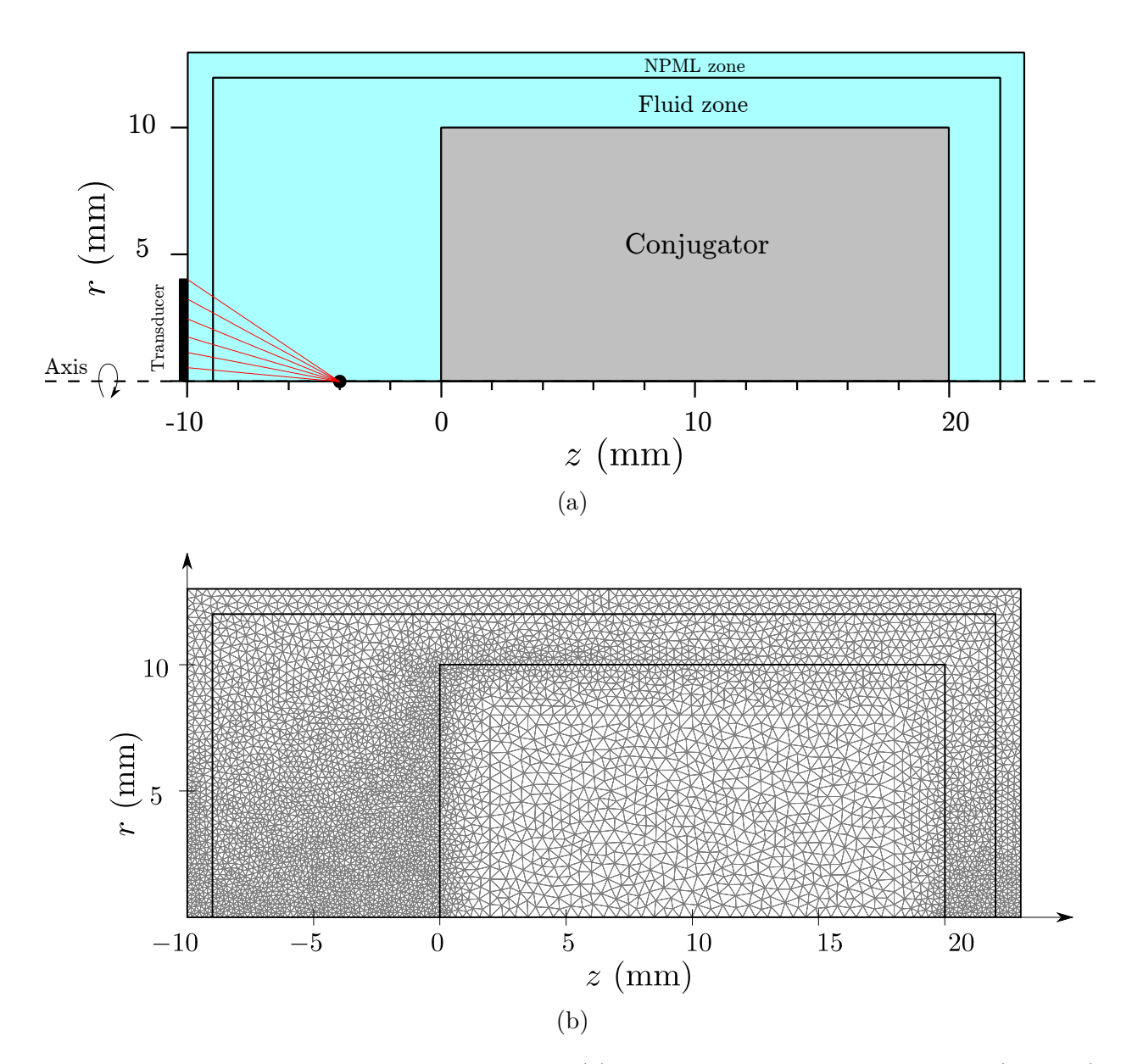


Fig. 4.33. Axisymmetric simulation of WPC: (a) the numerical setup and a sketch (to scale); and (b) the coarsest numerical mesh with the minimum grid element size of 0.2 mm.

grid has 42,500 and 117,250 elements for the linear and non-linear cases, respectively. These grids are partitioned into 192 sections, which are assigned to 2.1 GHz CPUs (AMD Opteron 6172) on Compute Canada supercomputers. The total computational times for the linear and non-linear regimes were almost 32 and 200 minutes, respectively, for advancing 1 μ s in time.

Figures 4.34a and 4.34b show the conjugate signals, which are propagating to the left, at certain time moments. The spatial distributions of these signals are affected by two competing factors. First, the conjugator is continuously emitting conjugate signals, which have exponential amplification in time and propagate to the left. Second, the conjugate signals along different directions in the axisymmetric setup converge toward the nominal focus (z = -4 mm) due to the retro-focusing feature, which increases the signal strengths at the focal zone. The profile of the conjugate waves for the linear regime, shown in Fig. 4.34a, is more affected by the first factor. In this case, the newly emitted conjugate waves, which are closer to the conjugator boundary (z = 0), are stronger due to the exponential amplification in time. On the contrary, in the non-linear regime shown in Fig. 4.34b, although the first factor still appears to be dominant, the focusing feature could effectively influence the conjugate signal profile.

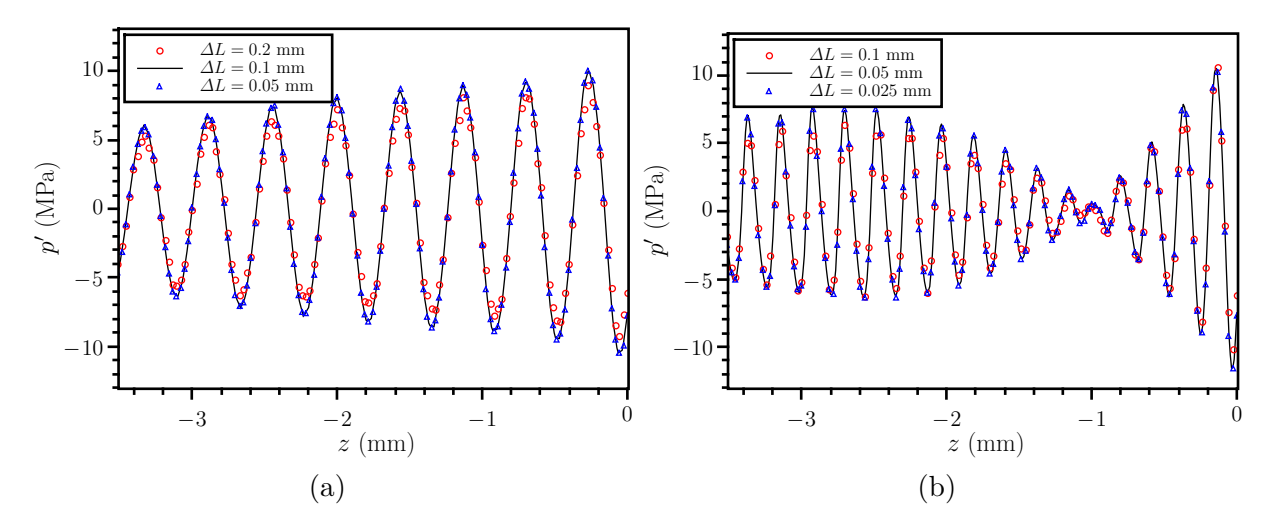


Fig. 4.34. Grid independence studies using three successively refined grids (see Fig. 4.33): pressure disturbance profiles along the axis in front of the conjugator for (a) the linear regime at $t \approx 30.3$ µs and (b) the non-linear regime at $t \approx 17$ µs. ΔL is the minimum characteristic length of grid elements.

The received signal at the nominal focus (z=-4 mm) and its frequency spectra before and after the modulation in the linear fluid flow regime are shown in Figs. 4.35b and 4.36a, respectively. As one should expect for WPC, the dominant frequency in the conjugate wave is 3.5 MHz, which is half of the modulation frequency in this case ($\Omega=7$ MHz). Comparison of the frequency spectra in Fig. 4.36a shows that the frequency content in the conjugate wave is more concentrated towards the working frequency (3.5 MHz), which demonstrates the parametric resonance property of WPC.

In the non-linear fluid flow regime (with $\gamma=6$), the strength of the transducer is increased 100 fold in order to distort the signal in the focal zone. Figure 4.35b shows the behavior of the signal at the nominal focus before the modulation. The observed asymmetric behavior is caused by phase variations between the fundamental frequency and its harmonics, which is due to the phase-shading of the focused flat transducer based on a constant speed of sound. In this non-linear case, the modulation frequency (Ω) is 14 MHz, and as seen in Fig. 4.36b, the second harmonic of the incident wave with a frequency of 7 MHz is conjugated. Thus, the results demonstrate clearly the parametric resonance in both the linear and non-linear WPC simulations at the respective frequencies. It is also to be noted that due to this parametric

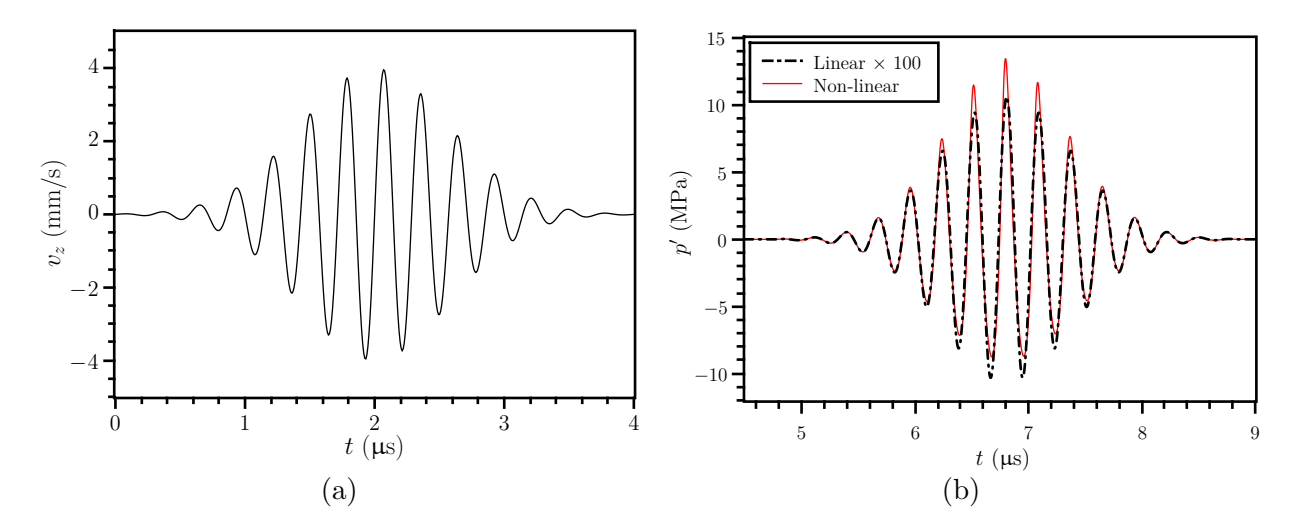


Fig. 4.35. Axisymmetric simulation of the WPC setup shown in Fig. 4.33a: (a) the stimulated axial velocity, v_z , by the transducer in time, provided by Eq. (4.22); (b) recorded pressure disturbance histories of the incident signal at the nominal focal point before the modulation.

resonance feature, the conjugate signals do not have the Gaussian distribution, as apposed to the incident signals shown in Fig. 4.35.

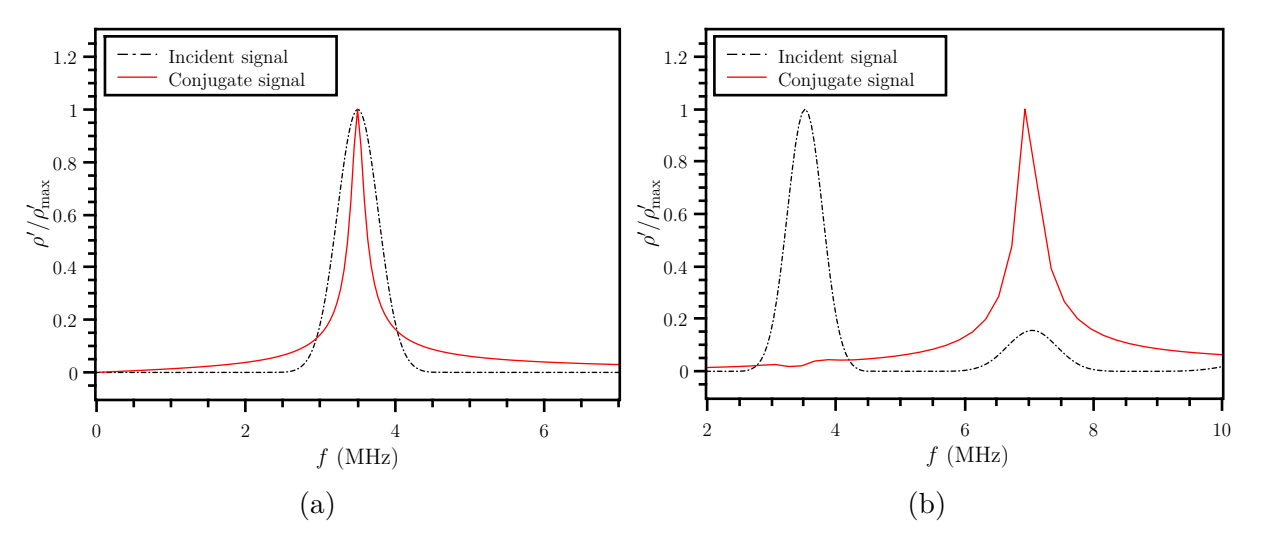


Fig. 4.36. Normalized frequency spectra of the density disturbances for the incident and conjugate signals (see Fig. 4.33a): (a) linear and (b) non-linear fluid flow regimes.

In order to demonstrate how the retro-focusing property of the WPC process is reproduced in the present numerical simulation, the time-averaged Poynting vector, \vec{P} , is defined as follows [73]:

$$\vec{P} = -\frac{1}{T} \int_0^T \boldsymbol{\sigma} \cdot \vec{v} \, dt \,, \tag{4.23}$$

where σ is the stress tensor; \vec{v} is the velocity vector; and T is the time period of the received conjugate signal. Figure 4.37a shows the histories of the axial component of the Poynting vector, P_z , at the nominal focus. They clearly demonstrate the amplification feature of the WPC process. The negative value of P_z shows that the energy flows back toward the focal region. According to the analytical relations provided by Merlen et al. [52] for the paraxial WPC, the conjugate waves are exponentially amplified obeying the e^{At} law, where A is directly related to the modulation frequency. Hence, the conjugate waves in the non-linear regime, which has higher modulation frequency, are amplified at a higher rate, as indeed seen in Fig. 4.37a. The normalized magnitude of the Poynting vector along the vertical line at

z=-4 mm (i.e., in the focal plane) is depicted in Fig. 4.37b, which clearly demonstrates retro-focusing of the conjugate signal in both regimes. Comparison of these two cases suggests that non-linear conjugate waves provide better focusing. There are two underlying reasons of that: the frequency of the conjugate waves in the non-linear regime is twice that in the linear one, which leads to better spatial resolution. Moreover, the shorter wavelength in the non-linear regime increases the ratio of the conjugator active length to the signal wavelength, which improves the conjugation efficiency in different directions. This property is essential to achieve better retro-focusing in the WPC processes.

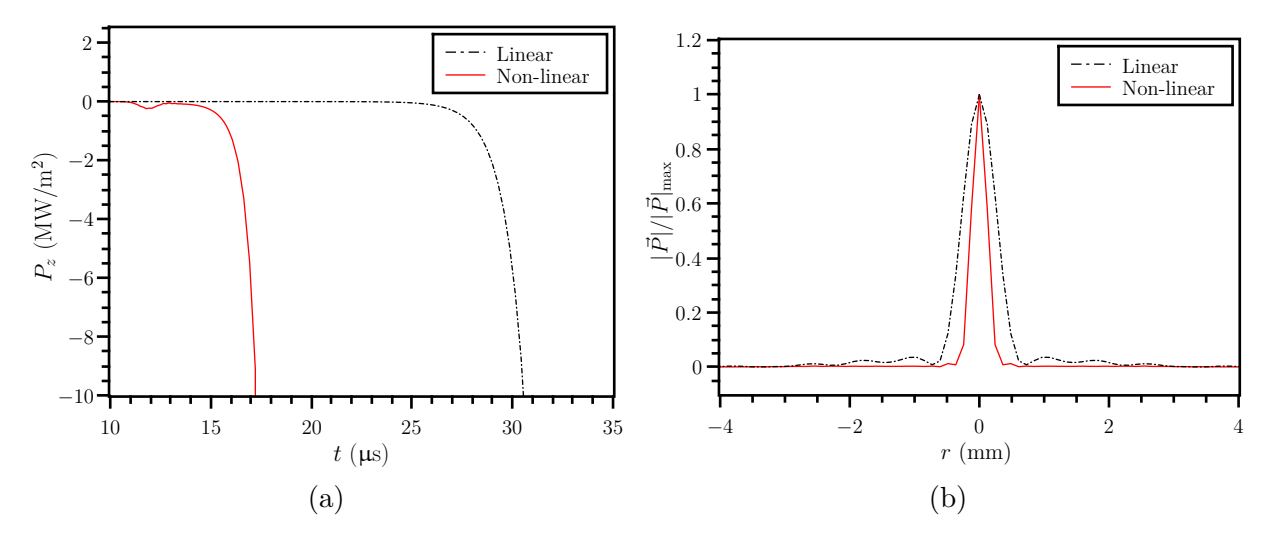


Fig. 4.37. Variation of the Poynting vector in the axisymmetric WPC setup shown in Fig. 4.33a: (a) the axial component, P_z , versus time at the nominal focal point (z = -4 mm); (b) the normalized magnitude, $|\vec{P}|/|\vec{P}|_{\text{max}}$, along the vertical line passing through the nominal focal point (z = -4 mm) at $t \approx 17.3$ µs for the non-linear regime and at $t \approx 30.43$ µs for the linear one.

To analyze the retro-focusing property of the WPC process in more detail, the normalized strengths of the pressure disturbance modes of the incident and conjugate waves are shown in Fig. 4.38 along the axis and the vertical line at z = -4 mm (i.e., in the nominal focal plane) for both linear and non-linear regimes. These distributions in Fig. 4.38 are obtained by analyzing the conjugate wave packets propagating toward the focal zone. As it is seen, the respective frequency modes, which are 3.5 MHz in the linear regime and 7 MHz in the non-linear one, exhibit an extremum in the focal region in both z and r planes. As it was

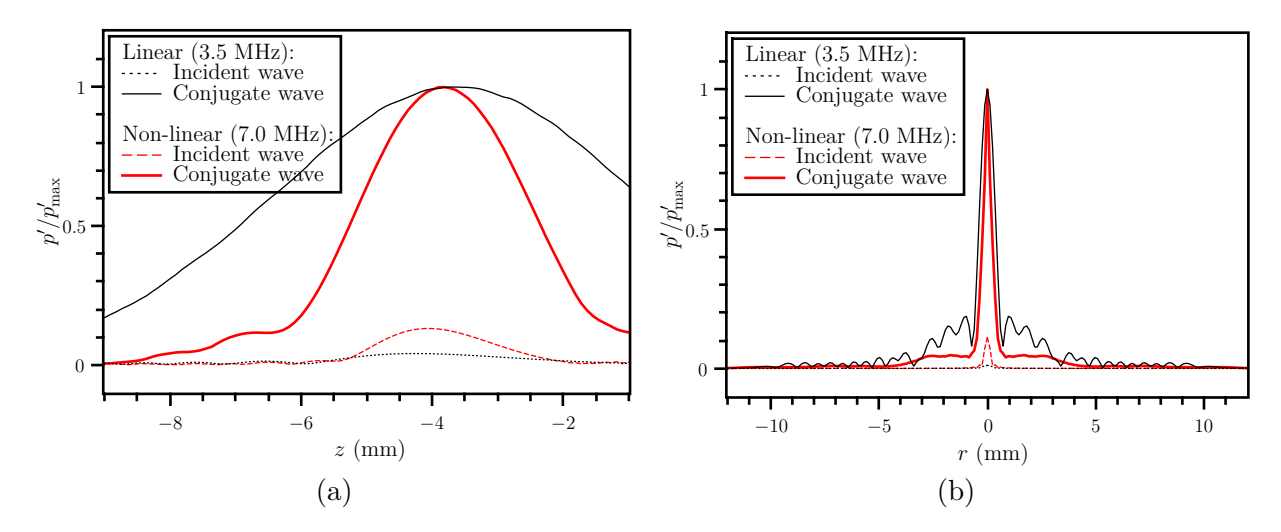


Fig. 4.38. Normalized strengths of the pressure disturbance modes in the linear (black lines) and non-linear (red lines) regimes (see Fig. 4.33a): (a) along the axis (r = 0) and (b) along the vertical line passing through the focal point (z = -4 mm).

mentioned before, the high-frequency mode pertaining to the non-linear regime has narrower lobes, which leads to better focusing in both directions. This feature is due to better spatial resolution and more efficient conjugation processes in all directions of incidence.

The velocity and Poynting vector contours are shown in Fig. 4.39. Comparison of Figs. 4.39a and 4.39b shows that the wave propagation within the conjugator is more organized and focused for high-frequency waves, which also mitigates unintended wave evacuations through the conjugator boundaries. Figures 4.39c and 4.39d demonstrate the magnitude of the Poynting vectors along with the corresponding vectors themselves, which are in line with the results provided in Fig. 4.37b. As it is seen, in the non-linear regime associated with higher conjugate frequency, the Poynting vectors are more inclined toward the focal region, leading to better focusing.

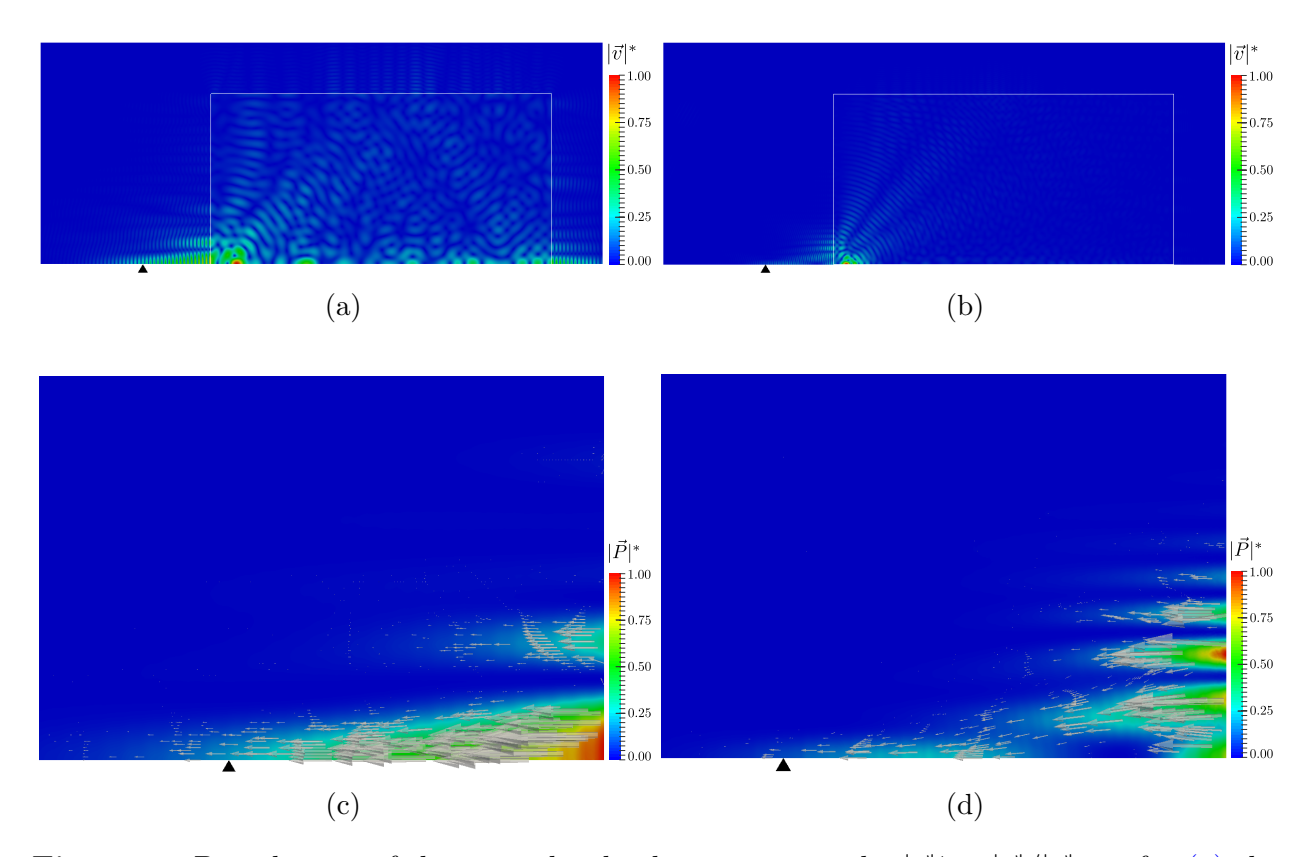


Fig. 4.39. Distribution of the normalized velocity magnitude, $|\vec{v}|^* = |\vec{v}|/|\vec{v}|_{\text{max}}$, for (a) the linear regime at $t \approx 30.3$ µs and (b) the non-linear regime at $t \approx 17$ µs. Normalized Poynting vector magnitude, $|\vec{P}|^* = |\vec{P}|/|\vec{P}|_{\text{max}}$, for (c) the linear regime at $t \approx 30.3$ µs and (d) the non-linear regime at $t \approx 17$ µs. The black triangle points to the nominal focal point located at z = -4 mm. The thin line in (a) and (b) shows the conjugator boundaries in the setup shown in Fig. 4.33a.

4.3 Interaction of Bubbles with WPC

In this section, interactions of bubbles with the WPC process are investigated. The idea is to place a bubbly zone in front of the conjugator and assess how the presence of bubbles can affect the modulation process and the recorded signals for different stimulation frequencies. These assessments are meant to investigate the possibility of using the WPC process for estimating dimensions of bubbles within different bubble clouds. In the following test cases, the upstream sensor, S_1 , is located in front of the conjugator to record the conjugate waves,

and the downstream sensor, S_2 , detects the direct signals on the other side of the conjugator. In order not to generate new bubbles in the domain and to prevent the existing bubbles from being unstable, the simulation is stopped as soon as the cavitation threshold is detected. Although in the transient stimulations higher cavitation thresholds are reported [13, 77], in the present study, the static cavitation threshold (absolute pressure lower than the vapor pressure) is considered to be more conservative for the measurement purposes.

4.3.1 Interaction of WPC with Bubble-Plane Clouds

In this subsection, a paraxial WPC with the conjugator length of 40 cm is used as illustrated in Fig. 4.40. Such a long conjugator is needed to ensure the modulation process for both the even and odd phase patterns, as elaborated in detail by Merlen et al. [52] and in Fig. 4.32. This conjugator is stimulated by different frequencies in the range of 150–400 kHz with intervals of 10 kHz. This frequency range is chosen to include the main peak of the frequency response curve for a bubble with the radius of 10 μ m. The other physical properties of this simulation are the same as those provided in Table 4.5.

Each case of this analysis consists of two stages: first, a one-wavelength stimulating sinusoidal signal with the frequency which is half of the modulation one is generated by a transducer located at the left boundary, as shown in Fig. 4.40a. Then, after $T + 13.33 \,\mu s$ (T is the period of the stimulation signal), the transducer is replaced by an absorbing boundary, and a bubble cloud is placed in the middle of the left fluid zone, as illustrated in Fig. 4.40b. During the modulation process, the waves inside the conjugator are amplified and propagate toward the bubble-plane cloud. Stimulating it, these waves propagate back into the conjugator and affect the modulation process. The bubble-plane cloud has bubbles with the radius of 10 μ m and the physical void fraction ($\bar{\beta}_0$) of 5×10^{-4} , which is the same cloud as the one evaluated in Fig. 4.20. The minimum grid element size and the time step are set to 0.12 mm and 10 ns, respectively.

Bubble-plane clouds, which have the minimum possible thickness (see Fig. 2.2a), are conceptual models and are not usually formed in realistic situations. These clouds can be seen as 1D vibrators, which their dynamic responses are the same as those for the constituting bubbles. In that sense, as opposed to realistic bubble clouds (e.g., bubble-layer and spherical

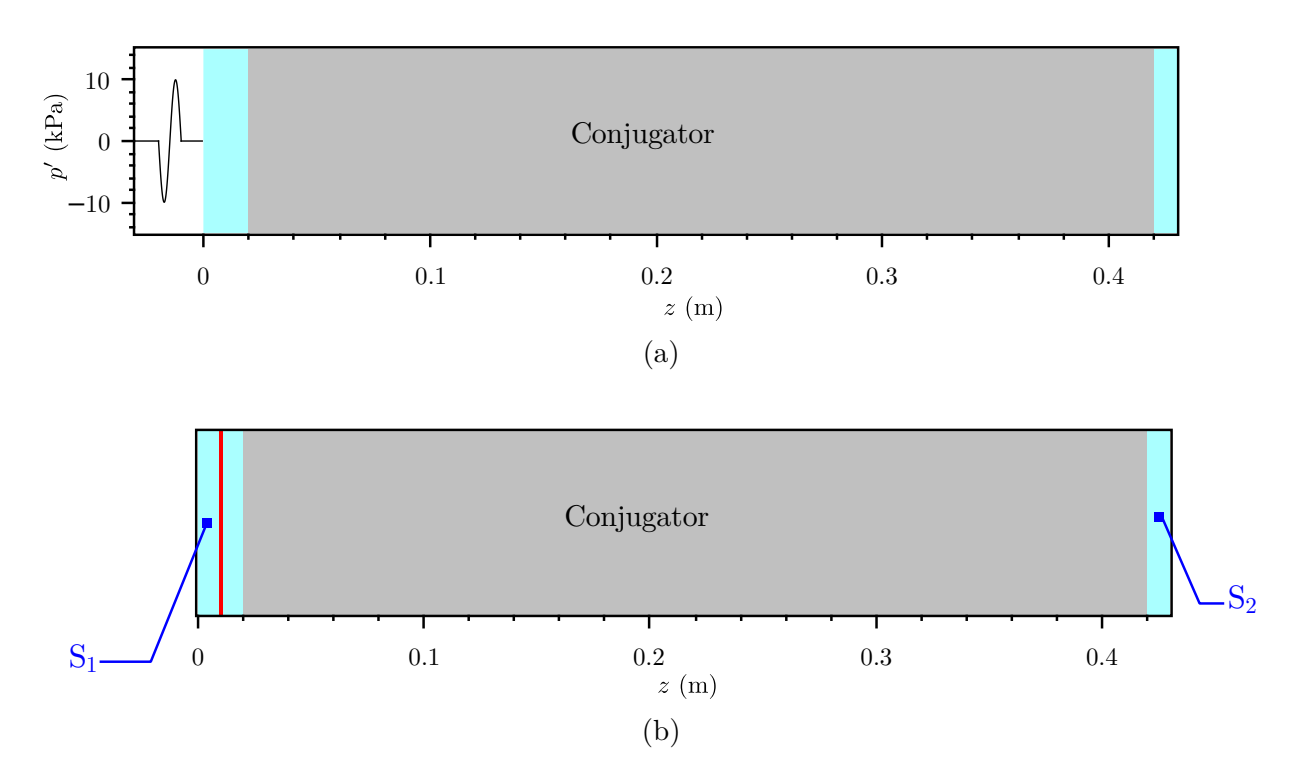


Fig. 4.40. Interaction of a paraxial WPC with a bubble-plane cloud $(R_0 = 10 \text{ μm}, \bar{\beta}_0 = 5 \times 10^{-4})$: (a) the stimulation phase by a one-wavelength sinusoidal signal; and (b) the modulation phase, when the bubble-plane cloud is placed and the left boundary becomes absorbing. The grey zone is the conjugator, the blue ones are filled with water, the red zone is the bubble cloud, and the white one is the transducer. The signals are recorded at the upstream, S₁, and the downstream, S₂, sensors.

bubble clouds), the conjugate signals passing through the bubble-plane cloud and reaching the upstream sensor (S_1) do not necessarily carry descriptive information regarding the bubble-plane cloud dynamics. Hence, in this set of simulations, the direct waves, recorded at the downstream sensor S_2 , were employed to assess effects of the bubble-plane cloud dynamics on the modulation process.

Defining the exponential amplification factor Γ , Merlen et al. [52] showed that both conjugate and direct waves exponentially grow in time. The variation of this factor versus the stimulation frequency at S₂ is presented in Fig. 4.41a for the cases with and without the bubble-plane cloud. As depicted, Γ generally grows with the stimulation frequency since the conjugator contains more number of wavelengths for higher stimulation frequencies, and,

hence, stronger amplification is expected. As illustrated in Fig. 4.41a, in the absence of the bubble-plane cloud, there are some local variations in the trend of Γ for different stimulation frequencies, which are due to two main factors. First, the even/odd phase pattern can locally change Γ , as discussed in the previous test cases (see Fig. 4.32). Second, the simulation might be terminated earlier for some stimulation frequencies due to occurrence of cavitation. This barrier might prevent the phase pattern within the conjugator to reach the fully-developed state, leading to changes in the amplification factor.

Placing the bubble-plane cloud in front of the conjugator affects the modulation process in different ways. Although the bubble-plane cloud sends some energy back to the conjugator, this energy does not necessarily increase Γ . The reason for such a behavior is the fact that the waves emitted by the bubble-plane cloud might not participate in the modulation process due to the parametric resonance feature of the WPC phenomenon. In addition, the generated signals by the bubble-plane cloud might noticeably influence the even/odd phase pattern within the conjugator, which affects amplification of signals within the conjugator.

Figure 4.41b compares the frequency spectra of the pressure disturbances for the direct waves and for the signals generated by the bubble-plane cloud at the stimulation frequency of 150 kHz. As expected, scattered waves from the bubble-plane cloud populates different modes including the bubble natural frequency ($\approx 332 \text{ kHz}$), the stimulation frequency, and the respective super- and sub-harmonics. However, the modulation process amplifies mostly the stimulation frequency, 150 kHz, while other modes are filtered out to some extent. Somewhat similar behaviors are observed in Figs. 4.41c and 4.41d for the stimulation frequencies of 250 kHz and 330 kHz, respectively. However, the mode associated with free oscillations of the bubble, $f_{\rm b}$, is participating in the modulation process as it is getting closer to the stimulation frequency. Figure 4.41d perfectly demonstrates this effect, in which the frequency spectra of the pressure disturbances for the direct waves has a wider distribution. As explained before, it is to be noted that the maximum response of the bubble-plane cloud occurs at f = 324.5 kHz, slightly lower than the bubble natural frequency, which is due to the non-linear oscillation of this plane.

Consequently, it appears that the amplification factor, Γ , would be highly affected by bubble-plane clouds for stimulation frequencies which are close to the natural frequency of the constituting bubble. However, whether this effect would augment or diminish the

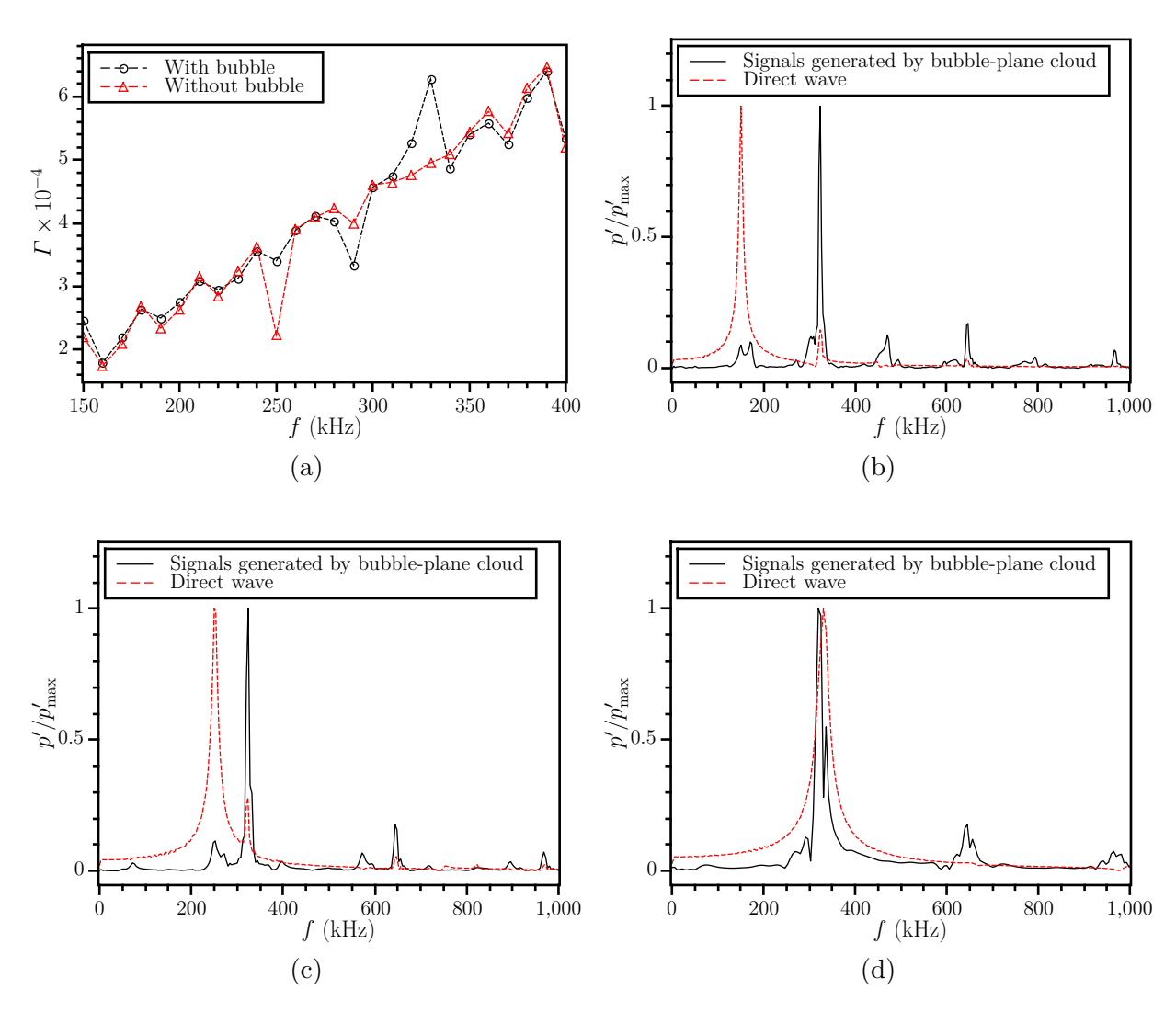


Fig. 4.41. Interaction of the paraxial WPC shown in Fig. 4.40 with a bubble-plane cloud $(R_0 = 10 \text{ } \mu\text{m}, \bar{\beta}_0 = 5 \times 10^{-4})$: (a) exponential amplification factor; and normalized frequency spectra of the presence disturbances for the stimulation frequencies of (b) 150 kHz, (c) 250 kHz, and (d) 330 kHz.

amplification factor depends on the phases of the signals scattered from the bubble-plane cloud, which is seen in Fig. 4.41a for the stimulation frequencies between 280 kHz and 350 kHz. Hence, by choosing a conjugator with adequate length and changing the modulation frequency, size of bubbles within bubble-plane clouds can be estimated by recording the amplification factors and comparing them with the design values.

As discussed in the previous case, changes of the phase pattern made by bubble-plane clouds might significantly affect the amplification factor. Therefore, it is of interest to investigate how much the location of the bubble-plane cloud, which affects the phase pattern in the setup shown in Fig. 4.40, would influence the modulation process. For this goal, the bubble-plane cloud illustrated in Fig. 4.40 is displaced 5 mm first to the left and then to the right side of the initial position of the bubble-plane cloud (z = -10 mm). Variations of Γ with the stimulation frequency are presented in Fig. 4.42a. As demonstrated, the overall trend, which is noticeable fluctuations of Γ near the natural frequency of the constituting bubble, is observed. However, due to changes of interacting signal phases by displacing the bubble-plane cloud, variations of Γ near the bubble natural frequency might be not quite pronounced for specific bubble-plane locations, such as the case in which the cloud is located at z = -5 mm.

To better interpret the results, the relative intensity (I^*) , as another indicator, is defined as follows:

$$I^* = \frac{I}{I^0}; \quad I = \frac{1}{T_2 - T_1} \int_{T_1}^{T_2} p' v_n \, dt,$$
 (4.24)

where I is the signal intensity, I^0 is the intensity in the absence of bubbles, $v_{\rm n}$ is the normal velocity component to a desired plane, and T_1 and T_2 define the time domain extents over which the intensity is evaluated. Figures 4.42b–4.42d show the intensity of the direct waves for 20 signal periods starting from $t=100~\mu {\rm s}$ for different bubble cloud locations. As depicted, the intensities have general growing trends, which agree with variations of Γ ; however, in this case, I^* is a better indicator. For each bubble cloud location, the maximum of I^* occurs near the natural frequency of the constituting bubbles, $f_{\rm b}$. As previously discussed, other peaks might also present due to changes of the phase pattern by displacing the bubble-plane cloud. Hence, I^* can be employed to better interpret the signals when Γ is not fully descriptive.

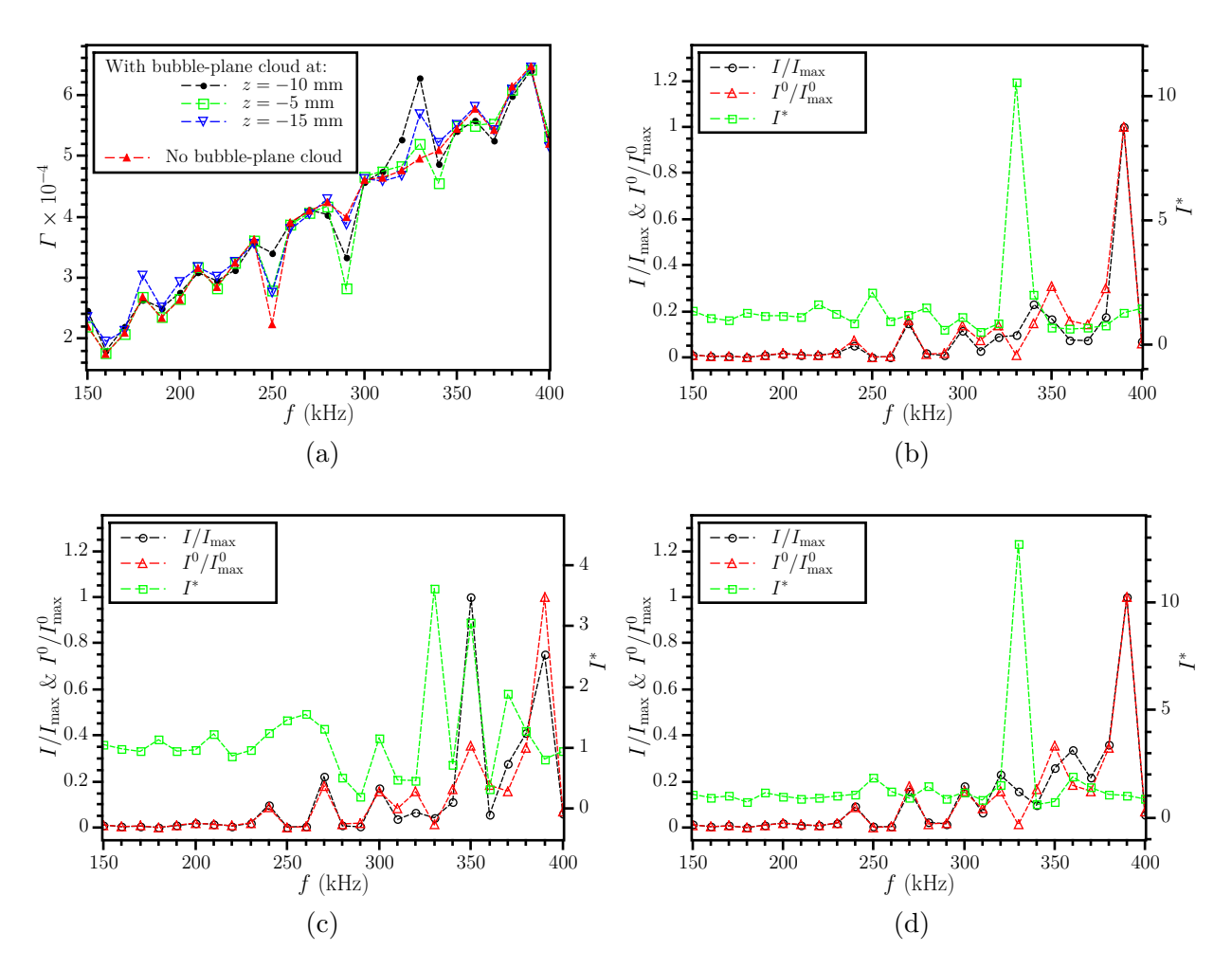


Fig. 4.42. Interaction of the paraxial WPC shown in Fig. 4.40 with a bubble-plane cloud ($R_0 = 10 \, \mu \text{m}$, $\bar{\beta}_0 = 5 \times 10^{-4}$) at different locations: (a) variations of the exponential amplification factor (Γ) with the stimulation frequency; and the normalized intensities (I/I_{max} , I^0/I_{max}^0) and the relative intensity (I^*) versus the stimulation frequency when the bubble cloud is located at (b) $z = -10 \, \text{mm}$, (c) $z = -5 \, \text{mm}$, and (d) $z = -15 \, \text{mm}$.

The results shown in Fig. 4.42 suggest that for obtaining a more reliable estimation for the bubble size dimension in such setups, the conjugator can be slightly displaced in order to better exclude the phase pattern effects on the amplification process.

4.3.2 Interaction of WPC with Single Bubbles

Plane clouds can be considered as sets of bubbles oscillating simultaneously; therefore, their interactions with WPC might significantly influence the modulation process, as shown in the test cases assessed in Section 4.3.1. On the contrary, the signals emitted by a stimulated single bubble are quite weak to have noticeable impact on the conjugator. To verify this statement, an axisymmetric numerical setup shown in Fig. 4.43a is employed, where the conjugator has a length of 40 cm and a diameter of 16 cm. In this case, the conjugator and the surrounding fluid zone have the same properties as those provided in Table 4.5. In order to eliminate false reflections from outer boundaries, the computational domain is wrapped in an NPML layer with the thickness of 1 cm and σ_{max} of 3×10^5 (see Fig. 4.43a).

A number of simulations were conducted with this setup. In each of them, the conjugator is initially stimulated by a signal with the main frequency which is in the range of 150–400 kHz with intervals of 10 kHz. These initial disturbances are generated by a point mass source located on the conjugator axis at the distance of 1 cm from its surface. This point source generates initial disturbances during $0 \le t \le 32 \mu s$, as follows:

$$\dot{m} = A \cdot \exp(-B(t - t_0)^2) \cdot \sin(2\pi f_0(t - t_0)),$$
(4.25a)

$$A = 16 \pi \times 10^{-11} \frac{\text{kg}}{\text{s}}, \ B = 2 \times 10^{10} \frac{1}{\text{s}^2}, \ t_0 = 16 \times 10^{-6} \text{ s},$$
 (4.25b)

where f_0 is the main stimulation frequency. In each simulation, the point source is substituted with a single bubble with the radius of 10 μ m at t = 35 μ s, as depicted in Fig. 4.43a. In this case, the minimum grid size element and the time step are 0.3 mm and 10 ns, respectively. In addition, the concentric spheres employed to estimate the stimulating pressure by Eq. (2.49) have radii of 0.2 and 0.3 mm. The numerical grid employed for these simulations is illustrated in Fig. 4.43b. The signals are recorded at the upstream (S₁) and downstream (S₂) sensors, which are located on the axis at z = 1.25 cm and z = 43.5 cm, respectively (see Fig. 4.43a).

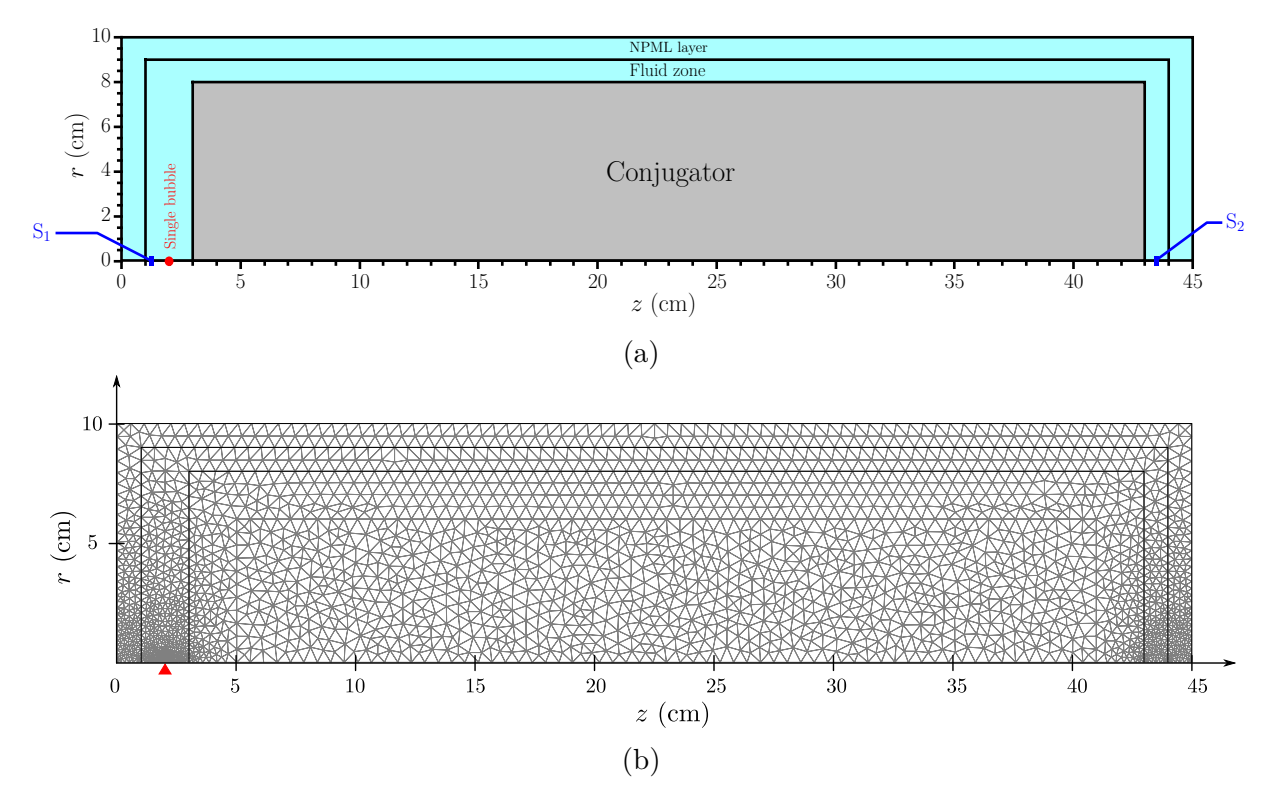


Fig. 4.43. Interaction of an axisymmetric WPC with a single bubble ($R_0 = 10 \mu m$): (a) the numerical setup and the sketch. The gray zone is the conjugator, the blue zones are filled with water, the red circle shows the location of the single bubble, and S_1 and S_2 are the upstream and downstream sensors. (b) The employed numerical grid; the red triangle indicates the location of the single bubble.

Figures 4.44a and 4.44b show changes of Γ with the stimulation frequency, and, as depicted, the signals emitted by the single bubble are not strong enough to affect the amplification process of the conjugator. It is to be noted that Γ of conjugate waves varies almost linearly with the stimulation frequency, as shown in Fig. 4.44a. This behavior is due to the fact that the modulation process occurs in different directions of the axisymmetric conjugator, engaging different active lengths of the conjugator. Hence, the even/odd phase pattern of the modulation process would be less effective in the axisymmetric WPC.

To better demonstrate interactions of the single bubble with the axisymmetric WPC, intensities of the conjugate and direct waves are obtained for 55 signal periods starting

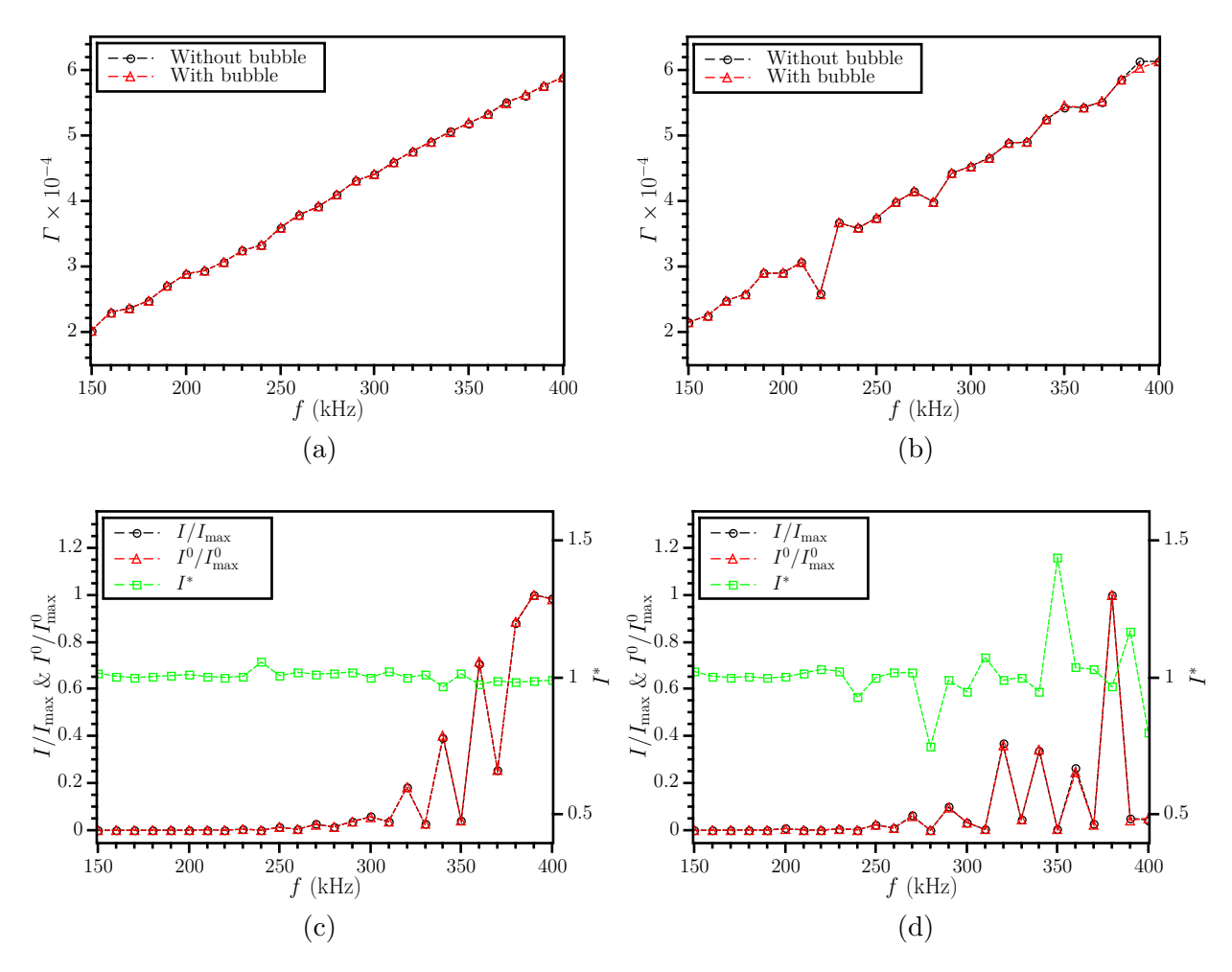


Fig. 4.44. Interaction of a single bubble $(R_0 = 10 \ \mu\text{m})$ with the axisymmetric WPC shown in Fig. 4.43a: variations of the exponential amplification factor (Γ) with the stimulation frequency for (a) the conjugate and (b) direct waves; and the normalized intensities $(I/I_{\text{max}}, I^0/I_{\text{max}}^0)$ and the relative intensity (I^*) versus the stimulation frequency for (c) the conjugate and (d) direct waves.

from $t = 100 \,\mu\text{s}$. Figures 4.44c and 4.44d show that the intensities of the conjugate and direct waves have growing trends with the stimulation frequency, which are in line with the variations of Γ . As shown, presence of the single bubble has no significant impact on the intensities even for stimulation frequencies close to f_b , where $I^* \approx 1$ with subtle variations at the upstream and downstream sensors.

More detailed results for the stimulation frequency of 330 kHz, which is close to the natural frequency of the bubble $(f_{\rm b})$, are provided in Fig. 4.45. In this case, the cavitation barrier is intentionally suppressed to assess effects of the violent bubble responses on the WPC process. Subjected to strong conjugate waves, the bubble starts to show aggressive non-linear responses, as demonstrated in Fig. 4.45a, which eventually result in transient cavitation of the bubble. Figure 4.45b shows that due to non-linearity of these responses, many vibration modes present, where the natural one ($\approx 330 \text{ kHz}$) is dominant. Even though, in line with the results provided in Fig. 4.45, dynamics of the single bubble have no significant influence on the WPC process as illustrated in Figs. 4.45c and 4.45d, where the pressure disturbance histories at the upstream and downstream sensors remain largely unchanged in the presence of the bubble.

4.3.3 Interaction of WPC with Bubble-Layer Clouds

In realistic situations, bubbles usually come in large numbers with various patterns. In this subsection, interactions of bubble-layer clouds with the WPC process are investigated in paraxial domains. The clouds analyzed in this subsection are assumed to have uniform initial bubble distributions.

For this aim, the thin bubble layer, which was previously assessed in Figs. 4.23c, 4.23d and 4.25, is placed in front of the paraxial WPC setup shown in Fig. 4.46. This bubble-layer cloud has a length of 0.25 mm, void fraction of 0.01, and individual bubbles with the radius of 10 μ m. Similarly to the setup shown in Fig. 4.40, the conjugator is first stimulated by a one-wavelength sinusoidal signal, which is generated by a transducer located at the left boundary. After $T+13.33~\mu$ s, where T is the stimulation signal period, the bubble-layer cloud is placed in the middle of the left fluid zone, and the left boundary becomes an absorbing one. In these simulations, the minimum grid element size is 83.3 μ m, and the time step is set

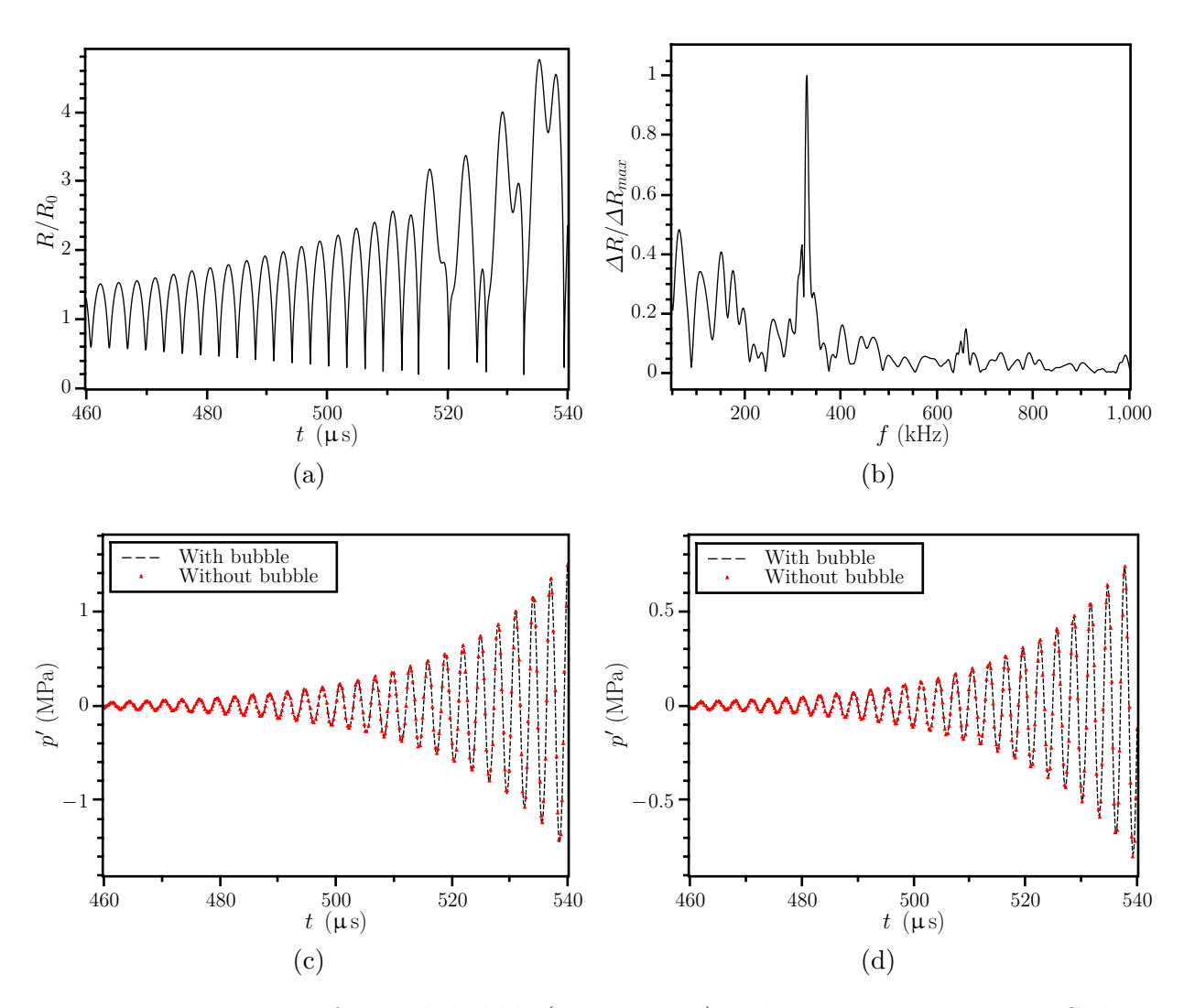


Fig. 4.45. Interaction of a single bubble ($R_0 = 10 \mu \text{m}$) with the axisymmetric WPC shown in Fig. 4.43a for the stimulation frequency of 330 kHz: (a) the bubble radius history; (b) the normalized frequency spectrum of the bubble radius variations; and the pressure disturbance histories at (c) the upstream and (d) downstream sensors.

to 3 ns. The other physical and simulation properties are the same as those for the paraxial cases, provided in Table 4.5 and Section 4.3.1.

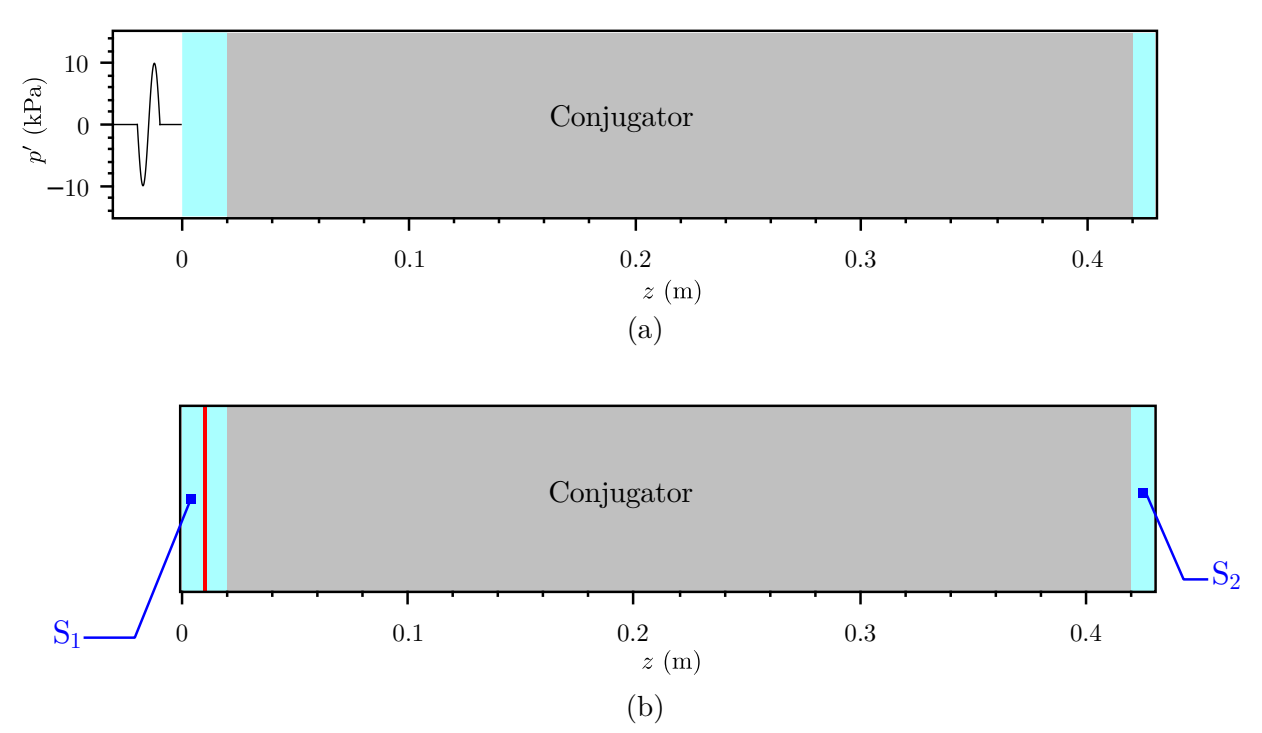


Fig. 4.46. Interaction of a paraxial WPC with a bubble-layer cloud: (a) the stimulation phase by a one-wavelength sinusoidal signal; and (b) the modulation phase, when the bubble-layer cloud is placed and the left boundary becomes absorbing. The grey zone is the conjugator, the blue ones are filled with water, the red zone is the bubble-layer cloud, and the white one is the transducer. The signals are recorded at the upstream, S_1 , and the downstream, S_2 , sensors.

Having passed through the bubble cloud, the conjugate waves are recorded by the upstream sensor, S_1 . Hence, the data recorded at this sensor appears to have more information with regard to the bubble dynamics. Direct waves, on the other hand, have no direct interaction with the bubble cloud. Therefore, these signals, which are recorded at the downstream sensor (S_2) , might better show how the bubble cloud dynamics affect the modulation process. In this test case, the conjugator is stimulated with frequencies in the range of 150–400 kHz with intervals of 10 kHz. As an initial stimulation, the transducer generates a one-wavelength sinusoidal signal with a frequency which is half of the modulation one. Figure 4.47a shows

that the exponential amplification factor (Γ) of the conjugate waves, which are recorded at S_1 , significantly decreases for the stimulation frequencies higher than the natural frequency of the individual bubbles within the cloud ($f_b = 331.9 \text{ kHz}$). This filtering feature is in correspondence with the bubble cloud dynamics shown in Figs. 4.23c and 4.23d. This noticeable decrease of Γ can be used as an indicator to estimate bubble dimensions within a cloud. It is to be noted that the natural modes of the cloud (see Table 4.3) have no appreciable impact on Γ of the conjugate signals.

In order to see how the cloud dynamics affect the modulation process, variations of Γ with different stimulation frequencies for the direct waves are presented in Fig. 4.47b. In contrast with the stimulation of the bubble-plane cloud shown in Fig. 4.41a, neither the natural frequencies of the bubble-layer cloud nor the natural frequency of the individual bubble influence Γ of direct waves. The reason for such a difference between the bubble-plane and bubble-layer cloud dynamics is the fact that in bubble layers, oscillations of all individual bubbles are not synchronized. Thus, the signals scattered from the bubble-layer clouds at their natural frequencies are not as strong as those emitted by bubble-plane clouds. Hence, Γ of the direct waves, as an indicator showing changes of the modulation process by the presence of bubble clouds, is not significantly affected. It is also to be noted that no filtering feature is observed in Fig. 4.47b since the direct waves do not pass through the bubble cloud.

Similarly to the stimulation of bubble-plane clouds (see Figs. 4.41a and 4.42a), local variations of Γ have two main reasons: first, the even/odd wave pattern within the conjugator changes with different stimulation frequencies and also with the presence of the bubble layer. Second, the fully-developed modulation process might not be reached in some cases due to the cavitation barrier. That is the reason for slight differences between Γ of conjugate and direct waves even in the absence of the bubble cloud (red lines in Figs. 4.47a and 4.47b), while fully-developed conjugate and direct waves in paraxial WPC processes have the same Γ [52].

To extract more information from the conjugate and direct waves, the intensity (I) and relative intensity (I^*) , introduced by Eq. (4.24), are computed for 20 periods of the stimulation signals, starting from $t = 100 \,\mu s$. In the absence of the bubble layer, the intensities of the conjugate and direct waves show the same behavior as that of the amplification factor, as

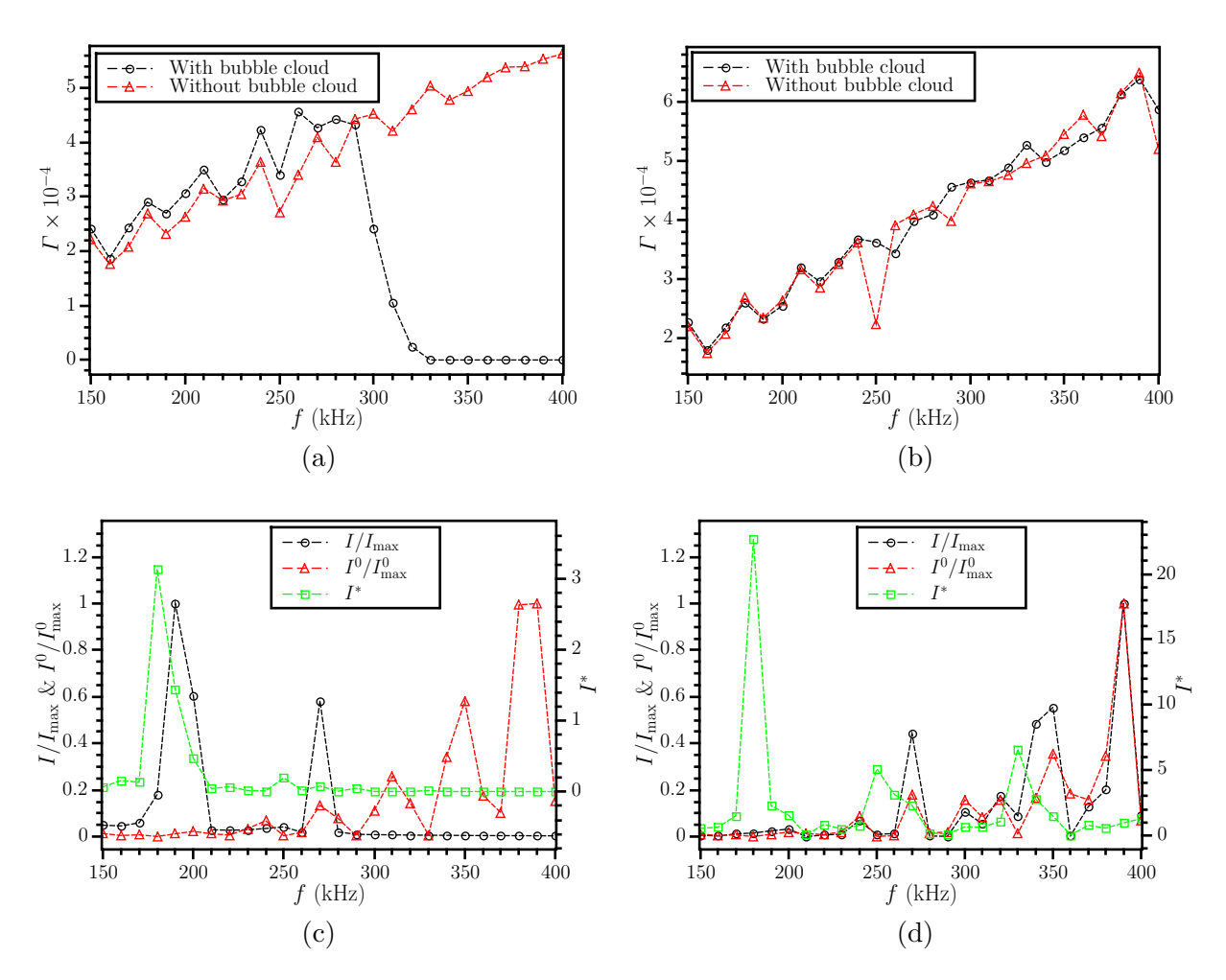


Fig. 4.47. Interaction of a thin bubble-layer cloud (L=0.25 mm, $\beta_0=0.01$, $R_0=10$ µm) with the paraxial WPC shown in Fig. 4.46: variations of the exponential amplification factor (Γ) with the stimulation frequency for (a) the conjugate and (b) direct waves; and the normalized intensities ($I/I_{\rm max}$, $I^0/I_{\rm max}^0$) and the relative intensity (I^*) versus the stimulation frequency for (c) the conjugate and (d) direct waves.

depicted in Figs. 4.47c and 4.47d. In other words, these intensities generally increase with the stimulation frequency, and they also show some local variations. As previously discussed, these variations occur when the even/odd signal pattern changes with the stimulation frequency, and when the signals within the conjugator have no enough time to fully evolve due to the cavitation barrier.

In this case, the conjugate waves, which pass through the bubble cloud, appear to carry more information about the bubble layer. As shown in Fig. 4.47c, the intensity of the conjugate waves has two peaks occurring at the cloud natural frequencies (see Table 4.3). Moreover, the filtering behavior is observed for the frequencies higher than f_b . To exclude the modulation amplification factor from I, the relative intensity can be discussed. As depicted in Fig. 4.47c, I^* of the conjugate waves also demonstrates the filtering feature. However, compared to I, the first peak is slightly dislocated, and the second peak is almost diminished, which might be due to changes of the phase pattern or the cavitation condition as a result of the bubble-layer presence. The advantage of using I^* is more evident for direct waves shown in Fig. 4.47d, where the peaks are better distinguished compared to variations of I. However, similarly to the conjugate waves, the peaks might be slightly dislocated and additional peaks might occur due to the reasons previously discussed. In addition, Fig. 4.47d shows no filtering behavior for direct waves, which is in line with the results presented in Fig. 4.47b since these waves do not pass through the cloud.

Generally, I and I^* are more sensitive to the presence of bubble clouds than Γ , and, as a result, they can better accentuate small changes in signal profiles. For instance, I^* of both the conjugate and direct waves show significant variations at the stimulation frequency of 180 kHz in Figs. 4.47c and 4.47d, while Γ is not able to accentuate any impact at this frequency (see Figs. 4.47a and 4.47b). To investigate this difference, the pressure disturbance histories of the conjugate and direct waves along with their exponential signal envelopes are shown in Fig. 4.48 for the stimulation frequency of 180 kHz. Although the signal histories are quite affected by the presence of the bubble cloud and the signal envelopes are easily distinguishable in Fig. 4.48, the exponential factors associated with these envelopes (Γ) do not properly represent the variations occurred in signal profiles after including the bubble cloud.

In addition, although Γ of the direct waves at f = 180 kHz in the absence of the bubble

cloud is slightly higher than the one when the cloud presents (see Fig. 4.47b), its signal strength is quite weaker in the considered time duration, as illustrated in Fig. 4.48b. However, given enough time, signals with higher Γ eventually overtake those with lower amplification factors. Another point to be noted is the asymmetric trend of the conjugate wave history when the bubble cloud presents, as shown in Fig. 4.48a. The reason for such an asymmetrical behavior is non-linear oscillations of the bubbles in the cloud, which are filtered out within the conjugator and are absent in the direct waves (see Fig. 4.48b).

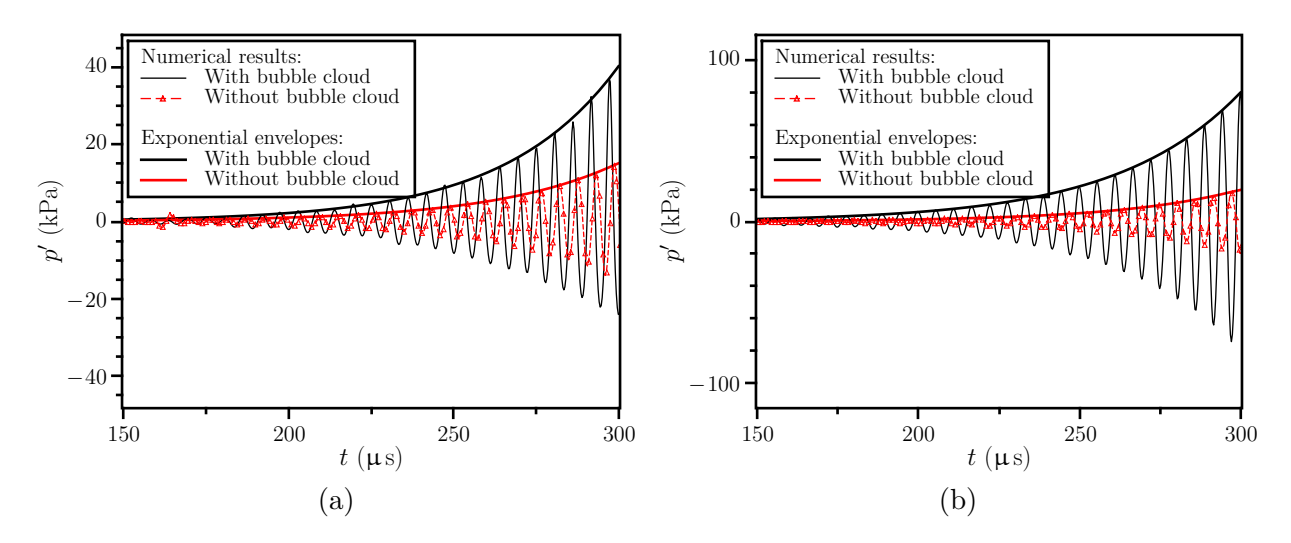


Fig. 4.48. Interaction of a thin bubble-layer cloud (L = 0.25 mm, $\beta_0 = 0.01$, $R_0 = 10$ µm) with the paraxial WPC shown in Fig. 4.46: pressure disturbance histories at the stimulation frequency of 180 kHz for (a) the conjugate and (b) direct waves.

To investigate how the thickness of a bubble-layer cloud affects the interactions with the WPC process, the cloud in Fig. 4.46 was replaced by a thicker bubble-layer cloud with the thickness of 2.5 mm and the void fraction of 0.01, which is similar to the one evaluated in Figs. 4.23e and 4.23f. The other physical and simulation properties are the same as those for the previous test case.

Similarly to the thin bubble-layer cloud, there is no appreciable changes in Γ of direct waves due to the presence of the cloud, as illustrated in Fig. 4.49b. However, there is a significant decrease in Γ near the natural frequency of the constituting bubbles for the conjugate waves, demonstrating the filtering effect in Fig. 4.49a. Comparing Figs. 4.47a

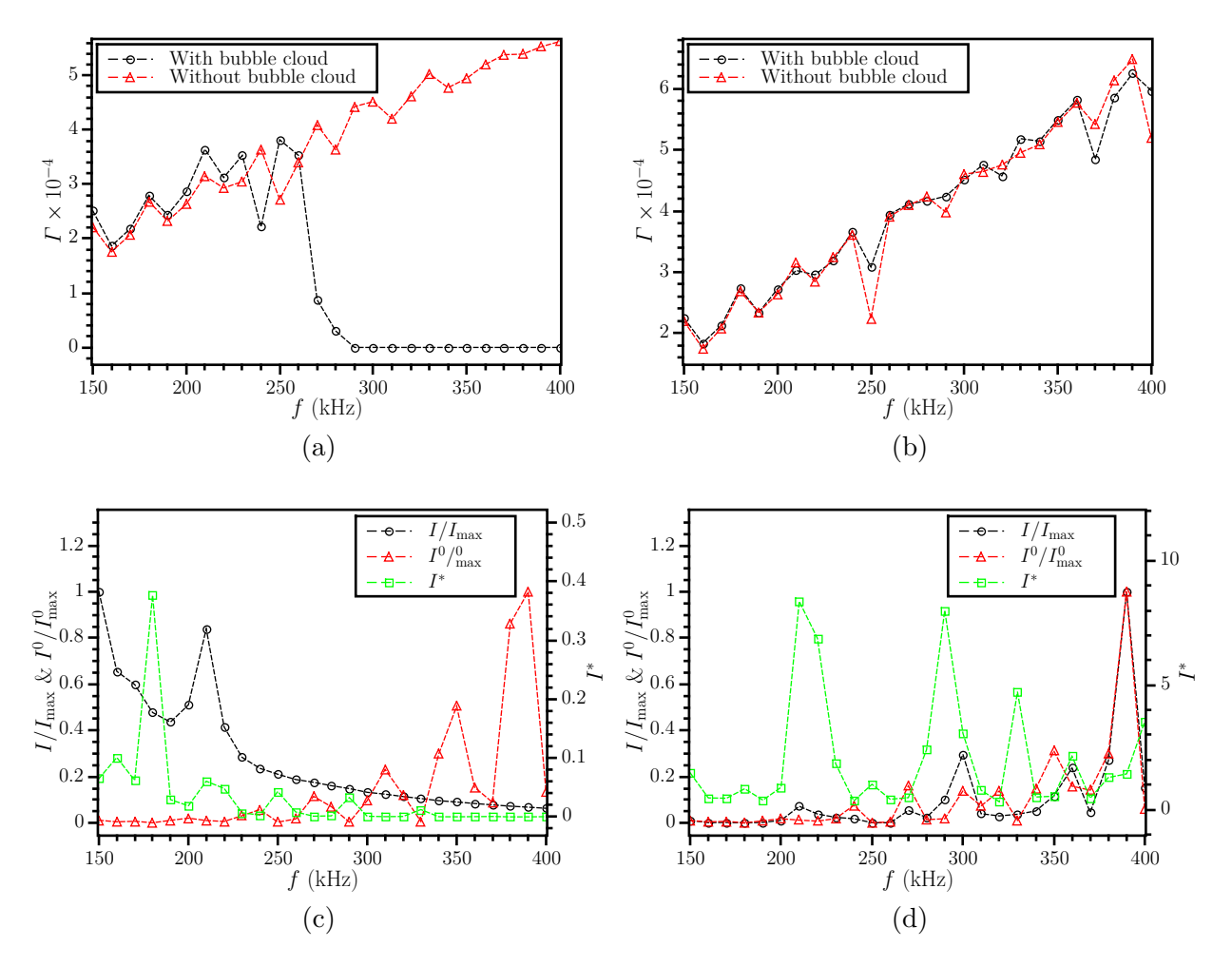


Fig. 4.49. Interaction of a thick bubble-layer cloud (L=2.5 mm, $\beta_0=0.01$, $R_0=10$ µm) with the paraxial WPC shown in Fig. 4.46: variations of the exponential amplification factor (Γ) with the stimulation frequency for (a) the conjugate and (b) direct waves; and the normalized intensities ($I/I_{\rm max}$, $I^0/I_{\rm max}^0$) and the relative intensity (I^*) versus the stimulation frequency for (c) the conjugate and (d) direct waves.

and 4.49a, one notices that the decline of Γ occurs for lower frequencies in the thicker cloud, which might be misleading for the bubble size measurement. The reason for this discrepancy is that signals with frequencies close and lower than $f_{\rm b}$ also have quite low propagation speeds within the bubble cloud. Hence, these signals have no enough time to pass through the thick cloud and reach S_1 before cavitation occurs in the domain.

As other indicators, I and I^* for both the conjugate and direct waves are provided in Figs. 4.49c and 4.49d versus different stimulation frequencies, evaluated for 19 signal periods starting from $t = 100 \,\mu s$. Similarly to the previous test case with the thin bubble-layer cloud, these indicators better accentuate the cloud natural frequencies. The filtering effect, which occurs for frequencies higher than f_b , is evident from I^* of the conjugate waves shown in Fig. 4.49c. As also depicted, I of the conjugate waves almost gradually decreases by increasing the stimulation frequency, showing that even signals with quite low frequencies have no enough time to effectively pass through this thick bubble-layer cloud. On the contrary, the filtering behavior is absent in Fig. 4.49d for the direct waves as they do not encounter the bubble cloud. However, the direct waves still have some signatures of the cloud dynamics, which can be better revealed by I^* . Compared to I, I^* better distinguishes the extremums, as shown in Fig. 4.49d.

In all the provided cases, the numerical simulations stop as soon as any cavitation is detected in the domain. To better show how the modulation process filters out some features of the cloud dynamics, the cavitation barrier was lifted for the previous interaction of the thick bubble-layer cloud (L=2.5 mm, $\beta_0=0.01$, $R_0=10$ µm) with the WPC process at the stimulation frequency of 250 kHz. The pressure disturbance histories of the conjugate and direct waves are provided in Figs. 4.50a and 4.50b. As depicted, even when the trend of the conjugate wave history is quite asymmetric due to strong non-linear oscillations of constituting bubbles, the amplified direct waves are still symmetric in time. This behavior justifies the results provided before in the sense that although the direct waves have some information regarding the cloud dynamics, they are mainly governed by the modulation process—the fact which does not hold for the conjugate waves as they directly pass through the bubble cloud.

In this part, interactions of WPC with poly-disperse bubble clouds are studied. For this aim, first, the cloud consisting of bubbles with the radii of 10 μ m and 14 μ m, which was

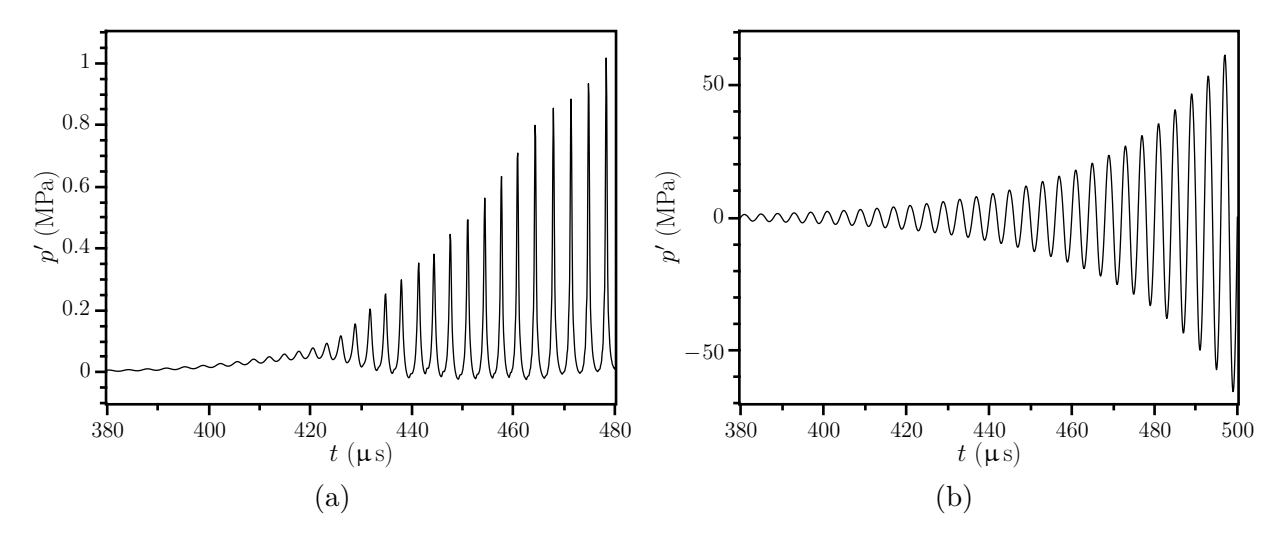


Fig. 4.50. Interaction of a thick bubble-layer cloud (L=2.5 mm, $\beta_0=0.01$, $R_0=10$ µm) with the paraxial WPC shown in Fig. 4.46: pressure disturbance histories at the stimulation frequency of 250 kHz for (a) the conjugate and (b) direct waves in the absence of the cavitation phenomenon.

previously investigated in Fig. 4.24, is assessed in the setup shown in Fig. 4.46. This cloud has the thickness of 0.25 mm and the void fraction of 0.01. With the same simulation and physical properties as those in the previous respective cases, this cloud is stimulated by signals with frequencies in the range of 150–460 kHz with intervals of 10 kHz. As shown in Fig. 4.24, dynamics of this cloud is a mix of those for two mono-disperse clouds, in which two filtering processes are observed at the stimulation frequencies starting from 233.7 and 331.9 kHz (see Fig. 4.24c). Interestingly, Γ of the conjugate waves, depicted in Fig. 4.51a, also shows the same behavior, to some extent. As demonstrated, the first filtering process occurs for the stimulation frequencies between 230–260 kHz, which is mainly due to the effects of bubbles with the radius of 14 μ m. The second filtering feature occurs for the stimulation frequencies higher than 330 kHz, owing to the dynamics of bubbles with the radius of 10 μ m. These results are in line with the dynamics of this cloud provided in Fig. 4.24c. Similarly to the mono-disperse bubble layers, the cloud dynamics has no significant effect on Γ of the direct waves, as illustrated in Fig. 4.51b.

In this case, I and I^* are also obtained for 16 signal periods starting from $t = 100 \mu s$. Although both of these indicators for the conjugate waves demonstrate the filtering behavior,

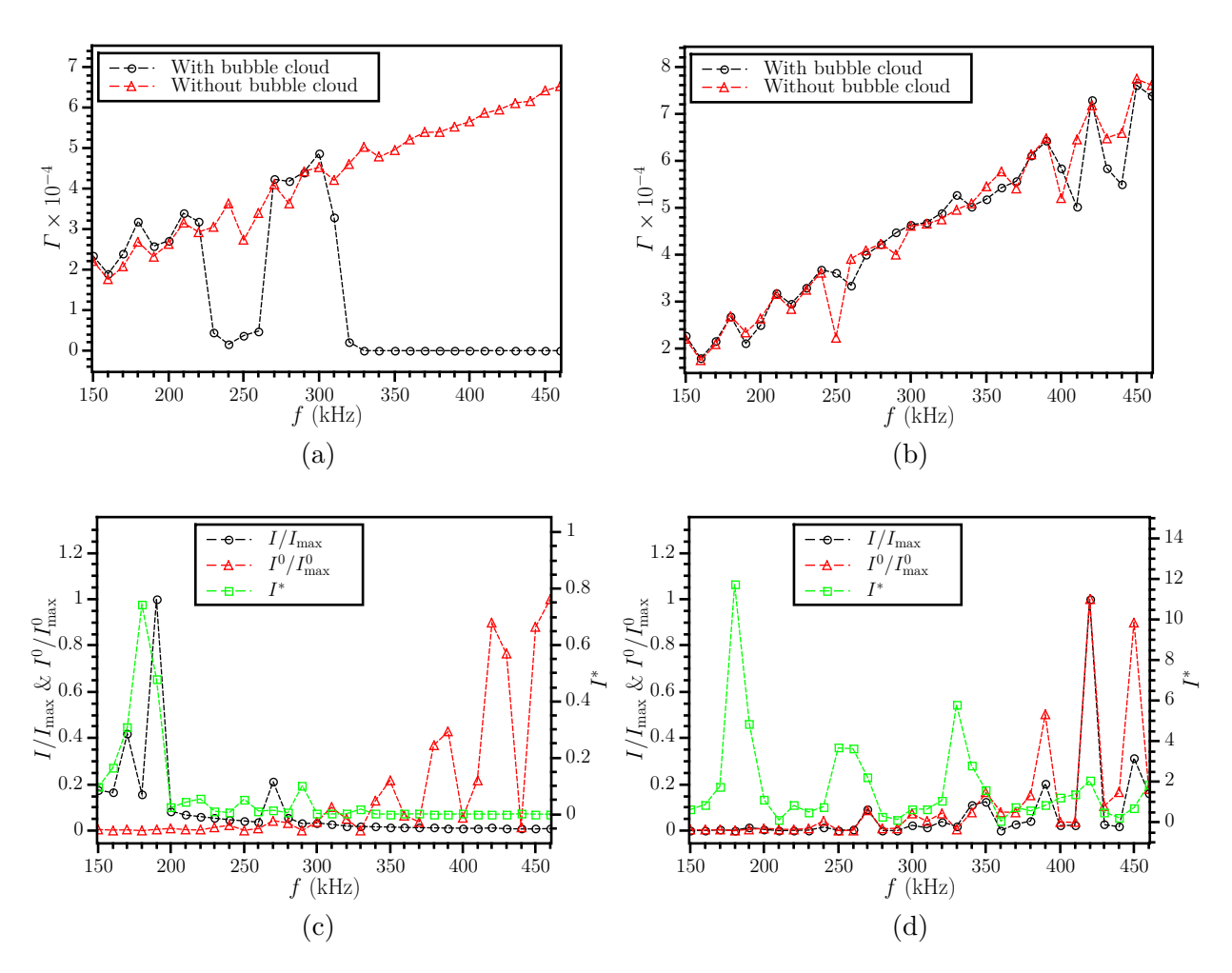


Fig. 4.51. Interaction of the paraxial WPC shown in Fig. 4.46 with a poly-disperse thin bubble-layer cloud (L=0.25 mm, $\beta_0=0.01$, $R_0=10$ µm, 14 µm): variations of the exponential amplification factor (Γ) with the stimulation frequency for (a) the conjugate and (b) direct waves; and the normalized intensities ($I/I_{\rm max}$, $I^0/I_{\rm max}^0$) and the relative intensity (I^*) versus the stimulation frequency for (c) the conjugate and (d) direct waves.

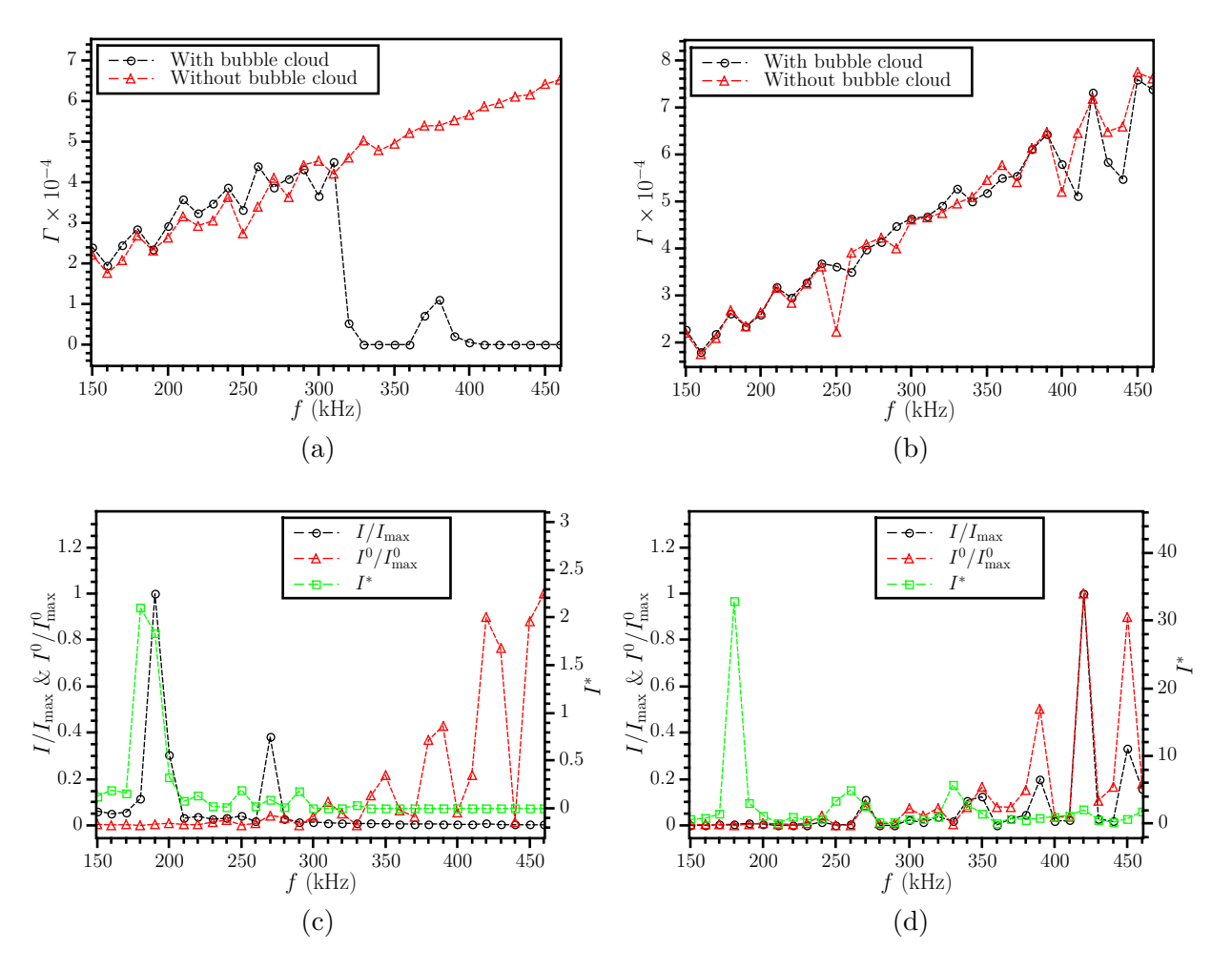


Fig. 4.52. Interaction of the paraxial WPC shown in Fig. 4.46 with a poly-disperse thin bubble-layer cloud (L=0.25 mm, $\beta_0=0.01$, $R_0=8$ µm, 10 µm): variations of the exponential amplification factor (Γ) with the stimulation frequency for (a) the conjugate and (b) direct waves; and the normalized intensities ($I/I_{\rm max}$, $I^0/I_{\rm max}^0$) and the relative intensity (I^*) versus the stimulation frequency for (c) the conjugate and (d) direct waves.

the two filtering phases are better pronounced by I, as shown in Fig. 4.51c. As also expected, I and I^* of the direct waves show no filtering trend; however, I^* can better distinguish some peaks, as illustrated in Fig. 4.51d. Generally, I^* of direct waves are affected by both the bubble cloud dynamics and the variations of the phase pattern. In this case, the peaks of I^* for the direct waves, shown in Fig. 4.51d, are very close to the natural frequencies of this poly-disperse cloud (see Fig. 4.24).

The bubble layer of the previous numerical setup was replaced with another poly-disperse bubble-layer cloud consisting of bubbles with the radii of 8 μ m and 10 μ m. This bubble cloud was previously assessed in Fig. 4.24. The thickness and the volume fraction of this cloud are 0.25 mm and 0.01, respectively. This cloud also has two filtering processes at the stimulation frequencies starting from 331.9 and 420.1 kHz, which are the natural frequencies of the individual bubbles within this cloud (see Fig. 4.24c). Considering Γ of the conjugate waves in Fig. 4.52a, one notices two filtering processes, one for the stimulation frequencies in the range of 330–360 kHz and the other for the frequencies higher than 420 kHz. These results are consistent with those shown in Fig. 4.24. In addition, similarly to the previous poly-disperse cloud, Γ of the direct waves does not appear to be a good indicator for studying the cloud dynamics since it does not properly accentuate the signatures of the cloud, as previously explained.

The relative intensity, I^* , of both the conjugate and direct waves, which are obtained for 16 signal periods starting from $t = 100 \,\mu\text{s}$, again distinguish a number of peaks. Similarly to the previous test cases, these peaks occur due to both the cloud dynamics and the variations of the phase pattern, as illustrated in Figs. 4.52c and 4.52d. In terms of the filtering feature of the conjugate waves, although both I and I^* depict the first process, the second filtering process is not well resolved in Fig. 4.52c.

4.3.4 Interaction of WPC with Spherical Bubble Clouds

In this subsection, interactions of an axisymmetric WPC with spherical bubble clouds (Fig. 2.2d) with uniform initial bubble distributions are studied. The employed numerical setup for these simulations is illustrated in Fig. 4.53a. Similarly to the one shown in Fig. 4.43a, in each simulation case, the conjugator is initially stimulated by a point source emitting

signals with the main frequency in the range of 150–400 kHz and intervals of 10 kHz, based on the relation provided by Eqs. (4.25) for $0 \le t \le 32$ µs. This point mass source is located on the axis at the distance of 1 cm from the conjugator surface.

Then, a spherical bubble cloud with the diameter of 1 cm and β_0 of 5×10^{-5} , which contains bubbles with the radius of 10 μ m, replaces the point source at t=35 μ s, as illustrated in Fig. 4.53a. In this case, the grid elements are properly refined near the spherical bubble cloud, as illustrated in Fig. 4.53b. To adequately represent the cloud surface, the geometrically non-linear elements (with curved edges) are used (see Appendix A.1). The minimum grid size element and the time step are set to 0.3 mm and 10 ns, respectively. The other physical and simulation properties are the same as those in the previous respective cases (see Table 4.5 and Section 4.3.2). The conjugate and direct waves are recorded at the upstream (S₁) and downstream (S₂) sensors, which are located on the axis at z=1.25 cm and z=43.5 cm, respectively.

Compared to interactions of the paraxial WPC with the bubble-layer clouds (Section 4.3.3), Γ of the conjugate waves, illustrated in Fig. 4.54a, shows some differences. First, no filtering feature is observed for the frequencies higher than $f_{\rm b}$ because the modulation process occurs along many different directions within the axisymmetric conjugator. As a result, there is a number of conjugate signals which do not pass through the cloud, and, therefore, they are not filtered. Instead of the filtering behavior, Γ even shows some increases due to the cloud presence, as depicted in Fig. 4.54a. This behavior is due to the violent non-linear responses of bubbles within the cloud, which can increase Γ of the conjugate waves. Second, Γ of the conjugate waves varies almost linearly with the stimulation frequency in the absence of the bubble cloud, as shown in Fig. 4.54a. The reason for such a behavior is, again, the modulation of signals in different directions in the axisymmetric domain, engaging different active lengths of the conjugator. Hence, the even/odd phase pattern of the modulation process would be less effective in the axisymmetric than the paraxial WPC.

Figure 4.54b shows Γ of the direct waves versus the stimulation frequency. As depicted, the presence of the bubble cloud has no significant impact on Γ at S_2 , owing to the fact that the conjugator filters out the cloud dynamic features to a great extent. Similarly, the intensity of the direct waves, which is obtained for 55 signal periods starting from $t = 100 \mu s$, keeps its trend after including the bubble cloud. Hence, the relative intensity, I^* , remains

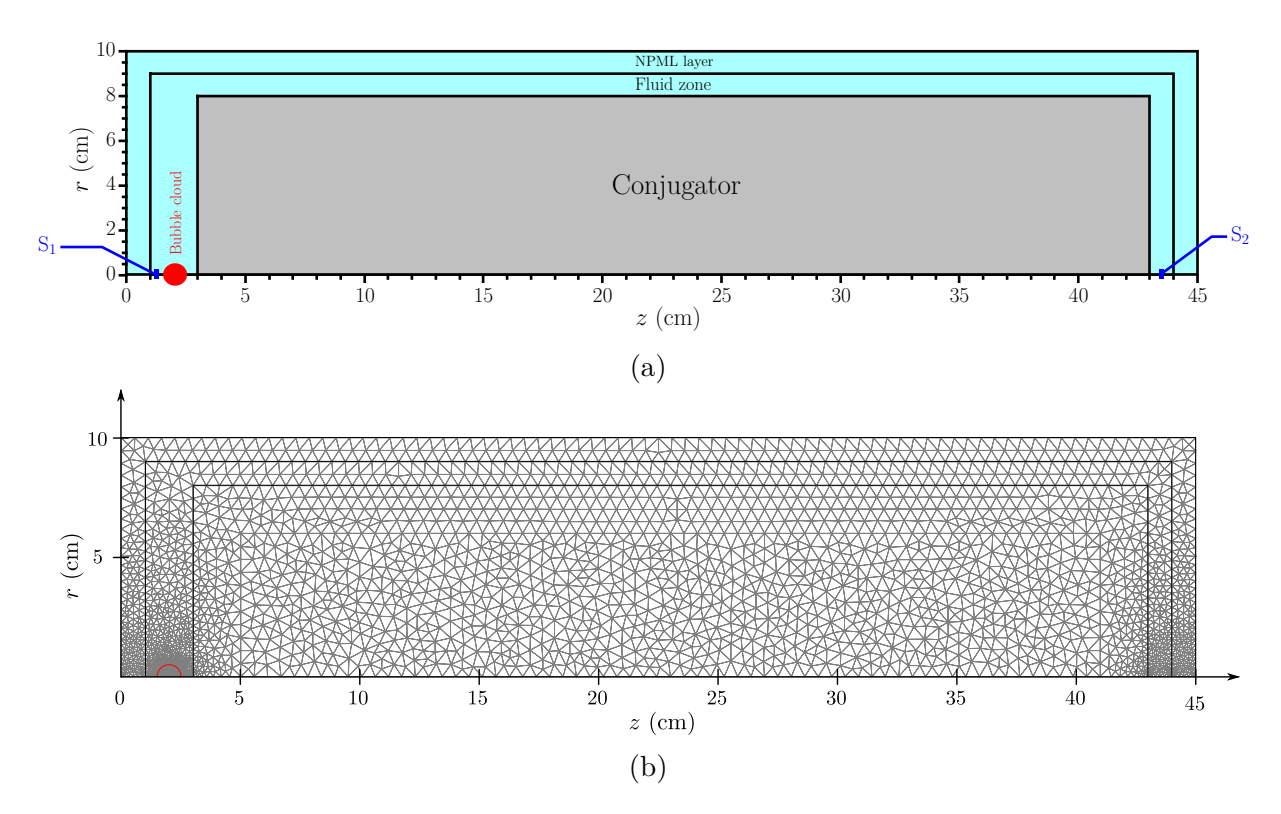


Fig. 4.53. Interaction of an axisymmetric WPC with a spherical bubble cloud ($A_0 = 0.5$ cm, $\beta_0 = 5 \times 10^{-5}$, $R_0 = 10$ µm): (a) the numerical setup and the sketch. The gray zone is the conjugator, the blue zones are filled with water, the red sphere is the bubble cloud, and S_1 and S_2 are the upstream and downstream sensors. (b) The employed numerical grid.

close to 1 for the direct waves, as demonstrated in Fig. 4.54d.

As demonstrated in Fig. 4.54c, I of the conjugate waves shows an overall growth by increasing the stimulation frequency. However, in the presence of the cloud, some local variations are observed around the natural frequencies of the cloud in the trans-resonant regime. The intensity appears to be more sensitive than Γ to variations of the phase patterns, which might also contribute to these local variations of I. The relative intensity of the conjugate waves, shown in Fig. 4.54c, highly diminishes for the frequencies higher than $f_{\rm b}$ (331.9 kHz) due to the filtering feature in this frequency range. Hence, I^* of the conjugate waves serves as a better indicator for estimation of the bubble size dimensions in this case.

To better evaluate interactions of the axisymmetric WPC with this cloud ($A_0 = 0.5$ cm,

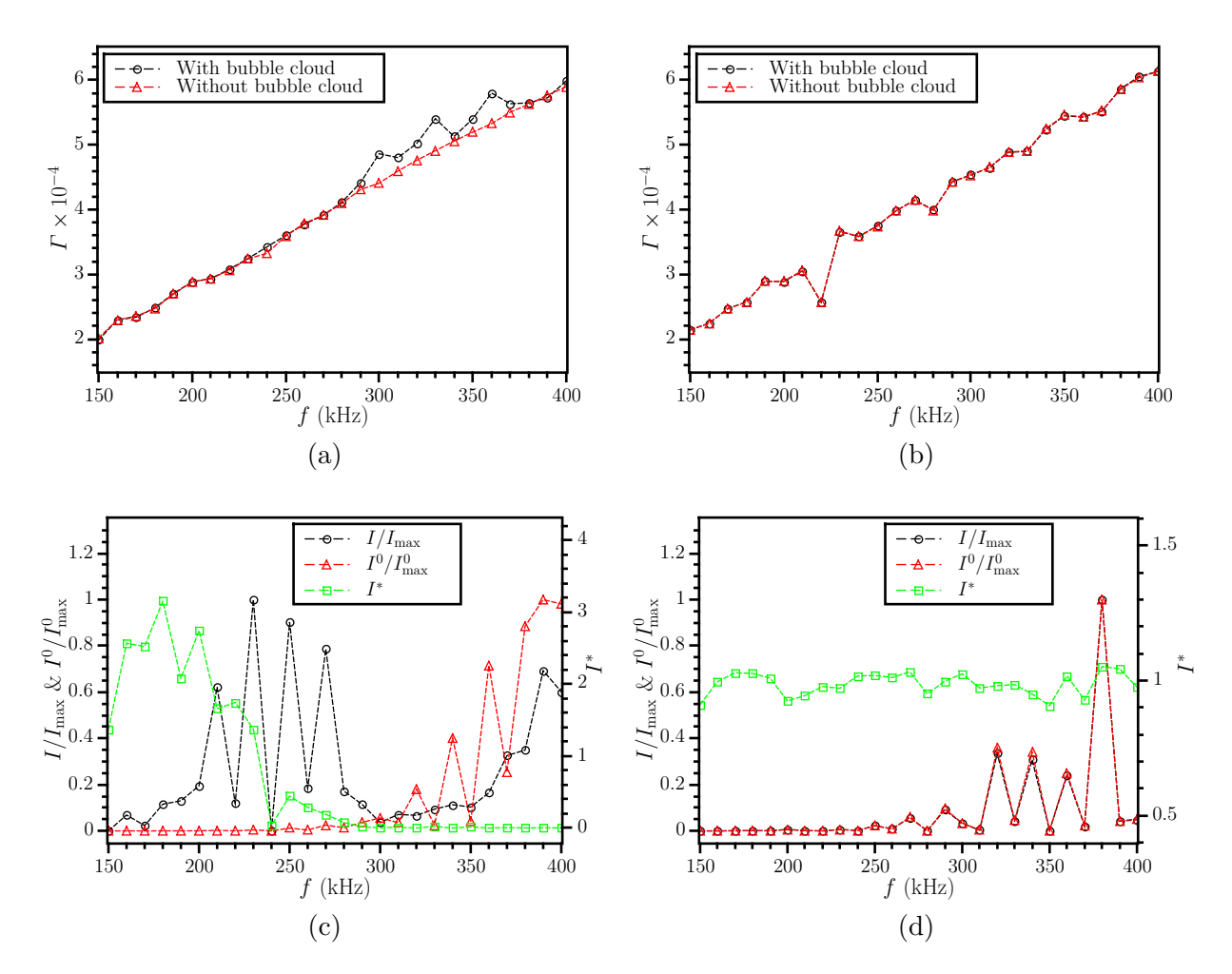


Fig. 4.54. Interaction of the axisymmetric WPC shown in Fig. 4.53a with a dilute spherical bubble cloud ($A_0 = 0.5$ cm, $\beta_0 = 5 \times 10^{-5}$, $R_0 = 10$ µm): variations of the exponential amplification factor (Γ) with the stimulation frequency for (a) the conjugate and (b) direct waves; and the normalized intensities ($I/I_{\rm max}$, $I^0/I_{\rm max}^0$) and the relative intensity (I^*) versus the stimulation frequency for (c) the conjugate and (d) direct waves.

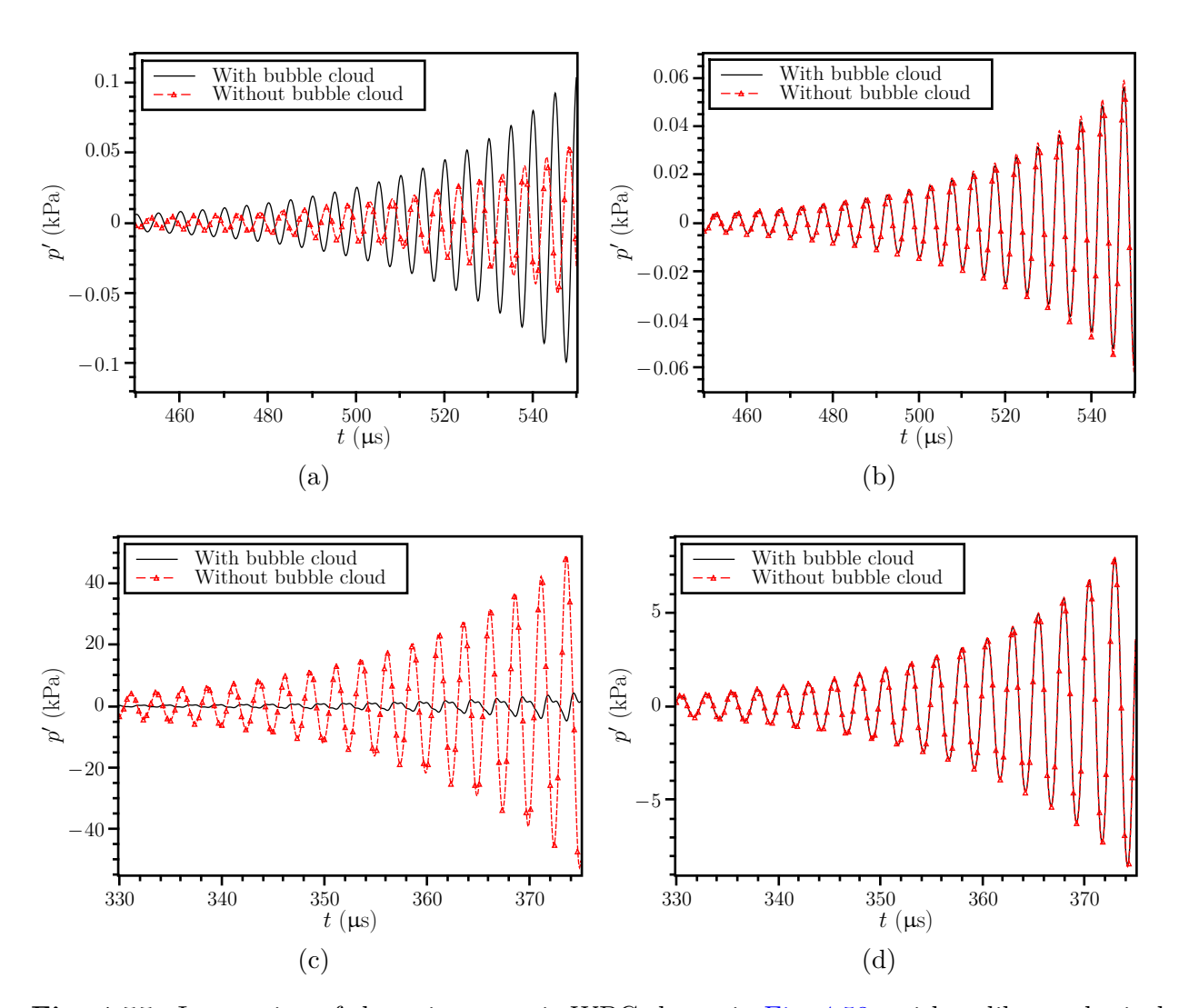


Fig. 4.55. Interaction of the axisymmetric WPC shown in Fig. 4.53a with a dilute spherical bubble cloud ($A_0 = 0.5$ cm, $\beta_0 = 5 \times 10^{-5}$, $R_0 = 10$ µm): pressure disturbance histories for the stimulation frequency of 200 kHz recorded at (a) S_1 and (b) S_2 , and for the stimulation frequency of 400 kHz recorded at (c) S_1 and (d) S_2 .

 $\beta_0 = 5 \times 10^{-5}$, $R_0 = 10 \ \mu\text{m}$), the pressure disturbance histories recorded at S_1 and S_2 are provided. Figures 4.55a and 4.55b show how the pressure signals are affected in the presence of the bubble cloud for the stimulation frequency of 200 kHz at the upstream and downstream sensors, respectively. Being in line with the results provided for the intensity in Figs. 4.54c and 4.54d, the direct signals at S_2 are not noticeably affected by the cloud while stronger conjugate waves are recorded at S_1 in the presence of this cloud.

For the stimulation frequency of 400 kHz, as illustrated in Fig. 4.55d, although the signals recorded at S_2 are not significantly influenced, Fig. 4.55c shows that the conjugate waves are significantly filtered out by the cloud. These results are again consistent with those shown in Figs. 4.54c and 4.54d. Another interesting feature observed in Fig. 4.55c is distortions of the conjugate wave profile after passing through the bubble cloud. This behavior is due to peculiar non-linear responses of bubbles within the cloud which are strongly stimulated at this frequency (especially those which are closer to the conjugator). These non-linear features of the bubble dynamics might misleadingly result in higher estimations for Γ , as also depicted in Fig. 4.54a for the stimulation frequencies higher than 300 kHz. In this sense, Γ is not always a reliable indicator as it conveys no information regarding the signal strength.

The filtering feature, observed in the previous test cases, is better illustrated in pressure disturbance contours. Figure 4.56a shows the pressure disturbance contour within the fluid zone in front of the conjugator for the stimulation frequency of 200 kHz at $t=500~\mu s$. As depicted, the conjugate waves can pass through the bubble cloud with slight distortions of the wave fronts. On the contrary, this cloud significantly blocks the conjugate waves with the frequency of 400 kHz, which is illustrated in Fig. 4.56b at $t=360~\mu s$. As a result, the wave fronts are noticeably deflected to turn around the cloud. As previously discussed, this filtering feature is due to very low propagation speeds of waves within the cloud for the frequencies higher than the natural frequency of bubbles within the cloud. This filtering process occurs even for such a dilute bubble cloud with the initial void fraction of 5×10^{-5} .

It is of interest to investigate how bubble clouds with higher volume fractions interact with WPC processes. Hence, in the previous axisymmetric numerical setup (Fig. 4.53a), the initial volume fraction of the cloud is increased 100 fold, to be 5×10^{-3} . The other physical and simulation properties are the same as those for the previous numerical setup shown in Fig. 4.53a.

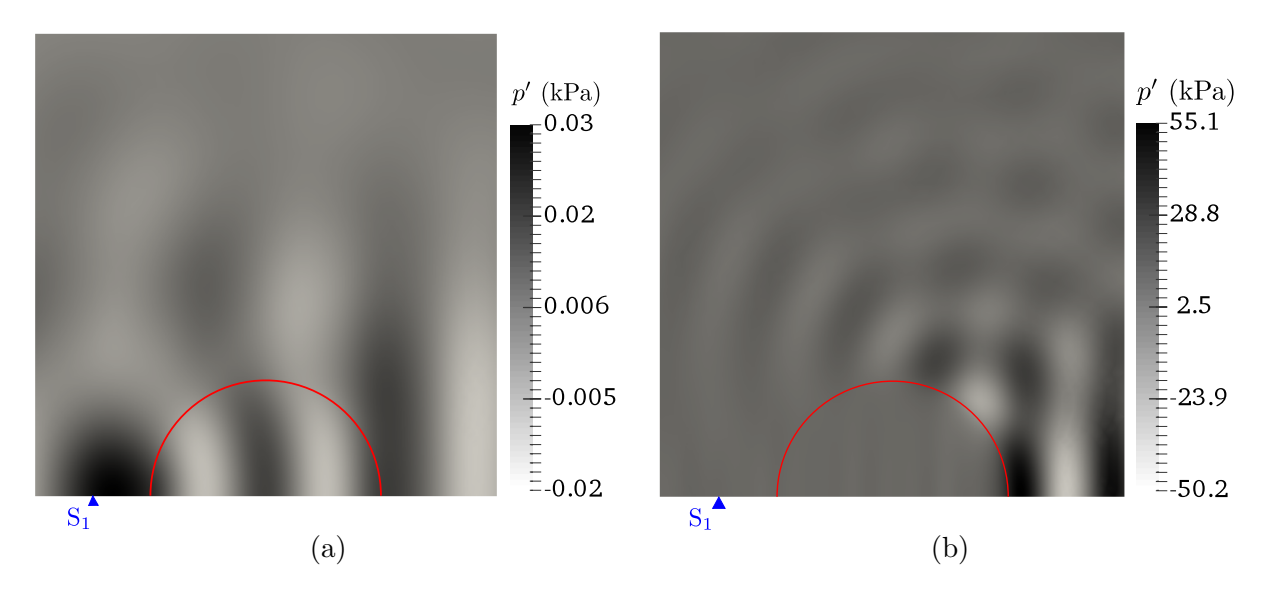


Fig. 4.56. Interaction of the axisymmetric WPC shown in Fig. 4.53a with a dilute spherical bubble cloud ($A_0 = 0.5$ cm, $\beta_0 = 5 \times 10^{-5}$, $R_0 = 10$ µm): pressure disturbance contours for the stimulation frequency of (a) 200 kHz at t = 500 µs and for the stimulation frequency of (b) 400 kHz at t = 360 µs. The cloud boundary is shown in red, and the location of S_1 is indicated by the blue triangle.

To ensure that waves are properly resolved, a grid independence study for the stimulation frequency of 200 kHz is carried out, for which short-wavelength signals within this dense cloud are expected. Figure 4.57 shows the pressure disturbance profiles along the axis, in front of the conjugator $(0.0 \le z \le 30 \text{ mm})$, for three successively refined grids at $t = 500 \text{ }\mu\text{s}$. As depicted, p' shows no noticeable changes after the last grid refinement step. Hence, the minimum grid element size (ΔL) is set to 0.3 mm for this set of simulations. The time step is also set to 10 ns, which is the same as the one for interactions of WPC with the dilute bubble cloud (Figs. 4.54–4.56).

The amplification factor of the conjugate and direct waves are provided in Figs. 4.58a and 4.58b, respectively. While the presence of the bubble cloud makes no significant impact on Γ of the direct waves, slight deviations are detected in the amplification factor of the conjugate waves for certain stimulation frequencies. However, similarly to the previous test case for the dilute bubble cloud (Figs. 4.54a and 4.54b), Γ does not appear to be a proper indicator for estimation of the bubble size dimension. As to the intensities, which are

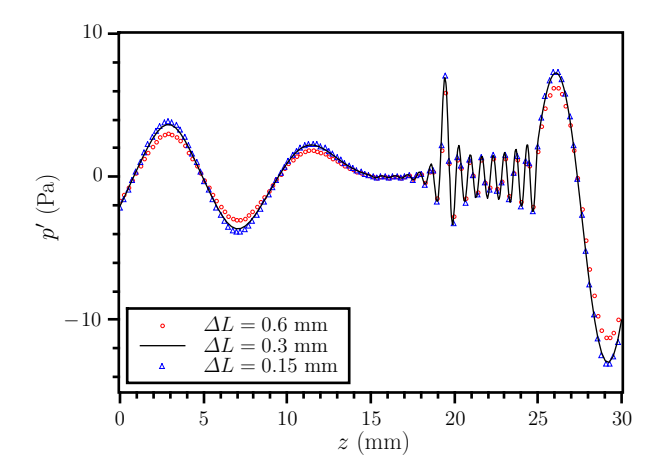


Fig. 4.57. Interaction of the axisymmetric WPC shown in Fig. 4.53a with a dense spherical bubble cloud ($A_0 = 0.5$ cm, $β_0 = 5 \times 10^{-3}$, $R_0 = 10$ μm): the grid independence study using three successively refined grids for evaluation of the pressure disturbance profiles along the axis in front of the conjugator at t = 500 μs. ΔL is the minimum characteristic length of the grid elements.

evaluated for 74 signal periods starting from $t = 100 \,\mu\text{s}$, no appreciable changes are observed for direct waves in the presence of the cloud. Therefore, as shown in Fig. 4.58d, I^* remains close to 1 for different stimulation frequencies. On the other hand, intensities of the conjugate waves, illustrated in Fig. 4.58c, appear to have more signatures of the cloud dynamics, which can be used to measure the bubble dimensions.

As previously discussed, the intensity of the conjugate waves generally increases with the stimulation frequency since the upstream sensor can be reached by the amplified signals which have not directly passed through the cloud. A more descriptive indicator in this case is I^* of the conjugate waves, which shows a decreasing trend in Fig. 4.58c. Since for the frequencies close and higher than f_b the filtering feature of the bubble cloud is more effective, this decreasing trend in I^* of the conjugate waves is expected. However, in contrast with the dilute cloud case shown in Fig. 4.54c, there is no sharp reduction in I^* of the conjugate waves when the stimulation frequency exceeds f_b . This behavior is due to the fact that the propagation speeds of signals within a cloud reduces by increasing the volume fraction [38]. As a result, the signals with frequencies quite lower than f_b also need a long time to effectively pass through the cloud and reach S_1 , but the simulation can not proceed for such a long time

due to the cavitation barrier. Owing to this reason, the natural modes of the cloud are not properly distinguished in Fig. 4.58c.

To overcome this issue in experiments, the modulation depth of the conjugator can be reduced (as far as the supercritical condition of the WPC process still holds) in order to provide more time for the conjugate waves to effectively pass through the cloud before the cavitation occurs. However, this is not a feasible option for the numerical analyses as it

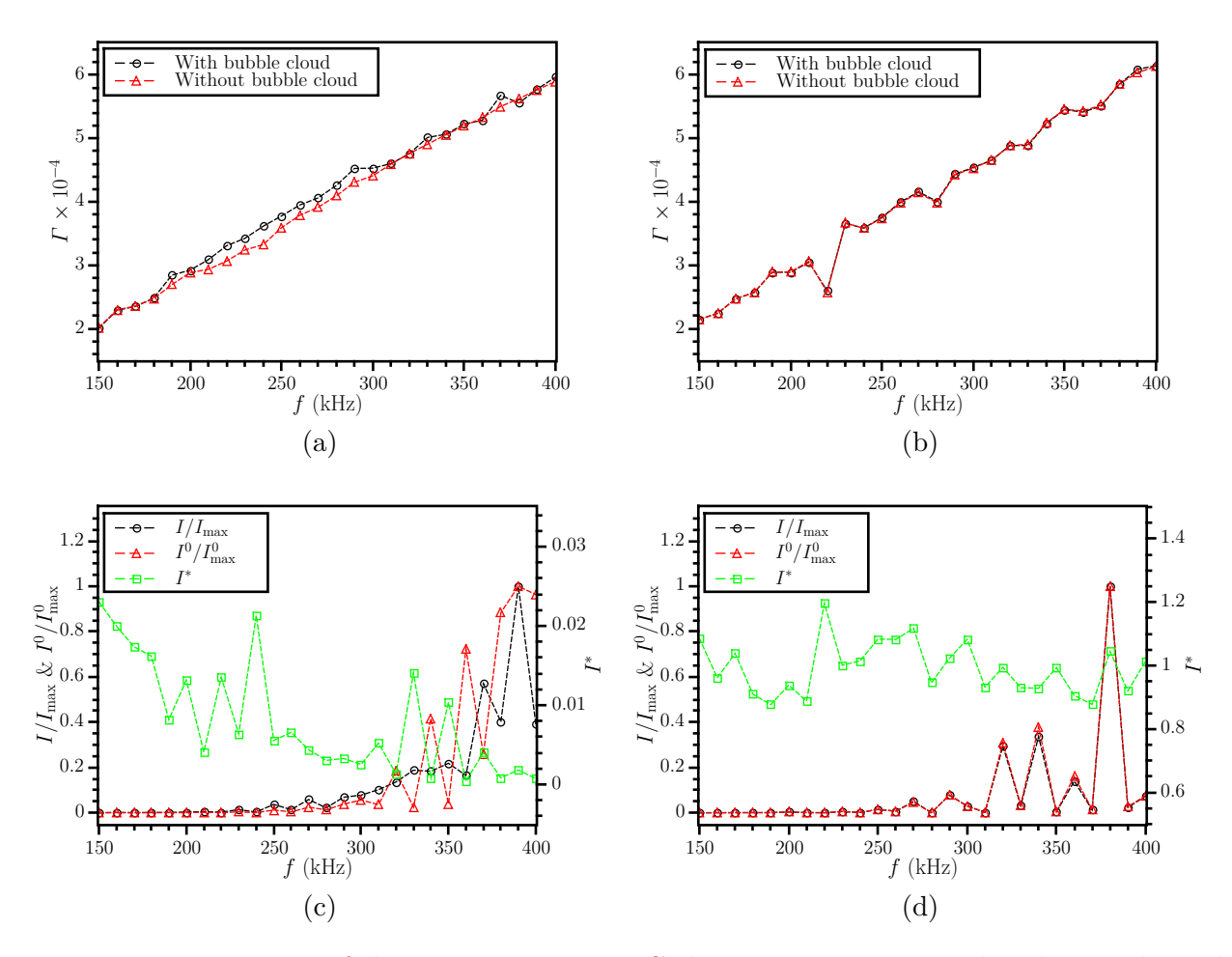


Fig. 4.58. Interaction of the axisymmetric WPC shown in Fig. 4.53a with a dense spherical bubble cloud ($A_0 = 0.5$ cm, $\beta_0 = 5 \times 10^{-3}$, $R_0 = 10$ µm): variations of the exponential amplification factor (Γ) with the stimulation frequency for (a) the conjugate and (b) direct waves; and the normalized intensities ($I/I_{\rm max}$, $I^0/I_{\rm max}^0$) and the relative intensity (I^*) versus the stimulation frequency for (c) the conjugate and (d) direct waves.

substantially increases the simulation time.

To better investigate propagation of the signals within the dense cloud previously analyzed, the pressure disturbance contours for two different stimulation frequencies are provided. Figure 4.59a illustrates slight penetration of the conjugate waves into the bubble cloud at $t=500~\mu s$ for the stimulation frequency of 200 kHz. As shown, the wavelengths of the signals within the cloud significantly decrease, yielding a lower propagation speed at a given temporal frequency. Comparing Figs. 4.56a and 4.59a shows how the bubble volume fraction affects penetration of the acoustic signals into the bubble clouds, which eventually influences the intensity recorded at S_1 . The pressure disturbance contour for the stimulation frequency of 400 kHz is also illustrated in Fig. 4.59b at $t=360~\mu s$. As expected, a strong filtering feature is observed at this frequency, and, as a result, the conjugate signals are noticeably distorted by the bubble cloud.

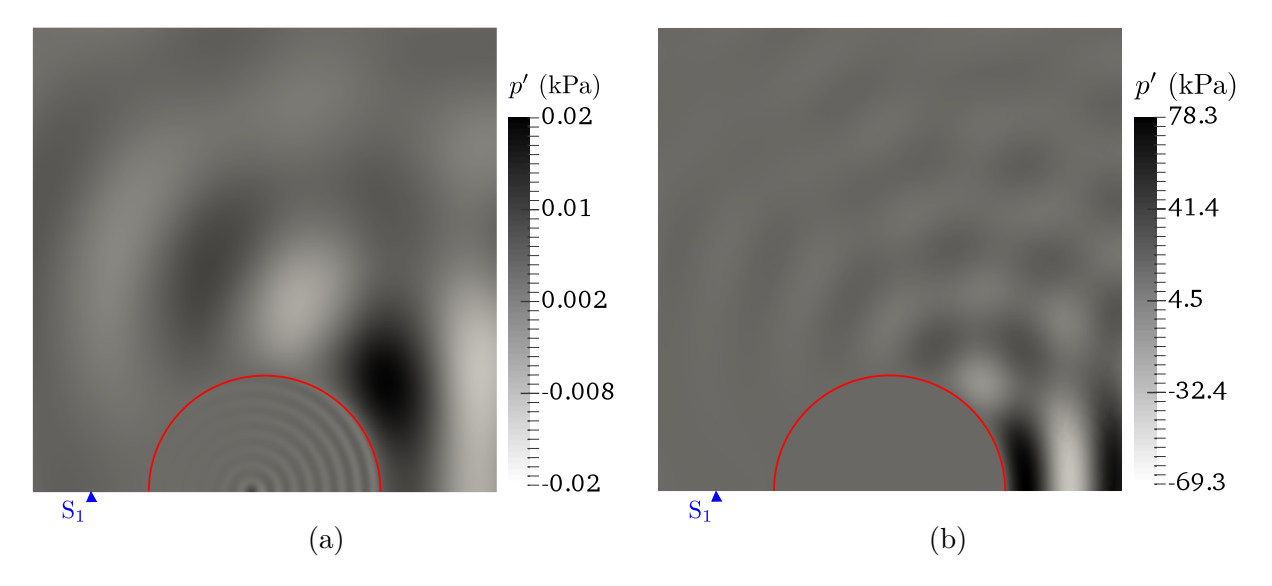


Fig. 4.59. Interaction of the axisymmetric WPC shown in Fig. 4.53a with a dense spherical bubble cloud ($A_0 = 0.5$ cm, $\beta_0 = 5 \times 10^{-3}$, $R_0 = 10$ µm): pressure disturbance contours for the stimulation frequency of (a) 200 kHz at t = 500 µs and for the stimulation frequency of (b) 400 kHz at t = 360 µs. The cloud boundary is shown in red, and the location of S_1 is indicated by the blue triangle.

4.4. CONCLUSION 163

4.4 Conclusion

In this chapter, first, extensive and detailed verifications of the numerical model were carried out in Section 4.1, including the grid convergence, the performance of the proposed modified NDG scheme, wave propagation in solid and fluid media, the effectiveness of the NPML boundaries, interaction of waves with fluid-solid interfaces, and dynamic behaviors of different bubble clouds. The numerical results in Section 4.1 showed acceptable accuracy as compared with the available data in the literature.

After being assured of the accuracy and the performance of the proposed numerical model, two WPC setups were considered in Section 4.2: a simplified paraxial one, for which an analytical solution is available; and a full axisymmetric setup with the linear and weakly non-linear flow regimes. The numerical results properly reproduced the key WPC features, such as retro-focusing of signals at the focal zone and the parametric resonance. For the first time, the signals generated by the physical modulation process were shown within both solid and fluid media.

Then, the idea of using WPC setups for measuring bubble dimensions were examined in Section 4.3. For this goal, four types of bubble clouds were considered: single bubbles, bubble-plane clouds, bubble-layer clouds, and spherical bubble clouds. The numerical results showed that the cloud dynamics can have noticeable impact on the modulation process within the conjugator when the bubbles are dynamically synchronized, which happens for bubble-plane clouds. The reason for such an observation is the fact that emitted signals from individual bubbles, per se, are usually quite weak during the measurement phase, and they are not able to significantly change the amplification factor, Γ .

The bubble dynamics of more realistic clouds, such as bubble-layer and spherical bubble ones, are not synchronized. For these clouds, the numerical results revealed that the conjugate and direct waves have some informative signatures with regard to the bubble cloud dynamics. For instance, conjugate signals with specific range of frequencies are significantly filtered by the clouds. To extract these signatures, different indicators were suggested in this study, such as the exponential amplification factor (Γ) , the intensity (I), and the relative intensity (I^*) , which have their own benefits.

The results provided in this chapter confirmed the idea of using WPC-related techniques

for measuring bubble dimensions within different bubble clouds. This goal was obtained via employing proper indicators, which could effectively extract informative signatures from the conjugate and direct signals.

CHAPTER 5

Final Remarks

In this chapter, the main contributions, key outcomes, and final conclusions are provided in Section 5.1. A number of recommendations for the future research in this field follow in Section 5.2.

5.1 Conclusions

In the first part of the present study, a high-order 2D/axisymmetric Wave Phase Conjugation (WPC) simulator was developed. The underlying physical model was chosen to be sufficiently sophisticated so that realistic setups with multiple solid, fluid, and bubbly regions could be simulated. The model considers propagation of the acoustic waves in the conjugator, the surrounding fluid zones, and other solid objects, if present. The non-linear effects in fluid zones can be accounted for, if necessary. The modulation effect of the magnetic field in the conjugator was modeled via a source term in the governing equations. This is the first time that such a comprehensive and detailed model for the WPC process has been considered in the literature.

The governing equations were solved via high-order spatial and temporal schemes. In space, the employed Nodal Discontinuous Galerkin (NDG) method was modified by using independent bases for the solution and flux terms to reduce aliasing errors in the non-linear regime. Other essential components of the numerical method are proper treatment of the

wave transmissions/reflections at material interfaces via the flux differencing method and elimination of spurious wave reflections from outer boundaries of the computational domain with Nearly Perfectly Matched Layer (NPML) layers. All ingredients of the numerical method were verified, individually and in various combinations, by an extensive set of test problems of gradually increasing complexity.

The developed simulator was then applied to analyze the acoustic fields of WPC processes. Two setups were considered: a simplified paraxial one and a full axisymmetric simulation with the linear and weakly non-linear fluid flow regimes. It was demonstrated that in all cases the simulator reproduced accurately the main WPC properties, such as the signal retro-focusing and the parametric resonance. For this comprehensive model, the physical modulation process within the conjugator was visualized for the first time, and the influence of the stimulation frequencies on the conjugation efficiency was observed.

Thus, the developed WPC simulator was deemed to be useful for numerical experiments within a range of practical WPC applications for which the axisymmetric formulation is meaningful. The first such example, investigated by Modarreszadeh et al. [120], is the application of the WPC solver to the estimation of bubble size dimensions via the wave phase conjugation, in which different bubble clouds are placed between the transducer and the conjugator. This application was thoroughly assessed in the second part of this research.

In this study, four different bubble sets were investigated: 1) single bubbles in axisymmetric domains; 2) bubble-plane clouds, in which all the bubbles are located on a specific plane in paraxial domains; 3) bubble-layer clouds, which have finite axial lengths in paraxial domains; and 4) spherical bubble cloud, in axisymmetric domains. To simulate dynamic behaviors of each bubble within these clouds, the modified version of the Keller-Miksis (KM) model, proposed by Parlitz et al. [14], was used. In addition, special considerations were given to properly estimation of the driving pressure for each bubble. Since for strong excitation of bubbles the KM model is highly stiff, a C^{∞} -diffeomorphism map was used to solve for the bubble dynamics in a transformed domain, in which the KM model is less stiff. Then, by implementing the volume-averaging technique, the effects of bubble dynamics were incorporated into both the linear and non-linear fluid flow governing equations via introducing additional source terms. Due to inconsistent required time steps for bubbly and bubble-less zones, marching in time was de-coupled for the flow evolution and bubble excitation. The

5.1. CONCLUSIONS 167

proposed modified Runge-Kutta (RK)-NDG method was then used to numerically solve the governing equations.

This numerical model was then employed to investigate different dynamic aspects of the four aforementioned bubble clouds, such as linear and non-linear harmonics, filtering features, non-linear behaviors, and effects of the poly-dispersity. After such a comprehensive assessment of different bubble clouds, their interactions with the WPC process were studied. While the effects of a single bubble on the modulation process are negligible, the numerical experiments revealed that bubble-plane clouds are able to significantly influence the modulation process within the conjugator when the natural frequency of the individual bubbles is stimulated. The reason for such a behavior is the fact that the bubbles within bubble-plane clouds are dynamically synchronized. However, due to sensitivity of the modulation process to the signal phase pattern within the conjugator, the scattered waves from the bubble-plane clouds might have either positive or negative effects on the amplification factor, Γ . Thus, Γ of the direct waves appeared to be a proper indicator for estimation of the bubble size dimensions within the bubble-plane clouds.

In contrast with bubble-plane clouds, the bubble dynamics of bubble-layer and spherical bubble clouds are not synchronized. As a result, investigation of these bubble sets showed that the signals emitted by these clouds are not usually strong enough to noticeably influence the modulation process. Hence, although the direct waves have some characteristics of the bubble cloud dynamics, analyzing them, per se, is not sufficient for proper estimation of the bubble size dimensions. On the contrary, assessing different bubble clouds revealed that the conjugate waves have some determinative signatures of the cloud dynamics, which can be used for the measurement purposes. For instance, the propagation speed of a signal within bubble clouds significantly depends on its frequency. If it exceeds the natural frequency of bubbles within the cloud, the propagation speed considerably diminishes—which can be seen as a filtering process. In this sense, the bubble clouds can effectively block the conjugate signals with a specific range of frequencies. Hence, compared to the direct signals, assessing the conjugate waves was more helpful for measuring bubble size dimensions in realistic clouds—regardless of the fact that in realistic axisymmetric modulation processes, the conjugate waves are the ones enjoying a number of interesting features such as the signal retro-focusing and compensations for the signal phase distortions.

In this study, the exponential amplification factor (Γ) , the intensity (I), and the relative intensity (I^*) were used to extract signatures of the cloud dynamics out of the conjugate and direct waves. These indicators have their own pros and cons with regard to the measurement goals. The parameter Γ conveys no information on the signal strength, and it is very sensitive to variations of the wave profile. Hence, it can be a good indicator for weak signals. It is to be noted that finding Γ , in general, is not always straight-forward, and it depends on the curve-fitting algorithm. On the contrary, I^* can be easily computed, but it may ignore subtle variations of the signal profile. The current study showed that when the whole conjugate signals pass through the clouds (such as bubble-layer clouds in paraxial domains), Γ appears to be a good indicator for measuring bubble size dimensions. Otherwise, I^* is deemed to be more reliable, such as for the spherical bubble clouds in axisymmetric domains.

In summary, it is of interest to employ WPC for estimation of the bubble size dimensions due to its intrinsic features, such as the retro-focusing and the compensating for phase distortions. The present study showed that the conjugate waves passing through bubble clouds have some useful signatures of the cloud dynamics. These signatures can be extracted via proper post-processing of the results and using determinative indicators, such as the exponential amplification factor or the relative intensity.

5.2 Future Work

With regard to the first part of this study, which was providing a general WPC simulator, a number of recommendations are as follows:

- Effects of the signal attenuation within fluid media can be taken into account by using realistic models.
- Conjugators might be made of anisotropic materials. This feature can be included in the simulator.
- The amplification process within the conjugator can not continue for a long period of time since some non-linear features emerge. These non-linear behaviors, which lead to saturation of the signals within the conjugator, can be added in the model.

5.2. FUTURE WORK 169

• In a number of specific applications, employing the weak shock theory might be not the best option. In those cases, the energy equation can be added to the system of governing equations, and the fully non-linear equations can be solved.

- The current simulator can be generalized for 3D flows on meshes with tetrahedral elements in order to model general cases, which are not necessarily axisymmetric.
- For the future 3D simulator, the current explicit temporal scheme would be inefficient. The implicit Discontinuous Galerkin (DG) scheme in time is a viable option in this regard.
- Besides, in the future 3D solver, the p-adaptive multi-grid methods will be beneficial in terms of the numerical performance.

As to the second part of this study, which employs the WPC-based devices for measuring bubble size dimensions, the future work may include the following considerations:

- The current numerical study gave some idea regarding the potentials of WPC-based devices for measuring bubble size dimensions. Before taking further steps, a comprehensive set of experiments needs to be carried out to confirm the results of this numerical study.
- A few indicators were employed in this study to measure dimensions of the bubbles. Other indicators can be introduced and assessed during the future experiments.
- More general and complicated bubble clouds can be investigated in the future. For instance, bubble clouds with arbitrary geometries and poly-dispersities.
- Beside the bubble size dimensions, the extracted data from the conjugate or direct waves may be used to detect bubble movements as well.
- More general numerical methods, such as the Eulerian-Lagrangian approach, can be implemented to better simulate different bubble clouds.

APPENDIX A

Mapping, Interpolation, and Integration

In this appendix, first, the non-linear transformation, which relates the physical grid elements to the reference ones, is elaborated. Then, the nodal sets which were used in this study for the numerical representation/interpolation and integration are provided.

A.1 Geometrical Transformation

In order to obtain a general numerical formulation, all grid elements in the z-r domain are transformed into a unique reference element defined in the ξ - η coordinate system. The reference elements in 1D and 2D/axisymmetric domains are illustrated in Fig. A.1.



Fig. A.1. Reference elements in the ξ - η coordinate system: (a) 1D and (b) 2D/axisymmetric elements.

In general, a non-linear transformation, \mathcal{L} , is defined to map the reference element to arbitrary grid elements, as depicted in Fig. A.2 for the 2D/axisymmetric domain. To obtain \mathcal{L} , equidistant geometric interpolation nodes with associated Lagrangian shape functions are considered on the reference element. These interpolation nodes for an element, which is geometrically non-linear of order four, are illustrated by red circles in Fig. A.2.

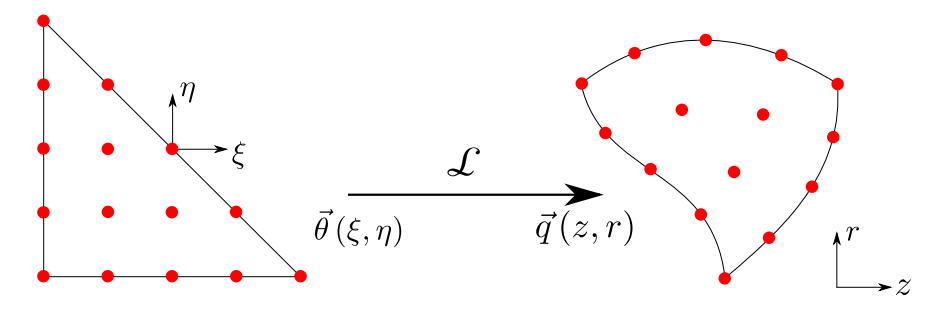


Fig. A.2. Mapping of the reference element in the ξ - η coordinate to a physical element in the z-r domain with the non-linear transformation $\mathcal{L}(\vec{\theta}) = \vec{q}$. The red circles are geometric interpolation nodes for this fourth-order element.

The non-linear transformation, which takes $\vec{\theta}(\xi, \eta)$ to $\vec{q}(z, r)$, is defined as follows:

$$\vec{q} = \mathcal{L}(\vec{\theta}) = \sum_{j=1}^{N} \vec{q}_j \, \psi_j(\vec{\theta}) \,, \tag{A.1}$$

where \vec{q}_j is the coordinate of the interpolation node j in the z-r domain, and ψ_j is the Lagrangian shape function associated with that node. In the above equation, N is the total number of interpolation nodes, which equals (p+1)(p+2)/2 for an element with the geometrical order of p. For such an element, the shape function for the node j would be:

$$\psi_j(\vec{\theta}) = \sum_{m=0}^p \sum_{n=0}^{p-m} a_{mn} \, \xi^m \, \eta^n \,. \tag{A.2}$$

The coefficients a_{mn} in Eq. (A.2) are found with the following property of the Lagrangian

shape functions:

$$\psi_{j}(\vec{\theta_{i}}) = \begin{cases} 1 & i = j \\ 0 & i \neq j \end{cases}; \quad i, j = 1, \dots, N.$$
 (A.3)

For sufficiently small vectors, the non-linear transformation, \mathcal{L} , can be approximated by its Jacobian J at their locations as follows:

$$d\vec{q} = \frac{\partial \mathcal{L}}{\partial \theta} d\vec{\theta} \tag{A.4}$$

$$= \boldsymbol{J} \, \mathrm{d}\vec{\theta} \,; \quad \boldsymbol{J} = \begin{bmatrix} z_{\xi} & z_{\eta} \\ r_{\xi} & r_{\eta} \end{bmatrix} . \tag{A.5}$$

Hence,

$$\begin{bmatrix} dz \\ dr \end{bmatrix} = \begin{bmatrix} z_{\xi} & z_{\eta} \\ r_{\xi} & r_{\eta} \end{bmatrix} \cdot \begin{bmatrix} d\xi \\ d\eta \end{bmatrix}; \tag{A.6}$$

as a result,

$$\begin{cases} dz = z_{\xi} d\xi + z_{\eta} d\eta \\ dr = r_{\xi} d\xi + r_{\eta} d\eta \end{cases}$$
 (A.7)

In addition, the gradient operators in the two coordinate systems are related as follows:

$$\vec{\nabla}^{\theta} = \begin{bmatrix} \frac{\partial}{\partial \xi} \\ \frac{\partial}{\partial \eta} \end{bmatrix} = \begin{bmatrix} z_{\xi} & r_{\xi} \\ z_{\eta} & r_{\eta} \end{bmatrix} \cdot \begin{bmatrix} \frac{\partial}{\partial z} \\ \frac{\partial}{\partial r} \end{bmatrix}$$
(A.8)

$$= \mathbf{J}^{\mathrm{T}} \,\vec{\nabla} \tag{A.9}$$

A.2 Numerical Interpolation and Integration

In order to interpolate and integrate variables within the reference elements shown in Fig. A.1, different sets of nodes are required. In this study, the Williams-Shunn (WS) nodal sets [7]

were used for the interpolation/representation of variables within the 2D/axisymmetric reference element shown in Fig. A.1b, where (p+1)(p+2)/2 nodes are required to represent a polynomial of order p. Distributions of the WS nodal sets for different polynomial orders are illustrated in Table A.1. This table also provides the integration order for these sets of nodes. These orders are the highest polynomial order which their numerical integration can be exactly carried out if the WS nodes are used for this purpose. However, in this study, the Witherden-Vincent (WV) nodal sets [8], which have stronger quadrature rules, were employed for the numerical integration over the 2D/axisymmetric reference element. Distributions of the WV nodal sets and their respective integration orders for different node numbers are provided in Table A.2.

Table A.1. Properties of the WS nodal sets [7]: the polynomial of order p which is represented by N nodes and associated with the quadrature rule of order q; and the nodal distributions within the 2D/axisymmetric reference element.

Node number (N)	1	3	6	10
Polynomial order (p)	0	1	2	3
Integration order (q)	1	2	4	5
ξ - η element				
Node number (N)	15	21	28	
Polynomial order (p)	4	5	6	
Integration order (q)	7	8	10	
ξ - η element				

Table A.2. Properties of the WV nodal sets [8]: the quadrature rule of order q associated with N nodes; and the nodal distributions within the 2D/axisymmetric reference element.

Node number (N)	1	3	6	7	12
Integration order (q)	1	2	4	5	6
ξ - η element					
Node number (N)	15	16	19	25	28
Integration order (q)	7	8	9	10	11
ξ - η element					
Node number (N)	33	37	42	49	
Integration order (q)	12	13	14	15	
ξ - η element					

Due to the selected numerical scheme in this study, some variables need to be represented along the edges of the 2D/axisymmetric reference element (or within the 1D reference element). In the current model, the Gauss-Legendre (GL) nodes [9] were used for such a purpose, where polynomials of order p need p+1 nodes to be represented. These nodes were also employed for the numerical integration within the 1D reference element, which their integration orders

are 2p + 1. Distributions of the GL nodal sets and their integration orders for different node numbers are provided in Table A.3.

To represent each node within the reference elements shown in Fig. A.1, the barycentric coordinate system $(\lambda_1, \lambda_2, \lambda_3)$ is used. The relation between the barycentric and the Cartesian (ξ, η) coordinate systems is:

$$\vec{r} = \sum_{i} \lambda_i \, \vec{v}_i \,, \tag{A.10}$$

where $\vec{r} = (\xi, \eta)$ is the coordinate of the respective node, and $\vec{v}_i = (\xi, \eta)$ is the coordinate of the *i*-th reference element vertex. These vertices are illustrated as red circles in Fig. A.1 for both the 1D and 2D/axisymmetric reference elements. In what follows, the barycentric coordinates and the integration weights (w) of the WS [7], WV [8], and GL [9] nodal sets for different node numbers (N) are provided in Tables A.4–A.6, respectively.

Table A.3. Properties of the GL nodal sets [9]: the polynomial of order p which is represented by N nodes and associated with the quadrature rule of order q; and the nodal distributions within the 1D reference element.

Node number (N)	1	2	3	4	5
Polynomial order (p)	0	1	2	3	4
Integration order (q)	1	3	5	7	9
ξ - η element				• • • • •	••••
Node number (N)	6	7	8	9	10
Polynomial order (p)	5	6	7	8	9
Integration order (q)	11	13	15	17	19
ξ - η element					

Table A.4. Barycentric coordinates $(\lambda_1, \lambda_2, \lambda_3)$ and the integration weights (w) for WS nodal sets [7] for different node numbers, N.

N	λ_1	λ_2	λ_3	w
1	0.3333333333333333	0.3333333333333333	0.3333333333333333	1.0000000000000000
3	0.66666666666666	0.16666666666666	0.16666666666666	0.333333333333333
	0.1666666666666667	0.66666666666666	0.1666666666666667	0.333333333333333333333333333333333333
	0.1666666666666667	0.1666666666666667	0.666666666666666666666666666666666666	0.33333333333333333
6	0.816847572980440	0.091576213509780	0.091576213509780	0.109951743655333
	0.091576213509780	0.816847572980440	0.091576213509780	0.109951743655333
	0.091576213509780	0.091576213509780	0.816847572980440	0.109951743655333
	0.108103018168072	0.445948490915964	0.445948490915964	0.223381589678000
	0.445948490915964	0.108103018168072	0.445948490915964	0.223381589678000
	0.445948490915964	0.445948490915964	0.108103018168072	0.223381589678000
10	0.634210747745723	0.295533711735893	0.070255540518384	0.112098412070887
	0.634210747745723	0.070255540518384	0.295533711735893	0.112098412070887
	0.295533711735893	0.634210747745723	0.070255540518384	0.112098412070887
	0.070255540518384	0.634210747745723	0.295533711735893	0.112098412070887
	0.295533711735893	0.070255540518384	0.634210747745723	0.112098412070887
	0.070255540518384	0.295533711735893	0.634210747745723	0.112098412070887
	0.888871894660414	0.055564052669793	0.055564052669793	0.041955512996649
	0.055564052669793	0.888871894660414	0.055564052669793	0.041955512996649
	0.055564052669793	0.055564052669793	0.888871894660414	0.041955512996649
	0.333333333333333333333333333333333333	0.333333333333333333333333333333333333	0.333333333333333333333333333333333333	0.201542988584730
15	0.751183631106484	0.201503881881800	0.047312487011716	0.055749810027115
	0.751183631106484	0.047312487011716	0.201503881881800	0.055749810027115
	0.201503881881800	0.751183631106484	0.047312487011716	0.055749810027115
	0.047312487011716	0.751183631106484	0.201503881881800	0.055749810027115
	0.201503881881800	0.047312487011716	0.751183631106484	0.055749810027115
	0.047312487011716	0.201503881881800	0.751183631106484	0.055749810027115
	0.928258244608532	0.035870877695734	0.035870877695734	0.017915455012303
	0.035870877695734	0.928258244608532	0.035870877695734	0.017915455012303
	0.035870877695734	0.035870877695734	0.928258244608532	0.017915455012303
	0.516541208464066	0.241729395767967	0.241729395767967	0.127712195881265
	0.241729395767967	0.516541208464066	0.241729395767967	0.127712195881265
	0.241729395767967	0.241729395767967	0.516541208464066	0.127712195881265
	0.051382424445842	0.474308787777079	0.474308787777079	0.076206062385535

	0.474308787777079	0.051382424445842	0.474308787777079	0.076206062385535
	0.474308787777079	0.474308787777079	0.051382424445842	0.076206062385535
21	0.817900980028499	0.148565812270887	0.033533207700614	0.028969269372473
	0.817900980028499	0.033533207700614	0.148565812270887	0.028969269372473
	0.148565812270887	0.817900980028499	0.033533207700614	0.028969269372473
	0.033533207700614	0.817900980028499	0.148565812270887	0.028969269372473
	0.148565812270887	0.033533207700614	0.817900980028499	0.028969269372473
	0.033533207700614	0.148565812270887	0.817900980028499	0.028969269372473
	0.604978911775133	0.357196298615681	0.037824789609186	0.046046366595935
	0.604978911775133	0.037824789609186	0.357196298615681	0.046046366595935
	0.357196298615681	0.604978911775133	0.037824789609186	0.046046366595935
	0.037824789609186	0.604978911775133	0.357196298615681	0.046046366595935
	0.357196298615681	0.037824789609186	0.604978911775133	0.046046366595935
	0.037824789609186	0.357196298615681	0.604978911775133	0.046046366595935
	0.943774095634672	0.028112952182664	0.028112952182664	0.010359374696538
	0.028112952182664	0.943774095634672	0.028112952182664	0.010359374696538
	0.028112952182664	0.028112952182664	0.943774095634672	0.010359374696538
	0.645721803061366	0.177139098469317	0.177139098469317	0.075394884326738
	0.177139098469317	0.645721803061366	0.177139098469317	0.075394884326738
	0.177139098469317	0.177139098469317	0.645721803061366	0.075394884326738
	0.188982808265134	0.405508595867433	0.405508595867433	0.097547802373242
	0.405508595867433	0.188982808265134	0.405508595867433	0.097547802373242
	0.405508595867433	0.405508595867433	0.188982808265134	0.097547802373242
28	0.867911210117950	0.107951981846011	0.024136808036039	0.015710461340183
	0.867911210117950	0.024136808036039	0.107951981846011	0.015710461340183
	0.107951981846011	0.867911210117950	0.024136808036039	0.015710461340183
	0.024136808036039	0.867911210117950	0.107951981846011	0.015710461340183
	0.107951981846011	0.024136808036039	0.867911210117950	0.015710461340183
	0.024136808036039	0.107951981846011	0.867911210117950	0.015710461340183
	0.700872570380723	0.270840772921567	0.028286656697710	0.028205136280616
	0.700872570380723	0.028286656697710	0.270840772921567	0.028205136280616
	0.270840772921567	0.700872570380723	0.028286656697710	0.028205136280616
	0.028286656697710	0.700872570380723	0.270840772921567	0.028205136280616
	0.270840772921567	0.028286656697710	0.700872570380723	0.028205136280616
	0.028286656697710	0.270840772921567	0.700872570380723	0.028205136280616
	0.536654684206138	0.316549598844617	0.146795716949245	0.066995957127830
	0.536654684206138	0.146795716949245	0.316549598844617	0.066995957127830

0.316549598844617	0.536654684206138	0.146795716949245	0.066995957127830
0.146795716949245	0.536654684206138	0.316549598844617	0.066995957127830
0.316549598844617	0.146795716949245	0.536654684206138	0.066995957127830
0.146795716949245	0.316549598844617	0.536654684206138	0.066995957127830
0.960045625755614	0.019977187122193	0.019977187122193	0.005272170280495
0.019977187122193	0.960045625755614	0.019977187122193	0.005272170280495
0.019977187122193	0.019977187122193	0.960045625755614	0.005272170280495
0.736556464940004	0.131721767529998	0.131721767529998	0.044552936679504
0.131721767529998	0.736556464940004	0.131721767529998	0.044552936679504
0.131721767529998	0.131721767529998	0.736556464940004	0.044552936679504
0.029729306413078	0.485135346793461	0.485135346793461	0.033815712804198
0.485135346793461	0.029729306413078	0.485135346793461	0.033815712804198
0.485135346793461	0.485135346793461	0.029729306413078	0.033815712804198
0.33333333333333333	0.333333333333333333333333333333333333	0.333333333333333333333333333333333333	0.083608212215637

Table A.5. Barycentric coordinates $(\lambda_1, \lambda_2, \lambda_3)$ and the integration weights (w) for WV nodal sets [8] for different node numbers, N.

\overline{N}	λ_1	λ_2	λ_3	w
1	0.3333333333333333	0.3333333333333333	0.3333333333333333	1.00000000000000000
3	0.6666666666666666666	0.16666666666666	0.166666666666666	0.333333333333333
	0.1666666666666667	0.6666666666666667	0.1666666666666667	0.333333333333333333333333333333333333
	0.1666666666666667	0.1666666666666667	0.6666666666666667	0.33333333333333333
6	0.816847572980459	0.091576213509771	0.091576213509771	0.109951743655322
	0.091576213509771	0.816847572980459	0.091576213509771	0.109951743655322
	0.091576213509771	0.091576213509771	0.816847572980459	0.109951743655322
	0.108103018168070	0.445948490915965	0.445948490915965	0.223381589678011
	0.445948490915965	0.108103018168070	0.445948490915965	0.223381589678011
	0.445948490915965	0.445948490915965	0.108103018168070	0.223381589678011
7	0.797426985353087	0.101286507323456	0.101286507323456	0.125939180544827
	0.101286507323456	0.797426985353087	0.101286507323456	0.125939180544827
	0.101286507323456	0.101286507323456	0.797426985353087	0.125939180544827
	0.059715871789770	0.470142064105115	0.470142064105115	0.132394152788506
	0.470142064105115	0.059715871789770	0.470142064105115	0.132394152788506
	0.470142064105115	0.470142064105115	0.059715871789770	0.132394152788506
	0.3333333333333333	0.3333333333333333	0.3333333333333333	0.2250000000000000
12	0.636502499121399	0.310352451033784	0.053145049844817	0.082851075618374

	0.636502499121399	0.053145049844817	0.310352451033784	0.082851075618374
	0.310352451033784	0.636502499121399	0.053145049844817	0.082851075618374
	0.053145049844817	0.636502499121399	0.310352451033784	0.082851075618374
	0.310352451033784	0.053145049844817	0.636502499121399	0.082851075618374
	0.053145049844817	0.310352451033784	0.636502499121399	0.082851075618374
	0.873821971016996	0.063089014491502	0.063089014491502	0.050844906370207
	0.063089014491502	0.873821971016996	0.063089014491502	0.050844906370207
	0.063089014491502	0.063089014491502	0.873821971016996	0.050844906370207
	0.501426509658179	0.249286745170910	0.249286745170910	0.116786275726379
	0.249286745170910	0.501426509658179	0.249286745170910	0.116786275726379
	0.249286745170910	0.249286745170910	0.501426509658179	0.116786275726379
15	0.754280040550053	0.198683314797352	0.047036644652595	0.055878732903200
	0.754280040550053	0.047036644652595	0.198683314797352	0.055878732903200
	0.198683314797352	0.754280040550053	0.047036644652595	0.055878732903200
	0.047036644652595	0.754280040550053	0.198683314797352	0.055878732903200
	0.198683314797352	0.047036644652595	0.754280040550053	0.055878732903200
	0.047036644652595	0.198683314797352	0.754280040550053	0.055878732903200
	0.932538702890824	0.033730648554588	0.033730648554588	0.016545050110792
	0.033730648554588	0.932538702890824	0.033730648554588	0.016545050110792
	0.033730648554588	0.033730648554588	0.932538702890824	0.016545050110792
	0.516845234809193	0.241577382595404	0.241577382595404	0.127944171230156
	0.241577382595404	0.516845234809193	0.241577382595404	0.127944171230156
	0.241577382595404	0.241577382595404	0.516845234809193	0.127944171230156
	0.051380614990564	0.474309692504718	0.474309692504718	0.077086646185986
	0.474309692504718	0.051380614990564	0.474309692504718	0.077086646185986
	0.474309692504718	0.474309692504718	0.051380614990564	0.077086646185986
16	0.728492392955404	0.263112829634638	0.008394777409958	0.027230314174435
	0.728492392955404	0.008394777409958	0.263112829634638	0.027230314174435
	0.263112829634638	0.728492392955404	0.008394777409958	0.027230314174435
	0.008394777409958	0.728492392955404	0.263112829634638	0.027230314174435
	0.263112829634638	0.008394777409958	0.728492392955404	0.027230314174435
	0.008394777409958	0.263112829634638	0.728492392955404	0.027230314174435
	0.898905543365938	0.050547228317031	0.050547228317031	0.032458497623198
	0.050547228317031	0.898905543365938	0.050547228317031	0.032458497623198
	0.050547228317031	0.050547228317031	0.898905543365938	0.032458497623198
	0.658861384496480	0.170569307751760	0.170569307751760	0.103217370534718
	0.170569307751760	0.658861384496480	0.170569307751760	0.103217370534718

	0.170569307751760	0.170569307751760	0.658861384496480	0.103217370534718
	0.081414823414554	0.459292588292723	0.459292588292723	0.095091634267285
	0.459292588292723	0.081414823414554	0.459292588292723	0.095091634267285
	0.459292588292723	0.459292588292723	0.081414823414554	0.095091634267285
	0.333333333333333333333333333333333333	0.333333333333333333333333333333333333	0.333333333333333333333333333333333333	0.144315607677787
19	0.741198598784498	0.221962989160766	0.036838412054736	0.043283539377289
	0.741198598784498	0.036838412054736	0.221962989160766	0.043283539377289
	0.221962989160766	0.741198598784498	0.036838412054736	0.043283539377289
	0.036838412054736	0.741198598784498	0.221962989160766	0.043283539377289
	0.221962989160766	0.036838412054736	0.741198598784498	0.043283539377289
	0.036838412054736	0.221962989160766	0.741198598784498	0.043283539377289
	0.910540973211095	0.044729513394453	0.044729513394453	0.025577675658698
	0.044729513394453	0.910540973211095	0.044729513394453	0.025577675658698
	0.044729513394453	0.044729513394453	0.910540973211095	0.025577675658698
	0.623592928761935	0.188203535619033	0.188203535619033	0.079647738927210
	0.188203535619033	0.623592928761935	0.188203535619033	0.079647738927210
	0.188203535619033	0.188203535619033	0.623592928761935	0.079647738927210
	0.020634961602525	0.489682519198738	0.489682519198738	0.031334700227139
	0.489682519198738	0.020634961602525	0.489682519198738	0.031334700227139
	0.489682519198738	0.489682519198738	0.020634961602525	0.031334700227139
	0.125820817014127	0.437089591492937	0.437089591492937	0.077827541004774
	0.437089591492937	0.125820817014127	0.437089591492937	0.077827541004774
	0.437089591492937	0.437089591492937	0.125820817014127	0.077827541004774
	0.333333333333333	0.333333333333333	0.333333333333333	0.097135796282799
25	0.807930600922879	0.163701733737182	0.028367665339939	0.025297757707289
	0.807930600922879	0.028367665339939	0.163701733737182	0.025297757707289
	0.163701733737182	0.807930600922879	0.028367665339939	0.025297757707289
	0.028367665339939	0.807930600922879	0.163701733737182	0.025297757707289
	0.163701733737182	0.028367665339939	0.807930600922879	0.025297757707289
	0.028367665339939	0.163701733737182	0.807930600922879	0.025297757707289
	0.601233328683459	0.369146781827811	0.029619889488730	0.034184648162959
	0.601233328683459	0.029619889488730	0.369146781827811	0.034184648162959
	0.369146781827811	0.601233328683459	0.029619889488730	0.034184648162959
	0.029619889488730	0.601233328683459	0.369146781827811	0.034184648162959
	0.369146781827811	0.029619889488730	0.601233328683459	0.034184648162959
	0.029619889488730	0.369146781827811	0.601233328683459	0.034184648162959
	0.530054118927344	0.321812995288836	0.148132885783821	0.063904906396424

	0.530054118927344	0.148132885783821	0.321812995288836	0.063904906396424
	0.321812995288836	0.530054118927344	0.148132885783821	0.063904906396424
	0.148132885783821	0.530054118927344	0.321812995288836	0.063904906396424
	0.321812995288836	0.148132885783821	0.530054118927344	0.063904906396424
	0.148132885783821	0.321812995288836	0.530054118927344	0.063904906396424
	0.935889253566113	0.032055373216944	0.032055373216944	0.013352968813150
	0.032055373216944	0.935889253566113	0.032055373216944	0.013352968813150
	0.032055373216944	0.032055373216944	0.935889253566113	0.013352968813150
	0.715677797886871	0.142161101056565	0.142161101056565	0.045957963604745
	0.142161101056565	0.715677797886871	0.142161101056565	0.045957963604745
	0.142161101056565	0.142161101056565	0.715677797886871	0.045957963604745
	0.333333333333333333333333333333333333	0.33333333333333333	0.333333333333333333333333333333333333	0.081743329146286
28	0.843349783661853	0.149324788652082	0.007325427686064	0.010290289572953
	0.843349783661853	0.007325427686064	0.149324788652082	0.010290289572953
	0.149324788652082	0.843349783661853	0.007325427686064	0.010290289572953
	0.007325427686064	0.843349783661853	0.149324788652082	0.010290289572953
	0.149324788652082	0.007325427686064	0.843349783661853	0.010290289572953
	0.007325427686064	0.149324788652082	0.843349783661853	0.010290289572953
	0.664408374196864	0.289581125637706	0.046010500165430	0.040332476640501
	0.664408374196864	0.046010500165430	0.289581125637706	0.040332476640501
	0.289581125637706	0.664408374196864	0.046010500165430	0.040332476640501
	0.046010500165430	0.664408374196864	0.289581125637706	0.040332476640501
	0.289581125637706	0.046010500165430	0.664408374196864	0.040332476640501
	0.046010500165430	0.289581125637706	0.664408374196864	0.040332476640501
	0.943029164771256	0.028485417614372	0.028485417614372	0.010431870512895
	0.028485417614372	0.943029164771256	0.028485417614372	0.010431870512895
	0.028485417614372	0.028485417614372	0.943029164771256	0.010431870512895
	0.794729034575507	0.102635482712247	0.102635482712247	0.038630759237019
	0.102635482712247	0.794729034575507	0.102635482712247	0.038630759237019
	0.102635482712247	0.102635482712247	0.794729034575507	0.038630759237019
	0.579560086593644	0.210219956703178	0.210219956703178	0.070515684111717
	0.210219956703178	0.579560086593644	0.210219956703178	0.070515684111717
	0.210219956703178	0.210219956703178	0.579560086593644	0.070515684111717
	0.008216198068218	0.495891900965891	0.495891900965891	0.016606273054585
	0.495891900965891	0.008216198068218	0.495891900965891	0.016606273054585
	0.495891900965891	0.495891900965891	0.008216198068218	0.016606273054585
	0.123068146471296	0.438465926764352	0.438465926764352	0.067316154079468

	0.438465926764352	0.123068146471296	0.438465926764352	0.067316154079468
	0.438465926764352	0.438465926764352	0.123068146471296	0.067316154079468
	0.3333333333333333	0.3333333333333333	0.3333333333333333	0.085761179732224
33	0.851337792510240	0.127279717233589	0.021382490256170	0.015083677576511
	0.851337792510240	0.021382490256170	0.127279717233589	0.015083677576511
	0.127279717233589	0.851337792510240	0.021382490256170	0.015083677576511
	0.021382490256170	0.851337792510240	0.127279717233589	0.015083677576511
	0.127279717233589	0.021382490256170	0.851337792510240	0.015083677576511
	0.021382490256170	0.127279717233589	0.851337792510240	0.015083677576511
	0.685310163906392	0.291655679738341	0.023034156355267	0.021783585038608
	0.685310163906392	0.023034156355267	0.291655679738341	0.021783585038608
	0.291655679738341	0.685310163906392	0.023034156355267	0.021783585038608
	0.023034156355267	0.685310163906392	0.291655679738341	0.021783585038608
	0.291655679738341	0.023034156355267	0.685310163906392	0.021783585038608
	0.023034156355267	0.291655679738341	0.685310163906392	0.021783585038608
	0.628249751683556	0.255454228638517	0.116296019677927	0.043227363659414
	0.628249751683556	0.116296019677927	0.255454228638517	0.043227363659414
	0.255454228638517	0.628249751683556	0.116296019677927	0.043227363659414
	0.116296019677927	0.628249751683556	0.255454228638517	0.043227363659414
	0.255454228638517	0.116296019677927	0.628249751683556	0.043227363659414
	0.116296019677927	0.255454228638517	0.628249751683556	0.043227363659414
	0.950707273127329	0.024646363436336	0.024646363436336	0.007931642509973
	0.024646363436336	0.950707273127329	0.024646363436336	0.007931642509973
	0.024646363436336	0.024646363436336	0.950707273127329	0.007931642509973
	0.781484344681292	0.109257827659354	0.109257827659354	0.028486052068877
	0.109257827659354	0.781484344681292	0.109257827659354	0.028486052068877
	0.109257827659354	0.109257827659354	0.781484344681292	0.028486052068877
	0.023592498108917	0.488203750945542	0.488203750945542	0.024266838081452
	0.488203750945542	0.023592498108917	0.488203750945542	0.024266838081452
	0.488203750945542	0.488203750945542	0.023592498108917	0.024266838081452
	0.457074985970148	0.271462507014926	0.271462507014926	0.062541213195903
	0.271462507014926	0.457074985970148	0.271462507014926	0.062541213195903
	0.271462507014926	0.271462507014926	0.457074985970148	0.062541213195903
	0.119776702682814	0.440111648658593	0.440111648658593	0.049918334928061
	0.440111648658593	0.119776702682814	0.440111648658593	0.049918334928061
	0.440111648658593	0.440111648658593	0.119776702682814	0.049918334928061
37	0.864707770295443	0.110922042803464	0.024370186901094	0.014965401105165

0.864707770295443	0.024370186901094	0.110922042803464	0.014965401105165
0.110922042803464	0.864707770295443	0.024370186901094	0.014965401105165
0.024370186901094	0.864707770295443	0.110922042803464	0.014965401105165
0.110922042803464	0.024370186901094	0.864707770295443	0.014965401105165
0.024370186901094	0.110922042803464	0.864707770295443	0.014965401105165
0.748507115899952	0.163597401067851	0.087895483032197	0.024179039811594
0.748507115899952	0.087895483032197	0.163597401067851	0.024179039811594
0.163597401067851	0.748507115899952	0.087895483032197	0.024179039811594
0.087895483032197	0.748507115899952	0.163597401067851	0.024179039811594
0.163597401067851	0.087895483032197	0.748507115899952	0.024179039811594
0.087895483032197	0.163597401067851	0.748507115899952	0.024179039811594
0.722357793124188	0.272515817773430	0.005126389102382	0.009590681003544
0.722357793124188	0.005126389102382	0.272515817773430	0.009590681003544
0.272515817773430	0.722357793124188	0.005126389102382	0.009590681003544
0.005126389102382	0.722357793124188	0.272515817773430	0.009590681003544
0.272515817773430	0.005126389102382	0.722357793124188	0.009590681003544
0.005126389102382	0.272515817773430	0.722357793124188	0.009590681003544
0.623545995553676	0.308441760892118	0.068012243554207	0.034641276140848
0.623545995553676	0.068012243554207	0.308441760892118	0.034641276140848
0.308441760892118	0.623545995553676	0.068012243554207	0.034641276140848
0.068012243554207	0.623545995553676	0.308441760892118	0.034641276140848
0.308441760892118	0.068012243554207	0.623545995553676	0.034641276140848
0.068012243554207	0.308441760892118	0.623545995553676	0.034641276140848
0.956980637782314	0.021509681108843	0.021509681108843	0.006052337103539
0.021509681108843	0.956980637782314	0.021509681108843	0.006052337103539
0.021509681108843	0.021509681108843	0.956980637782314	0.006052337103539
0.557255427416334	0.221372286291833	0.221372286291833	0.058278485119200
0.221372286291833	0.557255427416334	0.221372286291833	0.058278485119200
0.221372286291833	0.221372286291833	0.557255427416334	0.058278485119200
0.021846107094921	0.489076946452539	0.489076946452539	0.023994401928895
0.489076946452539	0.021846107094921	0.489076946452539	0.023994401928895
0.489076946452539	0.489076946452539	0.021846107094921	0.023994401928895
0.146117171480399	0.426941414259800	0.426941414259800	0.055601967530453
0.426941414259800	0.146117171480399	0.426941414259800	0.055601967530453
0.426941414259800	0.426941414259800	0.146117171480399	0.055601967530453
0.33333333333333333	0.333333333333333333333333333333333333	0.33333333333333333	0.067960036586832
0.879757171370171	0.118974497696957	0.001268330932872	0.005010228838501

0.879757171370171	0.001268330932872	0.118974497696957	0.005010228838501
0.118974497696957	0.879757171370171	0.001268330932872	0.005010228838501
0.001268330932872	0.879757171370171	0.118974497696957	0.005010228838501
0.118974497696957	0.001268330932872	0.879757171370171	0.005010228838501
0.001268330932872	0.118974497696957	0.879757171370171	0.005010228838501
0.770608554774997	0.172266687821356	0.057124757403648	0.024665753212564
0.770608554774997	0.057124757403648	0.172266687821356	0.024665753212564
0.172266687821356	0.770608554774997	0.057124757403648	0.024665753212564
0.057124757403648	0.770608554774997	0.172266687821356	0.024665753212564
0.172266687821356	0.057124757403648	0.770608554774997	0.024665753212564
0.057124757403648	0.172266687821356	0.770608554774997	0.024665753212564
0.686980167808088	0.298372882136258	0.014646950055654	0.014436308113534
0.686980167808088	0.014646950055654	0.298372882136258	0.014436308113534
0.298372882136258	0.686980167808088	0.014646950055654	0.014436308113534
0.014646950055654	0.686980167808088	0.298372882136258	0.014436308113534
0.298372882136258	0.014646950055654	0.686980167808088	0.014436308113534
0.014646950055654	0.298372882136258	0.686980167808088	0.014436308113534
0.570222290846683	0.336861459796345	0.092916249356972	0.038571510787061
0.570222290846683	0.092916249356972	0.336861459796345	0.038571510787061
0.336861459796345	0.570222290846683	0.092916249356972	0.038571510787061
0.092916249356972	0.570222290846683	0.336861459796345	0.038571510787061
0.336861459796345	0.092916249356972	0.570222290846683	0.038571510787061
0.092916249356972	0.336861459796345	0.570222290846683	0.038571510787061
0.961218077502598	0.019390961248701	0.019390961248701	0.004923403602400
0.019390961248701	0.961218077502598	0.019390961248701	0.004923403602400
0.019390961248701	0.019390961248701	0.961218077502598	0.004923403602400
0.876400233818255	0.061799883090873	0.061799883090873	0.014433699669776
0.061799883090873	0.876400233818255	0.061799883090873	0.014433699669776
0.061799883090873	0.061799883090873	0.876400233818255	0.014433699669776
0.645588935174913	0.177205532412544	0.177205532412544	0.042162588736993
0.177205532412544	0.645588935174913	0.177205532412544	0.042162588736993
0.177205532412544	0.177205532412544	0.645588935174913	0.042162588736993
0.022072179275643	0.488963910362179	0.488963910362179	0.021883581369429
0.488963910362179	0.022072179275643	0.488963910362179	0.021883581369429
0.488963910362179	0.488963910362179	0.022072179275643	0.021883581369429
0.453044943382323	0.273477528308839	0.273477528308839	0.051774104507292
0.273477528308839	0.453044943382323	0.273477528308839	0.051774104507292

	0.273477528308839	0.273477528308839	0.453044943382323	0.051774104507292
	0.164710561319092	0.417644719340454	0.417644719340454	0.032788353544125
	0.417644719340454	0.164710561319092	0.417644719340454	0.032788353544125
	0.417644719340454	0.417644719340454	0.164710561319092	0.032788353544125
49	0.919912157726236	0.070948605236455	0.009139237037308	0.004029853372018
	0.919912157726236	0.009139237037308	0.070948605236455	0.004029853372018
	0.070948605236455	0.919912157726236	0.009139237037308	0.004029853372018
	0.009139237037308	0.919912157726236	0.070948605236455	0.004029853372018
	0.070948605236455	0.009139237037308	0.919912157726236	0.004029853372018
	0.009139237037308	0.070948605236455	0.919912157726236	0.004029853372018
	0.813292641049419	0.168068645222414	0.018638713728166	0.011672621181576
	0.813292641049419	0.018638713728166	0.168068645222414	0.011672621181576
	0.168068645222414	0.813292641049419	0.018638713728166	0.011672621181576
	0.018638713728166	0.813292641049419	0.168068645222414	0.011672621181576
	0.168068645222414	0.018638713728166	0.813292641049419	0.011672621181576
	0.018638713728166	0.168068645222414	0.813292641049419	0.011672621181576
	0.715222356931451	0.190535589476394	0.094242053592155	0.028720586925201
	0.715222356931451	0.094242053592155	0.190535589476394	0.028720586925201
	0.190535589476394	0.715222356931451	0.094242053592155	0.028720586925201
	0.094242053592155	0.715222356931451	0.190535589476394	0.028720586925201
	0.190535589476394	0.094242053592155	0.715222356931451	0.028720586925201
	0.094242053592155	0.190535589476394	0.715222356931451	0.028720586925201
	0.666975644801868	0.314648242812451	0.018376112385681	0.015602572830576
	0.666975644801868	0.018376112385681	0.314648242812451	0.015602572830576
	0.314648242812451	0.666975644801868	0.018376112385681	0.015602572830576
	0.018376112385681	0.666975644801868	0.314648242812451	0.015602572830576
	0.314648242812451	0.018376112385681	0.666975644801868	0.015602572830576
	0.018376112385681	0.314648242812451	0.666975644801868	0.015602572830576
	0.565252664877114	0.338950611475277	0.095796723647609	0.031315476284969
	0.565252664877114	0.095796723647609	0.338950611475277	0.031315476284969
	0.338950611475277	0.565252664877114	0.095796723647609	0.031315476284969
	0.095796723647609	0.565252664877114	0.338950611475277	0.031315476284969
	0.338950611475277	0.095796723647609	0.565252664877114	0.031315476284969
	0.095796723647609	0.338950611475277	0.565252664877114	0.031315476284969
	0.968376547498023	0.015811726250989	0.015811726250989	0.002960774637905
	0.015811726250989	0.968376547498023	0.015811726250989	0.002960774637905
	0.015811726250989	0.015811726250989	0.968376547498023	0.002960774637905

0.859652894200028	0.070173552899986	0.070173552899986	0.016444737562625
0.070173552899986	0.859652894200028	0.070173552899986	0.016444737562625
0.070173552899986	0.070173552899986	0.859652894200028	0.016444737562625
0.547242573159301	0.226378713420350	0.226378713420350	0.046783361728709
0.226378713420350	0.547242573159301	0.226378713420350	0.046783361728709
0.226378713420350	0.226378713420350	0.547242573159301	0.046783361728709
0.010006086461747	0.494996956769126	0.494996956769126	0.009573846182460
0.494996956769126	0.010006086461747	0.494996956769126	0.009573846182460
0.494996956769126	0.494996956769126	0.010006086461747	0.009573846182460
0.051658637123960	0.474170681438020	0.474170681438020	0.017396148000763
0.474170681438020	0.051658637123960	0.474170681438020	0.017396148000763
0.474170681438020	0.474170681438020	0.051658637123960	0.017396148000763
0.189275571732049	0.405362214133975	0.405362214133975	0.042713781571461
0.405362214133975	0.189275571732049	0.405362214133975	0.042713781571461
0.405362214133975	0.405362214133975	0.189275571732049	0.042713781571461
0.333333333333333	0.33333333333333333	0.33333333333333333	0.044335387382184

Table A.6. Barycentric coordinates (λ_1, λ_2) and the integration weights (w) for GL nodal sets [9] for different node numbers, N.

N	λ_1	λ_2	w
1	0.50000000000000000	0.50000000000000000	1.00000000000000000
2	0.788675134594813	0.211324865405187	0.5000000000000000
	0.211324865405187	0.788675134594813	0.5000000000000000
3	0.887298334620742	0.112701665379258	0.27777777777778
	0.5000000000000000	0.5000000000000000	0.4444444444444444
	0.112701665379258	0.887298334620742	0.277777777777778
4	0.930568155797026	0.069431844202974	0.173927422568727
	0.669990521792428	0.330009478207572	0.326072577431273
	0.330009478207572	0.669990521792428	0.326072577431273
	0.069431844202974	0.930568155797026	0.173927422568727
5	0.953089922969332	0.046910077030668	0.118463442528095
	0.769234655052841	0.230765344947159	0.239314335249683
	0.5000000000000000	0.5000000000000000	0.2844444444444444
	0.230765344947159	0.769234655052841	0.239314335249683
	0.046910077030668	0.953089922969332	0.118463442528095
6	0.966234757101576	0.033765242898424	0.085662246189585

	0.830604693233132	0.169395306766868	0.180380786524069
	0.619309593041598	0.380690406958402	0.233956967286345
	0.380690406958402	0.619309593041598	0.233956967286345
	0.169395306766868	0.830604693233132	0.180380786524069
	0.033765242898424	0.966234757101576	0.085662246189585
7	0.974553956171379	0.025446043828621	0.064742483084435
	0.870765592799697	0.129234407200303	0.139852695744638
	0.702922575688699	0.297077424311301	0.190915025252559
	0.5000000000000000	0.5000000000000000	0.208979591836735
	0.297077424311301	0.702922575688699	0.190915025252559
	0.129234407200303	0.870765592799697	0.139852695744638
	0.025446043828621	0.974553956171379	0.064742483084435
8	0.980144928248768	0.019855071751232	0.050614268145188
	0.898333238706813	0.101666761293187	0.111190517226687
	0.762766204958164	0.237233795041836	0.156853322938944
	0.591717321247825	0.408282678752175	0.181341891689181
	0.408282678752175	0.591717321247825	0.181341891689181
	0.237233795041836	0.762766204958164	0.156853322938944
	0.101666761293187	0.898333238706813	0.111190517226687
	0.019855071751232	0.980144928248768	0.050614268145188
9	0.984080119753813	0.015919880246187	0.040637194180787
	0.918015553663318	0.081984446336682	0.090324080347429
	0.806685716350295	0.193314283649705	0.130305348201468
	0.662126711701904	0.337873288298096	0.156173538520001
	0.5000000000000000	0.5000000000000000	0.165119677500630
	0.337873288298096	0.662126711701904	0.156173538520001
	0.193314283649705	0.806685716350295	0.130305348201468
	0.081984446336682	0.918015553663318	0.090324080347429
	0.015919880246187	0.984080119753813	0.040637194180787
10	0.986953264258586	0.013046735741414	0.033335672154344
	0.932531683344492	0.067468316655508	0.074725674575290
	0.839704784149512	0.160295215850488	0.109543181257991
	0.716697697064624	0.283302302935376	0.134633359654998
	0.574437169490816	0.425562830509184	0.147762112357376
	0.425562830509184	0.574437169490816	0.147762112357376
	0.283302302935376	0.716697697064624	0.134633359654998
	0.160295215850488	0.839704784149512	0.109543181257991

 $\begin{array}{llll} 0.067468316655508 & 0.932531683344492 & 0.074725674575290 \\ 0.013046735741414 & 0.986953264258586 & 0.033335672154344 \end{array}$

Bibliography

- [1] C. E. Brennen, Cavitation and bubble dynamics, Cambridge University Press, 2013.
- [2] W. Lauterborn, T. Kurz, Physics of bubble oscillations, Rep. Prog. Phys. 73 (2010) 106501. doi:10.1088/0034-4885/73/10/106501.
- [3] K. Maeda, T. Colonius, Bubble cloud dynamics in an ultrasound field, arXiv preprint arXiv:1805.00129 (2018). doi:10.1017/jfm.2018.968.
- [4] A. P. Brysev, L. M. Krutyansky, P. Pernod, V. L. Preobrazhensky, Nonlinear ultrasonic phase-conjugate beams and their application in ultrasonic imaging, Acoust. Phys. 50 (2004) 623–640. doi:10.1134/1.1825091.
- [5] R. Geisler, Untersuchungen zur laserinduzierten Kavitation mit Nanosekunden-und Femtosekundenlasern (nvestigation of laser induced cavitation with nano- and femtosecond lasers), Ph.D. thesis, 2004.
- [6] W. Lauterborn, T. Kurz, R. Mettin, C. Ohl, Experimental and theoretical bubble dynamics, Adv. Chem. Phys. 110 (1999) 295–380. doi:10.1002/9780470141694.ch5.
- [7] F. D. Witherden, P. E. Vincent, An analysis of solution point coordinates for flux reconstruction schemes on triangular elements, J. Sci. Comput. 61 (2014) 398–423. doi:10.1007/s10915-014-9832-2.
- [8] F. D. Witherden, P. E. Vincent, On the identification of symmetric quadrature rules for finite element methods, Comput. Math. Appl. 69 (2015) 1232–1241. doi:10.1016/j.camwa.2015.03.017.

[9] M. Abramowitz, I. A. Stegun, Handbook of mathematical functions: with formulas, graphs, and mathematical tables, volume 55, Courier Corporation, 1965.

- [10] K. Maeda, T. Colonius, Eulerian-lagrangian method for simulation of cloud cavitation, J. Comput. Phys. 371 (2018) 994–1017. doi:10.1016/j.jcp.2018.05.029.
- [11] F. G. Blake, The onset of cavitation in liquids, Technical Report 12, 1949.
- [12] E. Neppiras, B. Noltingk, Cavitation produced by ultrasonics: theoretical conditions for the onset of cavitation, Proceedings of the Physical Society. Section B 64 (1951) 1032. doi:10.1088/0370-1301/64/12/302.
- [13] R. Apfel, Acoustic cavitation prediction, J. Acoust. Soc. Am. 69 (1981) 1624–1633. doi:10.1121/1.385939.
- [14] U. Parlitz, V. Englisch, C. Scheffczyk, W. Lauterborn, Bifurcation structure of bubble oscillators, J. Acoust. Soc. Am. 88 (1990) 1061–1077. doi:10.1121/1.399855.
- [15] W. Lauterborn, E. Suchla, Bifurcation superstructure in a model of acoustic turbulence, Phys. Rev. Lett. 53 (1984) 2304. doi:10.1103/physrevlett.53.2304.
- [16] U. Parlitz, W. Lauterborn, Resonances and torsion numbers of driven dissipative nonlinear oscillators, Z. Naturforsch. 41 (1986) 605–614. doi:10.1515/zna-1986-0404.
- [17] P. Smereka, S. Banerjee, The dynamics of periodically driven bubble clouds, Phys. Fluids 31 (1988) 3519. doi:10.1063/1.866919.
- [18] B. Birnir, P. Smereka, Existence theory and invariant manifolds of bubble clouds, Commun. Pure Appl. Math. 43 (1990) 363–413. doi:10.1002/cpa.3160430304.
- [19] L. Rayleigh, On the pressure developed in a liquid during the collapse of a spherical cavity, Philos. Mag. 34 (1917) 94–98. doi:10.1080/14786440808635681.
- [20] F. R. Gilmore, The growth or collapse of a spherical bubble in a viscous compressible liquid, Technical Report 26–4, Hydrodynamics Laboratory, California Institute of Technology, Pasadena, California, USA, 1952.

[21] J. B. Keller, M. Miksis, Bubble oscillations of large amplitude, J. Acoust. Soc. Am. 68 (1980) 628–633. doi:10.1121/1.384720.

- [22] S. Popinet, S. Zaleski, Bubble collapse near a solid boundary: a numerical study of the influence of viscosity, J. Fluid Mech. 464 (2002) 137–163. doi:10.1017/s002211200200856x.
- [23] A. Prosperetti, A. Lezzi, Bubble dynamics in a compressible liquid. part 1. first-order theory, J. Fluid Mech. 168 (1986) 457–478. doi:10.1017/s0022112086000460.
- [24] S. Kumar, C. E. Brennen, Some nonlinear interactive effects in bubbly clouds, J. Fluid Mech. 253 (1993) 565–591. doi:10.1017/s0022112093001909.
- [25] K. Morch, Energy considerations on the collapse of cavity clusters, in: Mechanics and Physics of Bubbles in Liquids, Springer, 1982, pp. 313–321. doi:10.1007/978-94-009-7532-3_29.
- [26] G. Chahine, Cloud cavitation: theory, in: Proc. 14th Symp. on Naval Hydrodynamics, Washington DC, USA, 1983, pp. 165–194. doi:10.1121/1.395376.
- [27] R. Omta, Oscillations of a cloud of bubbles of small and not so small amplitude, J. Acoust. Soc. Am. 82 (1987) 1018–1033. doi:10.1121/1.395376.
- [28] L. V. Wijngaarden, One-dimensional flow of liquids containing small gas bubbles, Annu. Rev. Fluid Mech. 4 (1972) 369–396. doi:10.1146/annurev.fl.04.010172.002101.
- [29] L. L. Foldy, The multiple scattering of waves. i. general theory of isotropic scattering by randomly distributed scatterers, Phys. Rev. 67 (1945) 107–119. doi:10.1103/physrev. 67.107.
- [30] F. E. Fox, S. R. Curley, G. S. Larson, Phase velocity and absorption measurements in water containing air bubbles, J. Acoust. Soc. Am. 27 (1955) 534–539. doi:10.1121/1. 1907955.
- [31] J. D. Macpherson, The effect of gas bubbles on sound propagation in water, Proceedings of the Physical Society. Section B 70 (1957) 85. doi:10.1088/0370-1301/70/1/312.

[32] E. Silberman, Sound velocity and attenuation in bubbly mixtures measured in standing wave tubes, J. Acoust. Soc. Am. 29 (1957) 925–933. doi:10.1121/1.1909101.

- [33] R. E. Caflisch, M. J. Miksis, G. C. Papanicolaou, L. Ting, Effective equations for wave propagation in bubbly liquids, J. Fluid Mech. 153 (1985) 259. doi:10.1017/ s0022112085001252.
- [34] L. V. Wijngaarden, On the equations of motion for mixtures of liquid and gas bubbles, J. Fluid Mech. 33 (1968) 465–474. doi:10.1017/s002211206800145x.
- [35] K. W. Commander, A. Prosperetti, Linear pressure waves in bubbly liquids: Comparison between theory and experiments, J. Acoust. Soc. Am. 85 (1989) 732–746. doi:10.1121/ 1.397599.
- [36] I. Koltsova, L. Krynskii, I. Mikhailov, I. Pokrovskaya, Attenuation of ultrasonic-waves in low-viscosity liquids containing gas-bubbles, Sov. Phys. Acoust. 25 (1979) 409–413.
- [37] A. Ruggles, R. Lahey, D. Drew, H. Scarton, An investigation of the propagation of pressure perturbations in bubbly air/water flows, J. Heat Transf. 110 (1988) 494–499. doi:10.1115/1.3250513.
- [38] L. d'Agostino, C. E. Brennen, Linearized dynamics of spherical bubble clouds, J. Fluid Mech. 199 (1989) 155–176. doi:10.1017/s0022112089000339.
- [39] L. d'Agostino, C. E. Brennen, On the acoustical dynamics of bubble clouds, in: Applied Mechanics, Bioengineering, and Fluids Engineering Conference, volume FED-2, American Society of Mechanical Engineers, Houston, Texas, 1983, pp. 72–75.
- [40] Y.-C. Wang, C. E. Brennen, Numerical computation of shock waves in a spherical cloud of cavitation bubbles, J. Fluid Eng. 121 (1999) 872–880. doi:10.1115/1.2823549.
- [41] D. Fuster, T. Colonius, Modelling bubble clusters in compressible liquids, J. Fluid Mech. 688 (2011) 352–389. doi:10.1017/jfm.2011.380.
- [42] R. S. Mackay, G. Rubissow, Decompression studies using ultrasonic imaging of bubbles, IEEE T. Bio-Med. Eng. BME-25 (1978) 537–544. doi:10.1109/tbme.1978.326288.

[43] P. Shirkovskiy, V. L. Preobrazhensky, P. Pernod, Coherent scattering of phase conjugate ultrasound waves in bubbly media, IEEE Trans. Ultrason. Ferroelectr. Freq. Control 62 (2015) 721–728. doi:10.1109/tuffc.2014.006764.

- [44] W. M. Fairbank, M. O. Scully, A new noninvasive technique for cardiac pressure measurement: Resonant scattering of ultrasound from bubbles, IEEE T. Bio-Med. Eng. BME-24 (1977) 107–110. doi:10.1109/tbme.1977.326112.
- [45] V. Newhouse, P. M. Shankar, Bubble size measurements using the nonlinear mixing of two frequencies, J. Acoust. Soc. Am. 75 (1984) 1473–1477. doi:10.1121/1.390863.
- [46] J. Chapelon, P. Shankar, V. Newhouse, Ultrasonic measurement of bubble cloud size profiles, J. Acoust. Soc. Am. 78 (1985) 196–201. doi:10.1121/1.392558.
- [47] M. Cavaro, C. Payan, J. Moysan, F. Baqué, Microbubble cloud characterization by nonlinear frequency mixing, J. Acoust. Soc. Am. 129 (2011) EL179–EL183. doi:10. 1121/1.3565474.
- [48] A. P. Brysev, L. M. Krutyanskii, V. L. Preobrazhenskii, Wave phase conjugation of ultrasonic beams, Phys.-Uspekhi 41 (1998) 793–805. doi:10.1070/PU1998v041n08ABEH000429.
- [49] B. Y. Zel'dovich, V. Popovichev, V. Ragul'skii, F. Faizullov, Connection between the wave fronts of the reflected and exciting light in stimulated Mandel'shtam-Brillouin scattering, JETP Lett. 15 (1972) 109–112. doi:10.1142/9789812832047 0033.
- [50] L. O. Svaasand, Interation between elastic surface waves in piezoelectric materials, Appl. Phys. Lett. 15 (1969) 300–302. doi:10.1063/1.1653007.
- [51] A. Merlen, Q. Zhang, Theory and simulation of wave phase conjugation, Ultrasonics 44 (2006) e1475–e1478. doi:10.1016/j.ultras.2006.05.170.
- [52] A. Merlen, Q. Zhang, P. Voinovich, E. Timofeev, Duality of the supercritical solutions in magnetoacoustic wave phase conjugation, Wave Motion 46 (2009) 255–268. doi:10.1016/j.wavemoti.2009.02.003.

[53] A. P. Brysev, F. V. Bunkin, L. M. Krutyansky, X. Yan, M. F. Hamilton, Focused nonlinear phase-conjugate waves generated by a solid parametric amplifier, J. Acoust. Soc. Am. 118 (2005) 3733–3736. doi:10.1121/1.2130965.

- [54] A. Merlen, V. L. Preobrazhensky, P. Pernod, Supercritical parametric phase conjugation of ultrasound. numerical simulation of nonlinear and nonstationary mode, J. Acoust. Soc. Am. 112 (2002) 2656–2665. doi:10.1121/1.1506687.
- [55] V. Preobrazhensky, Overthreshold nonlinearity of parametric sound wave phase conjugation in solids, Jpn. J. Appl. Phys. 32 (1993) 2247–2251. doi:10.1143/jjap.32.2247.
- [56] M. Fink, G. Montaldo, M. Tanter, Time reversal acoustics, in: IEEE Ultrasonics Symposium, volume 2, Institute of Electrical & Electronics Engineers (IEEE), 2004, pp. 850–859. doi:10.1109/ultsym.2004.1417870.
- [57] K. Yamamoto, P. Pernod, V. Preobrazhensky, Visualization of phase conjugate ultrasound waves passed through inhomogeneous layer, Ultrasonics 42 (2004) 1049–1052. doi:10.1016/j.ultras.2003.12.041.
- [58] A. Brysev, L. Krutyansky, P. Pernod, V. Preobrazhensky, Acoustic microscope based on magneto-elastic wave phase conjugator, Appl. Phys. Lett. 76 (2000) 3133–3135. doi:10.1063/1.126547.
- [59] L. Krutyansky, P. Pernod, A. Brysev, F. Bunkin, V. Preobrazhensky, Supercritical parametric wave phase conjugation as an instrument for narrowband analysis in ultrasonic harmonic imaging, IEEE Trans. Ultrason. Ferroelectr. Freq. Control 49 (2002) 409–414. doi:10.1109/58.996558.
- [60] Y. Pylnov, P. Pernod, V. Preobrazhensky, Acoustic imaging by second harmonic of phase-conjugate wave in inhomogeneous medium, Appl. Phys. Lett. 78 (2001) 553–555. doi:10.1063/1.1342205.
- [61] L. Krutyansky, V. Preobrazhensky, P. Pernod, O. Bou Matar, Nonlinear imaging of isoechogenic phantoms using phase conjugation of the second acoustic harmonic, Phys. Wave Phenom. 15 (2007) 186–190. doi:10.3103/s1541308x07030053.

[62] S. V. Preobrazhensky, S. V. L. Preobrazhensky, P. Pernod, O. Bou Matar, Testing for inhomogeneity of the nonlinear parameter in an acoustic medium by ultrasonic phase conjugation, Acoust. Phys. 54 (2008) 15–19. doi:10.1134/s106377100801003x.

- [63] V. Preobrazhensky, P. Pernod, Y. Pylnov, L. Krutyansky, N. Smagin, S. Preobrazhensky, Nonlinear acoustic imaging of isoechogenic objects and flows using ultrasound wave phase conjugation, Acta Acust. united Ac. 95 (2009) 36–45. doi:10.3813/aaa.918125.
- [64] Y. V. Pylnov, Detection of moving objects and flows in liquids by ultrasonic phase conjugation, Acoust. Phys. 51 (2005) 105. doi:10.1134/1.1851635.
- [65] V. L. Preobrazhensky, Parametrically phase-conjugate waves: applications in nonlinear acoustic imaging and diagnostics, Phys.-Uspekhi 49 (2006) 98–102. doi:10.1070/ PU2006v049n01ABEH005879.
- [66] A. P. Brysev, F. V. Bunkin, M. F. Hamilton, R. V. Klopotov, L. M. Krutyanskii, K. Yan, Parametric phase conjugation for the second harmonic of a nonlinear ultrasonic beam, Acoust. Phys. 49 (2003) 19–23. doi:10.1134/1.1537383.
- [67] A. Merlen, Q. Zhang, Paraxial theory of supercritical wave phase conjugation in a realistic magnetoacoustic conjugator, Appl. Phys. Lett. 89 (2006) 194102. doi:10.1063/ 1.2374691.
- [68] A. Merlen, Q. Zhang, Resonant solutions in wave phase conjugation induced by a limited magnetoacoustic conjugator, J. Acoust. Soc. Am. 119 (2006) 3637–3648. doi:10.1121/1.2197799.
- [69] P. Pernod, V. Preobrazhensky, Parametric phase conjugation of a wide-band acoustic pulse in supercritical mode, Appl. Phys. Lett. 76 (2000) 387–389. doi:10.1063/1. 125762.
- [70] S. B. Khelil, A. Merlen, V. Preobrazhensky, P. Pernod, Numerical simulation of acoustic wave phase conjugation in active media, J. Acoust. Soc. Am. 109 (2001) 75–83. doi:10.1121/1.1328794.

[71] P. Voinovich, A. Merlen, Two-dimensional numerical simulation of acoustic wave phase conjugation in magnetostrictive elastic media, J. Acoust. Soc. Am. 118 (2005) 3491–3498. doi:10.1121/1.2130964.

- [72] P. Voinovich, A. Merlen, E. Timofeev, K. Takayama, A godunov-type finite-volume scheme for unified solid-liquid elastodynamics on arbitrary two-dimensional grids, Shock Waves 13 (2003) 221–230. doi:10.1007/s00193-003-0211-4.
- [73] O. Bou Matar, V. Preobrazhensky, P. Pernod, Two-dimensional axisymmetric numerical simulation of supercritical phase conjugation of ultrasound in active solid media, J. Acoust. Soc. Am. 118 (2005) 2880–2890. doi:10.1121/1.2062467.
- [74] A. Modarreszadeh, E. Timofeev, High-order numerical simulation of axisymmetric wave phase conjugation, Comput. Fluids (2019) 104353. doi:10.1016/j.compfluid. 2019.104353.
- [75] K. B. Cunningham, M. F. Hamilton, A. P. Brysev, L. M. Krutyansky, Time-reversed sound beams of finite amplitude, J. Acoust. Soc. Am. 109 (2001) 2668–2674. doi:10. 1121/1.1368405.
- [76] J. Leadbetter, E. Timofeev, A. Merlen, D. Frost, On the high order numerical modeling of ultrasonic waves in fluids, in: Proc. of the 19th Annual Conference of CFD Society of Canada, Montreal, Quebec April 27–29, 2011.
- [77] J. Leadbetter, High Order Numerical Models for High Amplitude Ultrasonic Wave Propagation, Master's thesis, McGill University, 2011. URL: McGill-Library.
- [78] P. Shirkovskiy, V. Preobrazhensky, P. Pernod, S. Koshelyuk, Phase conjugation of ultrasound waves in comparison with backscattering in disordered medium, Wave Motion 60 (2016) 149–157. doi:10.1016/j.wavemoti.2015.08.007.
- [79] P. Shirkovskiy, N. Smagin, V. Preobrazhenskii, P. Pernod, Scattering of phase-conjugate ultrasonic waves by microinclusions in a liquid flow, Acoust. Phys. 62 (2016) 58–63. doi:10.1134/s1063771015060111.

[80] V. Preobrazhensky, P. Pernod, Y. Pylnov, L. Krutyansky, A. Brysev, Nonlinear diagnostics of statistical distribution of bubbles sizes by means of WPC, Technical Report 2.1.2, Joint Franco-Russian International Laboratory LIA LICS, 2016.

- [81] S. Ginter, M. Liebler, E. Steiger, T. Dreyer, R. E. Riedlinger, Full-wave modeling of therapeutic ultrasound: Nonlinear ultrasound propagation in ideal fluids, J. Acoust. Soc. Am. 111 (2002) 2049–2059. doi:10.1121/1.1468876.
- [82] M. F. Hamilton, D. T. Blackstock, et al., Nonlinear acoustics, volume 1, Academic press San Diego, 1998.
- [83] A. Brysev, P. Pernod, V. Preobrazhensky, Magneto-acoustic ceramics for parametric sound wave phase conjugators, Ultrasonics 38 (2000) 834–837. doi:10.1016/S0041-624X(99)00193-6.
- [84] W. M. Lai, D. H. Rubin, E. Krempl, D. Rubin, Introduction to continuum mechanics, Butterworth-Heinemann, 2009.
- [85] L. E. Kinsler, A. R. Frey, A. B. Coppens, J. V. Sanders, Fundamentals of acoustics, J. Wiley, 2000.
- [86] J.-P. Berenger, A perfectly matched layer for the absorption of electromagnetic waves, J. Comput. Phys. 114 (1994) 185–200. doi:10.1006/jcph.1994.1159.
- [87] Y. Li, O. Bou Matar, Y. Bao, Nearly perfectly matched layer (NPML) absorbing boundary condition for elastic waves propagation in solid, J. Acoust. Soc. Am. 131 (2012) 3443–3443. doi:10.1121/1.4708932.
- [88] S. Cummer, A simple, nearly perfectly matched layer for general electromagnetic media, IEEE Microw. Wirel. Compon. Lett. 13 (2003) 128–130. doi:10.1109/lmwc. 2003.810124.
- [89] W. Hu, A. Abubakar, T. M. Habashy, Application of the nearly perfectly matched layer in acoustic wave modeling, Geophysics 72 (2007) SM169–SM175. doi:10.1190/1. 2738553.

[90] K. Van den Abeele, Development of high-order accurate schemes for unstructured grids, Ph.D. thesis, Vrije Universiteit Brussel, 2009.

- [91] Z. Wang, High-order methods for the Euler and Navier-Stokes equations on unstructured grids, Prog. Aerosp. Sci. 43 (2007) 1-41. doi:10.1016/j.paerosci.2007.05.001.
- [92] T. Haga, H. Gao, Z. J. Wang, A high-order unifying discontinuous formulation for the Navier–Stokes equations on 3D mixed grids, Math. Model. Nat. Phenom. 6 (2011) 28–56. doi:10.1051/mmp/20116302.
- [93] H. Huynh, Z. Wang, P. Vincent, High-order methods for computational fluid dynamics: A brief review of compact differential formulations on unstructured grids, Comput. Fluids 98 (2014) 209–220. doi:10.1016/j.compfluid.2013.12.007.
- [94] P. E. Vincent, P. Castonguay, A. Jameson, A new class of high-order energy stable flux reconstruction schemes, J. Sci. Comput. 47 (2010) 50–72. doi:10.1007/ s10915-010-9420-z.
- [95] M. Yu, Z. Wang, On the accuracy and efficiency of several discontinuous high-order formulations, in: 51st AIAA Aerospace Sciences Meeting including the New Horizons Forum and Aerospace Exposition, AIAA 2013-0855, American Institute of Aeronautics and Astronautics (AIAA), Grapevine, Texas, 2013. doi:10.2514/6.2013-855.
- [96] Z. Wang, H. Gao, A unifying lifting collocation penalty formulation including the discontinuous Galerkin, spectral volume/difference methods for conservation laws on mixed grids, J. Comput. Phys. 228 (2009) 8161–8186. doi:10.1016/j.jcp.2009.07. 036.
- [97] W. H. Reed, T. Hill, Triangular mesh methods for the neutron transport equation, Los Alamos Report LA-UR-73-479 (1973).
- [98] B. Van Leer, Towards the ultimate conservative difference scheme. IV. A new approach to numerical convection, J. Comput. Phys. 23 (1977) 276–299. doi:10.1016/0021-9991(77)90095-x.

[99] B. Cockburn, S. Hou, C.-W. Shu, The Runge–Kutta local projection discontinuous Galerkin finite element method for conservation laws. IV. The multidimensional case, Math. Comput. 54 (1990) 545–545. doi:10.1090/s0025-5718-1990-1010597-0.

- [100] B. Cockburn, C.-W. Shu, Runge–Kutta discontinuous Galerkin methods for convection-dominated problems, J. Sci. Comput. 16 (2001) 173–261. doi:10.1023/a: 1012873910884.
- [101] F. Bassi, S. Rebay, High-order accurate discontinuous finite element solution of the 2D Euler equations, J. Comput. Phys. 138 (1997) 251–285. doi:10.1006/jcph.1997.5454.
- [102] F. Bassi, S. Rebay, A high-order accurate discontinuous finite element method for the numerical solution of the compressible Navier–Stokes equations, J. Comput. Phys. 131 (1997) 267–279. doi:10.1006/jcph.1996.5572.
- [103] J. S. Hesthaven, T. Warburton, Nodal Discontinuous Galerkin Methods: Algorithms, Analysis, and Applications, Springer New York, 2008. doi:10.1007/978-0-387-72067-8.
- [104] M. Yu, Z. Wang, Y. Liu, On the accuracy and efficiency of discontinuous Galerkin, spectral difference and correction procedure via reconstruction methods, J. Comput. Phys. 259 (2014) 70–95. doi:10.1016/j.jcp.2013.11.023.
- [105] D. I. Ketcheson, Highly efficient strong stability-preserving Runge-Kutta methods with low-storage implementations, SIAM J. Sci. Comput. 30 (2008) 2113–2136. doi:10. 1137/07070485x.
- [106] C. B. Macdonald, Constructing High-Order Runge-Kutta Methods with Embedded Strong-Stability-Preserving Pairs, Master's thesis, Simon Fraser University, 2003.
- [107] S. Gottlieb, C.-W. Shu, Total variation diminishing Runge–Kutta schemes, Math. Comput. 67 (1998) 73–85. doi:10.1090/s0025-5718-98-00913-2.
- [108] J.-P. Berenger, On the reflection from cummer's nearly perfectly matched layer, IEEE Microw. Wirel. Compon. Lett. 14 (2004) 334–336. doi:10.1109/LMWC.2004.829272.

[109] S. C. Spiegel, H. Huynh, J. R. DeBonis, De-aliasing through over-integration applied to the flux reconstruction and discontinuous galerkin methods, in: 22nd AIAA Computational Fluid Dynamics Conference, AIAA 2015-2744, American Institute of Aeronautics and Astronautics (AIAA), Dallas, TX, 2015. doi:10.2514/6.2015-2744.

- [110] R. J. LeVeque, Wave propagation algorithms for multidimensional hyperbolic systems, J. Comput. Phys. 131 (1997) 327–353. doi:10.1006/jcph.1996.5603.
- [111] R. J. LeVeque, Finite volume methods for hyperbolic problems, volume 31, Cambridge university press, 2002.
- [112] A. C. Hindmarsh, ODEPACK, a systematized collection of ode solvers, Scientific computing (1983) 55–64.
- [113] C. Geuzaine, J.-F. Remacle, Gmsh: a 3-d finite element mesh generator with built-in pre- and post-processing facilities, Int. J. Numer. Methods Fluids 79 (2009) 1309–1331. doi:10.1002/nme.2579.
- [114] J. Ahrens, B. Geveci, C. Law, Paraview: an end-user tool for large data visualization, The visualization handbook 717 (2005).
- [115] B. O. Enflo, C. M. Hedberg, Theory of nonlinear acoustics in fluids, volume 67, Springer Science & Business Media, 2006. doi:10.1007/0-306-48419-6.
- [116] A. I. Beltzer, Acoustics of solids, Springer Science & Business Media, 2012. doi:10. 1007/978-3-642-83370-0.
- [117] J. Diaz, A. Ezziani, Analytical solution for waves propagation in heterogeneous acoustic/porous media. part i: the 2d case, Commun. Comput. Phys. 7 (2010) 171. doi:10.4208/cicp.2009.08.148.
- [118] D. Komatitsch, C. Barnes, J. Tromp, Wave propagation near a fluid-solid interface: a spectral-element approach, Geophysics 65 (2000) 623–631. doi:10.1190/1.1444758.

[119] A. Modarreszadeh, E. Timofeev, A. Merlen, O. Bou-Matar, P. Pernod, High-order numerical simulation of axisymmetric wave phase conjugation, in: 26th Annual Conf. of the CFD Society of Canada, Paper MS-366, 8 pages, Winnipeg, Manitoba, 2018.

[120] A. Modarreszadeh, E. Timofeev, A. Merlen, P. Pernod, Numerical simulation of bubble size measurement via wave phase conjugation, in: 26th International Congress on Sound and Vibration (ICSV26), Montreal, Canada, 2019. URL: ICSV26.